

University of Louisville

ThinkIR: The University of Louisville's Institutional Repository

Electronic Theses and Dissertations

5-2015

Bi-stable buckled energy harvesters actuated via torque arms.

Daniel Allen Porter
University of Louisville

Follow this and additional works at: <https://ir.library.louisville.edu/etd>



Part of the [Mechanical Engineering Commons](#)

Recommended Citation

Porter, Daniel Allen, "Bi-stable buckled energy harvesters actuated via torque arms." (2015). *Electronic Theses and Dissertations*. Paper 2065.

<https://doi.org/10.18297/etd/2065>

This Doctoral Dissertation is brought to you for free and open access by ThinkIR: The University of Louisville's Institutional Repository. It has been accepted for inclusion in Electronic Theses and Dissertations by an authorized administrator of ThinkIR: The University of Louisville's Institutional Repository. This title appears here courtesy of the author, who has retained all other copyrights. For more information, please contact thinkir@louisville.edu.

BI-STABLE BUCKLED ENERGY HARVESTERS ACTUATED VIA TORQUE ARMS

By

Daniel Allen Porter
B.S., Mechanical Engineering 2007
M.S., Mechanical Engineering 2010

A Dissertation
Submitted to the Faculty of the
JB Speed School of Engineering University of Louisville
In Partial Fulfillment of the Requirements
for the Degree of

Doctor of Philosophy in Mechanical Engineering

Department of Mechanical Engineering
University of Louisville
Louisville, Kentucky

May 2015

Copyright 2015 by Daniel Allen Porter

All rights reserved

BI-STABLE BUCKLED ENERGY HARVESTERS ACTUATED VIA TORQUE ARMS

By

Daniel Allen Porter
B.S., Mechanical Engineering 2007
M.S., Mechanical Engineering 2010

A Dissertation Approved On

March 30, 2015

By the following Dissertation Committee:

Dr. Thomas A. Berfield
Dissertation Director

Dr. Roger Bradshaw
Mechanical Engineering

Dr. Stuart Williams
Mechanical Engineering

Dr. Shamus McNamara
Electrical & Computer Engineering

ACKNOWLEDGMENTS

Much thanks to my advisor, Dr. Berfield, for giving me direction and an opportunity to achieve something I never thought I could have in this life. The gift of confidence, knowledge, and teamwork will serve me well. I wish him the best.

I would like to thank my mother, father, sister, and brother for their love and support throughout this long endeavor. Knowing I have a loving family who encouraged me to grasp the best life has to offer keeps my resolve strong and my potential limitless.

Thanks to my friends, Kyle Hord, Trung Hoang, Russel Prater, Andrew Work, and Tim Broering who kept me sane during long and rigorous work hours, they are of great importance and may never know how greatly needed they were and are.

Lastly I would like to thank the Mechanical Engineering Department which through the long years has granted me the know-how to solve problems in the field of mechanical engineering. Problem solving is a feat no one should live without.

Most men and women struggle all their lives for fame or money... mine was and always will be knowledge.

ABSTRACT

BI-STABLE BUCKLED ENERGY HARVESTERS ACTUATED VIA TORQUE ARMS

Daniel Allen Porter

March 30, 2015

Vibrational energy harvesters (VEH) are one way to generate electricity. Though the energy quantities are not enough to run desktop computers, they can power remote devices such as temperature, pressure, and accelerometer sensors or power biological implants. New versions of the Bluetooth protocol can even be used with VEH technology to send wireless data. An important aspect of VEH devices is the power output, operating frequency, and bandwidth.

This dissertation investigates a novel method of actuating the primary buckled energy harvesting structure using torque arms as a force amplification mechanism. Buckled structures can exhibit snap-through and has the potential to broaden the operating frequency for the VEH. Macro and MEMS size prototypes are fabricated and evaluated via a custom made shaker table. The effect of compliance arms, which pin the center beam with piezoelectric strips, are also evaluated along with damping ratios. ANSYS models evaluating generated power are created for use in future optimization studies. Lastly, high energy orbitals (HEO) are observed in the devices.

Results show that buckling lowers and broadens the output power of the new devices. Reverse sweeps drastically increase the operating frequency during snap-through. Rectangular compliance arms made of poly-lactic acid (PLA) generated the most power of all compliance arms tested. HEO performance can be induced by perturbing the system while maintaining the same input force which increases power output.

TABLE OF CONTENTS

	Page
ACKNOWLEDGEMENTS.....	iii
ABSTRACT.....	iv
LIST OF TABLES.....	viii
LIST OF FIGURES.....	x
 CHAPTER	
I INTRODUCTION	1
A. Microelectromechanical System Benefits	2
B. Power Requirements for MEMS Sensors and Actuators.....	6
C. Renewable Energy and Energy Generating Materials.....	7
D. Buckled Structures and Their Potential Applications	12
E. Previous Work on Energy Harvesting	14
II NEW ENERGY HARVESTING CONCEPT AND MEMS	17
A. Design of a Bi-Stable Buckled Structure	18
B. Typical Fabrication Methods and Steps	20
C. Proof of Concept.....	26
III PZT AND PVDF PIEZOELECTRIC ENERGY HARVESTING	31
A. Piezoelectric Coefficients.....	34
B. Limitations of PZT Ceramics	37
C. Experiments to Evaluate Coefficients	40
D. PZT Fabrication Routines	42
E. PVDF Fabrication Routines.....	51
F. Experimental Poling Results.....	59
IV THEORETICAL GOVERNING EQUATIONS	66
A. Euler Buckling Analysis.....	66
B. Potential Energy Model	71

C.	Theoretical Mechanical Model Development	74
D.	Dynamic Analysis	79
V MEMS ANSYS MODELING		82
A.	Determining Piezoelectric Matrix for ANSYS	83
B.	Model and Elements for Analysis	85
C.	ANSYS Snap-through Loads and Displacements	89
VI MEMS ENERGY HARVESTER FABRICATION		91
A.	Design and Planned Fabrication Steps	92
B.	Bi-Stable Buckled Energy Harvester Utilizing PZT	99
VII PIEZOELECTRIC ENERGY HARVESTING MODEL.....		116
VIII MACRO ENERGY HARVESTER CONCEPT AND DESIGN.....		122
A.	Materials and Fabrication.....	122
B.	Quasi-Static Behavior.....	125
C.	Dynamic Behavior.....	130
D.	Experimental Discussion.....	138
E.	ANSYS Non-linear Harmonic Analysis.....	141
F.	ANSYS Voltage and Power Estimation.....	155
IX EFFECT OF COMPLIANCE ARM CONSTRAINTS		161
A.	Design Considerations and Specifications of Fabricated Devices ..	162
B.	Shaker Table Setup.....	164
C.	Optimum Load.....	165
D.	Evaluation of Damping	166
E.	Parametric Evaluation of Compliance Arms	168
F.	ANSYS Modal Frequency Simulations	169
G.	Power Generation	169
H.	Promotion into High Energy Orbits	178
I.	Discussion of Compliance Arm Effect and HEO	180
J.	Torque Arm Effect Conclusion	182
X SUMMARY		184
XI FUTURE WORKS		189
A.	Design Optimization Feasibility.....	189

B. High Energy Orbital Stitched Bandwidth.....	190
C. Potential Additional Advancements	191
REFERENCES	193
APPENDIX A (SYMBOLS AND ABBREVIATIONS)	209
APPENDIX B (FIGURES AND TABLES).....	211
APPENDIX C (CODE).....	228
APPENDIX D (MEMS FABRICATION RECIPES)	233
APPENDIX E (ENERGY HARVESTER METRICS).....	235
CURRICULUM VITA	239

LIST OF TABLES

TABLE	Page
1. Typical power and energy densities for some potential renewable energy sources.....	8
2. Operating frequencies and accelerations of machines, activities, and structures ([117], [124], [121], [60], [131]).....	9
3. Different energy harvesting mechanisms and their advantages [124].	10
4. Energy harvesting mechanisms and the equations that govern their power output [122].....	10
5. Durou's PZT energy harvesting device performance (top) and the comparison devices (bottom) [38].	11
6. MEMS energy harvesting devices with large resonant frequencies [104]. Park, <i>et al's</i> , work is shown as the last row in the table.....	11
7. Components for the mechanically enhanced ($Zr/Ti=53.5/46.5$) "Stock PZT Solution" from [156] and [157].	33
8. Standard symbols used in the characterization of piezoelectrics.....	34
9. Young's modulus, ultimate yield stress, and fracture strain for sol-gel based 2 μ m thick PZT dog bone shaped samples [104].....	38
10. Experimental thickness results for PVDF gel films after hotplate/annealing treatments.....	54
11. Materials used in the ANSYS model.	88
12. MEMS with PZT geometric variables and their assignments.	95
13. Tube furnace input parameters for UofL's cleanroom to get ~900 nm SiO ₂ .	100
14. PECVD recipe to obtain ~-700 MPa stressed silicon nitride.....	101
15. Silicon nitride etching recipe using March RIE.....	101
16. Material properties used in ANSYS analysis.....	126

17.	Proof mass displacements from resting position required to induce stability state switching for both finite element analysis model and experimental tests.....	128
18.	Maximum and minimum displacement points for FEA and experimental results.	129
19.	Undamped FEA and experimental natural frequencies.	131
20.	Power comparison of the TA device and DBC.....	138
21.	Damping ratios for the tested compressed and uncompressed devices using different methods.	168
22.	Forward sweep data for all devices tested.	171
23.	Reverse sweep data for all devices tested.	171
24.	Chirp results for the 8 mm length compliance arm devices. Bold indicates devices that can be induced into high energy orbitals.	179
25.	PZT samples setup and results.....	211
26.	A few results from the PVDF gel experiments.	216
27.	Performance index evaluation for forward swept experiments.	235
28.	Performance index evaluation for the reverse swept experiments.....	235
29.	NPD metric for the forward swept experiments.	236
30.	NPD metric for the reverse swept experiments.	236
31.	FoM _{BW} metric for the forward sweep experiments.	237
32.	FoM _{BW} metric for the reverse sweep experiments.....	237
33.	Swept volume, input displacement at max, and mass for the forward swept experiments.	238
34.	Swept volume, input displacement at max, and mass for the reverse swept experiments.	238

LIST OF FIGURES

FIGURE	Page
1 Rendering of the bi-stable piezoelectric energy harvester.	1
2 a) Simple schematic showing operation, b) 3D print showing buckled up, and c) buckled down position.	2
3 MEMS devices fabricated using cleanroom techniques a) gyroscope [59], b) accelerometer [54], c) PZT energy harvester [131], d) electrostatic micromotor [47].	4
4 Past and future market prediction for MEMS devices [17].	5
5 MEMS market by device [16].	5
6 Volumetric power for different energy sources versus lifetime [124].	7
7 Single pole double throw bi-stable membrane switch before a) and after actuation b) [53].	12
8 Thermally actuated membrane microvalve [109].	13
9 A PZT based micropump [99].	14
10 Bi-stable buckled beam constrained at both ends and in the middle.	17
11 First iteration of device with one big proof mass.	18
12 Final proof of concept device with polyimide torque arms and two separate proof masses.	19
13 PECVD silicon nitride stress versus RF frequency.	20
14 Non-piezoelectric prototype mask 1, the unstressed nitride layer. Scale bar is about the same for each mask layer shown below.	22
15 Non-piezoelectric prototype mask 2, chrome protection layer.	22
16 Non-piezoelectric prototype mask 3, stressed nitride layer.	23
17 Non-piezoelectric prototype mask 4, polyimide layer.	23
18 Non-piezoelectric prototype mask 5, DRIE layer.	24

19	Buckled cross structure a) before and b) after DRIE etching (backside).	25
20	Buckled mass structure a) before (topside) and b) after DRIE etching (backside) with no piezoelectric active layer.	25
21	SEM images of a) buckled cross structures and b) structures with proof masses.....	26
22	Buckled mass device with a) 1,500 μm and b) 600 μm long center beam.....	27
23	Displacement vs length for a buckled mass device with a 1,500 μm long center beam; measured on a Dektak profilometer.....	27
24	Macro scale model in one bi-stable buckled condition (mass arms up).....	28
25	Macro scale model in the other bi-stable buckled condition (mass arms down).....	29
26	3D printed adjustable bi-stable buckled prototype with locking gear.....	29
27	3D printed multi-node prototype.....	30
28	Visual examples detailing the meaning of the piezoelectric strain coefficient d_{ij}	36
29	Leakage current as a function of electric field for PZT (45/55) with thicknesses of a) 1.3 μm and b) 0.3 μm [29].....	39
30	Electric breakdown strength versus thickness for PZT (45/55) [29].....	39
31	PZT (1:1:1) on SiO_2 annealed at 450 C in an ambient atmosphere for samples a) 1b, b) 2b, c) 3b, and d) 4b.	43
32	PZT (1:1:1) on SiO_2 annealed at 550 C in an ambient atmosphere for samples a) 1b, b) 2b, c) 3b, and d) 4b.	44
33	PZT (1:1:1) on platinum sample die after one gel application and anneal a) perov1, b) perov2, c) perov3, and d) perov4.	46
34	PZT (1:1:1) on platinum sample die after the second gel application and anneal a) perov1, b) perov2, c) perov3, and d) perov4.	47
35	Schematic illustrating constructive interference of x-rays on a crystal structure [96].	48
36	GA-XRD results for PZT for a) known reference specimens [77], b) silicon wafer, Si/ SiO_2 /Ti/Pt, and samples with (1:1:1), and c) more thin to thick specimens to make sure process is repeatable.....	49

37	PZT (1:1:1) on platinum samples a), d), g) before and b), e), h) after etching. Also with c), f), i) photoresist removed.....	50
38	PZT (1:1:1) on platinum sample Perov4 a) after etching and removing photoresist and b) a zoomed in section to show undercut.....	51
39	a) PVDF pellets, b) PVDF powder, and c) DMF solvent.....	52
40	Angular velocity vs a) film thickness and b) β -phase for PVDF films from [22].	53
41	FTIR data for 10%wt PVDF films spun on at 1000 rpm and dried at 50 and 70 C.	55
42	SEM images for four of the PVDF films containing 2.9% hydrated salt by weight and dried at a) 100C, b) 115C, c) 130C, and d) 150C. Prior to annealing.	56
43	XRD sweeps for PVDF gel deposition samples (1 μ m thick) with the addition of 0.3% hydrated salt before annealing.	56
44	a) PVDF electroded device on aluminum foil and b) PVDF film that has been sputtered with aluminum via PVD.	57
45	Electrode materials a) ‘Anders Products’ carbon based wire glue, b) ‘Circuit Works’ CW2400 conductive epoxy, c) ‘Bare Conductive’ electrically conductive paint, and d) ‘MG Chemicals’ pure silver conductive epoxy.	58
46	a) All PVDF samples tested for the application of gel deposition, b) double sided electrode samples ready for poling, c) 4” wafer rings used to peel off PVDF.....	59
47	Failed and charred PVDF sample with conductive epoxy electrodes.	60
48	PZT contact poled examples.	61
49	High voltage power supply a) schematic, b) side view showing CCFL, b) top showing banana plug interfaces, and d) voltage multiplier immersed in mineral oil.....	62
50	a), b) Render of the designed corona poler and c), d) actual fabricated corona poler with heated bed.	63
51	Sawyer-Tower circuit used to generate ferroelectric hysteresis loops.	64
52	Saturated ferroelectric loop for a 250nm thick layer of PZT.	65

53	a) A beam buckling under an axial force. b) A cross section of the same beam. [10].....	67
54	Famous buckling cases [10].	69
55	Beam with axial force and distributed load [20].	69
56	Axial deflection with a given axial load [72].	72
57	Desired mechanical model for the bi-stable buckled device.	74
58	Theoretical model displacement for a 1.5 mm long silicon nitride beam with 300 MPa of compressive stress.	78
59	Theoretical model theta for a 1.5 mm long silicon nitride beam with 300 MPa of compressive stress.	78
60	Theoretical model moment for a 1.5 mm long silicon nitride beam with 300 MPa of compressive stress.	79
61	Theoretical model shear for a 1.5 mm long silicon nitride beam with 300 MPa of compressive stress.	79
62	a) Timoshenko section describing kinematics of deformation and b) an example of a dynamic pinned and clamped rod with proof mass and rotary actuated [81].	80
63	Center displacement for a buckled bi-stable MEMS membrane made out of SiO ₂ and polyimide A) given various diameters, B) picture of a 1,500 μm buckled membrane in the up position.....	83
64	Stress in the x-direction for a silicon nitride film constrained on three sides. Temperature is difference 1,000K.....	86
65	Graph of stress in the x-direction for the silicon nitride film.	86
66	ANSYS model of prototype with script file geometric variables. The names given here have changed in later versions.	87
67	Contour plot of the y-displacement for the prototype with the stressed portion of the beam at -360 MPa. Units are in mm and color indicates displacement in the y-direction.	88
68	Y-displacement of the stressed middle beam.	89
69	Displacement versus total load applied to center masses. Snap-through occurring at around 44uN for a pre-stress of -300 MPa, stressed and	

	unstressed nitride thickness of 0.5 and 0.5 μm respectively, and a beam length of 1,500 μm	90
70	MEMS fabricated prototype (left) and a macro scale prototype (right) of our device. Both with no active piezoelectric layer.....	92
71	Half model MEMS device with PZT parameters.....	94
72	Piezoelectric capable device photomask design showing a) all masks and alignment markers with b) stressed nitride, c) unstressed nitride, d) bottom electrode, e) PZT etch, f) top electrode, g) polyimide, h) DRIE masks stacked on top of each other.	96
73	Mask designs for the bi-stable buckled beam MEMS device a) overview, b) stressed nitride, c) unstressed nitride, d) bottom electrode, e) PZT etch, f) top electrode, g) polyimide, h) DRIE etch, i) zoom in of top electrode showing interdigitated array.	97
74	Other devices being fabricated with proposed device; cantilever beams with a) interdigitated and b) sandwiched electrodes, and c) a multi-node bi-stable snap-through device.	99
75	Device wafer with stressed nitride, unstressed nitride, and Ti/Pt bottom electrodes.....	102
76	Blistered wafer after firing at 650 C with a) all layers up to PZT and b) just stressed silicon nitride.	103
77	Microscope photos of Dev18 after the stressed and unstressed nitride etch a) electrode platform, b) center of buckled beam, c) center of buckled beam for wider device, and d) alignment markers.	105
78	Microscope photos of Dev18 after bottom electrode platinum liftoff for a) buckled beam anchor section, b) center of buckled beam, c) UofL logo on all die, and d) alignment markers.	106
79	Microscope photos of Dev18 after PZT etching a) bottom electrode delaminating, b) bottom electrode completely, c) partially, and d) not delaminated.	107

80	Microscope photos of Dev18 after top electrode etch for a) base of center buckled beam, b) top electrode next to delaminated bottom electrode, c) center of stressed beam, and d) base of cantilever interdigitated beam.	108
81	Microscope photos of Dev18 after polyimide etch for a) alignment markers, b) near base of cantilever beam electrodes, c) center of stressed buckled beam, and d) proof mass of a bi-stable device.	109
82	Backside microscope photos of Dev18 after DRIE etching but before being released a) alignment markers, b) acceptably aligned device, c) almost acceptable, d) very misaligned, e) close up of resist residue and crystal bond, and destroyed cantilever beams.....	111
83	Microscope photos of released Dev18 die a) DRIE cut edge of die, b) top side, c) side view showing top electrode pads, d) close up of mass tips, e) long center beam device focus, and f) short center beam focus.	112
84	SEM images of Dev18 released die a) short center beam device, b) long center beam device, c) angled view of long device, and d) electrodes for long device.....	113
85	SEM images of Dev18 center beam showing a) device, b) close up of polyimide, and c) cross section of beam showing stressed SiO ₂ , unstressed nitride, PZT, and polyimide.	114
86	a) General equivalent circuit model [118], b) equivalent circuit model using the first two modes [11].....	116
87	Definition of electromechanical coupling coefficient for a pure piezoelectric material using a thermodynamic cycle. Modified from [118].....	119
88	Molecular chain of PVDF in the a) non-polar α and b) polar β phase.	123
89	a) Stainless steel cutout dimensions, b) PLA planar dimensions, c) assembly exploded view, d) assembly collapsed view and associated PVDF beam section labeling scheme.	124
90	a) Base and clamping mechanisms to hold the device, b) device in buckled up state, and c) device in buckled down state.	125
91	Side view of device in a bi-stable state a) buckled upwards and b) buckled downwards.....	127

92	FEA model results for 0.25mm of center beam compression showing a) the mesh of the structure in the buckled “down” state, b) the vertical mass displacement through “snap-through”, c) the center beam deflection profile, and d) the axial (x-direction) strain for the center beam.	129
93	Peak-peak voltages for “forward” frequency sweeps of the “front” and “back” center beam PVDF sections under different constant RMS acceleration levels.	132
94	Peak-peak voltages for “backward” frequency sweeps of the “front” and “back” center beam PVDF sections at different constant RMS acceleration levels.....	132
95	V_{rms} device output values for backward and forward sweeps of all channels at driving accelerations of 0.5 and 0.9 g_{rms}	134
96	Time variant results at frequencies corresponding to the maximum back channel RMS voltage during backwards sweeps on the uncompressed beam at a) 0.5 g_{rms} and b) 0.9 g_{rms} ; the 0.13mm compressed beam at c) 0.5 g_{rms} and d) 0.9 g_{rms} ; and the 0.25mm compressed beam at e) 0.5 g_{rms} and f) 0.9 g_{rms}	136
97	Doubly constrained beam in the unbuckled state a), and RMS power results from b) a forward sweep, and c) a backwards sweep.....	137
98	Point masses and areas for ANSYS non-linear harmonic sweep.	141
99	Mesh for ANSYS non-linear harmonic sweep.....	142
100	Loading conditions for a non-linear sweep in ANSYS.....	143
101	ANSYS settings for the non-linear sweep.....	144
102	Maple solutions for a constant acceleration, linear frequency, sinusoidal sweep involving use of the Fresnel function.	147
103	Base displacement inputs for the a) forward and b) reverse sweeps equivalent to a 0.3 g_{rms} acceleration, time step is 0.001 seconds.....	148
104	Difference between the derived Excel and the true Maple function.	149
105	Displacement peak detection results for the base and tip of the 3x1 device in a a) forward and b) reverse 0.3 g_{rms} ANSYS sweep setup.	150
106	Peak outline results for the base and tip of the 3x1 device in a a) forward and b) reverse 0.3 g_{rms} ANSYS sweep setup.....	151

107	Comparison of the unbuckled harmonic sweep gains for the forward experimental, linear harmonic displacement driven, and linear harmonic acceleration driven at 0.3 g _{rms}	152
108	Comparison of the buckled harmonic sweep gains for the non-linear harmonic transient, forward experimental, linear harmonic displacement driven, and linear harmonic acceleration driven (with temperature induced buckling stress) 0.3 g _{rms} analysis.	153
109	Forward and reverse non-linear harmonic transient runs at 0.6g _{rms}	154
110	Cantilever beam response for a 80x10x0.75mm steel beam with a 10 gram mass at the end. The displacement load emulates a 0.3 g _{rms} acceleration.	155
111	Circuit components to consider in the FEA power estimation model.....	157
112	a) Circuit used in calculating power output from FEA model with negligible components removed and b) simplified circuit.	158
113	FEA buckled RMS power results at static driving frequencies compared to experimental sweeps for a 3x1 device with 8mm long compliance arms.	160
114	Main components of energy harvesting device, including the (a) torque arm PLA brace, the (b) steel shim stock center beam with PVDF strips, and the compliance arms constructed in the (c) pinned, (d) 3x1, and (e) 5x1 configurations.	163
115	(a) Render of designed shaker table, and (b) the as-fabricated shaker table. ..	165
116	Normalized voltage response versus load impedance for the (a) back and (b) front electrode, all tested using 8mm compliance arms.	166
117	(a) Voltage output and (b) gain response plots for the 3x1 mm device with 8 mm compliance arms.....	168
118	Power results for the 3x1 mm device in the (a) unbuckled forward sweep (b) buckled forward sweep (c) unbuckled reverse sweep and (d) buckled reverse sweep case. Compliance arms are 8 mm long.....	170
119	Power generation performance index metric for the forward (left) and reverse (right) cases.	174
120	Stitching method for the pinned device with 8mm compliance arms combining bandwidths.	175

121	Performance index from stitching for the pinned device with 8mm compliance arms.....	176
122	FoM _{BW} metric for the bi-stable buckled energy harvesters in the forward (left) and reverse (right) sweep direction.	177
123	Chirp response of the pinned device in the unbuckled (above), compared to the maintained high-energy orbital in the buckled configuration (below).	179
124	High energy orbit operation of a non-linear VEH [44].	180
125	Multiple node bi-stable device being fabricated.	191
126	PZT (1:2:1) on SiO ₂ annealed at 450 C in an ambient atmosphere for samples a) 1c, b) 2c, c) 3c, and d) 4c.	212
127	PZT (1:2:1) on SiO ₂ annealed at 550 C in an ambient atmosphere for samples a) 1d, b) 2d, c) 3d, and d) 4d.	212
128	One coat of PZT (1:1:1) on platinum before and after being annealed at 650 C in an O ₂ atmosphere for samples a) 1e, b) 1e, c) 1f, d) 2f, e) 1g, and f) 1g..	213
129	Two coat of PZT (1:1:1) on platinum before and after being annealed at 650 C in an O ₂ atmosphere for samples a) 1e, b) 1e, c) 1f, d) 2f, e) 1g, and f) 1g..	214
130	a) 250V DC power supply used for contact poling, b), c) prototype corona poling mechanism.....	215
131	FTIR-ATR results for 5% PVDF with and without hydrated salt. Gel spun on individual die at 1000 rpm.....	217
132	FTIR results for 10% PVDF with and without hydrated salt spun at 3000 rpm.....	217
133	FTIR results for 20% PVDF without hydrated salt spun at 5000 rpm.	218
134	RMS power vs frequency for the uncompressed glued pin device. Acceleration from 0.2 to 0.6 g _{rms}	218
135	RMS power vs frequency for the compressed glued pin device. Acceleration from 0.2 to 0.6 g _{rms}	219
136	RMS power vs frequency for the uncompressed pinned device. Acceleration from 0.2 to 0.6 g _{rms}	219
137	RMS power vs frequency for the compressed pinned device. Acceleration from 0.2 to 0.6 g _{rms}	220

138 RMS power vs frequency for the uncompressed 3x1 device. Acceleration from 0.2 to 0.6 g_{rms}. 220

139 RMS power vs frequency for the compressed 3x1 device. Acceleration from 0.2 to 0.6 g_{rms}. 221

140 RMS power vs frequency for the uncompressed 5x1 device. Acceleration from 0.2 to 0.6 g_{rms}. 221

141 RMS power vs frequency for the compressed 5x1 device. Acceleration from 0.2 to 0.6 g_{rms}. 222

142 Separate RMS power vs frequency runs for the compressed 3x1 device taken before and after the 5x1 device sweeps to show repeatability. Acceleration from 0.2 to 0.6 g_{rms}. 222

143 Peak power vs frequency for the uncompressed glued pin device. Acceleration from 0.2 to 0.6 g_{rms}. 223

144 Peak power vs frequency for the compressed glued pin device. Acceleration from 0.2 to 0.6 g_{rms}. 223

145 Peak power vs frequency for the uncompressed pinned device. Acceleration from 0.2 to 0.6 g_{rms}. 224

146 Peak power vs frequency for the compressed pinned device. Acceleration from 0.2 to 0.6 g_{rms}. 224

147 Peak power vs frequency for the uncompressed 3x1 device. Acceleration from 0.2 to 0.6 g_{rms}. 225

148 Peak power vs frequency for the compressed 3x1 device. Acceleration from 0.2 to 0.6 g_{rms}. 225

149 Peak power vs frequency for the uncompressed 5x1 device. Acceleration from 0.2 to 0.6 g_{rms}. 226

150 Peak power vs frequency for the compressed 5x1 device. Acceleration from 0.2 to 0.6 g_{rms}. 226

151 Separate peak power vs frequency runs for the compressed 3x1 device taken before and after the 5x1 device sweeps to show repeatability. Acceleration from 0.2 to 0.6 g_{rms}. 227

152 Microposit 1813 photoresist processing parameters for a 1.3 μm thickness
(left) and a liftoff recipe using 1813 and LOR-3A (right). 233

153 Microposit 1827 photoresist processing parameters for a 2.7 μm thickness
(left) and for a 3.8 μm thickness (right). 233

154 Polyimide application (left) and etching recipes (right)..... 233

155 SPR220 7.0 photoresist recipe (left) and deposition rates of chrome in the
physical vapor deposition KJL machine (right). 234

156 DRIE recipe used to etch silicon. 234

CHAPTER I

INTRODUCTION

This dissertation introduces the concept of a novel bi-stable buckled piezoelectric energy harvester. The harvester switches between bi-stable states using two proof masses, a stressed beam, and a pseudo pinned middle joint. A picture of the device is shown below in figure 1. A microelectromechanical systems (MEMS) scale device fabrication is attempted along with piezoelectric sol-gel deposition methods, piezoelectric poling routines, and a macro device concept for evaluating compliance arm geometry and constraint effects.

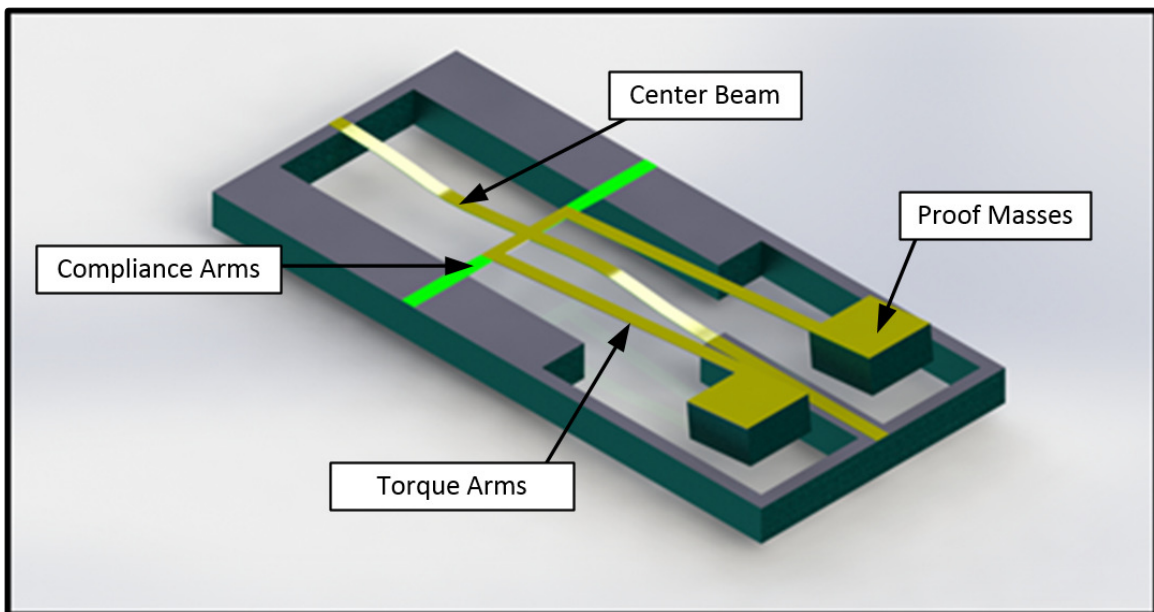


Figure 1. Rendering of the bi-stable piezoelectric energy harvester.

The new device is designed to generate large strains when bi-stable switching is achieved and to operate across a wide band of frequencies. Changing the proof mass size not only will change the operating frequency but lower the acceleration magnitude needed

induce snap-through. Additionally, the bi-stable performance of this device may show great promise to be utilized as an actuator or sensor in future research. Figure 2 below shows how the device works schematically along with a 3D printed prototype to confirm bi-stable actuation.

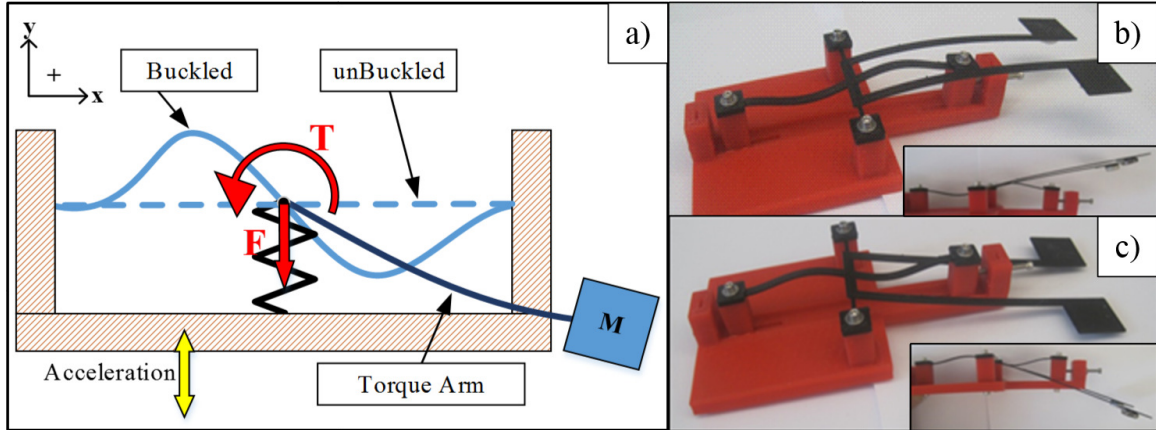


Figure 2. a) Simple schematic showing operation, b) 3D print showing buckled up, and c) buckled down position.

A. Microelectromechanical System Benefits

Over the last two decades, batch fabrication procedures performed for integrated circuits have dropped the cost for electronics worldwide. When it was realized that the same could be done for mechanical systems while simultaneously producing electronic circuits, the field of MEMS was born. A MEMS is roughly defined as a technology area that combines integrated circuits with mechanical devices such as sensors, actuators, energy harvesters, gears, etc.

Two of the most successful and famous MEMS inventions known to the layperson are the accelerometer and inkjet print head. In fact, these two examples describe the two wide categories into which MEMS are generally classified, which are actuators and sensors. Before 2005 not many people really understood what a MEMS device was due to the low volume consumer market presented to the world. Nowadays, these technologies are common place in cell phones and video game controllers such as the Nintendo Wii which incorporates a three axis accelerometer [145]. It is the demand and production in mass quantities that determines the success of an invention. Almost every smart phone in

production now operates with an accelerometer which only leads to the promise of cheaper and more reliable acceleration sensors.

Commercially, the first application of a MEMS device was in 1974, a pressure sensor that was fit inside a motor manifold to monitor absolute pressure and mass airflow. This allowed the device to optimize air-to-fuel ratio, which in turn, reduced the fuel consumption of the engine. After this, many more MEMS pressure sensing devices were introduced for other applications such as fuel and oil monitoring. MEMS accelerometers started showing up in the 1980's which led the U.S. government to require that all cars produced after April 1st 1989 to include airbags for both driver and passenger [145]. These magnificent creations could detect accelerations from 20g to 70g. By the 1990's, satellite accelerometers were incorporated into vehicles and had a full scale range of 100g to 500g; which allowed the microcontroller to have more time to decide if a deployment was needed or not [145].

Some MEMS devices are shown in figure 3 below including a) the iPhone 4 gyroscope [59], b) the core of a three axis accelerometer [54], c) a lead zirconate titanate (PZT) cantilever beam with proof mass [131], and d) an electrostatic micromotor [47]. The iPhone gyroscope is a commercial grade device while the others are research based contraptions. Other well-known devices are electrostatic energy harvesters, electromagnetic energy harvesters, lab-on-a chip (LOC), chemical pre-concentrators, deformable mirrors, filters, resonators, flow sensors, pressure transducers, inkjet print heads, and optical switches.

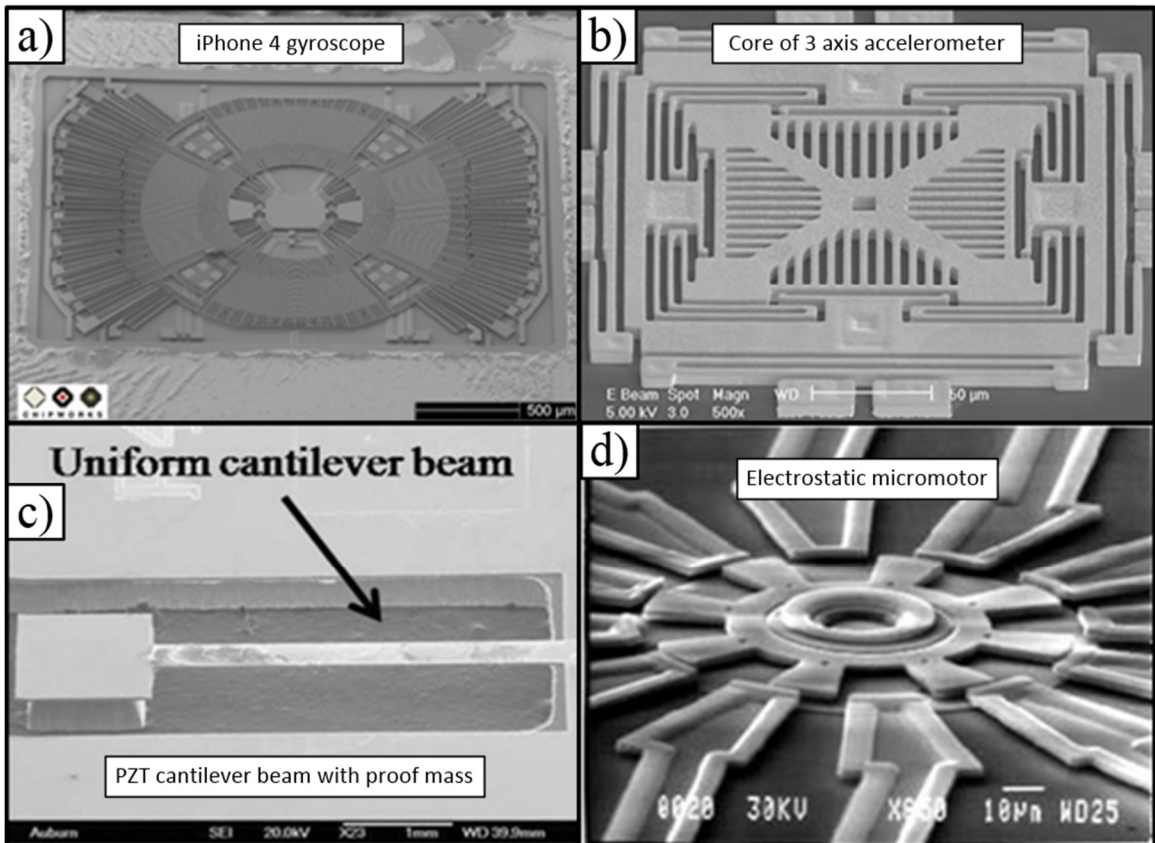


Figure 3. MEMS devices fabricated using cleanroom techniques a) gyroscope [59], b) accelerometer [54], c) PZT energy harvester [131], d) electrostatic micromotor [47].

Financial attributes linked to MEMS markets look promising with a compound annual growth rate (CAGR) of about 10% [16, 17]. This equates to more research being done in the sensor and actuator fields that will ultimately promote lower power devices. With low power devices comes the enhanced feasibility of operating them via energy scavenging methods. Figure 4 below shows the market trend for MEMS from 2006 projected to 2015. How the market fairs by device is shown in figure 5.

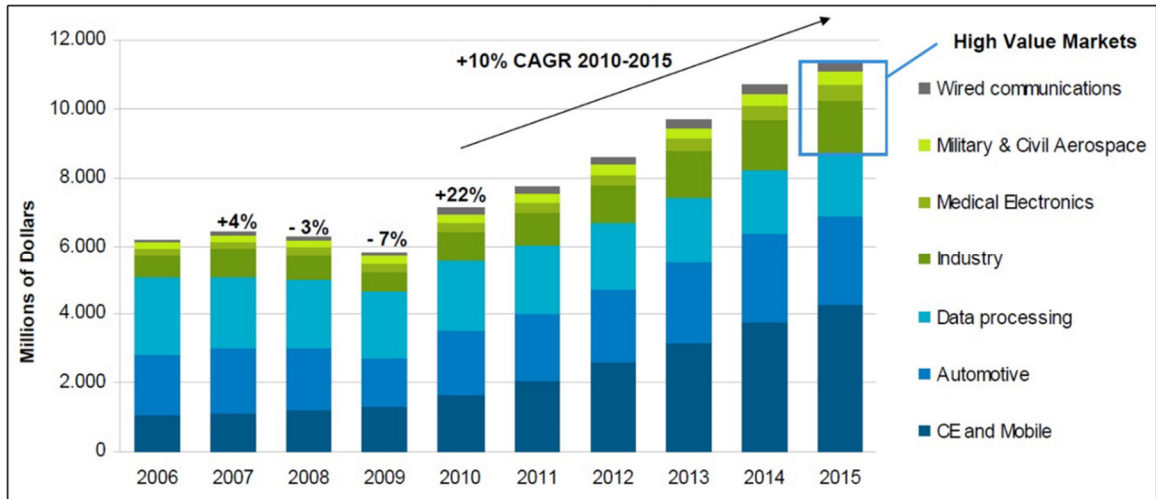


Figure 4. Past and future market prediction for MEMS devices [17].

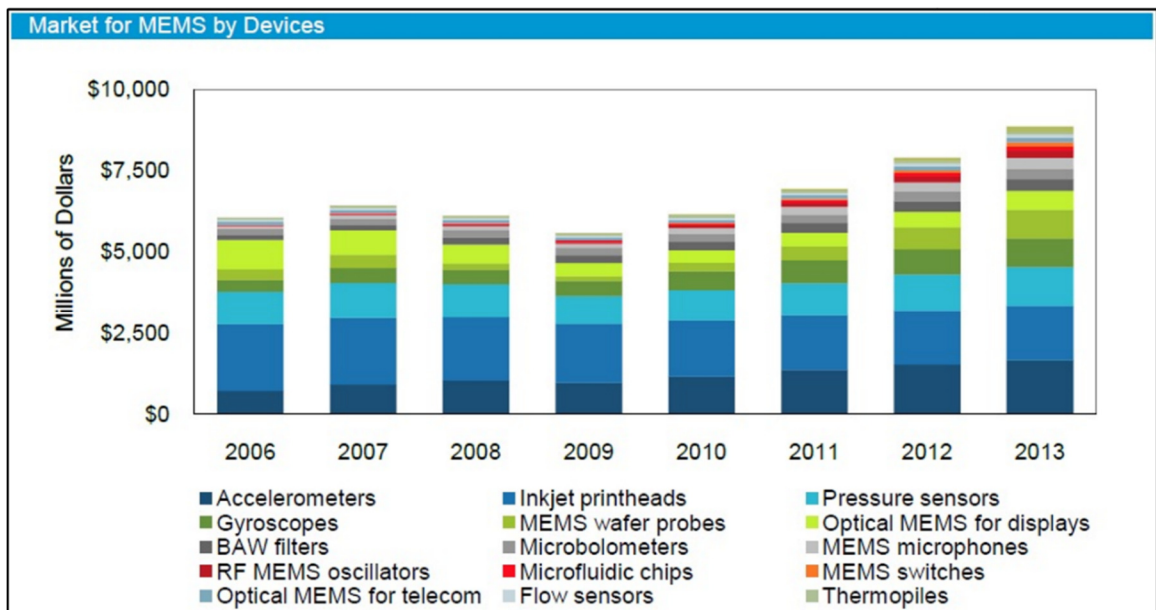


Figure 5. MEMS market by device [16].

Actually creating a MEMS device is quite complicated. Fabrication procedures are almost always limited to planar methods. This also lends to benefits because planar processing also means batch fabrication. Common fabrication procedures include thermal oxidation, wet etching, dry etching, planarization, bonding, chemical vapor deposition (CVD), electroplating, photolithography, sputtering, dicing, and many more. These abilities are generally not cheap and require very expensive equipment and specialized facilities.

B. Power Requirements for MEMS Sensors and Actuators

As progress in the area of MEMS sensors and actuators continually reduces the power required to operate them [139], new methods of actually supplying that power become viable. One such method is energy scavenging. Wireless transmitters such as the WiseNET use 10 to 100 μW on average [43] and are the perfect example of the types of devices that can be fitted for the utilization of an energy harvester. Lifetimes of transmitters like this have been experimentally determined to be between two to seven years when operating on traditional AA batteries [43]. If located in a secluded place or even a hard to reach area in a lab or manufacturing plant, frequent power supply replacements can be cumbersome.

Some considerations on power consumptions include 1 nJ per instruction for 32 bit microprocessors, 1-10 pJ per instruction or an application specific integrated circuit (ASIC), for wireless transmission the rate is about 50 μJ per bit for sending and 2 μJ per bit to receive, Bluetooth power requirements are around 100 nJ per bit in the 2.4 Ghz band, inertial measurements per axis (accelerometers) consume about 100 μW , pressure sensors consume about 10 μW [108]. Bio MEMS applications have used electrostatic micropumps that consume about 8mW while pumping 30 mL per min [99]. More specific devices include the STLM20 temperature sensor, which draws 12 μW of power while idle, an analog to digital converter (ADC) that uses less than 1 μW at 8 bit sampling (4 KS/s), and an IMEC transmitter that uses 0.65 nJ per 16 bit burst [95].

Unfortunately larger devices such as laptops are not currently feasible candidates for today's energy harvesting based power sources due to their large power usage of 10 to 40 watts [95]. This is not only due to the magnitude of power consumption but also the duration of continuous usage. Additionally, laptops are not always used in an environment experiencing regular vibrations from walking, driving, etc. Cellular telephones have a much better chance of experiencing continual motion because users take these devices with them wherever they go.

C. Renewable Energy and Energy Generating Materials

Energy generation methods that utilize gasoline or diesel as a fuel supply, such as the combustion engine, are limited in that their fuel supply origin is finite. The same can be said about coal or other natural resources that are limited in quantity. Ways to conserve these valuable resources include making equipment that is more energy efficient and that use renewable energy sources such as solar, wind, biofuels, or ambient vibrations. A key factor to consider is the energy density of the medium that is available to the device being used. Figure 6 and table 1 below show some expected power and energy densities for different renewable energy sources. Some of these values are volumetric while others are referenced to a specific area and give the energy flux. Though vibrational energy harvesting (VEH) might now have the power generating ability to match a gasoline engine, it does offer to benefit of continuously charging a small devices capacitor bank.

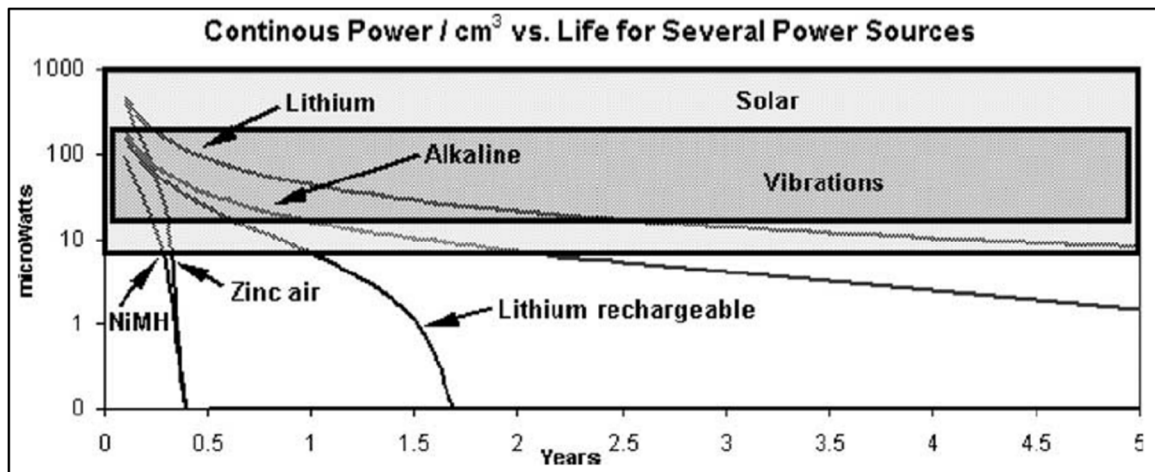


Figure 6. Volumetric power for different energy sources versus lifetime [124].

Table 1. Typical power and energy densities for some potential renewable energy sources.

Power Source	Power/Energy Density	Assumptions	Reference
Primary Batteries	2,880 J/cm ³		[122]
Micro Fuel Cell	3,500 J/cm ³		[122]
Super Capacitor	50-100 J/cm ³		[122]
Solar	Outside: 15,000 μ W/cm ² Inside: 10 μ W/cm ²		[122]
Thermoelectric	40-60 μ W/cm ²	$\Delta T \sim 5^\circ\text{C}$	[122]
Human Generated	330 μ W/cm ³		[122]
Wind	380 μ W/cm ²	Vel=5 m/s and 5% conversion eff.	[122]
Vibrations	Piezoelectric: 375 μ W/cm ³ Electrostatic: 213 μ W/cm ³ Electromagnetic: 119 μ W/cm ³		[122], [24], [92], [138]

The focus of this work is vibrational energy harvesting which, as shown in table 1, can be more effective than indoor solar lighting or an area that is not constantly exposed to bright light. A major concern in the vibrational energy harvesting community occurs when the operating frequency of the device, and its associated operating bandwidth, does not match that of the vibration source which ultimately results in negligible power generation for a given application. Below are some common vibrational sources with expected frequencies and accelerations. Taking note that the range of frequencies primarily fall between 1 and 200 Hz, energy harvesters designed above this range will most likely not be very effective. The majority of accelerations fall below one g which indicates that testing should incorporate many data points in the 0.05 to 1 g span.

Table 2. Operating frequencies and accelerations of machines, activities, and structures ([117], [124], [121], [60], [131]).

Source	Frequency (Hz)	Acceleration (m/s ²)	Acceleration (g's)	Notes
Kitchen blender casing	121	6.4	0.652	
Clothes dryer	121	3.5	0.357	
Door frame just after door closes	125	3	0.306	
Small microwave oven	121	2.25	0.229	
HVAC vents in office building	60	0.2~1.5	0.020~0.153	
External windows next to a busy street	100	0.7	0.071	
Washing machine	109	0.5	0.051	
Notebook computer while CD is being read	75	0.6	0.061	
Second story of wood frame office building	100	0.2	0.020	
Refrigerator	50~240	0.1	0.010	
Car engine compartment handheld tools	200	12	1.223	
Handheld tools	8~500	0.1~80	0.010~8.155	
Vehicles	5~2000	0.5~110	0.051~11.213	
Statusys 3D printer	44.7	0.167	0.017	
W500 Lenovo laptop	119	1.952	0.199	
Milwaukee cordless drill	15.2	3.561	0.363	
External HD	119.3	0.137	0.014	
Washing machine	85	3.080	0.314	
Rockwell sander	92.5	1.354	0.138	
Monarch lathe splatter guard	24.5	0.510	0.052	
Monarch lathe chassis	284	1.413	0.144	
Delta drill press	41.3	3.993	0.407	
Delta vertical bandsaw	122.5	1.373	0.14	
HVAC roof	184.5	2.472	0.252	
Driving 2002 Toyota Camry	42.8	0.216	0.022	
Scraper bike	15	0.608	0.062	
Running	1.5~5.1	20.061~7.475	2.045~0.762	hori,vert
Walking	1~3.7	4.219~2.992	0.430~0.305	hori,vert
Portable home air compressor	43.7	20.630	2.103	
Electric tea pot	241	0.186	0.019	
Poster printer	92.5	1.962	0.2	
Server/computer	35.3	0.157	0.016	

There are three popular transducing methods used in the vibrational energy harvesting field: electrostatic, electromagnetic, and piezoelectric. Electrostatic devices are very easy to incorporate into a MEMS package. As an example, all one needs is an SOI wafer with doped silicon device layer (top) and the ability to etch and metalize the wafer.

However, to initiate any type of energy harvesting in an electrostatic manner, an initial electrical field would have to be applied. The resulting devices are very planar and tend to have very high natural frequencies. Electromagnetic devices have a relatively high power output when compared to electrostatic, but are complicated to amalgamate with a MEMS system. Improvements in fabricating pseudo wound wires using a planar process have been achieved in new inductor designs which could open future pathways for electromagnetic energy harvesting.

Piezoelectric materials can be incorporated into simple structures via a sol-gel or bulk wafer approach. Output voltages for these devices are also much higher than the alternatives, the downsides being the difficulty to integrate and the need for high stress and strain. Table 3 and table 4 show the comparisons of the different energy harvesting mechanisms and the equations that govern them. The high voltage and relatively high energy densities justifies picking PZT, a piezoelectric, as the energy harvesting mechanism of choice for this research.

Table 3. Different energy harvesting mechanisms and their advantages [124].

Mechanism	Advantages	Disadvantages
Piezoelectric	No voltage source needed Output voltage is 3–8 V	More difficult to integrate in microsystems
Electrostatic	Easier to integrate in microsystems	Separate voltage source needed Practical difficulties
Electro-magnetic	No voltage source needed	Output voltage is 0.1–0.2 V

Table 4. Energy harvesting mechanisms and the equations that govern their power output [122].

Type	Energy density (mJ cm ⁻³)	Equation	Assumptions
Piezoelectric	35.4	$(1/2)\sigma_y^2 k^2 / 2c$	PZT 5 H
Electromagnetic	24.8	$(1/2)B^2 / \mu_0$	0.25 T
Electrostatic	4	$(1/2)\epsilon_0 E^2$	3×10^7 V m ⁻¹

Numerous investigations have been done to study the feasibility and performance of PZT energy harvesters in various environments. Durou *et al.* [38] built a MEMS based PZT harvesting device and compared it to other similar designs. Resonant frequencies for his and the comparisons were in the desired range for such sources as shown in table 2. The type of device created as well as their respective volume, power, acceleration, and frequency is shown in table 5 below. Durou *et al* found that output voltages of 1 to 2 volts at the given oscillatory loads are more than enough for a DC-DC converter to operate and charge a capacitor.

Table 5. Durou's PZT energy harvesting device performance (top) and the comparison devices (bottom) [38].

Input [g]	Natural Frequency [Hz]	Voltage [V]	Output electrical Power[μ W]	Power density [μ W.cm ⁻³]
0.1	77	1.26	3.20	9.22
0.2	76	2.64	13.9	40.1

Author	Acceleration [m.s ⁻²]	Frequency [Hz]	Amplitude [μ m]	Power out [μ W]	Volume [mm ³]	FoM _v [%]	FoM _{int} [ppm]
LAAS	1.96	76	8.6	12.3	464	0.303	258
LAAS	0.98	77	4.2	3.20	464	0.156	205
Soliman	4.91	95	13.78	2 083	9 337	0.300	145
Wischke	10.00	296	2.9	68	800	0.041	88
Perpetuum PG17	0.98	100	2.48	5000	537 067	0.0154	10.4
Arevni	4.91	50	49.75	44 800	190 080	0.220	145

Not all devices that are fabricated for research purposes have relatively low resonant frequencies like those shown in table 5. Park *et al.* [104] fabricated their energy harvesting devices using a cantilever beam/mass setup that had a considerably larger resonant frequency. They compared it to other devices with large resonant frequencies. Table 6 shows the comparison of work by Park, *et al's*, and other MEMS based devices.

Table 6. MEMS energy harvesting devices with large resonant frequencies [104]. Park, *et al's*, work is shown as the last row in the table.

Device	Volume (cm ³)	Power (μ W)	Acceleration (g)	Frequency (Hz)	Power density (mWcm ⁻³)
d ₃₁ PZT	1.5×10 ⁻³ ^a	2.16	1	608	1.44 ^a
d ₃₁ AlN	5.3×10 ⁻⁴ ^a	2	4.0	1368	3.77 ^a
d ₃₁ PZT	4.1×10 ⁻³ ^a	40	1.9 ^a	1800	9.76 ^a
d ₃₁ PZT	1.5×10 ⁻³ ^a	2.15	2.0	462.5	1.43 ^a
d ₃₃ PZT	2.4×10 ⁻⁵ ^a	1.01	13.2 ^a	13900	42.1 ^a
d ₃₃ PZT	9.9×10 ⁻⁴	1.1	0.39	528	1.11

D. Buckled Structures and Their Potential Applications

Constructing diaphragms from silicon wafers that have been oxidized is a common, well characterized procedure for producing pressure transducers and are ([110], [151]). Valves, pumps, switches, and memory devices have been constructed utilizing bi-stable structures; this work extends that field to energy harvesters. Advantages of bi-stable devices are that virtually no power is needed to maintain its various stable states, and that the device must undergo large strains to reach alternative stable positions.

Walsh *et al.* [147] created bi-stable buckled diaphragms using silicon dioxide and polyimide that buckled back and forth given a vacuum pressure applied to one side. In that work, silicon dioxide was about 400 nm thick while the polyimide was 2.5 to 4.5 μm thick. An internal compressive stress of about 300 MPa (in the silicon dioxide) and a diameter size for the diaphragms of 300 μm exhibited -7.6 μm and 7.8 μm of buckled displacement in the middle of the released structure for the two bi-stable states [147]. A single pole, double throw switch was done by the same group by creating a 900 μm diameter diaphragm and coating the top with a 150 nm titanium/tungsten coating. These devices achieve buckling heights greater than 28 μm and switch at a pressure of roughly 40 kPa [53]. Gowrishetty *et al.*'s switch is shown in figure 7 below.

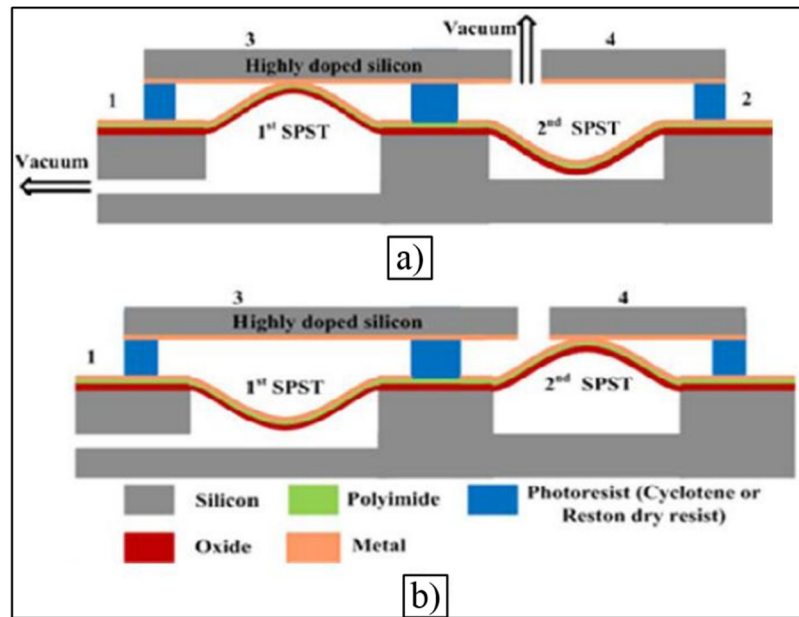


Figure 7. Single pole double throw bi-stable membrane switch before a) and after actuation b) [53].

Popescu, *et al.*, created a microvalve using a buckled membrane though it was not a bi-stable structure. To actuate the device, a polysilicon ring which was mounted to an aluminum layer was used. This ring was heated via electrical resistance which created enough strain to flip the device to a buckled deflection state. Ambient water then cooled the device which caused it to flip back to its original position. The diameter of their membrane is 4 and 5 mm while the thickness of their polysilicon, SiO₂, and aluminum is 16, 1, and 3 μm respectively. Buckled heights for these devices were on the order of 21.5 to 56 μm [109]. A schematic of their valve is shown in figure 8 below.

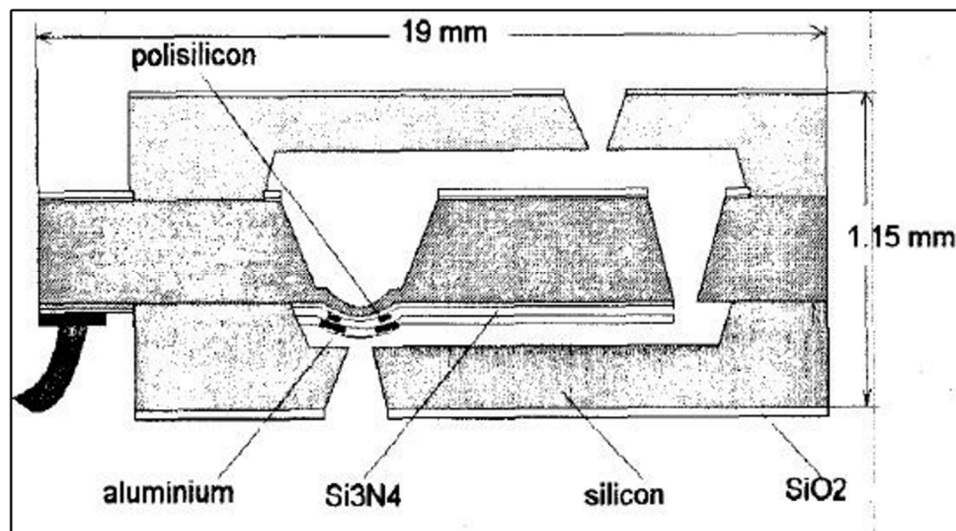


Figure 8. Thermally actuated membrane microvalve [109].

Micropumps utilize diaphragms for pushing a fluid medium through channels. Though these structures might not be entirely buckled, they almost certainly utilize large out of plane displacement to create a significant actuation volume. Nisar *et al.* [99] described micro pumps for biomedical purposes, many of which used “membrane” type actuation. One such device was a piezoelectric bi-morph that was essentially a disk of PZT on top of a thin glass membrane. The stroke for such a device is not large compared to other actuating methods, but piezoelectrics can drive with a high force and often a very fast response time. Pumping pressures for such devices can be upwards of 2.4 MPa but most are under 60 kPa [99]. A schematic for a PZT membrane micropump is shown in figure 9 below.

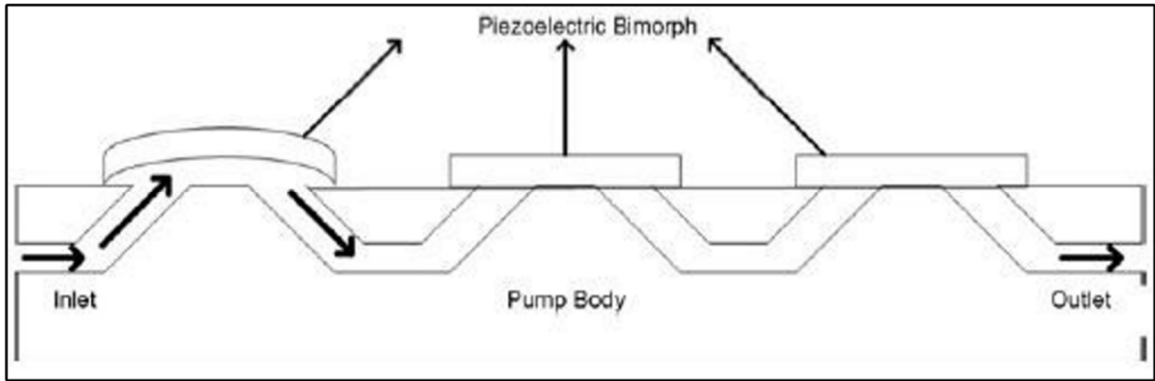


Figure 9. A PZT based micropump [99].

E. Previous Work on Energy Harvesting

Vibration-based energy harvesters offer a means for converting waste mechanical energy or ambient structural oscillations into electrical power. Though the average power generated by MEMS-scale energy harvesters is not large, $\sim 0.026\mu\text{W}$ (0.5g), $2.15\mu\text{W}$ (1g), to $60\mu\text{W}$ (2g) in the MEMS region [87, 39, 131, 125, 19, 137] it is still sufficient enough to sample and transmit sensor data wirelessly. Macro scale devices can generate powers of $8.4\text{nW}/\text{cm}^2$ (0.12% strain per bend), $118\mu\text{W}$ (0.2g), and $17.3\mu\text{W}$ (3g) [37, 12, 64]. For hard-to-reach electrically powered devices, such as remote sensors, energy harvesters can greatly extend the time required between burdensome service visits, offering some unique benefits over other power supplies such as batteries. However, to be considered a robust, viable alternative power source, vibration-based energy scavenging devices must perform well at low frequency ranges and at driving conditions with variable spectral energy density content characteristic of real-life operating environments.

The most simplistic vibration-based energy harvesting designs utilize a mono-stable cantilever with a single minimal potential energy well, meaning the resting position has only one preferred state. These devices have narrow operating bandwidths and require proper design/tuning for their specific functional settings [124, 121, 117]. Conversely, energy harvesting systems that have nonlinear dynamic responses generally have broadband excitation characteristics, ideal for chaotic input impulse situations [56]. One method for producing nonlinear behavior is to force a system into a multi energy well arrangement. Multi energy well systems can be created through selective placement of magnets [44] or electrostatic components, mechanical orientation [49], bio inspired bi-

stable structures [71], or through a mechanically bi-stable buckled structure [80, 84, 67, 144].

Due to their interesting dynamic response, energy harvester designs incorporating buckled structures have been the focus of many recent research efforts [56, 80, 84, 67, 144, 33, 88]. A more general spectrum of current bi-stable energy harvester research is covered in a recent comprehensive review by Harne *et al.* [56]. Mono-stable energy harvesters are favorable at low accelerations over most of the frequency range even when the frequency is swept in both directions. Intriguingly, buckled energy harvesting devices with low energy wells have larger voltage responses at super and sub-harmonic frequencies when compared to the same device in the unbuckled (low stress) state [89], if the inter-well actuation can be achieved. Another interesting behavior of buckled energy harvesters is their improved voltage output during chaotic vibrational inputs [144] and wider frequency bandwidths [67], [34]. These performance trends are enhanced during switching between stable buckled states, which involves large structure deformations during these high energy “snap-through” events, as described by [142].

Notable buckled energy harvesters include work by Majer, *et al.* [84] that experimented with a compressed, doubly-clamped beam with a proof mass in the middle. Their device had a wide frequency operating range, high voltage operation during bi-stable switching, and decaying output oscillation frequencies at multiples of the drive frequency right after switching. The driven electrical load had an impedance of $1\text{M}\Omega$ and exhibited bi-stable switching for accelerations between 4-5g's [84]. Another study by Cottone, *et al.* [33], featured an energy harvester with a proof mass positioned on a buckled beam. This design enabled a “frequency-up” response so that the electrostatic energy harvesting core could operate at a more efficient frequency regime (162Hz). The bi-stable oscillator device responded well to randomly generated noise in the 20-40Hz operating frequency, with inter-well jumps (snap-through) producing high voltage responses [33]. Lui, *et al.* [80], similarly found that a bi-stable energy harvester based on a dynamic mass-spring system with flexible hinges demonstrated superior performance compared to a linear oscillator when subjected to chirp and band-limited noise accelerations [80].

The bi-stable buckled energy harvester described herein is simple, robust, and uniquely designed to operate over a range of very low driving frequencies by using torque

arms to facilitate buckled state switching. In short, an “S” shaped buckled beam profile is generated by effectively pinning a compressed beam at its midpoint. In this work, we detail the procedure for fabricating the energy harvester, followed by presenting results from finite element simulations and experimental testing of the device bi-stability behavior and its associated electrical response.

CHAPTER II

NEW ENERGY HARVESTING CONCEPT AND MEMS

The focus of this work is a bi-stable buckled energy harvester that utilizes PZT and stressed nitride to promote buckling. Proof masses will be used and fabricated from the silicon substrate. A few design iterations were performed until a feasible construction plan was achieved. Desired outcomes of our device are that a large strain will be developed during actuation, the frequency band in which optimal energy will be harvested will be broad, and the contraction itself could be utilized for other tasks such as being used as an actuator.

In brief, the proposed device will use a stressed nitride beam coated with polyimide as the buckled part. Unstressed parts will be the torque arms used to actuate the stressed beam, the polyimide, and the chrome protection layer. A simple model of the doubly clamped main/center beam pseudo pinned in the middle is shown in figure 10 below.

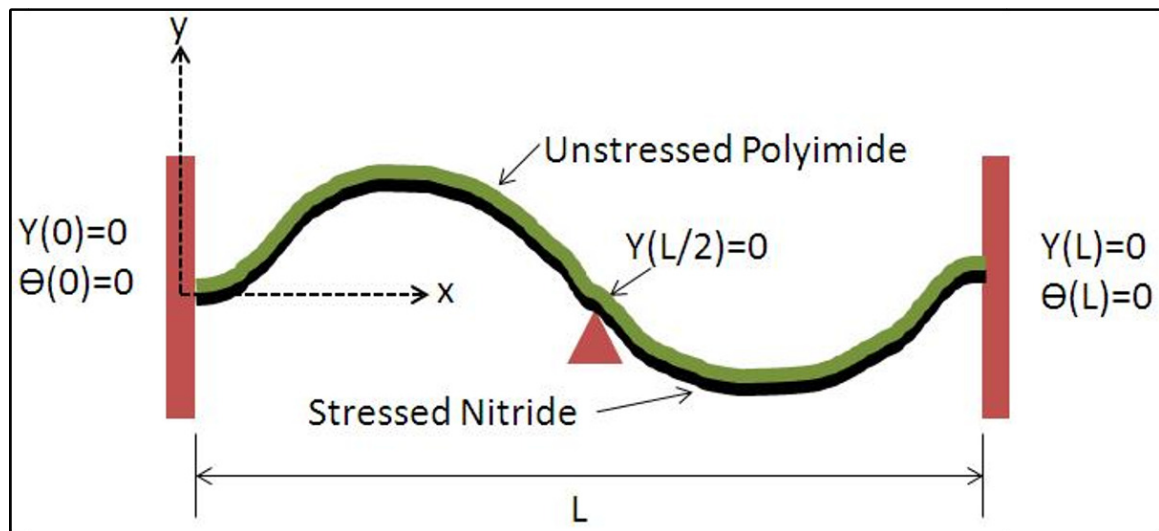


Figure 10. Bi-stable buckled beam constrained at both ends and in the middle.

To analyze how our device works and demonstrate feasibility of fabrication a prototype has been made. Initially designs in ANSYS have been created to determine the natural frequency, actuation force/torque, and displacement of a prescribed model. Finally a mathematical model has been formulated to predict buckled height, actuation force/torque, and hopefully energy harvested given an oscillatory input.

A. Design of a Bi-Stable Buckled Structure

Many iterations of our proof-of-concept had been drawn before we settled on a model that we held confidence in. Most problems occurred when we listed out fabrication steps; due to the inability to create certain structures or material removal steps that interfered with other steps. The biggest problem encounter was the creation of the proof mass. Preliminary designs utilized a single proof mass with two nitride/polyimide arms connecting it to the middle of the buckled beam as shown in figure 11. One major flaw in this design arises when we try to etch/cut out the proof mass while leaving a rigid island intact for the fully constrained stressed beam part. Our initial prototype will not include a piezoelectric material; but will demonstrate that buckling into an “S” shape can occur, we can predict its amplitude, and that the device can be switched into another buckled energy state.

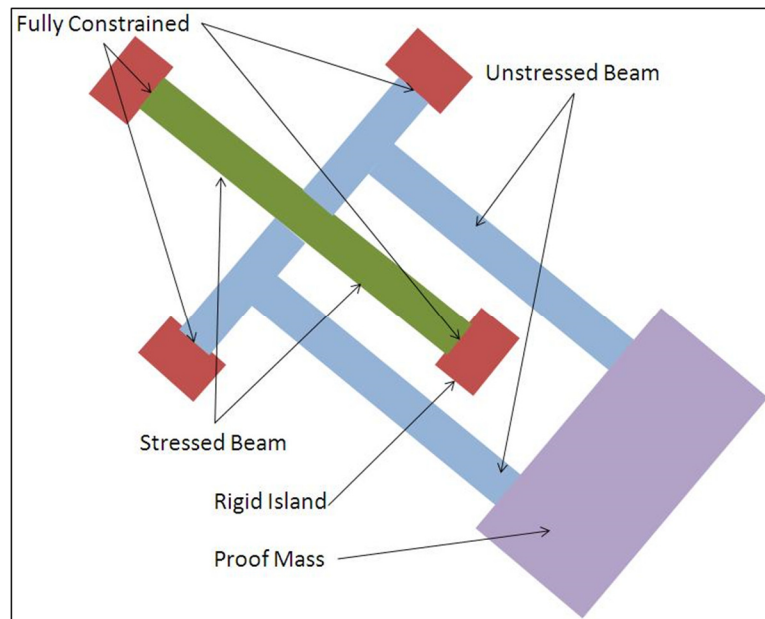


Figure 11. First iteration of device with one big proof mass.

The next iteration was to use two proof masses on each side of the device which would alleviate the problem of a rigid island. Another problem was brought to our attention when analyzing the beams that attached to the stressed portion of our device; the outer portion of the beams seemed too rigid to allow transfer of torque to the buckled portion. A simple solution was that the outer portion of the torque arms be made of only polyimide, which has a Young's modulus of about 8 GPa. Compared to the Young's modulus of nitride, 160-210 GPa, this produces a much more compliant torsional pin. The layout of this device is shown in figure 12 below.

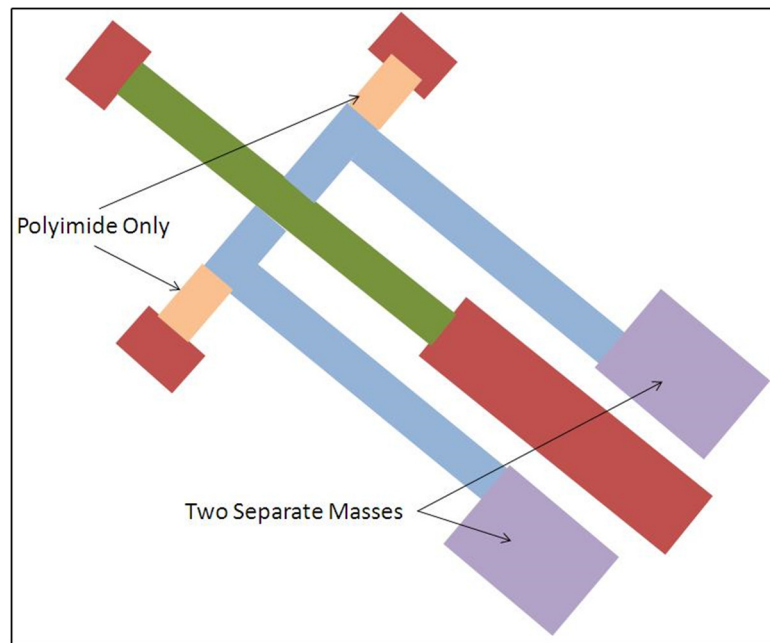


Figure 12. Final proof of concept device with polyimide torque arms and two separate proof masses.

Once the final concept was approved, the next step was to decide what parameters to vary for the ANSYS model. Planar geometric variables were the obvious first choice and would have a great impact on the performance of our device. Other variables to optimize include the pre-stress in the main buckled beam, thickness of the silicon proof mass, thickness of the chrome, thickness of the stressed nitride, and thickness of the unstressed nitride. ANSYS analysis is detailed in section 5 of this proposal. With dimensional geometry parameters settled, new prototypes can be fabricated.

B. Typical Fabrication Methods and Steps

Completed ANSYS models confirmed the desired buckling behavior of our devices, allowing photomasks to be designed. Two types of die were constructed: one only constituted of an array of cross structures that had one stressed beam and one non-stressed beam, the other was an array of our buckled devices. In case the complexity of the main devices prevented the fabrication of a successful buckled device, it was proposed that the simple cross structure would lend us a better chance at a proof of concept.

PECVD is the main method used at the University of Louisville to deposit nitride. First the stress profile for our PECVD machine was evaluated. Multiple runs were done so that the equipment's stress and deposition rates could be recorded. A graph of this experiment is shown in figure 13 below. The x-axis is the percent of time the radio frequency (RF) power is on over the total time for the low frequency (LF) and RF. The frequency magnitude for the RF and LF is about 13.56 MHz and 300 kHz respectively. Almost all experiments done were at 50 Watts and some pulse time between 0 and 20 seconds. Chamber pressure was modified to change the stress even further; due to the stress being proportional to the chamber pressure [103]. Wafer curvature measurements were performed so that Stoney's equation could be evaluated to back out residual stress.

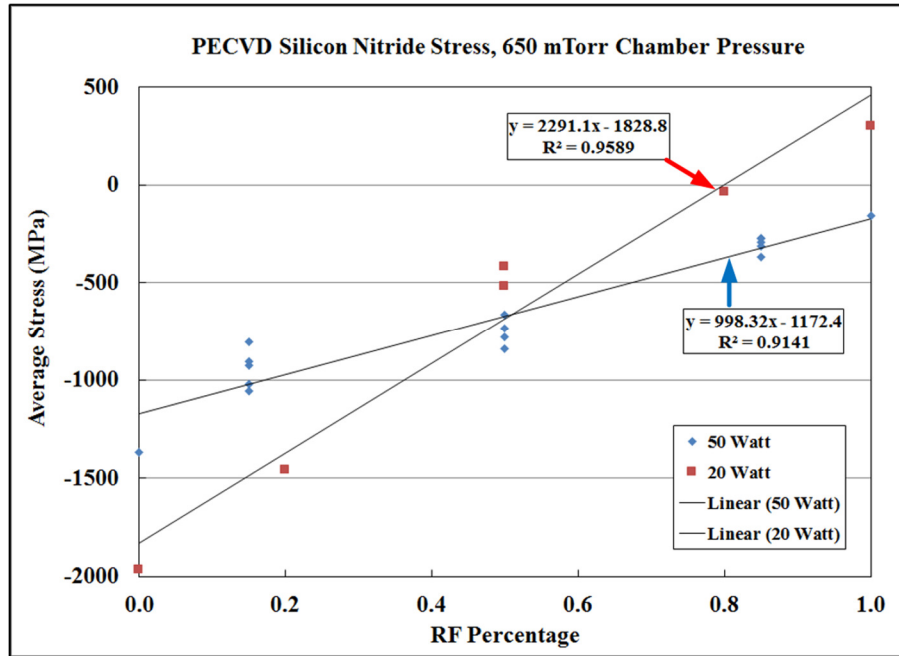


Figure 13. PECVD silicon nitride stress versus RF frequency.

Initial substrates are 250 μm thick and were chosen due to the ease of the DRIE process for the last step. Silicon dioxide is thermally grown in a wet environment for an etch stop during the DRIE process and was targeted for 500 nm in thickness. It is proposed that the unstressed and stressed nitride layers have deposition thicknesses of 500 nm also which seemed to allow for an effective transfer of force from the ANSYS model. Unstressed nitride will be put down first using the PECVD so that the force from the mass arms is efficiently transferred to the torque arms and to ensure the lever arms are unwarped. Likewise, the unstressed portion will go through the main portion of the stressed beam as shown in figure 14. An O_2 and CF_4 plasma was used to etch the nitride layers and was found to have a non-linear etch rate with time. Next, a chrome 250nm layer is placed down so that when the stressed nitride is deposited, and then etched, the unstressed nitride is unaffected. The last layer deposited on the wafer is roughly 4 μm of PI 2611 polyimide and that is patterned using an O_2 plasma etch. A DRIE process is done on the back of the wafer so that the masses and the silicon under the beams are etched out. This process is also used to separate the die. Five minutes in a buffered oxide etch (BOE) bath is used to “release” the buckled structures and masses.

There was some speculation about the amount of silicon dioxide that was being worn away during each nitride etch; because the etching time was non-linear and could become a problem in the DRIE process. If the oxide is worn too thin then the DRIE task could eat the nitride layer which constitutes our device. A solution to this problem is to grow the oxide much thicker. The photo resist used to pattern the silicon nitride etches cannot hold up for the amount of time required to etch through the layers so a thin film of patterned chrome was used instead.

The five masks created are the stressed nitride, chrome protection layer, unstressed nitride, polyimide layer, and the DRIE layer. A picture of each of the mask layers is shown in figure 14, figure 15, figure 16, figure 17, and figure 18 below. The chrome protection mask included serial numbers for each device but the letter sizing failed to hold up during the nitride etching. A University of Louisville logo was used as an aesthetic presence.

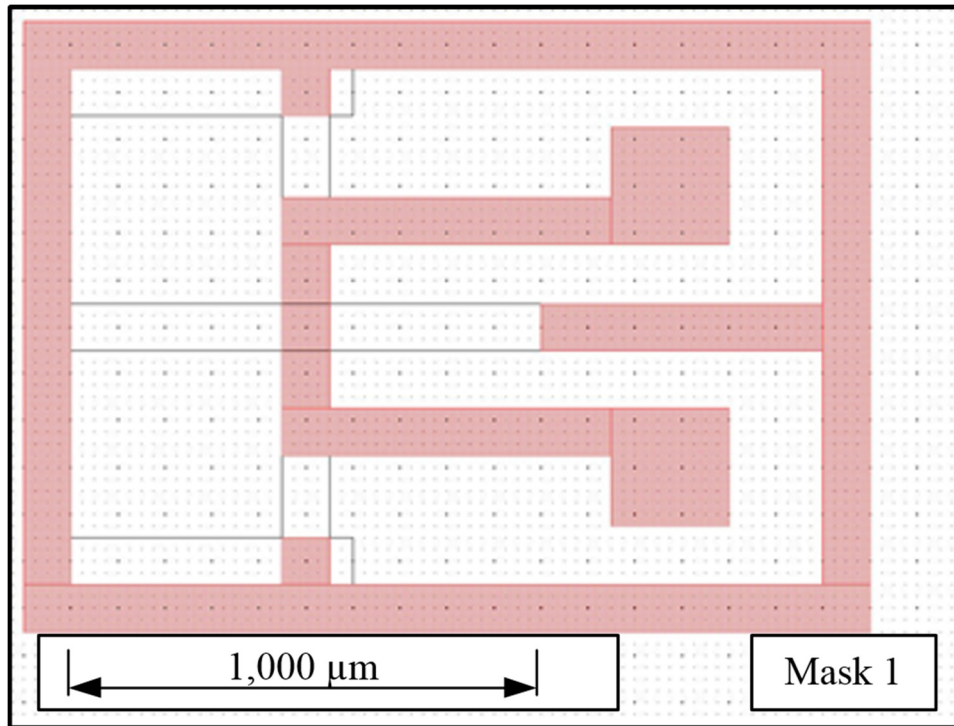


Figure 14. Non-piezoelectric prototype mask 1, the unstressed nitride layer. Scale bar is about the same for each mask layer shown below.

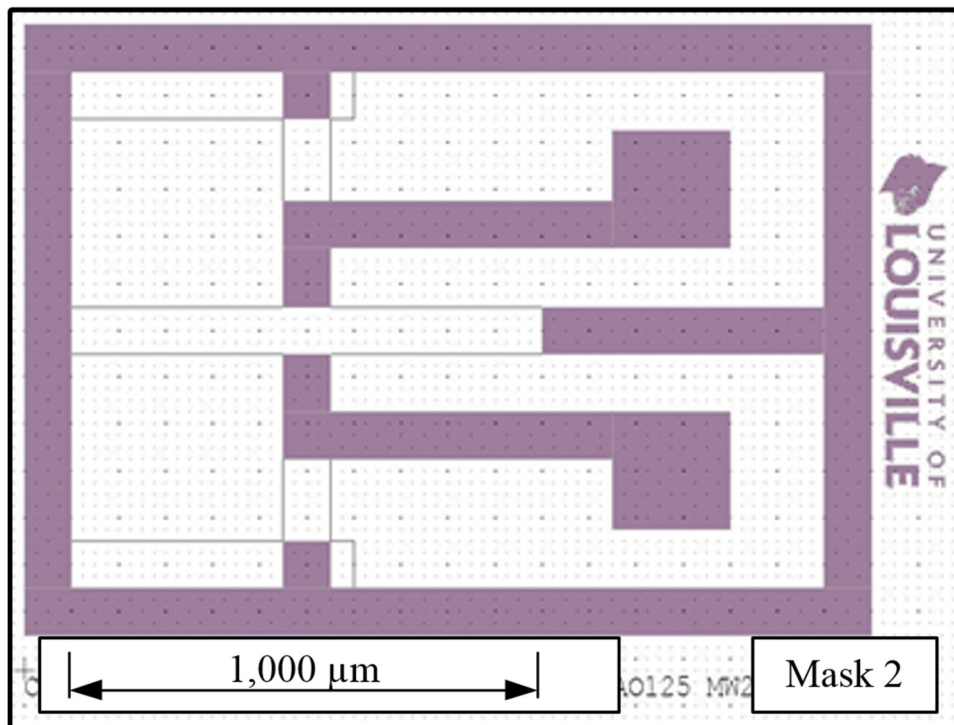


Figure 15. Non-piezoelectric prototype mask 2, chrome protection layer.

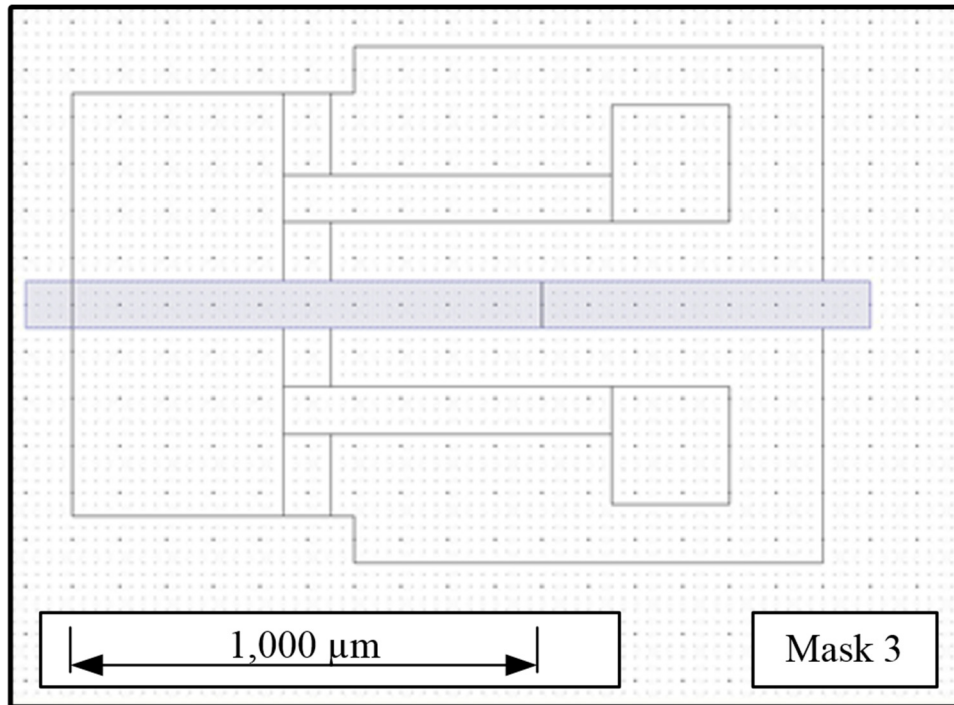


Figure 16. Non-piezoelectric prototype mask 3, stressed nitride layer.

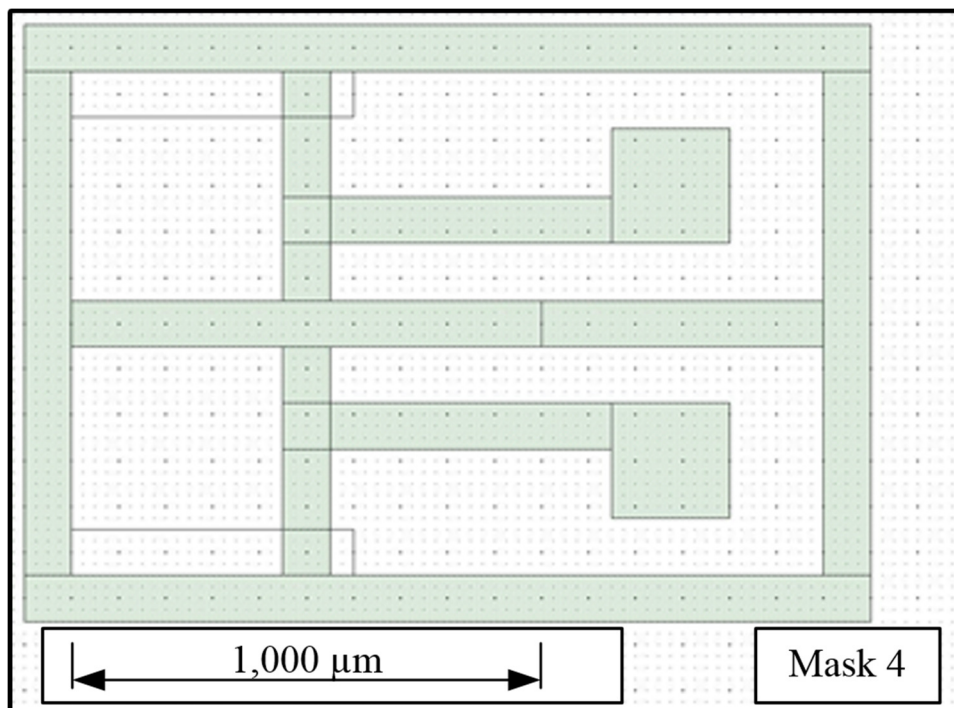


Figure 17. Non-piezoelectric prototype mask 4, polyimide layer.

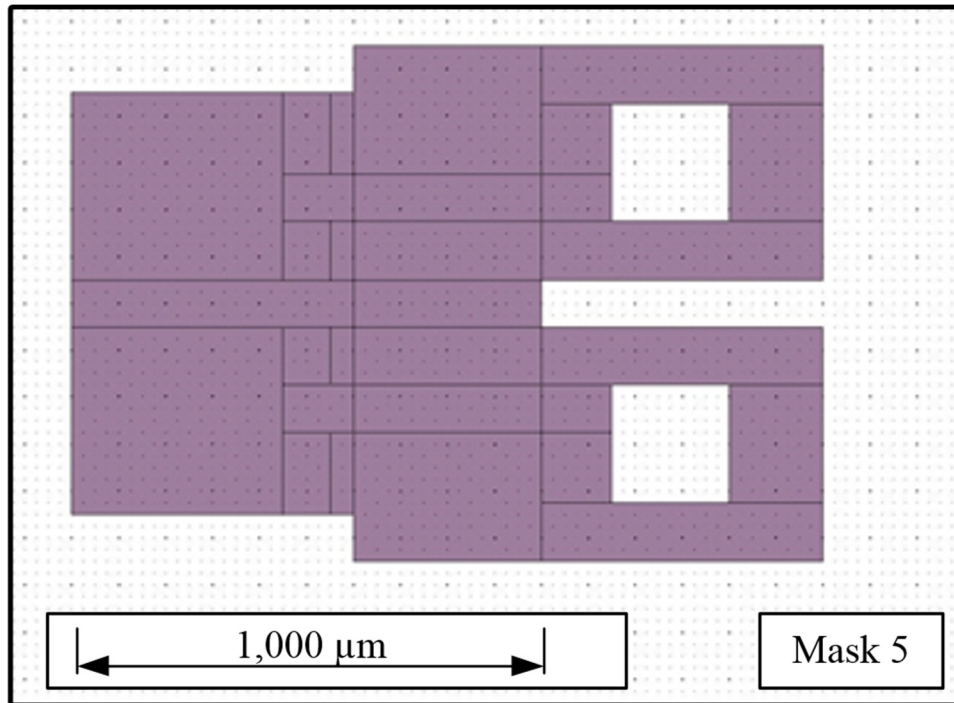


Figure 18. Non-piezoelectric prototype mask 5, DRIE layer.

Preliminary equipment characterization and device fabrication required about four months to complete. Separation of the individual die was done while etching the trenches for the release of the mass and beam structures. Other separation techniques failed due to either design error or die chipping from the dicing saw which resulted in an unusable device. Simple structures like the cross device shown in figure 19 below were used to test the feasibility of promoting a beam into an “s” shaped profile. The figure shows a fully fabricated device a) that has not been etched from the backside and a backside image of the device post etching b). One of many buckled mass devices is shown in figure 20 below.

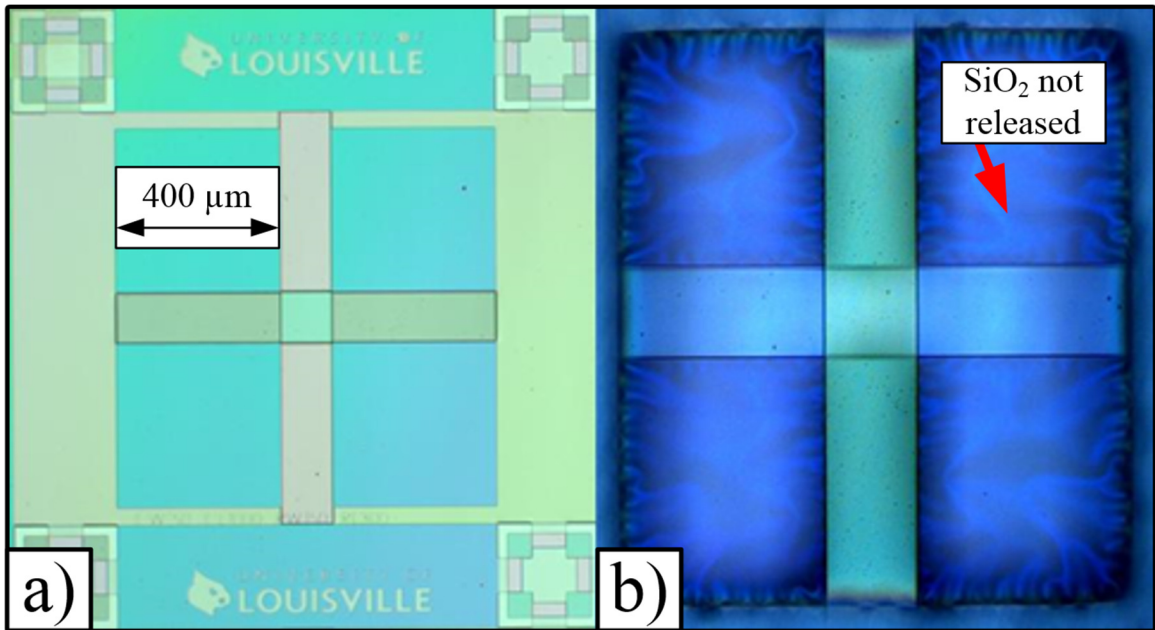


Figure 19. Buckled cross structure a) before and b) after DRIE etching (backside).

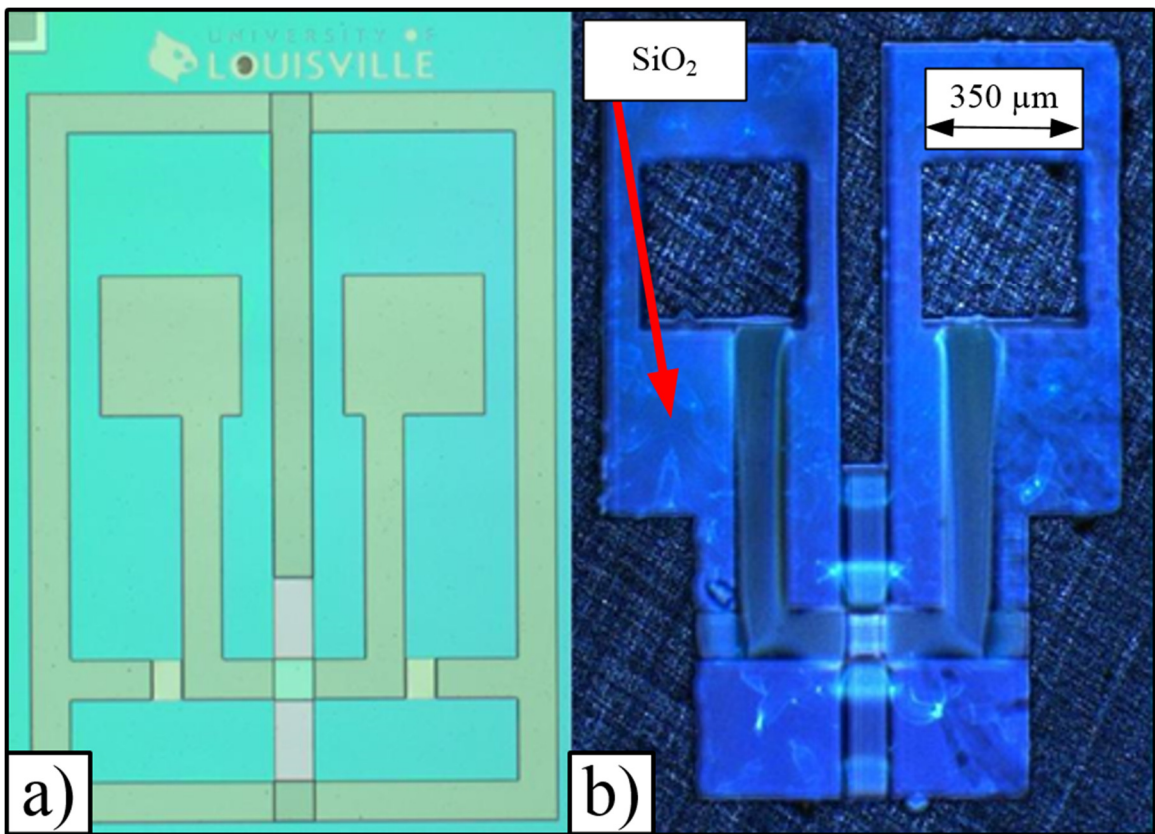


Figure 20. Buckled mass structure a) before (topside) and b) after DRIE etching (backside) with no piezoelectric active layer.

C. Proof of Concept

After prototype devices were fabricated, they were put into an SEM so that buckled shapes could be recorded. The majority of devices exhibited the correct buckled profile, demonstrating feasibility of the proposed design. The next design iteration in progress involves a similar device, but also with PZT and electrodes. SEM images of the prototype device arrays are shown figure 21 below.

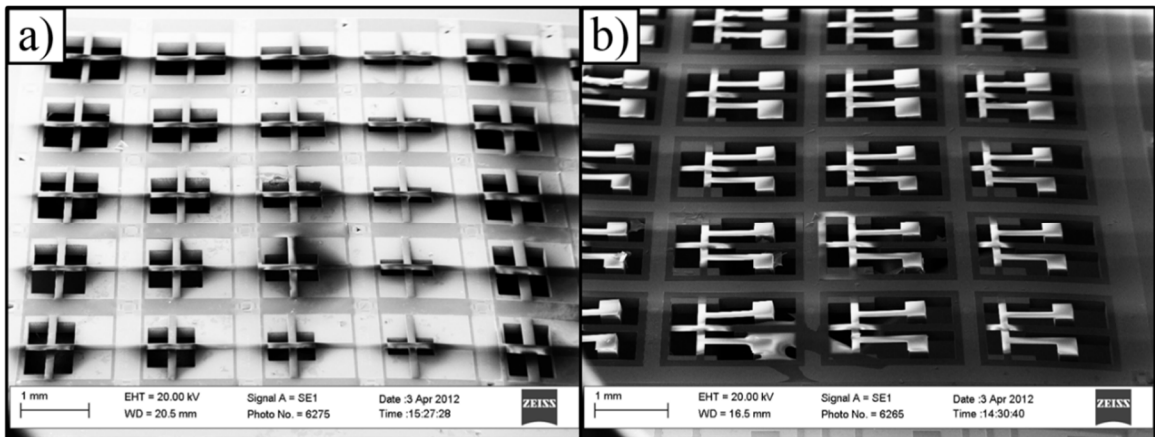


Figure 21. SEM images of a) buckled cross structures and b) structures with proof masses.

The prototype with the longest buckled span was 1,500 μm . An SEM image of this device is shown in figure 22 a) below. Width for the arms and beam was 100 μm , and was the same for all devices. Each die fabricated had 36 unique geometries, to allow evaluation of potential parameters that might prohibit a viable “s” shaped buckled profile. So far, none of the devices that have been fabricated have failed to buckle into the desired shape. The smallest length buckled beam was 500 μm , and still exhibited the correct form of buckling. A 600 μm buckled beam is shown in figure 22 b).

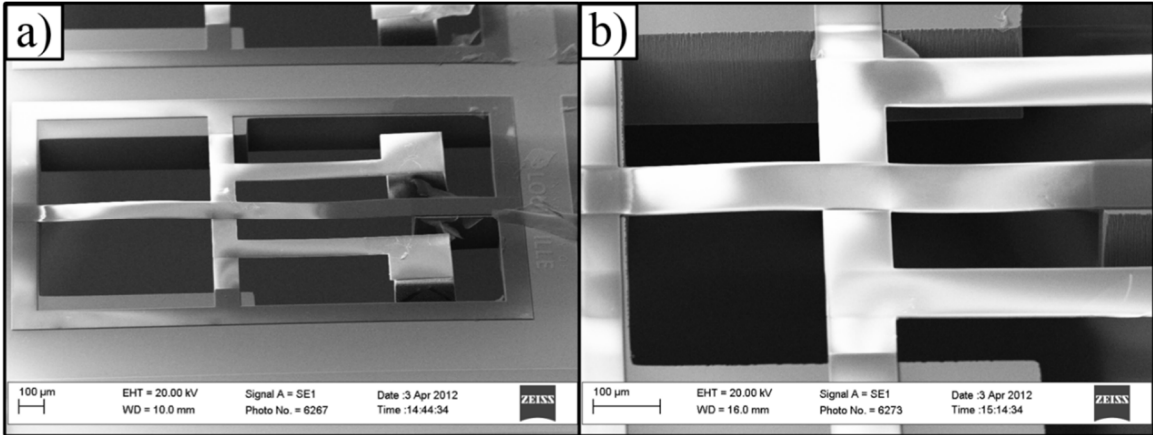


Figure 22. Buckled mass device with a) 1,500 μm and b) 600 μm long center beam.

Using a Dektak profilometer, the out-of-plane displacement was measured for this device and is shown in figure 23 below. A low force of 0.5 mg (4.905 μN) was used to scan the surface of the buckled center beam. The maximum out-of-plane deflection was 13.5 μm upwards and 14.5 μm downwards. Figure 23 shows a profilometer scan of the main buckled beam 1,500 μm in length along with ANSYS predictions of the initial buckled profile.

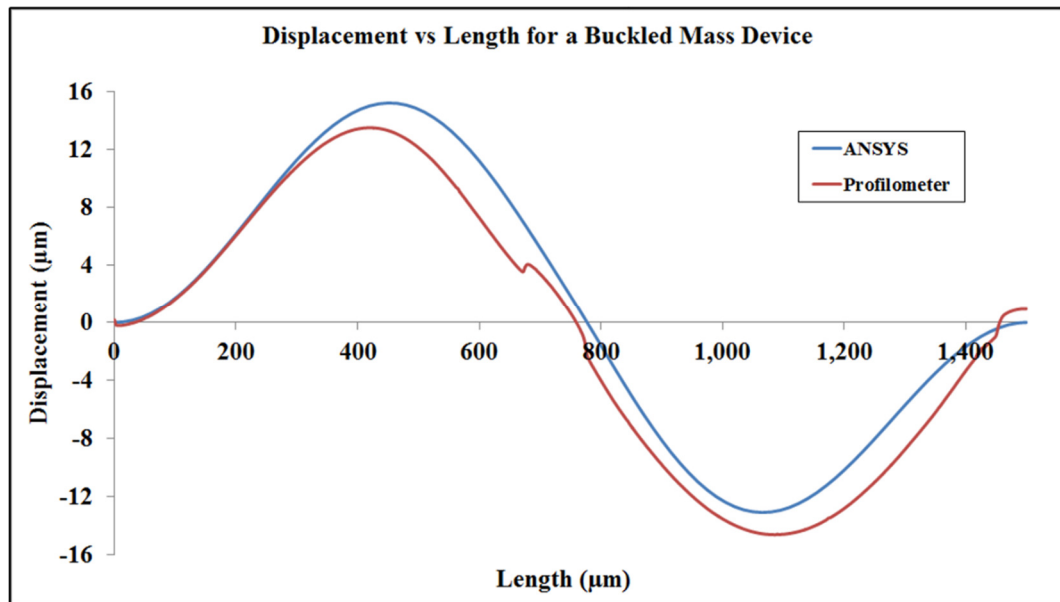


Figure 23. Displacement vs length for a buckled mass device with a 1,500 μm long center beam; measured on a Dektak profilometer.

A macro-scale non-piezoelectric prototype was constructed to prove bi-stability and allow for simple actuation experimentation. The center beam is made of stainless steel sheeting while the flexible outer arms are aluminum tape. Base plate material consists of half-inch polycarbonate while the mounts that constrain the center beam and flexible arms are made out of aluminum stock. To emulate pre-stress in the center beam, the mounting blocks were moved closer together until a desired height in the buckled “s” shaped beam was obtained. This first attempt at a prototype is shown in figure 24 and figure 25 below.

Determining induced stress in the center beam for the macro model would require assuming a shape function for the center beam, knowing the vertical and angular spring constants of for the center pseudo pin, and then using energy methods. An ANSYS model with varying built in stress would be the preferred way of backing out the unknown pre-stress given this particular situation.

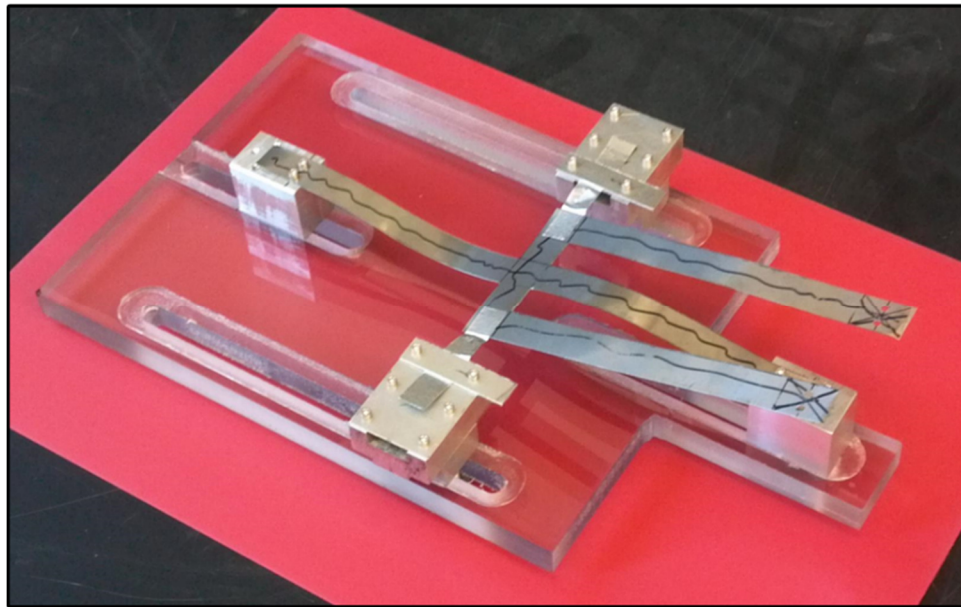


Figure 24. Macro scale model in one bi-stable buckled condition (mass arms up).

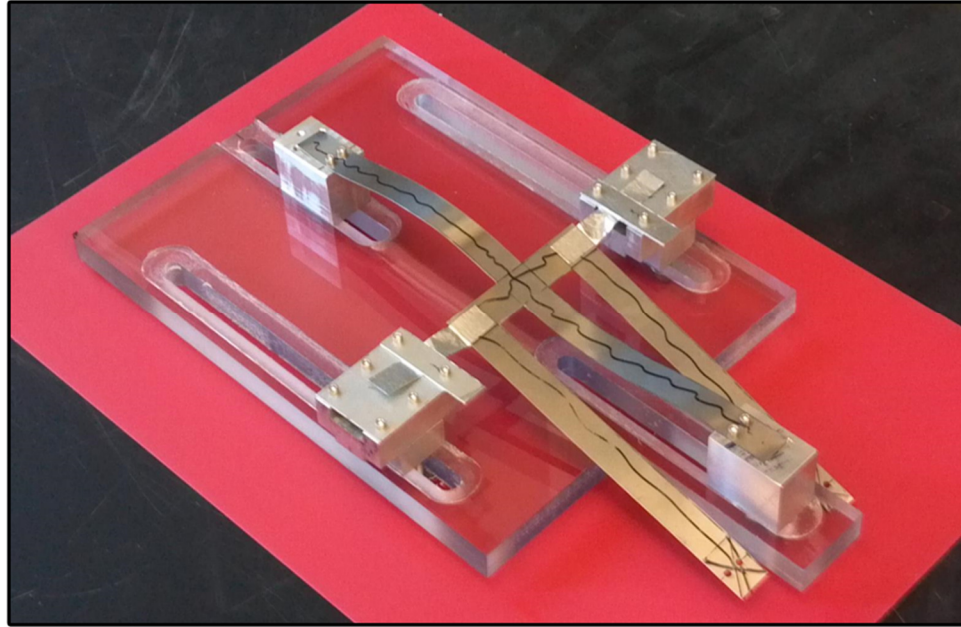


Figure 25. Macro scale model in the other bi-stable buckled condition (mass arms down).

Other prototypes were made to gauge the effect of compression on the center beam. The original acrylic prototype above had to be manually compressed and locked into position to emulate a pre-stressed beam and it was hard to do it symmetrically. To overcome this obstacle, a 3D printed version which included a symmetric rail gear and locking mechanism was designed. Simply turning the center gear gave even compression of the center beam. This design gave confidence and insight in the prototype stage; more precisely it showed how sensitive the buckling behavior is to small changes in compression distance. The design is shown in figure 26 below.

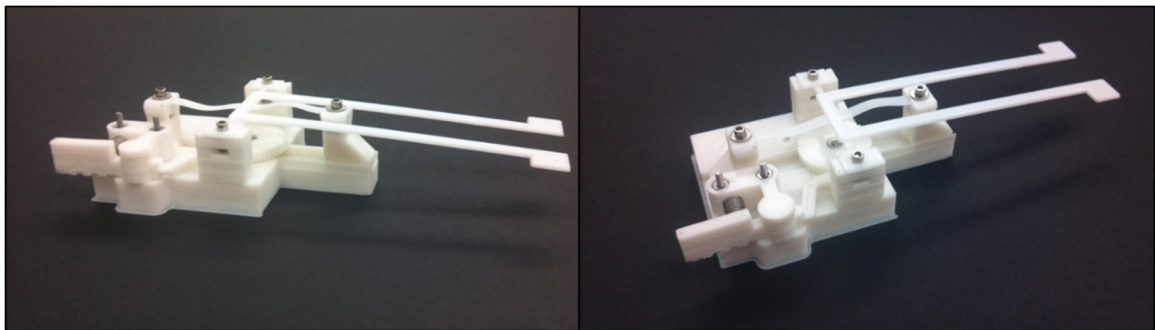


Figure 26. 3D printed adjustable bi-stable buckled prototype with locking gear.

As an add-on to possible future projects, a multimode version of the bi-stable device was construed to present the feasibility of snap-through wave type behavior. For simplification two 2-56 screw/nut linear push guides are designed on the ends to compress the device. Afterwards the side pillars are clamped down to ensure even compression for both nodes. The design is shown in figure 27 below. Shaking this device by hand presented an interesting snap-through behavior in which the center beams nodes would snap at different at different times during a single cycle randomly.

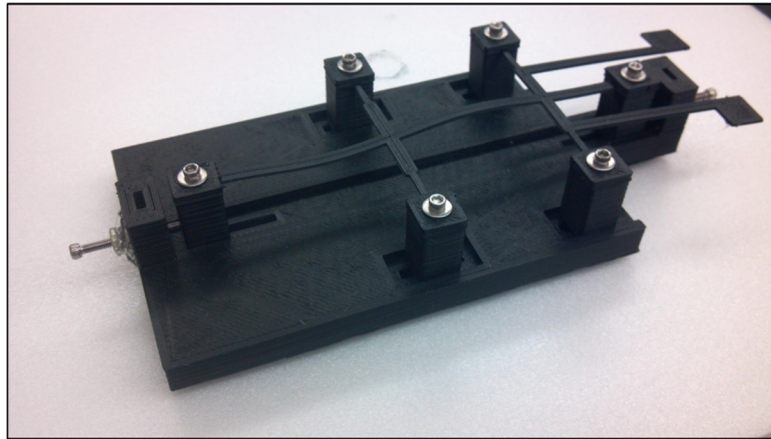


Figure 27. 3D printed multi-node prototype.

CHAPTER III

PZT AND PVDF PIEZOELECTRIC ENERGY HARVESTING

Lead zirconate titanate (PZT) is a material that when strained generates an electric field within the body. The opposite is also true; when an electric field is applied to the body of the material, a strain is induced. This is called the piezoelectric effect (or reverse piezoelectric effect) and was first observed by Pierre and Jacques Curie in 1880 [134]. It is most commonly found in crystalline or pseudo-crystalline materials. There are a total of 32 crystal classes that can be separately identified in the material science field, 11 of these classes are centrosymmetric and cannot be piezoelectric. The remaining 21 classes with the exception of one are piezoelectric [134].

Piezoelectric materials are usually judged by the amount of strain per unit electric field which is equivalent to units of displacement per electromotive force. A relationship between the amounts of strain the material can exhibit and the magnitude of the coefficients is generally present also, which may or may not affect the intended application. PZT, commonly used in ultrasonic transducers, has high piezoelectric coefficients but can only take a small amount of strain because it is a pure ceramic. Polyvinylidene fluoride (PVDF) is a thermoplastic fluoropolymer that is semicrystalline (40-50%) and can be made up to a thickness of about 100 μm . PVDF has piezoelectric coefficients much smaller than that of PZT (greater than one order of magnitude) but can take considerably larger strains [134].

PZT can be created by a high temperature bulk ceramic sintering process (1200°C) which yields high piezoelectric coefficients [58]. This method usually results in bulk materials that are then shaped into wafers so that they may be adhered to other substrates. As long as the adhesion layer is thin the practical mechanical effect is negligible. Wet etching using a liquid such as buffered hydrofluoric acid (BHF) is then used on the PZT material to thin it to a desired height. Xu *et al.* used a 1BHF:2HCl:4NH₄Cl:4H₂O solution

as the wet etchant. They found that the combination of the bulk PZT and wet etchant left a white residue on top of the exposed surface that turned out to be lead (II) chloride (PbCl_2) and an ammonium salt ($\text{NH}_4\text{Pb}_2\text{Cl}_5$). The removal process for this white residue was a dip process in 70°C DI water for several minutes. Another important observation was that the deposition of white residue affected the wet etching rate: the solution was to etch for 30 minutes and then dip in DI water at 70°C for 10 minutes. Repeating this process until a desired thickness is obtained resulted in a surface roughness of about 500 nm (RMS). Since this roughness was not desired in Xu *et al.*'s work, a polish step was performed afterward. By using a silicon/PZT unimorph the d_{31} coefficient was obtained for their adhesion/thinning process and was approximately -250×10^{-12} m/V [58]. The bulk PZT material used in Xu's work was most likely a PZT-5A or PZT-5H wafer judging from the magnitude of the d_{31} coefficient.

Another approach for utilizing piezoelectric materials in MEMS is to spin a PZT sol-gel onto the substrate and then prebake-fire the material until all of the solvent is driven out of the thin film. The final properties of the films depend on the ingredients of the sol-gel, the sequence of addition, and the aging of the PZT solution. Yi *et al.* proposed a sol-gel solution that utilizes high solubilities and is water based which in turn make the resulting mixture is chemically stable in ambient conditions. This solution can be stored for a period of about 4 months [156].

The stock PZT solution is first created by mixing 5g (5 grams) of lead acetate and 4g of acetic acid. This is done by pouring acetic acid (a liquid) into a Pyrex container on a hot plate at 40°C and letting the acid come to a stable temperature. Lead acetate (a solid powder) is then slowly combined with the acetic acid until it is dissolved fully. The combination of lead acetate and acetic acid will have its temperature increased to 100°C to remove water that causes nonuniform gelation when it comes into contact with titanium isopropoxide and zirconium propoxide. This mixture will be called component "A" for simplicity. At the same time, in a separate container, 3.848g of zirconium propoxide 70wt% in 1-propanol (a light yellow liquid) is combined with 2.032g of titanium isopropoxide (a light yellow liquid) and will be deemed component "B" for simplicity. After letting component A cool down to roughly 40°C, the two components A and B are mixed together completely. The resulting mixture is roughly clear and has a lower

viscosity than component B by itself. De-ionized water is then added to the mixture in the amount of 4 grams to promote the stability of the mixture and reduce the probability of precipitates. Lactic acid (1 gram, a liquid) is added to the mixture to maintain a constant viscosity. Glycerol (1.5g, a liquid) and ethylene glycol (1g, a liquid) is added as the last components of the mixture to enhance the mechanical characteristics of the resulting films and prevent them from cracking and peeling. Thicker films require more ethylene glycol and glycerol for sturdy performance [156]. This resulting mixture is known as the “Stock Solution” and is maintained in an ambient environment while being constantly stirred. The components for our stock PZT solution are shown in table 7 below.

Table 7. Components for the mechanically enhanced (Zr/Ti=53.5/46.5) "Stock PZT Solution" from [156] and [157].

Chemical	Molecular Formula	Quantities(g)	Combination
			Step
Lead acetate	Pb(OOCCH ₃) ₃ H ₂ O	5.000	1
Acetic acid	CH ₃ COOH	4.000	1
Zirconium propoxide (70 wt.% in 1-propanol)	Zr(OC ₃ H ₇) ₄	3.848	2
Titanium isopropoxide	Ti[OCH(CH ₃) ₂] ₄	2.032	2
Distilled water	H ₂ O	4.000	3
Lactic acid	CH ₃ CHOHCOOH	1.000	4
Glycerol	HOCH ₂ CHOHCH ₂ OH	1.500	5
Ethylene glycol	HOCH ₂ CH ₂ OH	1.000	6

A typical spin modification is to add 2-propanol and H₂O to the stock solution which creates a less viscous solution that spins down thinner films. Adding propanol tends to lower surface tension and can improve wettability for many substrates [156]. Syringes with in-line filters are used to pull stock solution from its bottle and then the filters are removed when releasing the stock solution into a graduated cylinder for volume measurement. The current stock solution is viscous enough to create a single post fired layer of 500 nm thickness [156]. The firing temp for the sol-gel based application is about 600 to 650°C with a temperature ramp of roughly 2 to 5°C per minute. Currently, our

atmosphere for firing PZT sol-gel is argon and is done in a “trash oven” which accommodates outgassing lead particles.

A. Piezoelectric Coefficients

The Institute of Electrical and Electronics Engineers (IEEE) have created a set of standards for piezoelectric materials. These standards include a common symbol set when explaining and characterizing piezoelectrics associated with specific loading and electric field orientations. Examples of these coefficients, their meaning, and the units associated with them are shown in table 8 below. Many more coefficients exist for the purpose of analyzing piezoelectricity and can be found in the IEEE Standard on Piezoelectricity [1].

Table 8. Standard symbols used in the characterization of piezoelectrics.

Symbol	Meaning	Units (SI)
P	Polarization	coulomb/meter ²
D	Electric displacement	coulomb/meter ²
E	Electric field	volt/meter
S	Strain of a material	unitless or meter/meter
T	Stress of a material	newton/meter ²
ε	Dielectric permittivity of the material	farad/meter
s	Elastic compliance constant	meter ² /newton
c	Elastic stiffness constant	newton/meter ²
d	Piezoelectric strain coefficient	meter/volt or coulomb/newton
e	Piezoelectric constant	coulomb/meter ²
k	Coupling factor	unitless

When a voltage is applied to two conductors with an insulator in-between an electric field, E , is formed. The electric displacement, D , is used as a substitute for the electric field so that one does not have to consider the internal polarization, P , of a material. A relation between the electric displacement and electric field through charge balance is given by

$$D = \epsilon_0 E + P \tag{Eq 1.}$$

where ϵ_0 is the permittivity of a vacuum. Electric displacement is the customary way to deal with electric fields. Stress and strain are indicated by the symbols T and S instead of the customary σ and ϵ used in mechanics. A very important coefficient used in the piezo field is the piezoelectric strain coefficient, d , which describes the amount of polarity that arises from one unit of stress. Another way to write the electric displacement is

$$D = dT + \epsilon E \quad \text{Eq 2.}$$

where ϵ is the permittivity of the material and is defined as

$$\epsilon = \epsilon_0 \epsilon_r \quad \text{Eq 3.}$$

It can be seen from Eq 1 that the polarization inside the material is taken into account by combining it with the pure electric field component. Properties such as the compliance, stiffness, and permittivity are measured either at constant strain, stress, electric field, or an electric displacement. This is indicated by placing a S , T , E , or D in the superscript of the coefficient. Strain can arise from the application of an electric field and/or a mechanical stress and is shown in equation form as

$$S = s^E T + dE \quad \text{Eq 4.}$$

and Eq 2 can be rewritten as

$$D = dT + \epsilon^T E \quad \text{Eq 5.}$$

which shows that it is very important to know how the material constants are measured because they will change under different circumstances. An example is when a material is constrained and cannot move in a particular direction; this would be an example of a constant strain measurement for that particular direction. If the electrodes are shorted and the coefficients are measured then that would be an example of a constant electric field ($E=0$).

Coefficients are utilized with subscripts that detail the direction of the electric field first and then the direction strain. The sign of the coefficient deals with whether the material expands or contracts and is a function of crystal axis orientation which is determined as a standard in [1]. If a field is generated parallel to an axis where strain is

applied then this is called the piezoelectric axis. For quartz and PZT this is the X and Z axis respectively. An illustration of what the coefficient d_{ij} details is shown in figure 28 below.

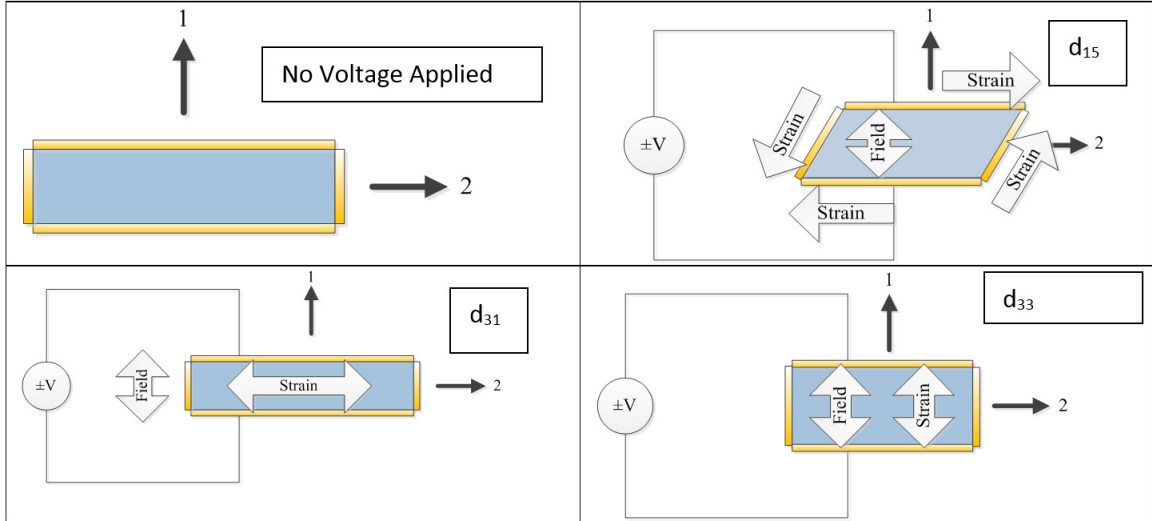


Figure 28. Visual examples detailing the meaning of the piezoelectric strain coefficient d_{ij} .

Generally in research models are two or three dimensional in nature, so it is rare that a one dimensional problem arises. Thus the coefficients for piezoelectric materials are reported as tensors rather than scalars, just like the mechanical properties. An example of the tensor structure for a solid ceramic PZT-5H block is shown in Eq 6 - Eq 9 below. Piezoelectric strain coefficients in the hundreds of pC/N are considered to be very high with respect to other known d_{ij} coefficients.

$$[s^E] = \begin{bmatrix} s_{11} & s_{12} & s_{13} & 0 & 0 & 0 \\ s_{12} & s_{11} & s_{13} & 0 & 0 & 0 \\ s_{13} & s_{13} & s_{33} & 0 & 0 & 0 \\ 0 & 0 & 0 & s_{44} & 0 & 0 \\ 0 & 0 & 0 & 0 & s_{44} & 0 \\ 0 & 0 & 0 & 0 & 0 & 2(s_{11} - s_{12}) \end{bmatrix} \quad \text{Eq 6.}$$

$$[d] = \begin{bmatrix} 0 & 0 & 0 & 0 & d_{15} & 0 \\ 0 & 0 & 0 & d_{15} & 0 & 0 \\ d_{31} & d_{31} & d_{33} & 0 & 0 & 0 \end{bmatrix} \quad \text{Eq 7.}$$

$$[\varepsilon^T] = \begin{bmatrix} \varepsilon_{11} & 0 & 0 \\ 0 & \varepsilon_{11} & 0 \\ 0 & 0 & \varepsilon_{33} \end{bmatrix} \quad \text{Eq 8.}$$

where the values of the compliance, piezoelectric strain, and permittivity for PZT-5H are given below [134]. One should note that the d_{ij} units should be changed to Coulombs per Newton when using these in ANSYS as to not confuse the resultant. Also, Eq 6 is primarily defined for a material that is poled in the z-direction; this will come in useful when deriving the ANSYS piezoelectric matrix [e] shown in a later section of this proposal.

$$\begin{aligned} s_{11} &= 16.5 \times 10^{-12} \text{ m}^2/\text{N} \\ s_{33} &= 20.7 \times 10^{-12} \text{ m}^2/\text{N} \\ s_{44} &= 43.50 \times 10^{-12} \text{ m}^2/\text{N} \\ s_{12} &= -4.78 \times 10^{-12} \text{ m}^2/\text{N} \\ s_{13} &= -8.45 \times 10^{-12} \text{ m}^2/\text{N} \\ d_{15} &= 741 \text{ pC/N} \\ d_{31} &= -274 \text{ pC/N} \\ d_{33} &= 593 \text{ pC/N} \\ \frac{\varepsilon_{11}}{\varepsilon_0} &= 3130 \\ \frac{\varepsilon_{33}}{\varepsilon_0} &= 3400 \end{aligned} \quad \text{Eq 9.}$$

B. Limitations of PZT Ceramics

As a brittle ceramic, PZT has limits on the amount of mechanical and electrical “stress” that can be applied to it. The limits of a device are dictated by failure criteria such as maximum stress/strain before cracking occurs, maximum electrical field before breakdown, the stress at which depolarization occurs, and other parameters. Generally sol-gel based PZT does not require poling during the sintering step which minimizes the depolarization problem; though poling can increase the d_{ij} coefficients dramatically [29].

Yagnamurthy *et al.*, evaluated properties for PZT thin films in actuator stacks [153]. Though it is unknown to the author what the composition ratios of the PZT solution being used was, the outcomes of their experiment was rather insightful in terms of limits. A Young’s modulus, tensile strength, and maximum elongation for PZT were measured to be 83.8 GPa, 460 MPa, and ~0.5 % respectively. Park *et al.*, investigated the ultimate yield strength of sol-gel spun PZT dog bone tensile samples with varying widths [104]. The total thickness for Park’s samples was 2 μm of PZT on top of 0.15 μm of platinum.

Obtaining 2 μm of PZT required multiple spin casts followed by curing and sintering steps at 400 and 650 $^{\circ}\text{C}$ respectively. Widths for the samples varied from 50 to 150 microns. Composition for this work was at the well-known multi-phase boundary of $\text{Pb}_{1.1}(\text{Zr}_{0.52}\text{Ti}_{0.48})\text{O}_3$ for which the piezoelectric coefficients are maximized. Table 9 below shows the elastic modulus, ultimate tensile strength, and fracture strain for Park *et al.*'s work. Other references for the yield strength of PZT show a much lower ultimate tensile strength for PZT, though the material is in bulk form and not a thin film [158].

Table 9. Young's modulus, ultimate yield stress, and fracture strain for sol-gel based 2 μm thick PZT dog bone shaped samples [104].

Width [μm]	Elastic modulus [GPa]		Ultimate tensile strength [MPa]		Fracture strain [%]	
	E	Average	S_{75}	Average	e_f	Average
50	69.3	72.8 \pm 3.7	241.0	263.4 \pm 21.1	0.361	0.383 \pm 0.031
	72.4		282.9		0.419	
	76.7		266.4		0.368	
100	74.6	75.0 \pm 1.3	242.5	238.6 \pm 4.5	0.337	0.331 \pm 0.006
	74.0		233.7		0.331	
	76.4		239.5		0.325	
150	72.1	73.3 \pm 1.8	224.0	221.1 \pm 13.9	0.335	0.320 \pm 0.021
	75.4		233.4		0.328	
	72.5		206.0		0.296	

Electrical breakdown for PZT is measured via leakage current and varies with thickness and applied electric field. Breakdown values depending on other factors like the method of deposition, constituency, maximum sintering temperature, and other parameters so it is difficult to quote a single value for breakdown electric field. Figure 29 below shows the leakage current as a function of electric field for PZT with a zirconia and titanium composition of 45% and 55% respectively. Two different film thicknesses are used to compose the graphs which show that an electric field below 50 kV/cm is considered ohmic since the current density and electric field have an almost linear relationship [29]. Cheng *et al.* [29] attributed the dip in figure 29 a) to charge trapping and explains that this transition region disappears as the film thickness decreases. A graph showing electric breakdown field versus PZT film thickness is shown in figure 30 below which exhibits reduced breakdown strength as the films become thicker. These leakage currents contribute to losses in energy harvesting that cannot be recovered.

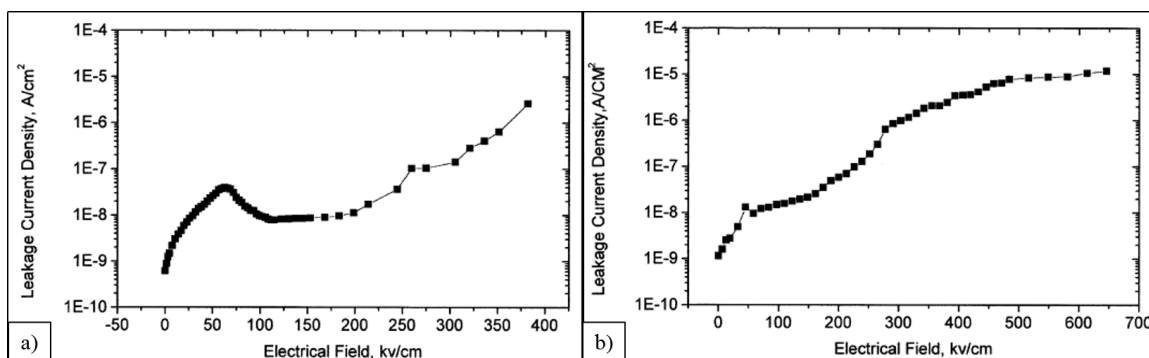


Figure 29. Leakage current as a function of electric field for PZT (45/55) with thicknesses of a) 1.3 μm and b) 0.3 μm [29].

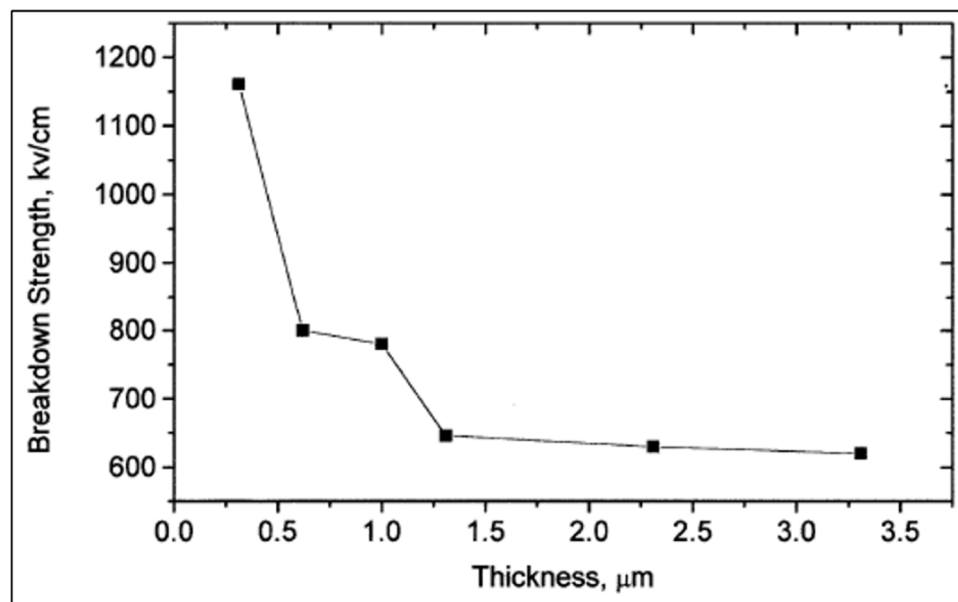


Figure 30. Electric breakdown strength versus thickness for PZT (45/55) [29].

Through sol-gel PZT deposition, very thin layers are deposited by 0.2 to 1 μm increments [100]. If layers thicker than 10 μm are desired then multiple spin or screen printed steps will have to be done, each with a high temperature sintering process [29]. The depositions are done in thin increments because organics and solvents have a tendency to create porous holes in the thin films which in turn may cause a short in electrode behavior. Also, the thermal stresses that are induced in the PZT during sintering are large, and cause cracking of the film itself, thus lowering performance dramatically.

C. Experiments to Evaluate Coefficients

Before confirming experimental data with theoretical models, it is important to evaluate the piezoelectric coefficients as well as the mechanical properties. There are many popular techniques to determine mechanical properties of thick and thin films but are not in the scope of this proposal. Piezoelectric coefficients such as the d_{ij} are important to evaluate for sol-gel based thin films because the many different methods to deposit, cure, and fire such materials can vastly change the resultant properties. As an example, the d_{ij} coefficients for PZT can vary as much as one order of magnitude, which of course could significantly impact a theoretical models outcome [79].

To truly compare a piezoelectric material to another it is tantamount that the method and type of d_{ij} coefficient are reported. Two classes of methods exist for the measurement of piezoelectric strain coefficients, direct and indirect methods. Direct methods are the obvious solutions to obtaining the piezo coefficients which include inducing the piezoelectric effect via strain and measuring the electric field or the reverse piezoelectric effect that involves applying an electric field and measuring the resulting displacement. Indirect methods involve linking the mechanical and electrical properties to back out the piezoelectric coefficients.

The first direct method is called the “normal load method” and involves compressing a piezoelectric material with a round or flat tip. Setting up this test is quite simple and involves a load cell, a capacitor electrically larger than that of the samples capacitance which helps the charge drain from the sample quickly (zero or constant field characteristic), and a data acquisition system that has a sampling rate that is higher than the electrical response of the electrical signal. Placing the capacitor in series with the sample causes the charge to drain into the capacitor which in turn increases the voltage drop across it. If the capacitance is known and the peak voltage difference is measured then the piezoelectric strain coefficient can be determined by

$$d_{33}(eff) = \frac{\partial D_3}{\partial T_3} = \frac{Q}{F} = \frac{C_0 V_0}{F} \quad \text{Eq 10.}$$

where D_3 is the longitudinal electrical displacement, T_3 is the normal stress on the sample surface, Q is the accumulated charge, F is the normal force on the sample, C_0 is the capacitance of the capacitor in series, and V_0 is the peak voltage acquired after compression.

The normal contact method is considered quasi-static which implies that the load can be applied once and the voltage can be measured. The d_{ij} coefficient determined from this method is an effective value because the stress is not uniform as it is applied to the sample surface.

A very interesting coefficient evaluation technique is the “periodic compressional force” method that is somewhat similar to the normal load method. To determine the piezoelectric strain coefficient of a new sample, a known and evaluated piezoelectric material is driven via compression waves using a solid ceramic/metal rod with a rounded tip through a liquid. Piezoelectric materials with well-defined d_{33} coefficients are placed into the mechanism and the charge Q is measured by integrating the current generated with respect to time. Afterwards the new sample with an unknown d_{33} coefficient is placed under the mechanism and excited with the same pulse waves. Again, current is measured and integrated with respect to time to acquire the charge produced. The tests should be conducted by executing the experiment under the same period of time. At the completion of the experiment the new d_{33} of the unknown sample is found using an equivalent force balance by

$$d_{33}(eff) = \frac{Q_m}{Q_R} d_{33,R} \quad \text{Eq 11.}$$

where Q_m is the collected charge of the unknown sample, Q_R is the collected charge of the reference sample, and $d_{33,R}$ is the piezoelectric strain coefficient of the well-defined material. Sensitivities (I think the author means errors) for this method produce d_{33} values that are roughly 0.03 pC. It is important that the user attempt to create the same coupling liquid droplet on the known and unknown sample so that the force is evenly distributed over the same area. This becomes a problem when both samples have different wetting properties. Professionals of this method recommend pulsing with a high enough frequency to maintain a steady current but not high enough that the lattice of the sample starts to resonate.

The “cantilever method” predicts the e_{31} coefficient for a piezoelectric material and has a rather simple setup. A beam constrained at one end and free on the other is mounted so that a tip may press down onto the free end deflecting it downward. Swiftly removing the tip that deflects the beam causes the structure to oscillate and create a voltage. A faster

tip actuation leads to a more accurate coefficient measurement. Electrodes sandwiching a piezoelectric film and rests atop a thicker substrate are measured from a distance of x_1 to x_2 with respect to the constrained end. A strain develops in the thin film (x direction) and can be estimated if the other directional strains (y and z) are assumed to be negligible. This strain is

$$S_1 = \frac{3\Delta h}{2l^3} \left(1 - \frac{x_1 + x_2}{2} \right) \quad \text{Eq 12.}$$

where Δh is the amount that the free end is deflected, and l is the total length of the beam. From above the longitudinal strain can directly be calculated from the known geometry. If the system is connected to an oscilloscope with a known resistance and capacitance, then the voltage versus time can be measured.

D. PZT Fabrication Routines

Using the mechanically enhanced PZT recipe from above, a multitude of die and wafers were spun using the stock solution, 2-propynol, and DI H₂O in a volumetric ratio of 1:1:1, 1:2:1, and 1:2:2 which was allowed to sit for one day before being filtered and applied. Definitions of these volumetric mixing ratios are listed through-out this document as (p:i:w) where p, i, and w are PZT, 2-propynol, and DI H₂O respectively. Thicknesses were measured before and after the firing step which converts pyrochlore to perovskite using a J.A. Woolman Co ellipsometer. The model used to fit the index of refraction is the Cauchy or Sellmeier relationship which is

$$n(\lambda) = A + \frac{B}{\lambda^2} + \frac{C}{\lambda^4} \quad \text{Eq 13.}$$

where λ is the wavelength of light and A, B, and C are constants to be solved for given a multi-angle/wavelength sweep. This model works well for translucent materials and already has obtained parameters for silicon substrates, SiO₂, and platinum. Thicknesses were obtained in the as-deposited, hot plate treatment, and anneal (fired) steps. The PZT results varied due to a numerous processing parameters such as age of stock solution, PZT mixing ratio, substrate material, coats in-between hot plate treatments, number of hot plate treatments, fired or not, deposition speeds, hot plate temperatures, temperature ramping speeds, annealing temperature, and gas flow during annealing step. Results for these

experiments are shown in the appendix under table 25. Another reference for PZT sol gel film processing parameters and their results is shown in [86].

Ultimately the desired outcome is a perovskite film that is not cracked. Annealing temperatures for PZT sol-gels are around 400 to 650 C [101] which cause large stresses to develop throughout the film. Higher annealing temps are more likely to give perovskite phase but also have a higher risk of cracking the films. A first attempt at spinning and annealing PZT on small silicon die with about 450 nm of SiO₂ are shown in figure 31 below. Thickness results from ellipsometry before annealing are also shown. These samples, whose names indicate the number of spin/hotplate treatments (1b-4b), performed well after a 450 C firing temperature for 30 minutes. The atmosphere was ambient which is likely to cause material particle loss in the films. No cracks were initiated for samples 1b and 2b (figure 31 a) and b)) with one and two hotplate treatments but did crack with three and four (figure 31 c) and d)) treatments due to thickness.

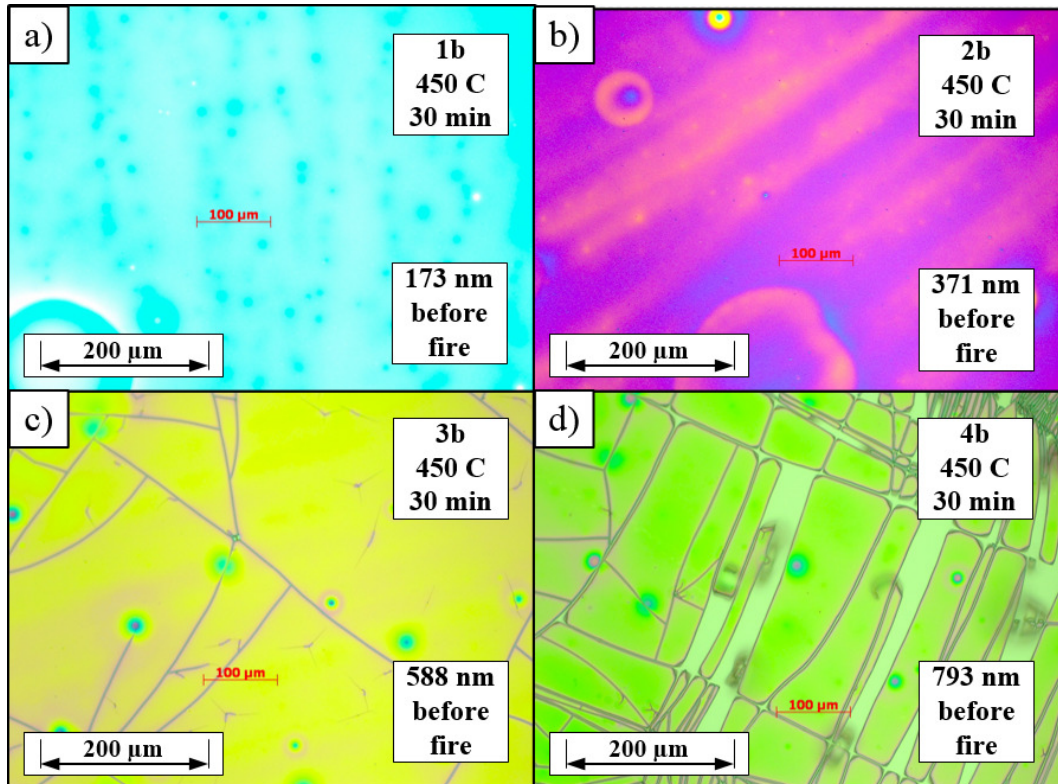


Figure 31. PZT (1:1:1) on SiO₂ annealed at 450 C in an ambient atmosphere for samples a) 1b, b) 2b, c) 3b, and d) 4b.

Additional PZT samples on SiO₂ named ‘a’ were created at the same time as the ‘b’ samples and had the same spin/hotplate profiles but annealed at 550C to reveal the results of a higher firing temperature. Cracking results can be seen in figure 32 below and show that all but sample 1a completely cracked. Further investigation into sample 1a showed that cracking did start to initiate which ultimately made annealing for the (1:1:1) PZT solution at 550C on SiO₂ infeasible. There are other options to test which could allow this setup to have a preferred outcome; it requires spinning at a faster rate to obtain thinner layers and then subsequently annealing each layer to create a stacked structure. This approach would take a substantial amount of time so finding another approach to satisfactory PZT films seems desired.

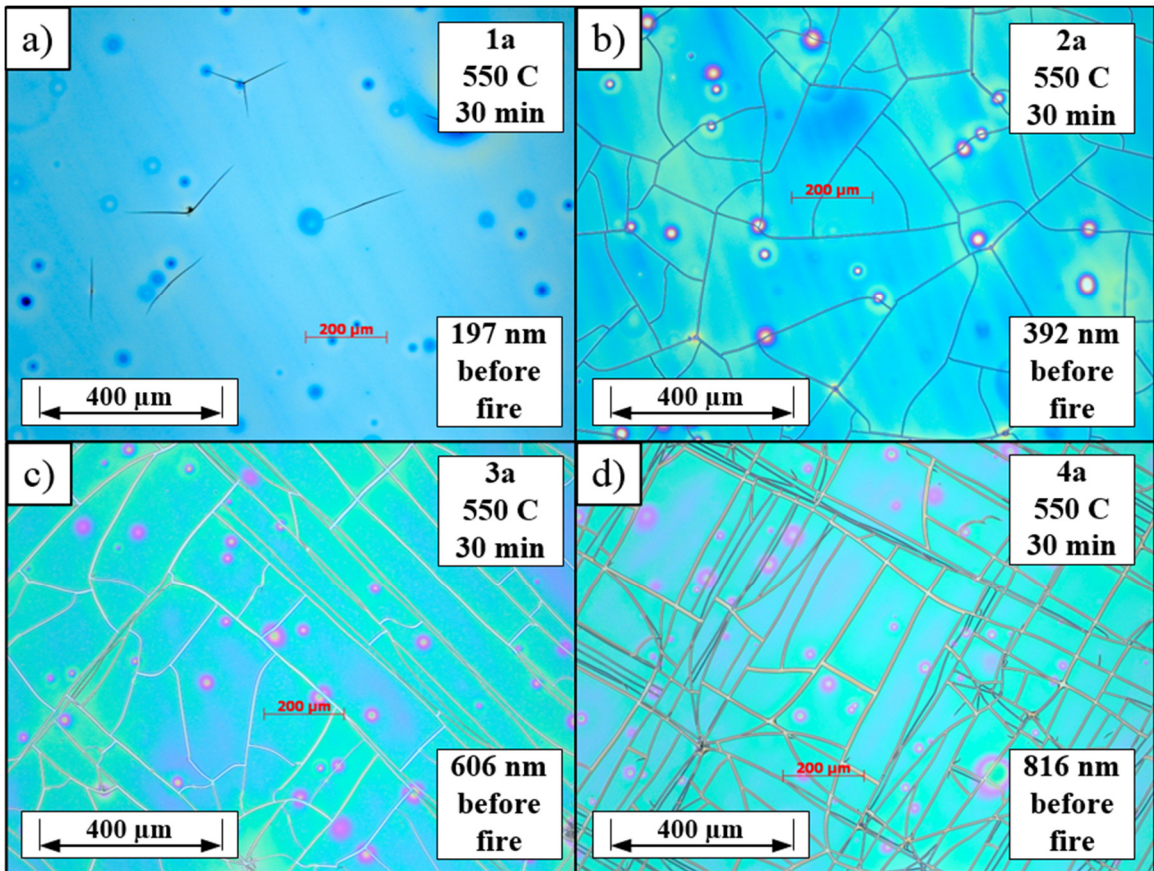


Figure 32. PZT (1:1:1) on SiO₂ annealed at 550 C in an ambient atmosphere for samples a) 1b, b) 2b, c) 3b, and d) 4b.

Other tests performed are the 'c' and 'd' samples which used a PZT solution with the mixture ratio of (1:2:1) and annealed at 450 and 550 C respectively. These tests had the same annealing atmospheric conditions as the 'a' and 'b' samples. Results for the annealing test can be seen in the appendix under figure 126 and figure 127. The 450 C samples looked good while all but one 550 C samples cracked. At this point it seemed mixing ratio was a bad parameter modification to obtain reasonable results.

Samples 'e', 'f', and 'g' were created to evaluate the effect of spin speed. Other parameters were modified for this test as it became apparent that these experiments should represent the substrate material for the actual device. Thus each die had a layer of titanium and platinum deposited on top of the SiO₂. The total thickness of the Ti/Pt layer was about 150nm. The annealing step atmospheric conditions are switched to O₂ as in [101] and will flowing at a rate of 1668 mL/min. Also changed was the hot plate temperatures to drive off solvents. The first hot plate was set to 150 C while the second one was put at a higher 450 C. Samples labeled 'f' were accidentally taken off the 150 C hotplate too early and placed on the 450 C one which caused violent solvent drive, thus sputtering the samples with flakes of PZT. Pictures of the die before and after the anneal step are shown in the appendix under figure 128 for one coating and figure 129 for two coating die. Sputtering of the 'f' sample devices caused a concern and it was realized that the remedy for potentially making this mistake would be to allow the die to drive out solvent in the trash furnace.

Thus the final set of experimental PZT samples were made and labeled Perov1, Perov2, Perov3, and Perov4. The numbering does not indicate the number of spins after a 175 C hotplate treatment this time. Most of the solvents were driven out for 10 minutes on the hotplate. These samples used PZT (1:1:1) spun on at 3000 rpm for 60 seconds (spread at 300 rpm for 15 seconds). To anneal the new samples, a furnace profile was created that ramped to 400 C from room temperature at a rate of 20 C/min. The samples are held at 400 C for 30 minutes the pushed to 650 C at the same rate and held for 1 hour then allowed to cool to 400C at 20 C/min. Results for the annealed samples are shown in figure 33 below.

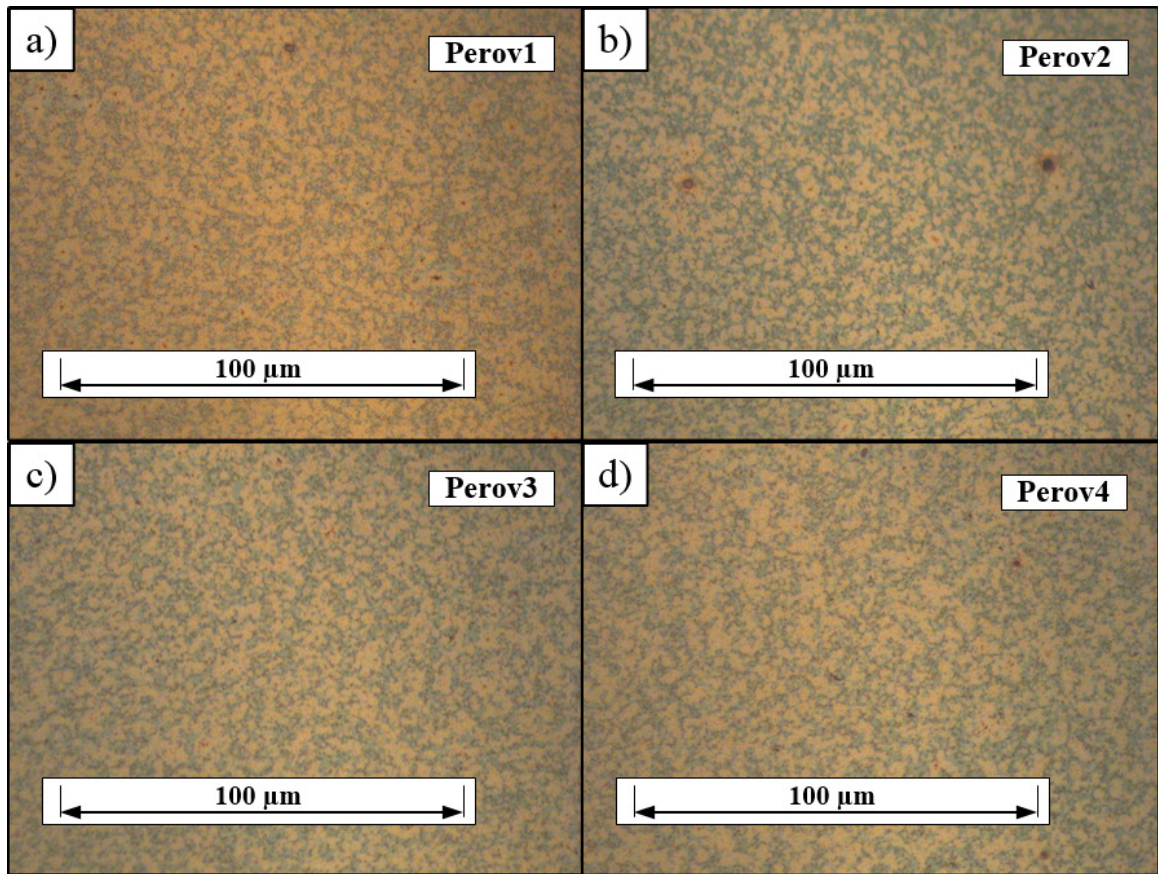


Figure 33. PZT (1:1:1) on platinum sample die after one gel application and anneal a) perov1, b) perov2, c) perov3, and d) perov4.

Un-cracked samples from the Perov line of die were encouraging, meaning a multi-fire approach would be suitable to give different thicknesses. PZT was then again processed on Perov1-4 and annealed which gave the un-cracked results shown in figure 34 below. This process is the one deemed the best given the stated requirements for the core MEMS device of this thesis. Ellipsometry done on the devices show that each coating of PZT gives about 75nm of material after the anneal. Etching the PZT and running a profilometry scan shows that thicknesses are about 11.4% higher than the ellipsometer approach. It is also worth noting that Toho thin film measurements for the Perov die put the estimated bi-axial stress at roughly 3.8 GPa (tensile) for one coat. This is extremely large and needs a substantial compressive stress layer to counteract it.

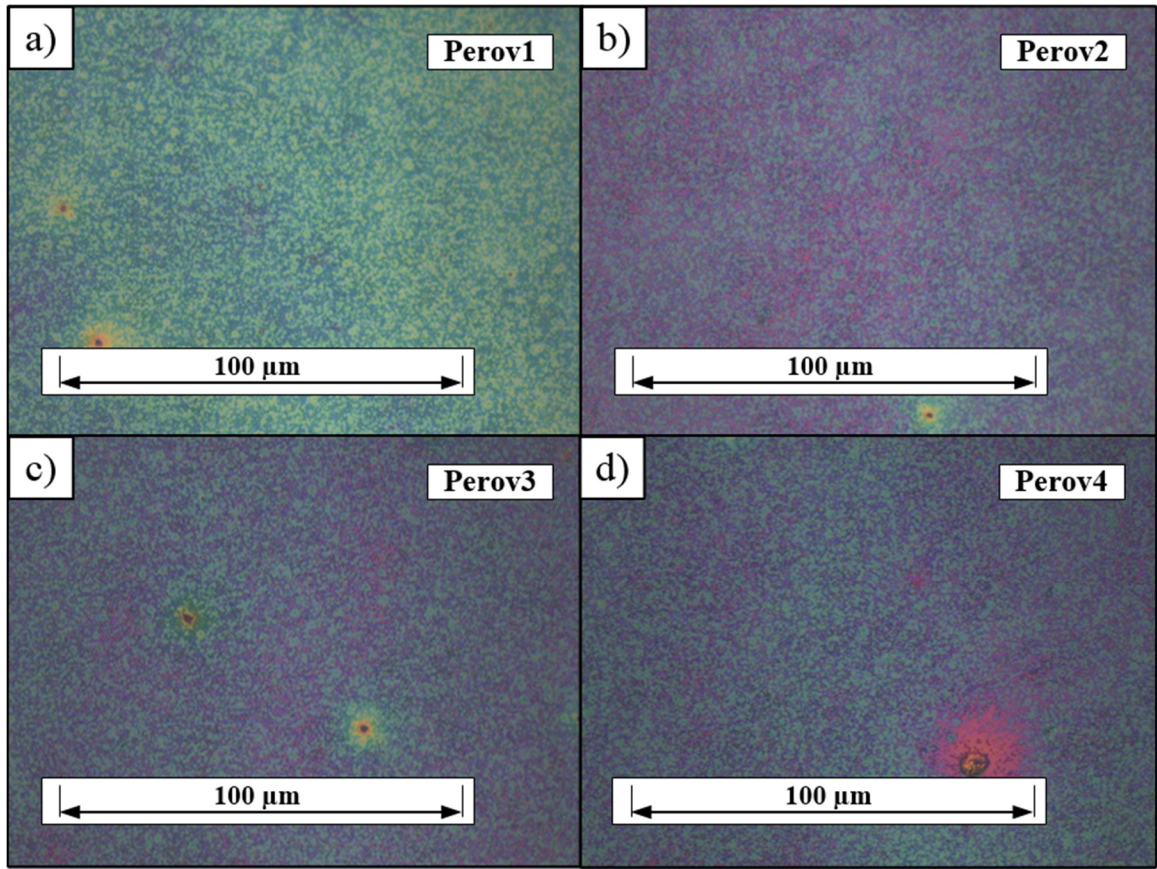


Figure 34. PZT (1:1:1) on platinum sample die after the second gel application and anneal a) perov1, b) perov2, c) perov3, and d) perov4.

One way of detecting what type of crystal phase exists in a material is X-ray called diffraction which relies on elastic scattering. Destructive interference will reduce the created secondary spherical waves except at a certain incident angle determine via Bragg's law

$$2d \sin \theta = n\lambda \quad \text{Eq 14.}$$

Where d is the distance between the diffracting planes, θ is the incoming x-ray incident angle, n is an integer, and λ is the wavelength of the x-ray beam. An example of constructive interference, which the x-rays tend to sum because the waves are in phase, is shown in figure 35 below.

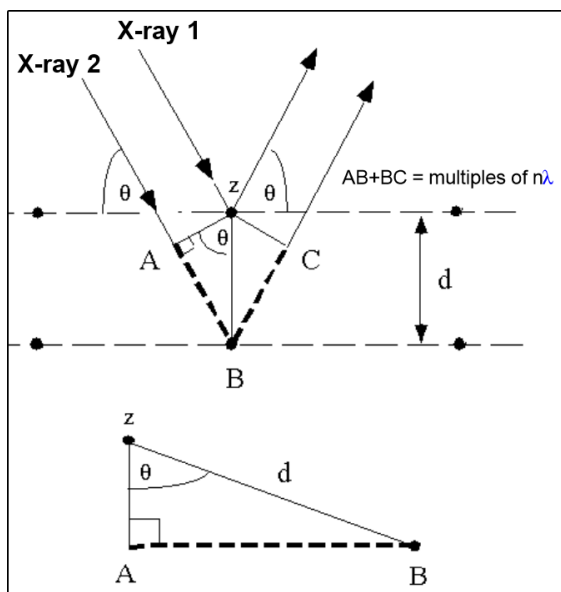


Figure 35. Schematic illustrating constructive interference of x-rays on a crystal structure [96].

X-ray diffraction was used on some of the samples to determine if the PZT contained perovskite or pyrochlore after processing. Perovskite is the most piezoelectric phase so making sure that coating and annealing parameters evolved this phase was essential. A glancing angle XRD approach allowed for thin film analysis because the X-ray detector would pick up less of a signal from the silicon substrate and other underling films. Literature that has XRD graphs for PZT and its derivatives in its various forms are [46], [77], [140], [94], [86], [75], [50], [32], and [143]. In figure 36 a) below there is a reference for PZT in the composition ranges of $\text{Pb}(\text{Zr}_x\text{Ti}_{1-x})\text{O}_3$ for $x=60, 52,$ and 40 that comes from [77]. These reference graphs come from the JCPDS data base and are labeled under the files 73-2022, 33-0784, and 50-0346 for Z58, Z52, and Z44. Alongside the reference is results we fabricated in figure 36 b) and c) that clearly show (100), (110), and (200) PZT perovskite phases.

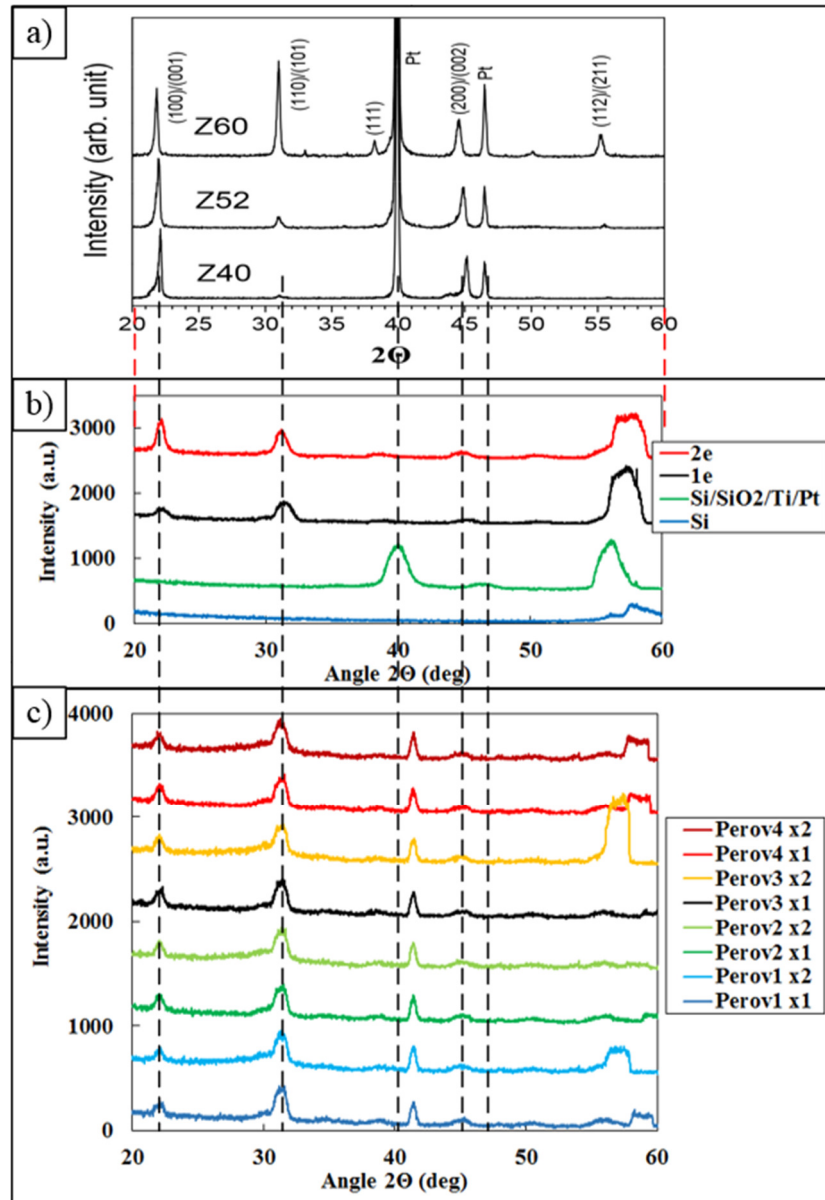


Figure 36. GA-XRD results for PZT for a) known reference specimens [77], b) silicon wafer, Si/SiO₂/Ti/Pt, and samples with (1:1:1), and c) more thin to thick specimens to make sure process is repeatable.

PZT wet etching is accomplished by mixing 1 part BOE, 2 parts HCl, and 4 parts DI-H₂O in a Teflon beaker [2], [21], [46]. Other additives include nitric acid, acetic acid, and ammonium chloride to clean up left over residue. Results of the Perov die with a photomask, after etching, and after the photomask is removed is shown in figure 37 below.

A typical fresh batch of PZT etchant will strip about 160 nm of annealed PZT in roughly 90 seconds so it is imperative to constantly watch the sample being etched.

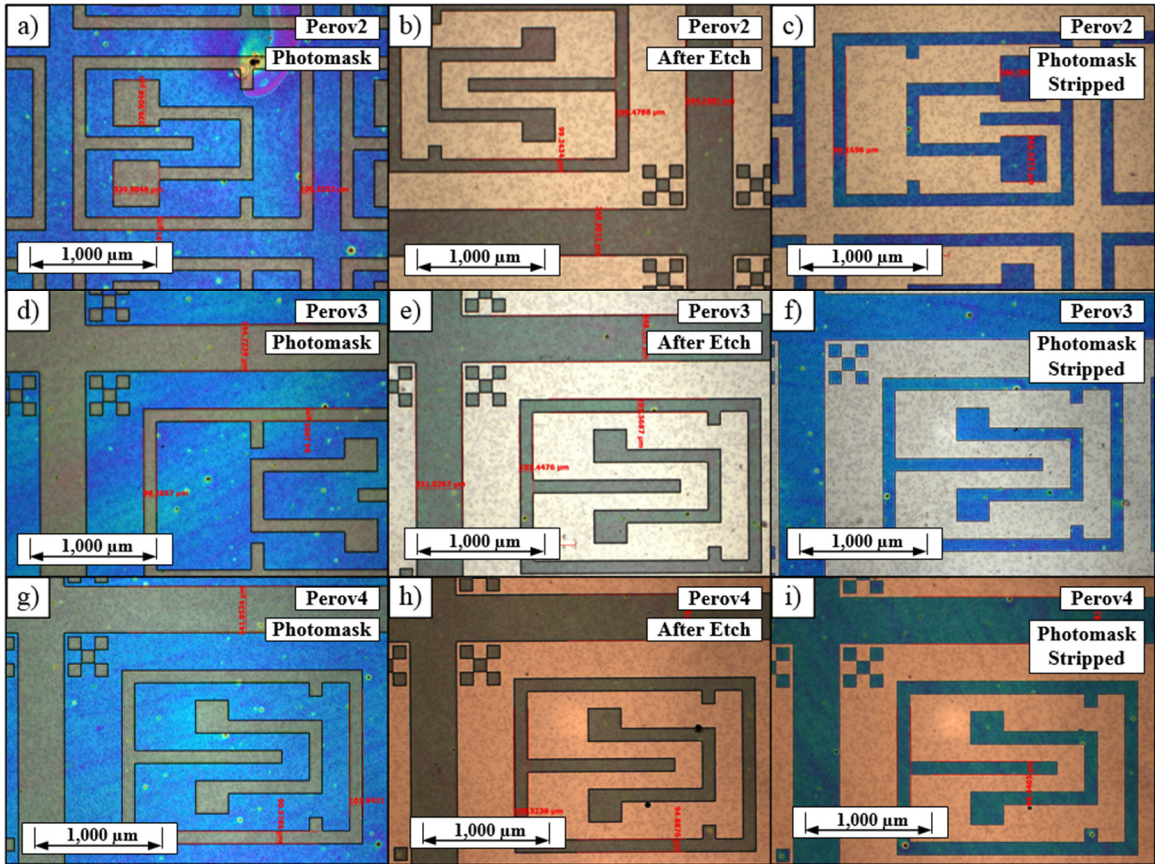


Figure 37. PZT (1:1:1) on platinum samples a), d), g) before and b), e), h) after etching. Also with c), f), i) photoresist removed.

Undercutting can be severe enough to render a device useless especially in interdigitated electrode configurations where the metal is close to the PZT edge. For this test the undercutting was about 3 μm when etched for 90 seconds and is shown in figure 38 below. Better control of the etching procedure can be done by diluting the stock etchant with more DI H_2O . Adding ammonium chloride to the etching solution can remove some of the PbCl_2 that creates a residue on the surface like as shown in [160].

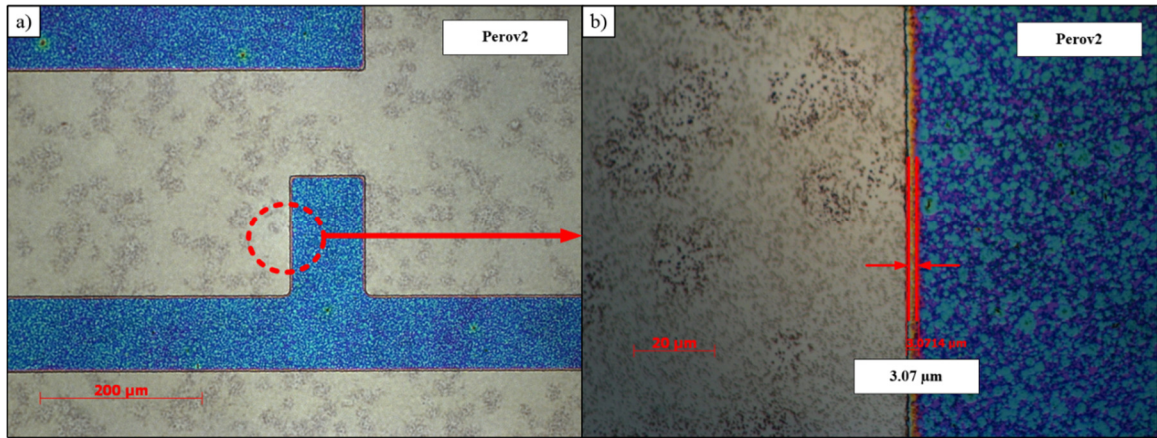


Figure 38. PZT (1:1:1) on platinum sample Perov4 a) after etching and removing photoresist and b) a zoomed in section to show undercut.

The success of the prior PZT samples give confidence in our ability to make piezoelectric spin-on ceramics. Actually applying these films to a non-planar profile, such as the proposed MEMS bi-stable buckled devices will require more experiments. At this point it is unknown what the 650C temperature profile is going to have on a stressed nitride layer. Thus it is essential that other piezoelectric materials be considered at this stage. Potential candidates include PVDF which can also be applied as a gel but has lower piezoelectric coefficients or sputtered AlN [13] [155] is CMOS compatible [148], though can be difficult to fabricate with repeatable results [61]. A comparison of promising piezoelectric materials used for energy harvesting can be found in [6].

E. PVDF Fabrication Routines

PVDF is a pseudo crystalline piezoelectric polymer that can be fabricated into a useful poled material for actuation, sensing, or energy generation. One beneficial characteristic of PVDF is that it does not require high processing temperatures like PZT [141]. Care has to be taken though as not to process at the Curie temperature of around 150C or else poled properties will be lost. A safe margin is to not allow the temperature to get above 100C for too long without an active field on the materials electrodes. Melting temperatures for PVDF are around 170 to 200 C [55]. Parameters that affect crystal phase formation of PVDF are solvent type, spin speed, drying temperature [113] [22], humidity, pressure, and annealing temperature/atmosphere. Other means of making piezoelectric

PVDF include hot pressing [116], stretching [26] [15] [126], Langmuir-Blodgett deposition methods [27], and electro-spraying [120]. An extensive overview of piezoelectric polymers can be found in [112] which also shows temperature limitations.

Creating the spin on PVDF gel involves mixing solvents and PVDF pellets/powders like the ones used in this research shown in figure 39 below. This mix is usually allowed to sit on a hot plate at about 50C until all of the solid material is dissolved into solution. The key to gel deposited PVDF is to have it solidify into the β phase, which is the most piezoelectric and ferroelectric form of the other five known crystalline phases α , β , γ , δ , and ϵ [3], [130]. Usually well-funded researchers will purchase a co-polymer like P(VDF-TrFE) to mix with solvents [130], which almost always forms β -phase PVDF due to the highly polarizability nature of VDF with a small amount of TrFe mixed in [70]. These co-polymers (\$80/gram) usually cost a lot of money [27] so it was believed to be beneficial to investigate the possibility of applying homo-polymer (\$5/gram) gels which are very inexpensive to make. Common solvents used in the gels include dimethyl sulfoxide (DMSO) [127], methyl ethyl ketone (MEK) [141], dimethylformamide (DMF) [22], and acetone. Additional additives which promote the β phase include hydrated salts like magnesium nitrate ($Mg(NO_2)_3 \cdot 6H_2O$) [28] [57] [135].



Figure 39. a) PVDF pellets, b) PVDF powder, and c) DMF solvent.

The mixture attempted in this research primarily used a 1:1 volume ratio of DMF:acetone which was then mixed with PVDF pellets/powder in the wt% (of both liquids) of 5, 10, or 20. All substrates are UV treated to remove any extra organics and to promote better adhesion. These gels were spun on a wafers at various speeds (500 to 4000 rpm) and then were transferred to a hot plate do drive out the solvents which converted said gel to a thin film. The temperature of the hotplate was key to promoting the film into

a preferential crystalline phase. β -phase is easily obtained in low temperature depositions (50-70 C) but the porosity is so great that poling is infeasible just like in [28] [57]. This porosity is indicated by a white cloudy color while less porous films will appear more translucent. Hydrated salts tend to be dried at higher temperatures \sim 115 C and still maintain plenty of β -phase.

Annealing the films after the first hot plate treatment can cause even more phase transformation and reduce porosity. The annealing process may be done on a hot plate in ambient atmospheric conditions or in a vacuum oven. Typical annealing temperatures are around 120 C [135] [57]. Annealing, especially vacuum annealing [63] also has the added benefit of increasing adhesion to the electrodes. More effects of annealing can be found in [127].

Typical PVDF thickness for gel deposition versus angular velocity and β -phase content is shown in figure 40 below which comes from Cardoso *et al.* [22]. Another source of thickness vs angular velocity is found in [63] though it is for P(VDF-TrFE). It is important to know the thickness of the deposited films due to a structural and mechanical standpoint but also because the known applied electric field needs to be monitored. From multiple experiments performed in the lab, a table of spun gel thick films versus spin profiles and other parameters are shown in table 10 below.

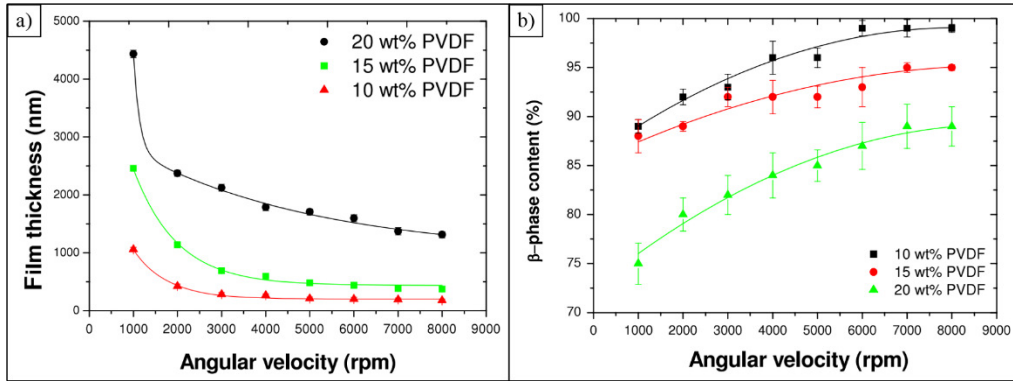


Figure 40. Angular velocity vs a) film thickness and b) β -phase for PVDF films from [22].

Table 10. Experimental thickness results for PVDF gel films after hotplate/annealing treatments.

PVDF (Mw)	Dilution (wt%)	Spin (rpm)	Spin Time (s)	Spread (rpm)	Spread Time (s)	Thickness (μm)	# of Coats
534,000	20	3000	15	300	60	7.1	1
534,000	20	3000	15	300	60	5.0	1
534,000	20	4000	15	300	60	4.3	1
275,000	10	500	0	0	20	7.0	2
275,000	10	500	0	0	20	7.0	3
275,000	5	500	0	0	20	2.0	2
275,000	10	500	0	0	20	4.8	2
275,000	5	500	0	0	20	1.9	2
275,000	10	500	0	0	20	2.5	1

Detecting the different types of phases in PVDF is accomplished using an FTIR (Fourier transform infrared spectroscopy) or a FTIR with an ATR (attenuated total reflectance) attachment. The ATR attachment is used for films which cannot be removed from the substrate. FTIR absorption bands for the α -phase are around 530, 615, 763, 795, 855, and 976 cm^{-1} while the bands for β -phase are about 467, 509, 840, 1175, 1275 cm^{-1} , and the γ -phase is 812 and 1233 cm^{-1} [97] [57] [135]. The machine used to conduct FTIR measurements is a Perkin Elmer SpectrumBX. If the films are annealed at atmosphere conditions then there is a good chance they can be peeled off of their respective wafers with care. 3D printed rings which allow the films to be taped on the outside are shown in figure 46 c) below. Kapton tape is used to adhere the film to the ring at which point it is slowly removed. An example of this with aluminum sputtered on top is shown in figure 44 b) below. While the films are on the printed rings, they are put into the FTIR to measure the crystallography. The slight difference in transmittance obtained drying at different temperatures for films with added hydrated salt is shown in figure 41 below. More FTIR and FTIR/ATR scans are shown in the appendix under figure 131, figure 132, and figure 133 which mostly compare the effects of the addition of 0.2%wt magnesium nitrate. Figure 133 shows that a dense 20% gel without the addition of salt and dried at 50 C gives an appreciable amount of β -phase.

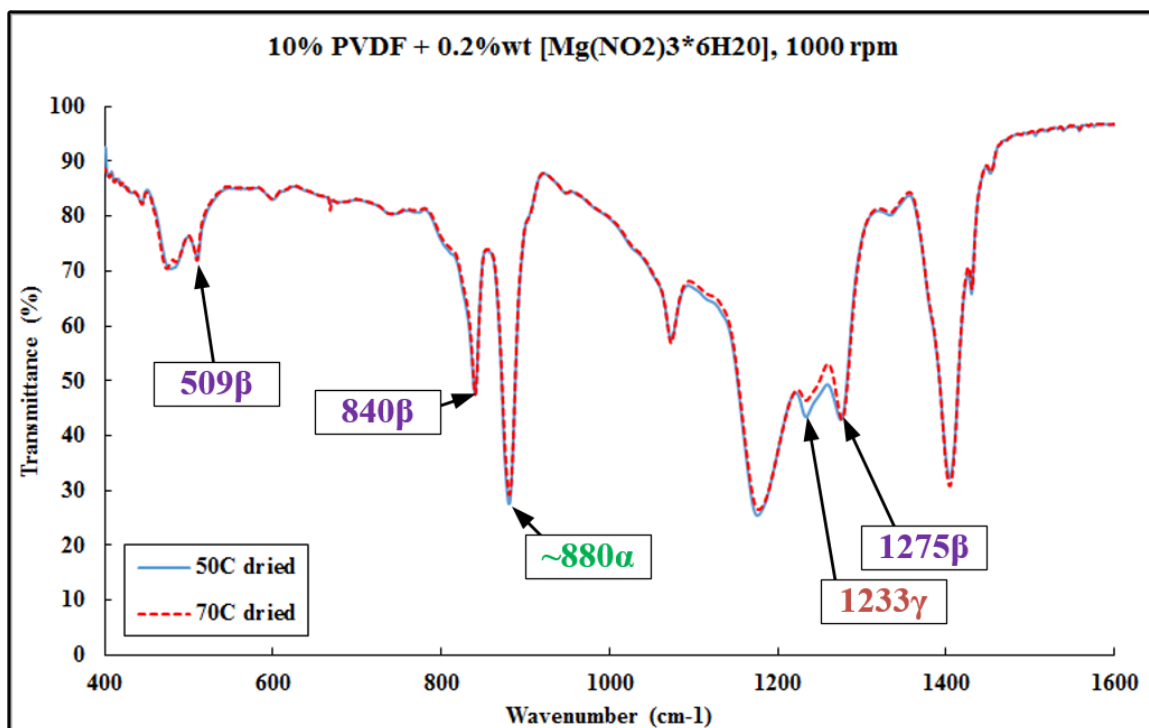


Figure 41. FTIR data for 10%wt PVDF films spun on at 1000 rpm and dried at 50 and 70 C.

Another way of detecting phases in PVDF is through X-ray diffraction just like the PZT samples from above. The effect of drying temperature on PVDF film phases is shown in figure 43 below. When the drying temperature is 100C or below the dominant phase in the films is β which shows up as a peak at around $2\theta=20.5^\circ$ but when the films are dried above 100C the α phase is dominant and shows up at $2\theta=17.8^\circ$ and 20.0° [135], [78], [83]. SEM images for four of the higher temperature drying cases are shown in figure 42 below. These drying temperature tests were done on a 1:1 DMF:Acetone solvent solution with 10% PVDF powder and 0.3% (Mg(NO₂)₃*6H₂O) which, when dried, gives about 2.9% hydrated salt by weight.

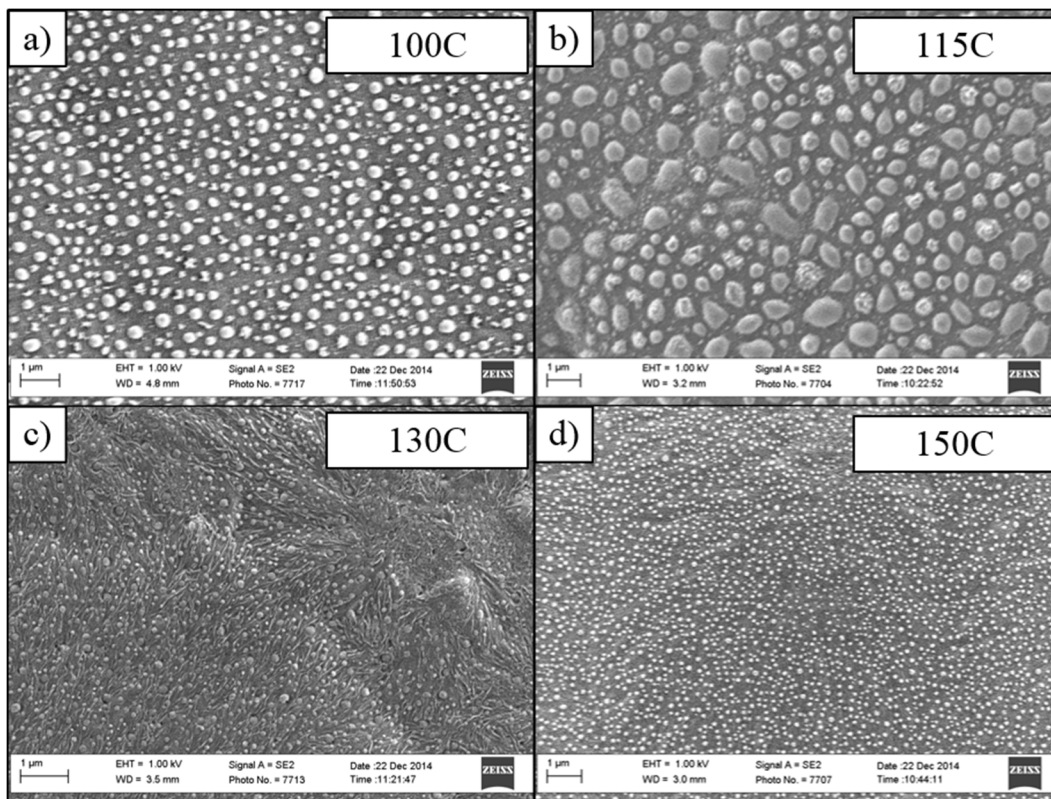


Figure 42. SEM images for four of the PVDF films containing 2.9% hydrated salt by weight and dried at a) 100C, b) 115C, c) 130C, and d) 150C. Prior to annealing.

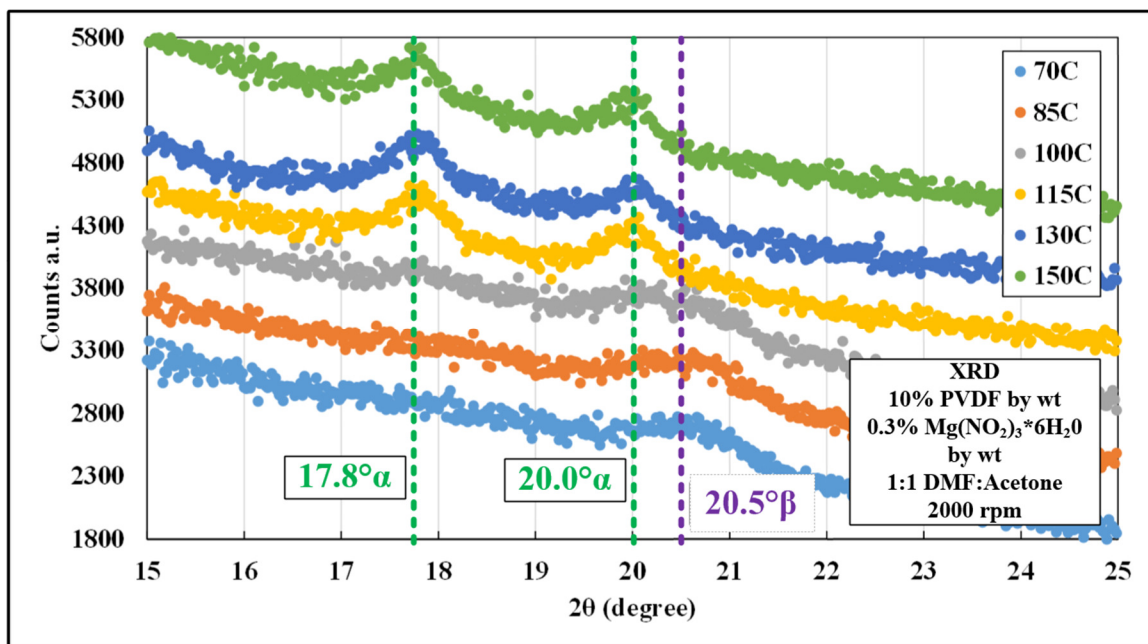


Figure 43. XRD sweeps for PVDF gel deposition samples (1μm thick) with the addition of 0.3% hydrated salt before annealing.

Etching PVDF can be accomplished by acetone solutions [55], dimethyl acetamide (DMA) [55], and reactive ion etching [63]. Acetone etching usually requires a solvent resistant mask because powerful liquids such as acetone will remove photo-resists. Patterns using chrome have been made by soaking dies and wafers in a sealed container with acetone at about 50 C (~550 nm/min) though there is some residue left over. The vapor pressure is high at that temperature so the lid of the container must be properly sealed. Another explored etching mechanism is by using an O₂ plasma at 100/100 watts of ICP and RIE power, respectively. Oxygen and CHF₃ flow rates of 40 and 10 sccm gave an etch rate of 86.6 nm/min when the wafer cooling flow was held at 10 torr of helium. Etching experiments with the hydrated salts tended to leave a residue which couldn't be removed with acetone or DMF.

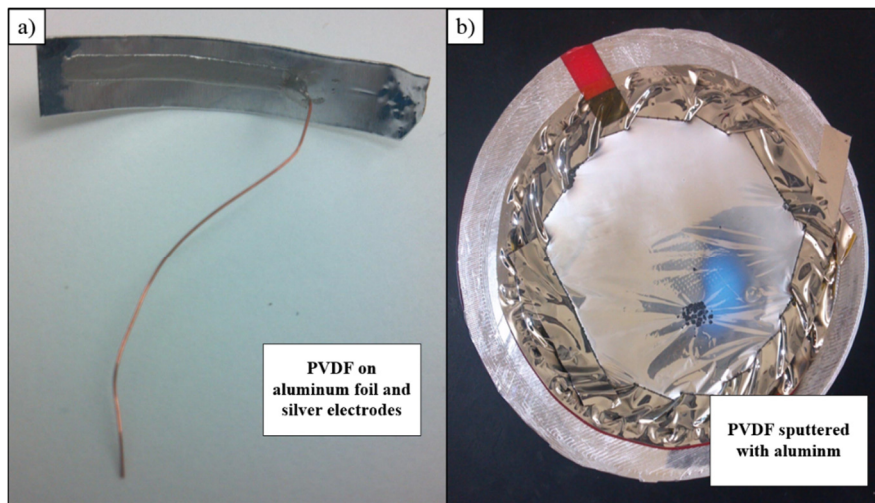


Figure 44. a) PVDF electroded device on aluminum foil and b) PVDF film that has been sputtered with aluminum via PVD.

Electroding of the materials was done either by sputtering aluminum or chrome onto the PVDF films using a PVD process. This would be quite expensive to do continuously in the cleanroom so it was decided to investigate other methods of applying conductive films. Figure 45 below shows four cheap materials investigated while attempting methods of creating electrodes. Figure 45 a) is a typical carbon based wire glue that was found to be too brittle when dried, figure 45 b) is a silver epoxy that is conductive when allowed to dry at room temperature, figure 45 c) is a conductive pen that gave results

similar to the conductive epoxy, and figure 45 d) is also a silver epoxy but needs to be cured at ~125 C to become electrically conductive. Since the product (CW2400) in figure 45 b) worked the best when applied in thin layers and didn't require a high curing temperature which could affect the phase of the PVDF, it was used in the majority of the experiments. Figure 46 b) shows PVDF devices with the CW2400 applied and cured. Some of the experiments were done on the conductive side of aluminum foil like the device shown in figure 44 a) above. Others were done on 100 μm steel plates like the ones shown in figure 46 b) below.

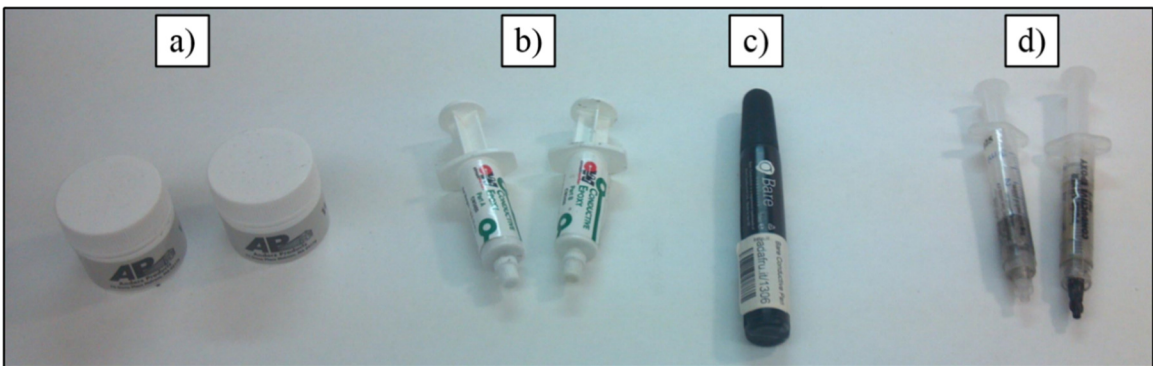


Figure 45. Electrode materials a) 'Anders Products' carbon based wire glue, b) 'Circuit Works' CW2400 conductive epoxy, c) 'Bare Conductive' electrically conductive paint, and d) 'MG Chemicals' pure silver conductive epoxy.

The appendix has a table of results for a few of the PVDF gel application tests in table 26. A majority of poling results are left out of this table due to the large amount of tests conducted in an attempt to obtain a highly repeatable poled film in an efficient amount of time. Ideally the PVDF films applied will be vacuum annealed at elevated temperatures so that adhesion is enhanced. Also the electrodes would be a sputtered metal such as aluminum or chrome since expensive platinum is only used with PZT due to its inert properties at high temperatures (650C). All experimental PVDF samples are shown in figure 46 a) below along with working silver epoxy devices and ring mechanisms that enable film removal from wafers.

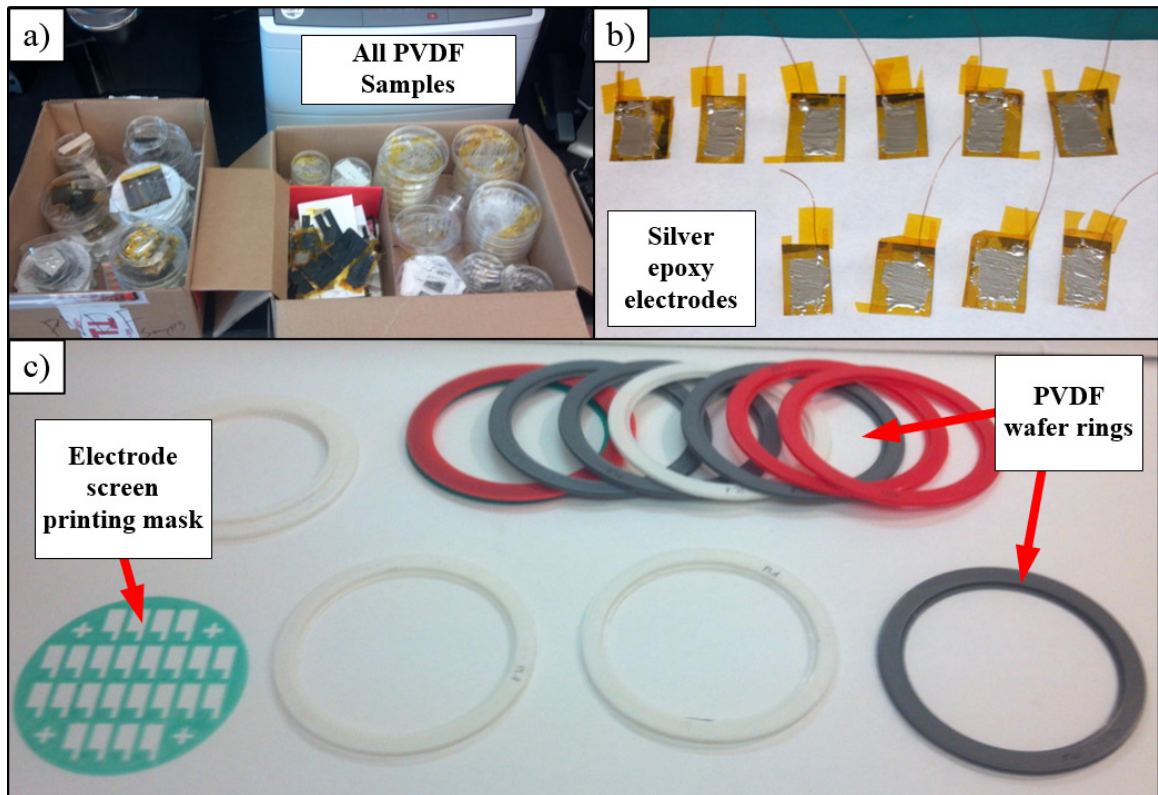


Figure 46. a) All PVDF samples tested for the application of gel deposition, b) double sided electrode samples ready for poling, c) 4" wafer rings used to peel off PVDF.

F. Experimental Poling Results

Polarizing the piezoelectric films after fabrication will align the dipoles and allow them to generate charges constructively. Two popular forms of poling are electrode “contact” and corona poling [26] [68] [15] [83] [85] [15] [14]. The electric fields need to achieve a good piezoelectric coefficient are 20 to 300 MV/m for PVDF [26] [15] [83] [65] [14] [129] [57] [69] and 10 to 100 MV/m for PZT [85] [143] [62] [23]. These poling techniques are usually done at elevated temperatures so that the dipoles align in a short amount of time though it can be done at room temperature [23].

Contact poling is where an AC or DC voltage is applied across a devices electrodes either at ambient or elevated temperatures. The applied voltages are considerably high and can potentially short if there is a low resistance path between the electrodes. Even shorting around the non-conductive material being poled can occur which could ruin a device. To ameliorate this potential failure with high voltages, the devices can be poled in a non-

conductive fluid [35]. DC voltages for PVDF are usually quite high if a thick layer is deposited (~50-300 V) but are low (5-20 V) for PZT due to the very thin profiles [75]. All devices that are contact poled had 30 AWG enameled wired epoxied to them

The 250 V_{dc} power supply used for contact polling of PVDF devices and is shown in the appendix under figure 130 a). Higher voltages were used in some cases which required a small CCFL inverter and a voltage multiplier bridge which allowed for DC power outputs as high as 3,000 V_{dc}. Devices were placed into an oven which varied in temperature from 25 to 110 C while being simultaneously poled. Some device would violently short so it was imperative that the ovens internal surrounding were electrically insulated using high temperature fiberglass sheeting and Kapton tape. Electrical shorting caused the PVDF material to be immediately ablated while the surrounding PVDF and the conductive epoxy would char like the sample in figure 47 below.

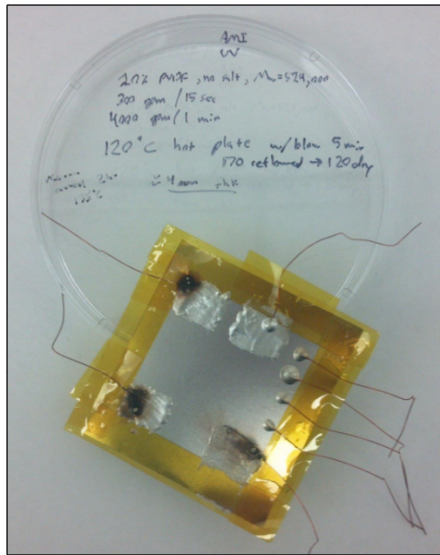


Figure 47. Failed and charred PVDF sample with conductive epoxy electrodes.

Poling samples of PZT was a little different than with the PVDF strips. At first a DC contact poling scheme was tried with an applied voltage of 3-12 V_{dc} which resulted in decent ferroelectric loops but to test a PZT coated wafer in multiple spots for repeatability required a faster approach. Thus a function generator was formed using an Arduino nano microcontrolled, an AD9850 wave generator, and a LM224N op-amp. Using two potentiometer as an amplitude/offset control and one as a frequency control, the PZT

devices could be simultaneously poled and checked for vibrational activity by listening for a high pitch squeal. Input voltages of up to $\pm 15 V_{ac}$ are used to achieve a poled section of PZT. This waveform generator can also be used to check for audible activity of the PVDF samples. A commercial sample with silver ink electrodes could be heard at a frequency of around 7 kHz while ones fabricated in this research were audible at around 6-7 kHz with an input of $10V_{ac}$. One of the better performing samples was a $1.9\mu m$ PVDF device that was poled under a 26 MV/m field at 100 C for 30 minutes. Some of the PZT samples that were poled using the function generator are shown in figure 48 below.



Figure 48. PZT contact poled examples.

A lot of the PVDF results tended to have random flaws which would short when being contact poled. This is mostly due to large electrode areas that increases the chance of encountering a hole in the PVDF. It also occurred to us that poling all of the devices in one step would save time so corona poling was investigated. Corona poling grid voltages of 5kV and bed temperatures of 20-120 C are typically used [83] [65] which means a high voltage power supply must be incorporated into a newly designed station. Distances from the grid are varied 3 to 50 mm [93] [52] [85] but we currently stayed with 5 to 10 mm. This distance is important because a strong field is desired on top of the PVDF that does not cause breakdown or arcing. Poling time is about 5 to 10 minutes for corona poled PZT

at an elevated temperature [85]. A makeshift high voltage power supply is shown in figure 49 below.

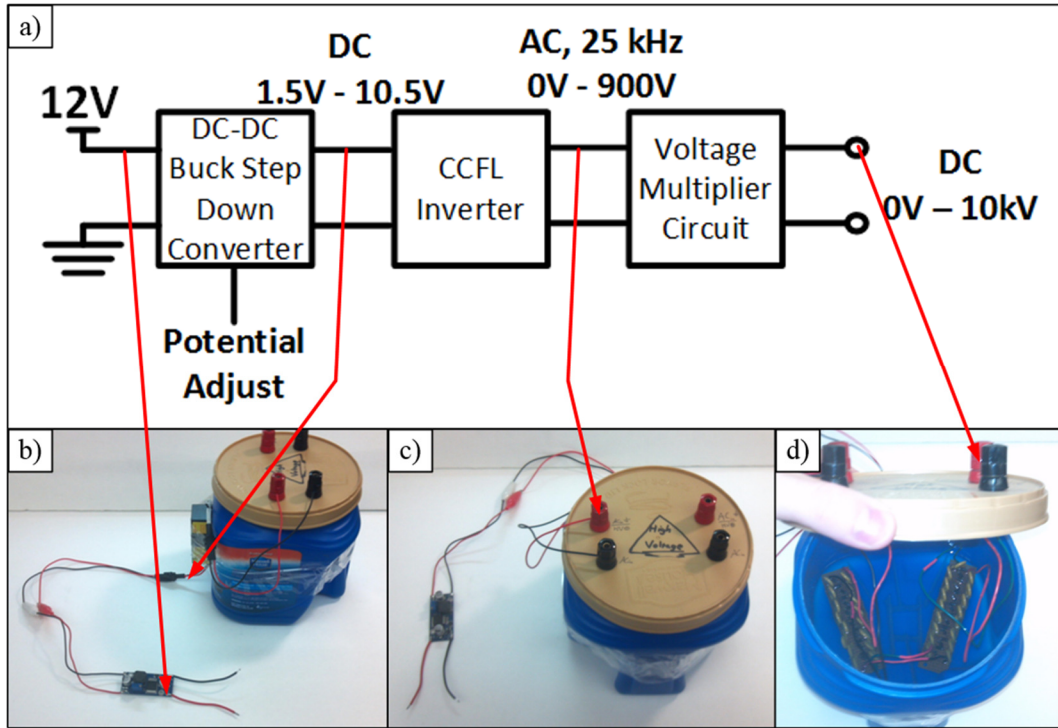


Figure 49. High voltage power supply a) schematic, b) side view showing CCFL, b) top showing banana plug interfaces, and d) voltage multiplier immersed in mineral oil.

A prototype corona poler is shown in the appendix under figure 130 a) and b). This simple mechanism was constructed out of 3D printed parts and a steel needle. The inside was insulated so that charges would be directed towards the bottom mesh. Grid voltages of 1,000 kV were easily achieved without arcing. This inspired a more professional design that is shown as a render and actual construction in figure 50 below. The needle used was a Ted Pella 0.6 μm radius tipped tungsten probe (Product No 13570-10) which creates a corona much easier than the steel needle. A heated platform is achieved using a Hotbed MK2 which is popular with most Reprap printers and can achieve temperatures of up to around 120 ± 0.5 C. The mesh grid is cut out of corrosion resistant type 304 stainless steel wire cloth (McMaster-Carr 85385T67) which had a wire diameter and open area of 0.017” and 48% respectively.

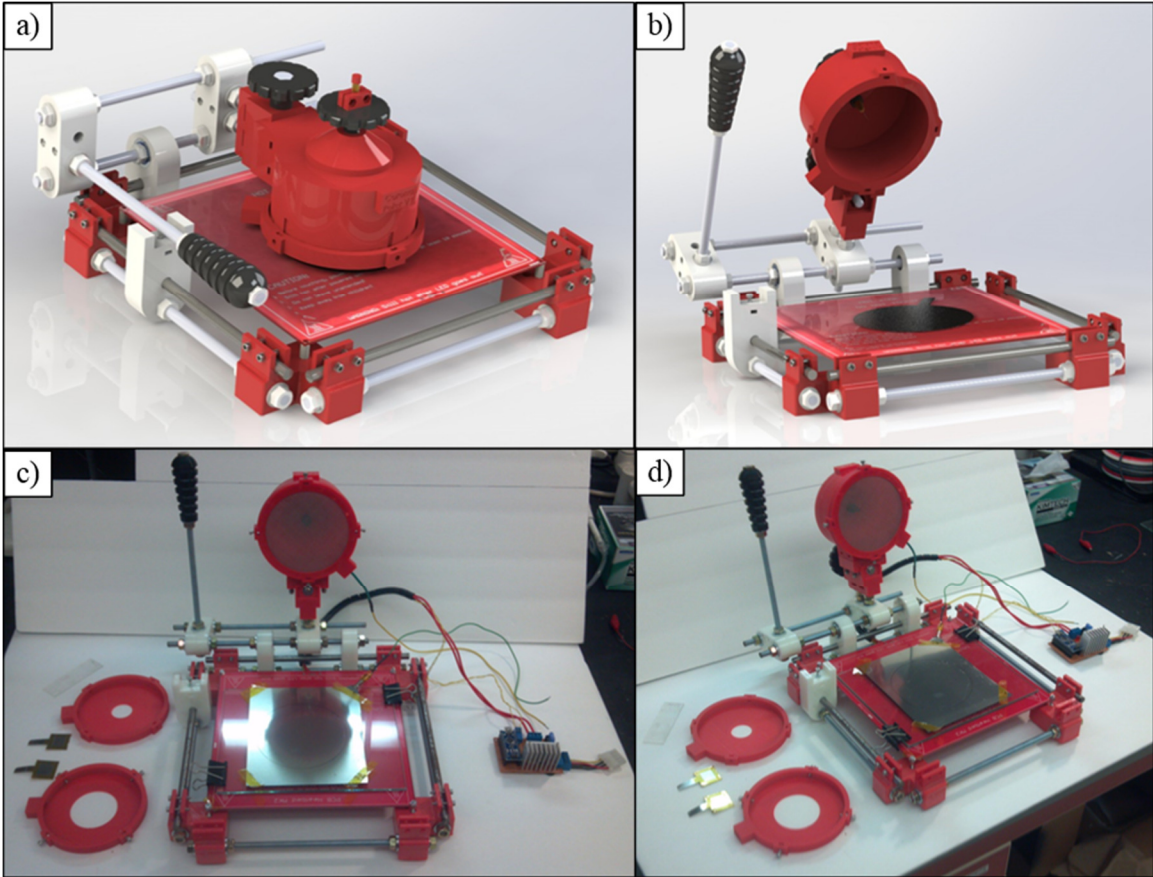


Figure 50. a), b) Render of the designed corona poler and c), d) actual fabricated corona poler with heated bed.

Testing the strength of poling induced in a piezoelectric material can be done in a few ways. The simplest method is to use a Sawyer-Tower circuit [14]. A schematic of the setup is shown in figure 51 below which incorporates an Arduino Nano and a simple AD9850 waveform generator. Our hysteresis testing circuit can go up to ± 500 V with the added on Model 2205 amplifier, though the oscilloscope is rated for $250 \text{ VAC}_{\text{rms}}$ so the field input is cut by a fourth using a voltage divider from $1 \text{ M}\Omega$ resistors.

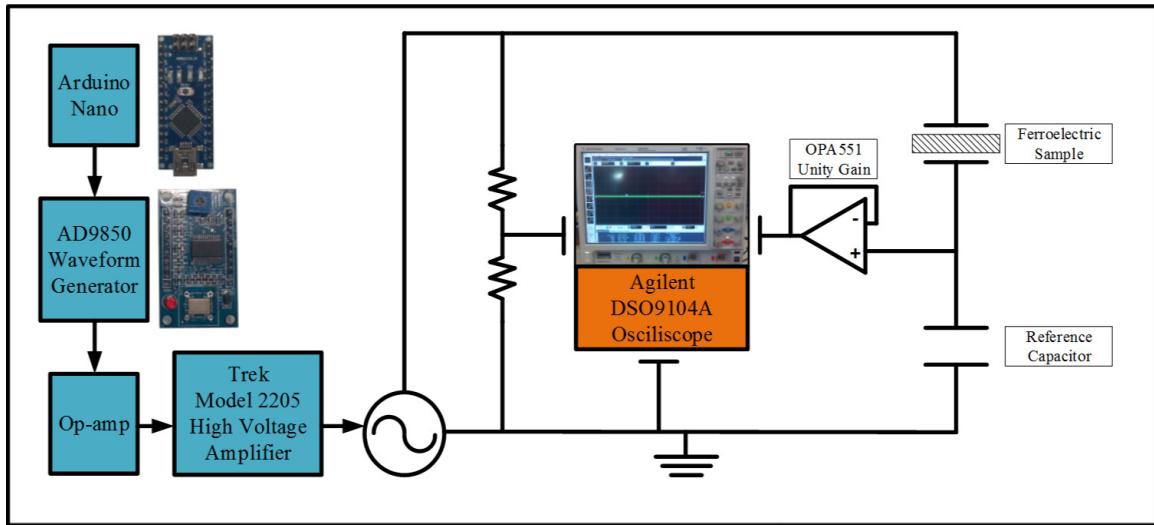


Figure 51. Sawyer-Tower circuit used to generate ferroelectric hysteresis loops.

PZT samples that were 250 nm thick were poled and characterized using the above Sawyer Tower circuit above. The top electrodes were simple CW2400 conductive epoxy with a circle diameter of about 1.5 mm and the bottom electrode was Ti/Pt on SiO₂. A small sinusoidal voltage of 14-15 V_{pp} was applied at frequencies ranging from 1-100 Hz which instantaneously poled. The hysteresis loop looked the best at about 50 Hz and is shown in figure 52 below. PVDF samples tend to short before they can saturate and exhibit “banana” loops at lower fields. These banana fields are no indication of high piezoelectric behavior thus cannot be reported as piezoelectric yet [128]. It is suspected that the films retained too much water since they were not vacuum annealed; instead they were annealed in an open atmosphere oven with no humidity control.

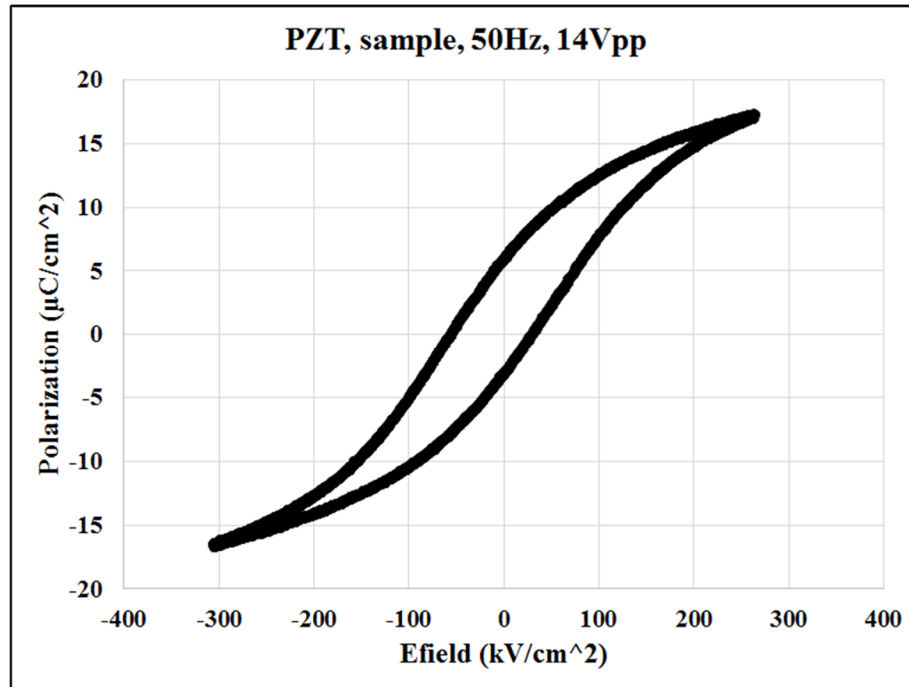


Figure 52. Saturated ferroelectric loop for a 250nm thick layer of PZT.

PZT samples tended to be more repeatable than PVDF at this point in the research. This outcome was important because the piezoelectric material application step for the proposed device occurs much later in the fabrication stage so a film that cannot be poled would be a tedious and expensive mishap. Since PZT was more reliable, it is the current candidate for the MEMS scale piezoelectric wafers. Another option to be researched is AlN which requires an aluminum target sputtered in a nitrogen atmosphere [148].

CHAPTER IV

THEORETICAL GOVERNING EQUATIONS

Equations whose purpose is to determine the buckled shape, amplitude, stability conditions, stress/strain, voltage, and generated power for the energy harvesting device are desired so that optimal geometry can be derived. These insights will allow us to design an efficient broadband energy harvester on the macro and micro scale. Others in literature have accomplished simple beam designs with popular boundary conditions such as displacement and angular rotation equal to zero at the ends but nothing in between the beam. Popular choices are the cantilever and doubly constrained beam. The proposed device is a doubly constrained beam with non-linear vertical/torsional springs located near the middle. This new energy harvester will require a bit more mathematical fortitude to compose due to the complexities of the constraints in the middle of the beam. This will either require the model to be done in two different sections or one section but with less accuracy. Emulating the middle constraints will require a linear spring and a torsional spring.

A. Euler Buckling Analysis

A bi-stable device is one that can be actuated into different positions and remain there while no external forces are applied. It is important to note that while an actuation mechanism such as electrostatics, magnetic, thermal expansion, pressure, point applied forces, or piezoelectrics can be used to switch a structure into two or more different positions; that force is no longer needed for the structure to be in static equilibrium. Buckling is described as a structures behavior above a prescribed critical load that acts against that structures restoring force [10].

Euler buckling describes the critical buckling load and shape for long, slender, ideal (perfectly straight) columns. He started out by analyzing the cross section of a free beam

under axial force as shown in figure 53 below. As seen in the figure, there is a compressive force and a resulting moment that tends to restore the beam.

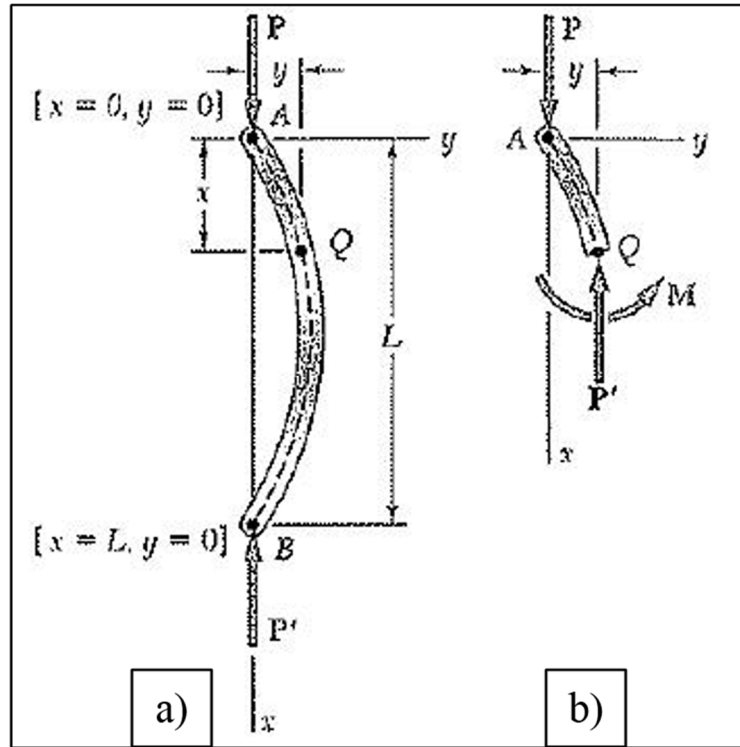


Figure 53. a) A beam buckling under an axial force. b) A cross section of the same beam. [10]

Static equilibrium under this loading gives the second order differential equation

$$\frac{d^2y}{dx^2} + \frac{P}{EI}y = 0 \quad \text{Eq 15.}$$

where y is the lateral displacement of the column, x is the distance along the unbuckled length of the column, P is the applied force, E is the Young's modulus of the beams material, and I is the moment of inertia for the cross section of the beam. This equation can be rewritten as

$$\frac{d^2y}{dx^2} + p^2y = 0 \quad \text{where } p = \sqrt{\frac{P}{EI}} \quad \text{Eq 16.}$$

which has the closed form solution of

$$y = A \sin px + B \cos px \quad \text{Eq 17.}$$

where A and B are unknown coefficients determined by the boundary conditions. If a beam of length L is simply supported so that $y(0)=0$ and $y(L)=0$ then the equation above breaks down to

$$A \sin pL = 0 \quad \text{Eq 18.}$$

The equation above has a trivial solution if the coefficient A is zero, but this is not the solution that is being sought. Another solution is available if the sin term is equated to 0 and we extract the many solutions to it; at this point the coefficient A becomes arbitrary. These solutions are

$$pL = n\pi \quad \text{where } n=1,2,3\dots$$

To get the critical load, P_{cr} , p is solved for when $n=1$ and when combined with the definition of p in Eq 16 the critical load becomes

$$P_{cr} = \frac{\pi^2 EI}{L^2} \quad \text{Eq 19.}$$

This is called Euler's Formula and describes the load at which the column buckles.

Recall that the coefficient $B=0$ and that combining Eq 16 and Eq 18 will give the buckled shape for the column as

$$y = A \sin \frac{\pi x}{L} \quad \text{Eq 20.}$$

where, again, A is arbitrary. To get this amplitude given a load P , we will have to use a field of mechanics called potential energy buckling.

There are generally four types of common buckled "long" columns that are associated in many textbooks which describe Euler Buckling. They are the "one fixed end, one free end", "both ends pinned", "one fixed end, one pinned end", and "both ends fixed" types. Each has an equivalent length that can be substituted into the variable L_e as shown in figure 54 below. Once L_e is known then the critical load can be found from

$$P_{cr} = \frac{\pi^2 * E * I}{L_e^2} \quad \text{Eq 21.}$$

A table showing each of the four famous cases is shown in Figure 54 below. For the purposes of this research, cases c) and d) are of interest because of the constrained nature of our microfabricated structure. Though our problem is complex, an understanding of the fundamental behavior of the system will lend us opportunities to predict displacement and performance of our device and thus optimize its design.

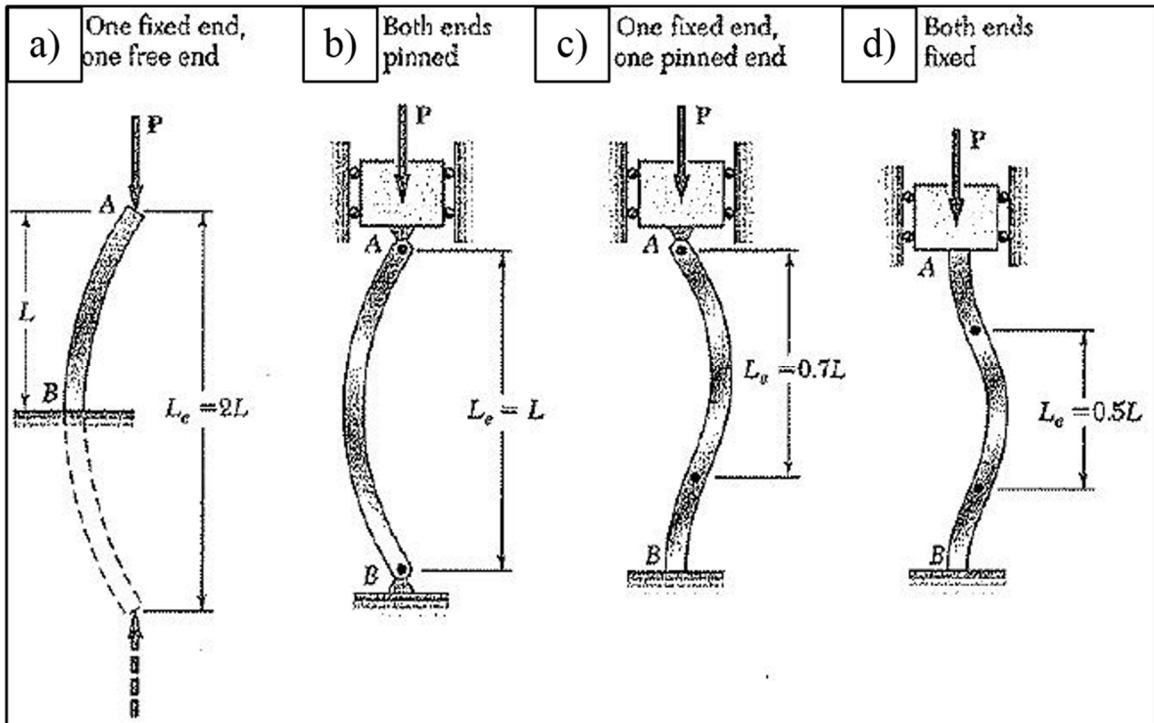


Figure 54. Famous buckling cases [10].

If the problem is changed to include a transverse load then the form of the differential equation and solution changes. An infinitesimally small section of a beam under a distributed load and an axial load is shown below in Figure 55. The distributed load will be set to zero later but for the initial part of the derivation, it will be kept.

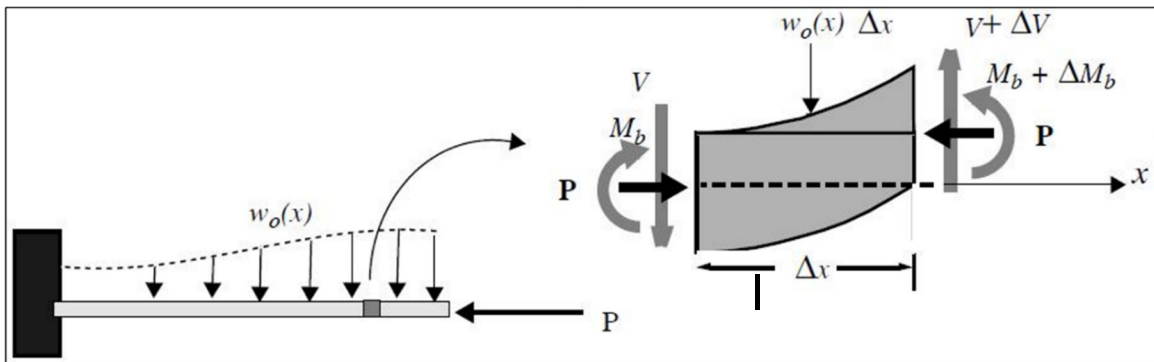


Figure 55. Beam with axial force and distributed load [20].

Summing forces in the v direction we get

$$-V - w_0\Delta x + (V + \Delta V) = 0 \quad \text{Eq 22.}$$

where V is the shear, w_0 is the distributed load, and x is the axial length to measure. The same can be done with the moment about the x-axis all the way at the left hand side of the element which comes out to be

$$-M_b - w_0 \frac{(\Delta x)^2}{2} + (V + \Delta V)\Delta x + (M_b + \Delta M_b) + P\Delta v = 0 \quad \text{Eq 23.}$$

where M_b is the moment about the left hand side of the element, P is the axially applied force, and v is the lateral deflection. If we take the limit as Δx goes to 0 then two differential equations come into being:

$$\frac{dV}{dx} = w_0(x) \quad \text{Eq 24.}$$

$$\frac{dM_b}{dx} + V + P \frac{dv}{dx} = 0 \quad \text{Eq 25.}$$

Combining Eq 24 and Eq 25 gives a general equation for buckling which is

$$\frac{d^2M_b}{dx^2} + P \frac{d^2v}{dx^2} = -w_0(x) \quad \text{Eq 26.}$$

Usually the right hand side of this equation is 0 if there is no distributed load such as gravity effects. Remembering that the moment is related to the beams transverse displacement by

$$\frac{M_b}{EI} = \frac{d^2v}{dx^2} \quad \text{Eq 27.}$$

for a small angle assumption then Eq 26 becomes

$$(EI) \frac{d^4v}{dx^4} + P \frac{d^2v}{dx^2} = 0 \quad \text{Eq 28.}$$

Using a more common notation of y instead of v as out of plane lateral displacement this equation is

$$(EI) \frac{d^4y}{dx^4} + P \frac{d^2y}{dx^2} = 0 \quad \text{Eq 29.}$$

which we will deem the governing equation for a beam under an axial load and transverse shear. This equation has a solution of the form

$$y(x) = C_1 + C_2x + C_3 \sin \lambda x + C_4 \cos \lambda x \quad \text{Eq 30.}$$

$$\text{where } \lambda = \sqrt{\frac{P}{EI}}$$

With this new displacement equation known, Eq 30, we only need to apply boundary conditions to solve for the unknowns $C1$, $C2$, $C3$, and $C4$. Eq 30 has a more popular name which is the “shape function”.

B. Potential Energy Model

In the previous section, Euler buckling gave a shape function for the static solution which outlined the arbitrary out-of-plane displacement for the pre-stressed center beam. Alone this result lends intuition to how the device looks but is not enough to calculate the stable stresses or strains in the beams; nor does it detail the magnitude of the out of plane displacement. To accomplish this, an “energy method” will need to be used which will account for the distribution of energy in the areas of normal strain, curvature, and work done by the loads.

A structure in static equilibrium will always try to find a minimum energy configuration when perturbed slightly. For a standard beam constrained at both ends has an axial deflection, δ , when an axial load, P , is applied at the end as shown in figure 56 below. The length of this beam is L so that the final horizontal length of the buckled structure is $L-\delta$.

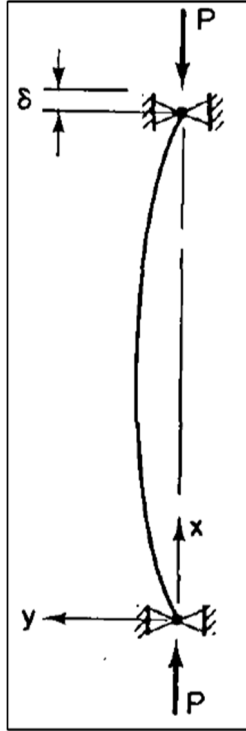


Figure 56. Axial deflection with a given axial load [72].

To determine δ the curvature of the beam has to be derived and simplified as

$$L = \int_0^{L-\delta} [1 + (y')^2]^{1/2} dx \quad \text{Eq 31.}$$

where y' is the first derivative of the shape function $y(x)$. If we assume that the deflection δ is small then the difference in δ and its cosine magnitude is also small compared to the length of the beam. This then gives

$$L \approx \int_0^L [1 + (y')^2]^{1/2} dx - \delta \quad \text{Eq 32.}$$

Solving for δ in equation Eq 32 and then performing a binomial expansion, keeping the first three terms gives

$$\delta \approx L + \int_0^L \frac{1}{2} (y')^2 dx - \int_0^L \frac{1}{8} (y')^4 dx - L \quad \text{Eq 33.}$$

It is easy to see from Eq 33 that the terms L cancel out, and the term $(y')^4$ is extremely small compared to $(y')^2$ so that we can assume $(y')^4$ to be zero. This makes the deflection

$$\delta \approx \int_0^L \frac{1}{2} (y')^2 dx \quad \text{Eq 34.}$$

so that the work done by the external force

$$W_{axial\ force} \approx P\delta \approx \frac{1}{2} P \int_0^L (y')^2 dx \quad \text{Eq 35.}$$

A structure such as the beam in Figure 56 also has internal strain associated with the curvature. The work done by releasing this energy is

$$W_{internal} = \frac{1}{2} \int_0^L M(x) d\theta = \frac{1}{2} \int_0^L EI(y'')^2 dx \quad \text{Eq 36.}$$

For the linear spring, energy is absorbed in the amount of

$$W_{linear,spring} = \frac{1}{2} ky(x)^2 \quad \text{Eq 37.}$$

where k is the linear spring constant derived from the vertical displacement of the side torque arms and $y(x)$ is the displacement of the location of the linear spring. The torque spring will also absorb energy proportional to the angle of twist of the torque arms and is

$$W_{torque,spring} = \frac{1}{2} \beta (y')^2 \quad \text{Eq 38.}$$

where β is the angular spring constant derived from the geometry of the torque arms. The potential energy of the entire system is then defined as

$$\Pi_p = W_{internal} - W_{linear,spring} - W_{torque,spring} - W_{axial\ force} \quad \text{Eq 39.}$$

The spring elements in Eq 39 have positive values because potential of the system is raised as more vertical or angular displacement is increased. Reiterating Eq 39 with Eq 35, Eq 36, Eq 37, and Eq 38 substituted in becomes

$$\Pi_p = \frac{1}{2} \int_0^L EI(y'')^2 dx - \frac{1}{2} ky(x)^2 - \frac{1}{2} \beta (y')^2 - \frac{1}{2} P \int_0^L (y')^2 dx \quad \text{Eq 40.}$$

where L , E , I , k , β , and P are known. The only unknowns are coefficients to the shape functions which can be backed out using the theory of minimum potential energy. To do this Eq 40 is differentiated with respect to each of the “n” coefficient which should result in “n” equations. Solving for the coefficients should give the theoretical displacements for the pre-stressed beam when used with the shape function.

C. Theoretical Mechanical Model Development

A model that predicts the resulting shape, displacement, actuation force/torque, and actuation acceleration should be developed given device geometry, properties, and prestresses. It is to be expected that this mechanical model will couple with the electrical side which will make it more complex; though the piezoelectric model will be analyzed separately before combining the two. As a continuation of the current works, eventually we would like to develop a buckling model that includes a vertical and torsional spring in the middle of the doubly clamped beam. A graphical interpretation of this setup is shown in figure 57 below.

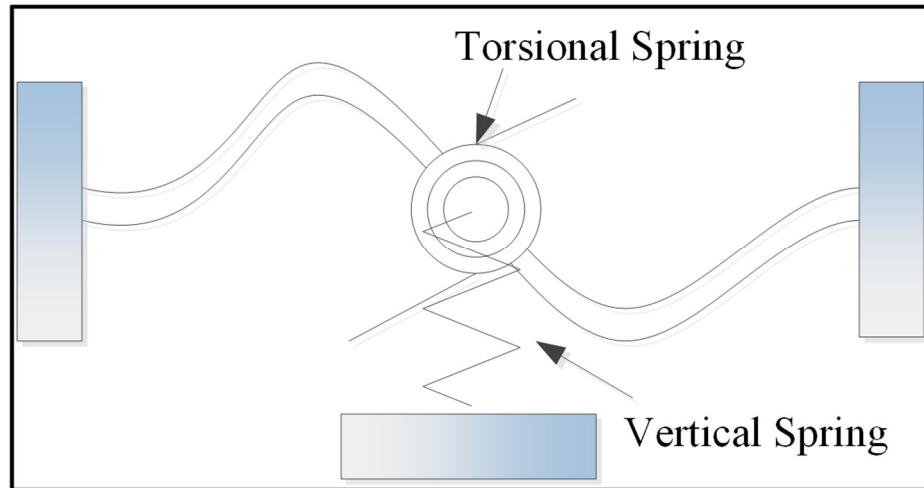


Figure 57. Desired mechanical model for the bi-stable buckled device.

A model with a vertical spring that predicts the buckled shape is currently working. Ultimately, the shape function for the mechanical model as a function of vertical spring constant, torsional spring constant, and pre-stressed beam properties will need to be determined so that an appropriate energy method may determine the static deflections.

Others have done post buckled non-linear shape and deflection analysis for beams [159] that usually require numerical simulations to solve, though no literature thus far suggests how to accomplish the task of solving the profile of a beam with two non-linear spring elements attached. Others have tried to tackle the problem by using an imperfection constant that is experimentally determined [48] though the shape function for the beam is

still assumed. Another interesting point is that most of the work done is for a single beam and not for a two beam model like in this work.

Maple16 was used to develop a finite difference model. This method models the governing equation, Eq 29, as a series of nodes and has a general matrix form. The differential parts to the governing equation have a central difference of the form

$$\begin{aligned}\frac{dy}{dx} &= \left(\frac{1}{2h}\right)(y_{i+1} - y_{i-1}) \\ \frac{d^2y}{dx^2} &= \left(\frac{1}{h^2}\right)(y_{i+1} - 2y_i + y_{i-1}) \\ \frac{d^3y}{dx^3} &= \left(\frac{1}{2h^3}\right)(y_{i+2} - 2y_{i+1} + 2y_{i-1} - y_{i-2}) \\ \frac{d^4y}{dx^4} &= \left(\frac{1}{h^4}\right)(y_{i+2} - 4y_{i+1} + 6y_i - 4y_{i-1} - y_{i-2})\end{aligned}\tag{Eq 41.}$$

When the central difference equations are substituted into the governing equation, a new nodal equation is formed that describes the vertical displacement of one node in terms of the others and is

$$0 = \left(\frac{1}{h^4}\right)(y_{i+2} - 4y_{i+1} + 6y_i - 4y_{i-1} - y_{i-2}) + \left(\frac{P}{EIh^2}\right)(y_{i+1} - 2y_i + y_{i-1})\tag{Eq 42.}$$

Boundary conditions for the proposed beam include no vertical displacement or angular rotation at the walls, as well as a linear vertical and torque spring at the center of the beam. This will give six boundary conditions total for our nodal beam. An important necessity of the central difference method is that extra nodes before and after the wall are needed to solve the proceeding matrix problem. The amount of extra nodes depends on the form of the boundary condition nodal equation. For the proposed beam the geometric boundary conditions are

$$y(0) = y(L) = \frac{dy}{dx}(0) = \frac{dy}{dx}(L) = 0\tag{Eq 43.}$$

While the shear and moment balance boundary conditions are

$$EI \frac{d^3y}{dx^3} \left(\frac{L}{2}\right) - k_{vd}y \left(\frac{L}{2}\right) = 0\tag{Eq 44.}$$

$$EI \frac{d^2y}{dx^2} \left(\frac{L}{2}\right) - \beta \frac{dy}{dx} \left(\frac{L}{2}\right) = 0\tag{Eq 45.}$$

where k_{vd} and β are the stiffness of the linear vertical and torsional spring respectively. When combined with the central difference method form, Eq 41, these boundary conditions become

$$y_0 = y_n = 0, y_{-1} = y_1, y_{n+1} = y_{n-1} \quad \text{Eq 46.}$$

$$\left(\frac{EI}{2h^3}\right)\left(y_{\frac{1}{2}n+2} - 2y_{\frac{1}{2}n+1} + 2y_{\frac{1}{2}n-1} - y_{\frac{1}{2}n-2}\right) = k_{vd}y_{\frac{1}{2}n} \quad \text{Eq 47.}$$

$$\left(\frac{EI}{h^2}\right)\left(y_{\frac{1}{2}n+1} - 2y_{\frac{1}{2}n} - y_{\frac{1}{2}n-1}\right) = \left(\frac{1}{2h}\right)\beta\left(y_{\frac{1}{2}n+1} - y_{\frac{1}{2}n-1}\right) \quad \text{Eq 48.}$$

As seen from (equations above) at the wall boundary conditions (nodes 0 and n) there need to be two extra nodes ($n-1$ and $n+1$). This gives a total of $n+1+2$ nodes with the extra $+1$ for node 0. Six boundary conditions will allow for relating one node in terms of the others; essentially lessening the number of equations forming the matrix by six. Each node forms its own governing equation around that node number. The resulting number of equations for the matrix are $n+1+2-6$ or $n-3$. This matrix is of the form

$$[A][y] + \lambda[B][y] = 0 \quad \text{Eq 49.}$$

and has Eigen values and vectors which reveal the buckling shape of the beam. If the matrix size is less than 8x8 then solving the case when the determinate is zero is very simple and straight forward. For larger matrices a better method of solving the Eigen values and vectors must be utilized. The current matrix solving method being used is the “inverse power method”. This method solves the first Eigen value and vector by the following routine:

- Create some counter j
- Solve the matrix $[E] = -[A]^{-1}[B]$
- Guess the $[y]$ vector
- Solve the new Eigen vector $[y]_{j+1} = [E][y]_j$
- Normalize the new Eigen vector $[y]^{j+1} = ([y]^{j+1}) / \text{maximum}([y]^{j+1})$
- Calculate Eigen value = $1 / \text{maximum}([y]^{j+1})$
- Evaluate the convergence value $\lambda^{j+1} - \lambda^j < \text{tolerance}$
- Check if convergence is acceptable
- If not converged then start again at the solve Eigen vector

Assuming the model converged using the inverse power method, the displacement profile and buckling load for the first mode will be known. The amplitude of the buckled shape will, however, be arbitrary. Energy methods will be used to determine a better estimate of the beams vertical amplitude. Before the beam is allowed to buckle, the amount of potential energy in the compressed beam is

$$PE_{before} = \frac{1}{2} \frac{\sigma^2 V}{E} \quad \text{Eq 50.}$$

where σ is the biaxial stress in the silicon nitride layer and V is the volume of the beam. The energy after buckling is defined in Eq 40 in discrete form. To discretize Eq 40 the integrations are treated using discrete calculus and transforms it into:

$$PE_{after} = \frac{1}{2} EI \left[h \left(\sum_{i=0}^n \left(A \frac{d^2 y}{dx^2}(i) \right)^2 - k_{vd} (Ay(i))^2 - \beta \left(A \frac{dy}{dx}(i) \right)^2 - \sigma h A_b \sum_{i=0}^n \left(A \frac{dy}{dx}(i) \right)^2 \right) \right] \quad \text{Eq 51.}$$

where A_b is the cross sectional area of the beam and A is a constant that modifies the amplitude of the beam. Equating Eq 50 and Eq 51 allows for the solving of the parameter A which then can be multiplied by the original Eigen vector to reveal estimated buckled beam amplitude. Theoretical models are computed in Maple16 using the Eigen buckling and energy analysis. A profile for a beam with length 1.5 mm, 2 μm thick, 100 μm wide, made of silicon nitride, and fabricated with 300 MPa of compressive stress is shown in figure 58 below along with angle of twist, moment, and shear in figure 59, figure 60, and figure 61 respectively.

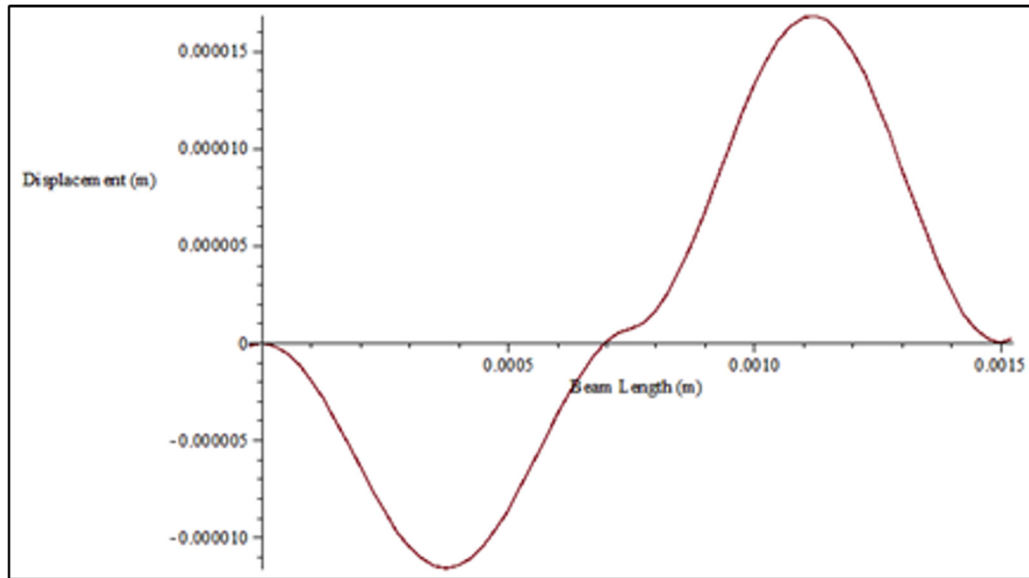


Figure 58. Theoretical model displacement for a 1.5 mm long silicon nitride beam with 300 MPa of compressive stress.

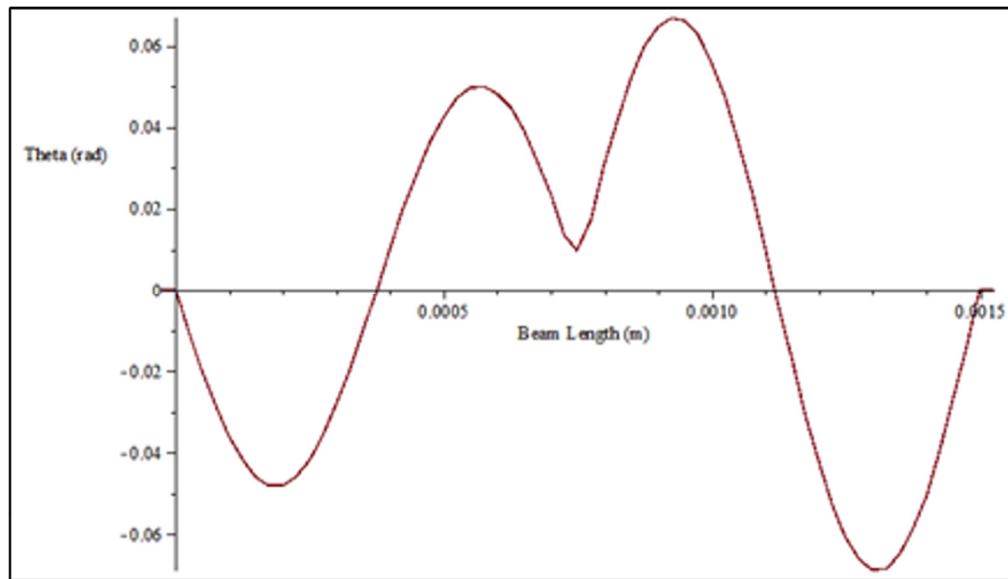


Figure 59. Theoretical model theta for a 1.5 mm long silicon nitride beam with 300 MPa of compressive stress.

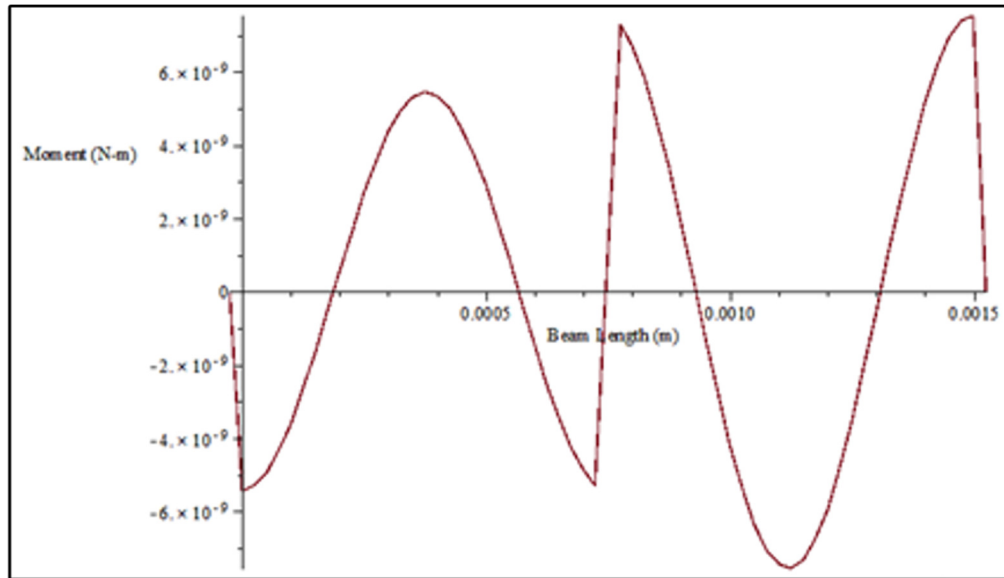


Figure 60. Theoretical model moment for a 1.5 mm long silicon nitride beam with 300 MPa of compressive stress.

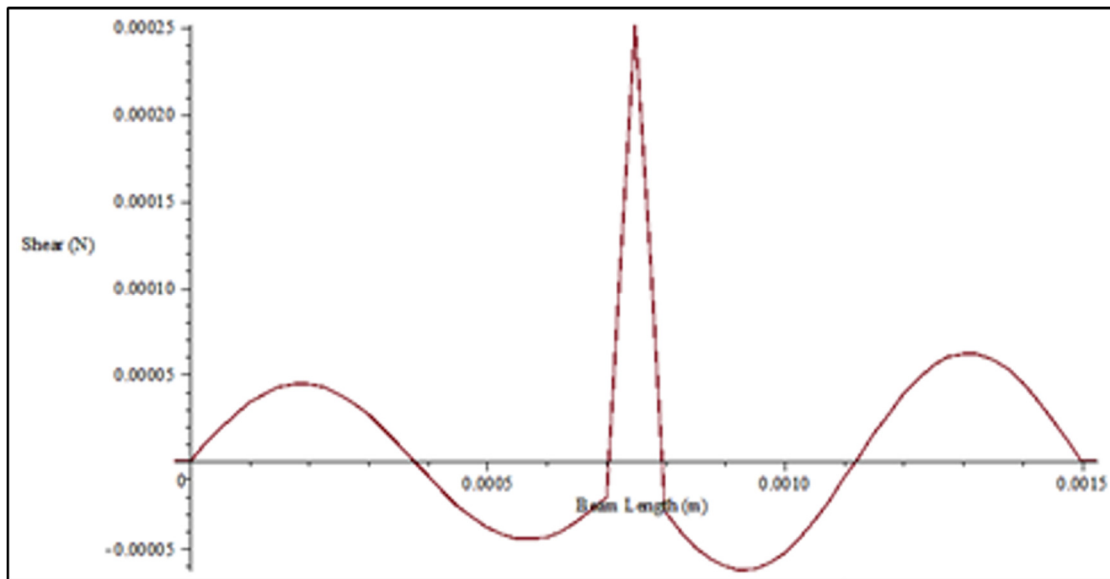


Figure 61. Theoretical model shear for a 1.5 mm long silicon nitride beam with 300 MPa of compressive stress.

D. Dynamic Analysis

Dynamic analysis of a beam is a bit more complicated [149], [81], [40], [114], [31]. Especially if one takes into consideration shear effects and dampening. Non-linear dynamic analysis of buckled beams and their chaotic motions have been extensively

studied for simple cases in a post buckled analysis [51], sub-harmonic resonance [41], at primary resonance [42], discrete modeling of complex structures [73], reduced order methods (no snap-through) [74], and investigations into how higher modes affect chaotic motion onset [132], [133].

Timoshenko beam theory (TBT) lends partial differential equations to describe how a beam section vibrates in space and time [149]. Unlike the Euler-Bernoulli model, TBT includes not only lateral displacement and bending moments, but also rotational displacements and shear deformations. A picture outlining an infinitesimally small section of a TB is shown in figure 62 a) and a beam using a proof mass and time deflection states in figure 62 b). It is important to note that shear deformation effects are included because the neutral axis is not always perpendicular to the face.

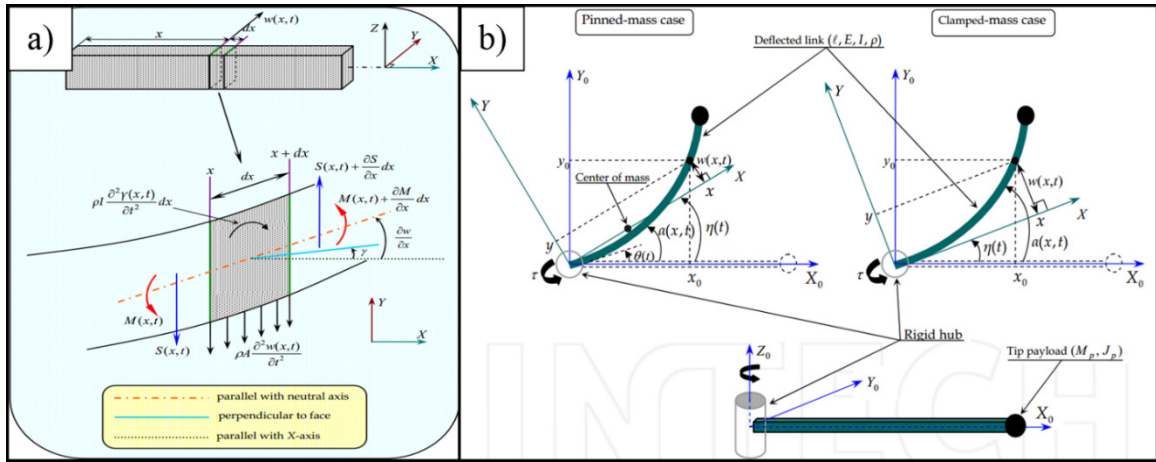


Figure 62. a) Timoshenko section describing kinematics of deformation and b) an example of a dynamic pinned and clamped rod with proof mass and rotary actuated [81].

The TBT yields two coupled equations by balancing moments and shear forces inside the element described by figure 62 a). Air dampening and structural dampening is including into the initial derivation of the TB motion PDEs. These equations are a function of vertical out-of-plane displacement $w(x, t)$ and the angle between the x-axis and perpendicular face line $\gamma(x, t)$

$$K_D I \frac{\partial^3 \gamma(x, t)}{\partial x^2 \partial t} + EI \frac{\partial^2 \gamma(x, t)}{\partial x^2} + kAG \left(\frac{\partial w(x, t)}{\partial x} - \gamma \right) - \rho I \frac{\partial^2 \gamma(x, t)}{\partial t^2} = 0 \quad \text{Eq 52.} \quad [81]$$

$$kAG \left(\frac{\partial^2 w(x,t)}{\partial x^2} - \frac{\partial \gamma(x,t)}{\partial x} \right) - \rho A \frac{\partial^2 w(x,t)}{\partial t^2} - A_D \frac{\partial w(x,t)}{\partial t} = 0 \quad \text{Eq 53.} \quad [81]$$

where K_D is the material dampening factor, I is the moment of inertia, kA is the effective shear area, G is the shear modulus, ρ is the density of the beam, and A_D is the air dampening factor. If the beam has a uniform cross section and a constant density, then one PDE describing vertical displacement can be acquired

$$\begin{aligned} & K_D I \frac{\partial^5 w(x,t)}{\partial x^4 \partial t} - \frac{K_D I \rho}{KG} \frac{\partial^5 w(x,t)}{\partial x^2 \partial t^3} + EI \frac{\partial^4 w(x,t)}{\partial x^4} \\ & - \rho I \left(1 + \frac{E}{KG} + \frac{K_D A_D}{\rho KAG} \right) \frac{\partial^4 w(x,t)}{\partial x^2 \partial t^2} \dots \frac{\rho^2 I}{KG} \frac{\partial^4 w(x,t)}{\partial t^4} - \frac{EI A_D}{kAG} \frac{\partial^3 w(x,t)}{\partial x^2 \partial t} \\ & + \frac{\rho I A_D}{kAG} \frac{\partial^3 w(x,t)}{\partial t^3} + \rho A \frac{\partial^2 w(x,t)}{\partial t^2} + A_D \frac{\partial w(x,t)}{\partial t} = 0 \end{aligned} \quad \text{Eq 54.} \quad [81]$$

which is a very large PDE to work with. Assumptions can be made that reduce the size of Eq 54 and are very useful. If dampening is neglected and initial conditions are set to zero, then the form of Eq 54 for the beam in figure 62 b) becomes

$$EI \frac{\partial^4 w(x,t)}{\partial x^4} - \rho I \left(1 + \frac{E}{KG} \right) \frac{\partial^4 w(x,t)}{\partial x^2 \partial t^2} + \frac{\rho^2 I}{KG} \frac{\partial^4 w(x,t)}{\partial t^4} + \rho A \frac{\partial^2 w(x,t)}{\partial t^2} = 0 \quad \text{Eq 55.} \quad [81]$$

Taking out rotary inertia and the distortion of shear deformation, the simple dynamic beam equation is arrived at

$$EI \frac{\partial^4 w(x,t)}{\partial x^4} + \rho A \frac{\partial^2 w(x,t)}{\partial t^2} = 0 \quad \text{Eq 56.} \quad [81]$$

Most of the equations above depend on a displacement or shape function. An expanded separated form of the solution $w(x,t)$ is found depending on the initial and boundary conditions used. An infinite sum of mode shapes and time-dependent coordinates can evaluate the approximate solution to the above equations. Compression effects are not augmented in the equation above, thus we must move to a different method to evaluate the ‘S’ shaped bi-stable buckled beams performance under a time varying load.

CHAPTER V

MEMS ANSYS MODELING

The finite element analysis (FEA) software that will be utilized for this research will be ANSYS version 13. ANSYS parametric design language (APDL) allows the user to script the entire analysis which lends versatility to future runs that may need a parameter change or slight model update. The theoretical model being derived for our work will be compared to an ANSYS model which we expect to be slightly more accurate. Reasons for this include the programs ability to complete non-linear analysis and solve for complicated snap-through behavior.

Prior work by the student on snap-through behavior of bi-stable buckled membranes has given confidence to ANSYS performance when compared to experimental data. Data for this project is shown below in figure 63. One explanation for the large divergence at bigger membrane diameters in figure 63 is the fact that the assumed shape function for the buckled structure is constant. It has been observed that at larger diameters that the shape function is better approximated using higher order terms than the one used to estimate displacements below. Though this might decrease the divergence in figure 63 a), it is the opinion of the author that ANSYS would still predict a more accurate displacement at the center of the membrane.

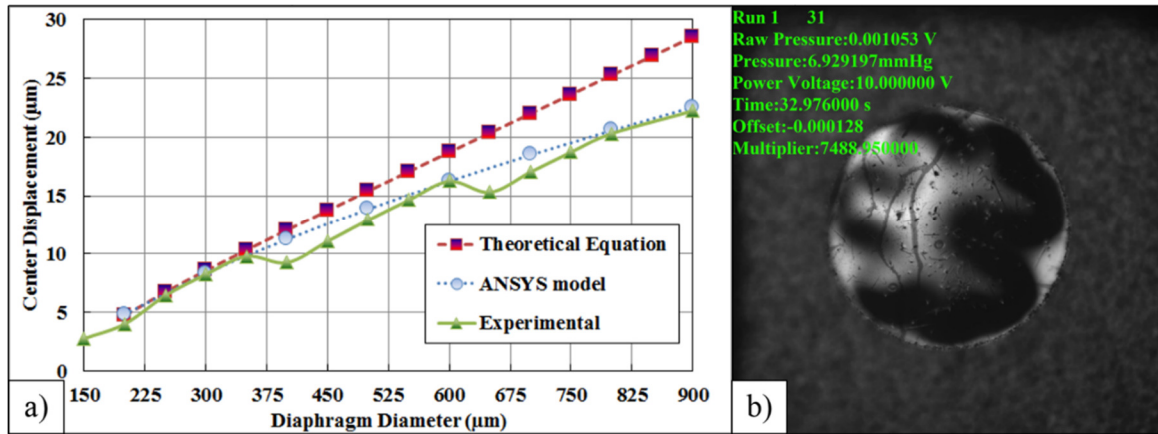


Figure 63. Center displacement for a buckled bi-stable MEMS membrane made out of SiO₂ and polyimide A) given various diameters, B) picture of a 1,500 µm buckled membrane in the up position.

Piezoelectric analysis is possible in ANSYS as well as other couple-field enabled elements. Some of these elements that support piezoelectric analysis are PLANE13, SOLID5, SOLID98, PLANE223, SOLID226, and SOLID227. SHELL281 are used for our models that only include mechanical effects and omit piezoelectric effects but will have to either be coupled with elements that can exhibit a piezoelectric effect or we will have to switch to a either a SOLID5 or SOLID226 (3D brick) element based model. This will make computational time increase drastically so it is the opinion of the author to first try a work around approach.

A. Determining Piezoelectric Matrix for ANSYS

The software FEA package that is being used, ANSYS, requires a unique piezoelectric matrix, permittivity, and stiffness matrix to solve a model. Permittivity is expressed simply as three values; PERX, PERY, and PERZ which are the relative permittivity values in three dimensions. Piezoelectric properties are defined in the three dimensional piezoelectric matrix $[e]$ and has the ANSYS form

$$ANSYS [e] = \begin{matrix} & x & y & z \\ x & e_{11} & e_{12} & e_{13} \\ y & e_{21} & e_{22} & e_{23} \\ z & e_{31} & e_{32} & e_{33} \\ xy & e_{41} & e_{42} & e_{43} \\ yz & e_{51} & e_{52} & e_{53} \\ xz & e_{61} & e_{62} & e_{63} \end{matrix} \quad \text{Eq 57.}$$

where e_{11} has units of stress per unit of electric field or equivalently charge per area. General published data (IRE standard) does not have the same format for $[e]$, instead they use shear terms rearranged in the form of

$$IRE [e] = \begin{matrix} & x & y & z \\ x & e_{11} & e_{12} & e_{13} \\ y & e_{21} & e_{22} & e_{23} \\ z & e_{31} & e_{32} & e_{33} \\ xy & e_{61} & e_{62} & e_{63} \\ yz & e_{41} & e_{42} & e_{43} \\ xz & e_{51} & e_{52} & e_{53} \end{matrix} \quad \text{Eq 58.}$$

Most times the $[e]$ matrix must be derived from the d_{ij} and s_{ij}^E coefficients. The derivation of the ANSYS piezoelectric matrix $[e]$ is straightforward. First the order of the piezoelectric $[d]$ matrix is determined which defines the amount of strain per unit electric field. For poling in the y-direction the $[d]$ matrix looks like

$$[d_y] = \begin{matrix} & x & y & z \\ x & 0 & d_{31} & 0 \\ y & 0 & d_{33} & 0 \\ z & 0 & d_{31} & 0 \\ xy & d_{15} & 0 & 0 \\ yz & 0 & 0 & d_{15} \\ xz & 0 & 0 & 0 \end{matrix} \quad \text{Eq 59.}$$

The compliance matrix for a material that is poled in the y-direction is defined differently than it is in Eq 6 because the coefficients are shifted around. It has the form

$$[s_y^E] = \begin{bmatrix} s_{11} & s_{13} & s_{12} & 0 & 0 & 0 \\ s_{13} & s_{11} & s_{13} & 0 & 0 & 0 \\ s_{12} & s_{13} & s_{33} & 0 & 0 & 0 \\ 0 & 0 & 0 & s_{44} & 0 & 0 \\ 0 & 0 & 0 & 0 & s_{44} & 0 \\ 0 & 0 & 0 & 0 & 0 & s_{66} \end{bmatrix} \quad \text{Eq 60.}$$

To derive the $[e]$ matrix used in ANSYS, one only needs to follow the equation that is defined as the matrix multiplication between the inverse of the compliance matrix and the piezoelectric $[d]$ matrix or simply

$$\text{ANSYS } [e_y] = [s_y^E]^{-1} [d_y] \quad \text{Eq 61.}$$

The matrix derived from Eq 61 is the one that should be inserted in ANSYS. So far an excel spreadsheet has been created that inputs the compliance, permittivity, and piezoelectric coefficients while outputting the ANSYS APDL test input for a run in either the x, y, or z poled directions.

B. Model and Elements for Analysis

Two different models will be needed to accurately reproduce the behavior of the bi-stable buckled device. Model #1 is a 2D planar model that determines what temperature parameter needs to be adjusted to emulate the stress in our nitride films via a fictitious thermal temperature expansion coefficient. Model #2 is a 3D shell layout that will apply the determined temperature of model #1 so that the given layers the experimentally measured compressive stress.

To emulate the stress in the nitride layer, model #1 uses a fictional coefficient of thermal expansion so that a temperature applied to the doubly constrained beam would strain equivalently to a fully constrained layer at a given stress. PLANE183, 8 nodes elements with a fictional thermal coefficient of 4×10^6 (m/m) per K, were used for the plasma enhanced chemical vapor deposition (PECVD) of silicon nitride (Si_3N_4). Silicon nitride can have a Young's modulus and Poisson's ratio of roughly 90-260 GPa [152] and 0.2-0.253 [146] respectively when deposited in the PECVD and can be controlled relatively well in the University of Louisville's cleanroom. These parameters rely heavily on the deposition temperature, which in the case of these buckled membranes, is 350 C. It is important to note that the analysis is done using plane strain due to the wide nature of the film. Using a Young's Modulus of 260 GPa and Poisson's ratio of 0.253, the stress in the x-direction for a silicon nitride film is shown in figure 64 below at a temperature change of 1000 K. As seen in the ANSYS model, stress in the x-direction is about 1.3 GPa for a temperature change of 1,000 K. This stress varies linearly as the temperature increases as shown in figure 65 below. Materials used for the ANSYS model are shown in Table 11 below. Using the slope of this graph, the equation to emulated silicon nitride stress in the film is

$$\Delta K = \left(\frac{1,300}{1000}\right) \sigma_{desired} \quad \text{Eq 62.}$$

where ΔK is the temperature change set in ANSYS and $\sigma_{desired}$ is the desired stress in the nitride film.

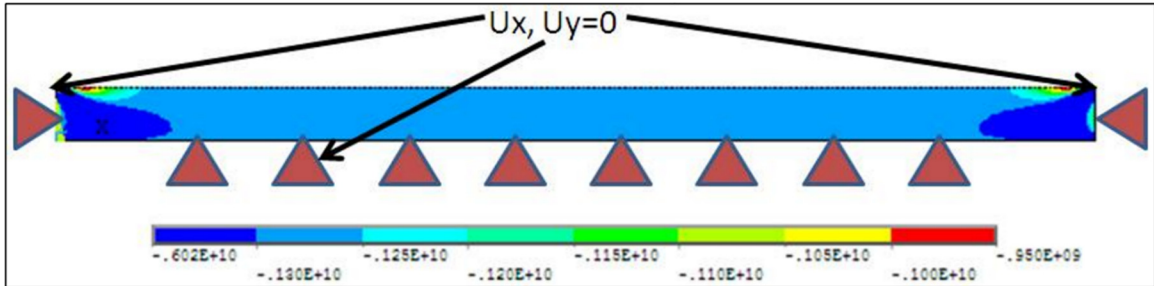


Figure 64. Stress in the x-direction for a silicon nitride film constrained on three sides. Temperature is difference 1,000K.

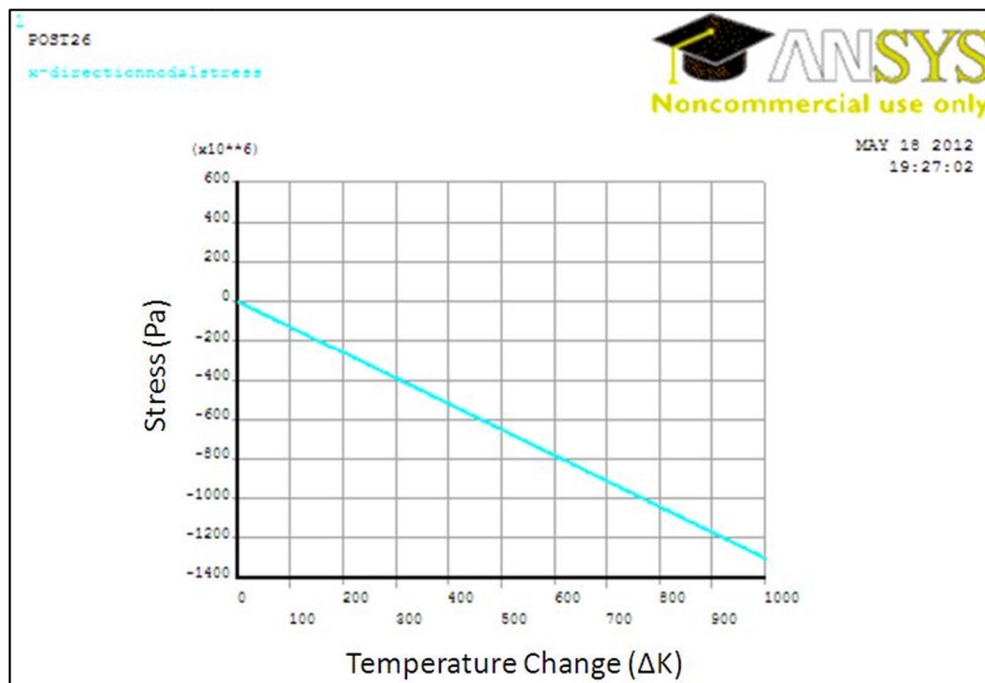


Figure 65. Graph of stress in the x-direction for the silicon nitride film.

A layout of the preliminary NSYS model number two with the planar geometric variables is shown in figure 66 below. This model will utilize SHELL281 elements which have eight nodes (all with six degrees of freedom u_x , u_y , u_z , rot_x , rot_y , rot_z) and are appropriate in analyzing thin to moderately thick shells. It also performs well for linear

and large rotation analysis; which is what will happen when the device changes from one buckled state to the next. Another interesting attribute to SHELL281 is that it utilizes the layered feature for shells. First-order shear deformation theory is used for elements of this type which would be beneficial if the thickness of our layers came within $1/10^{\text{th}}$ of the planar geometries. The names given in figure 66 have changed in future versions of the model. What is called “PolyArm” is now the compliance arm and the “TorqueArm” is now the length of the moment arm that extends from the center of the buckled beam to the tip mass.

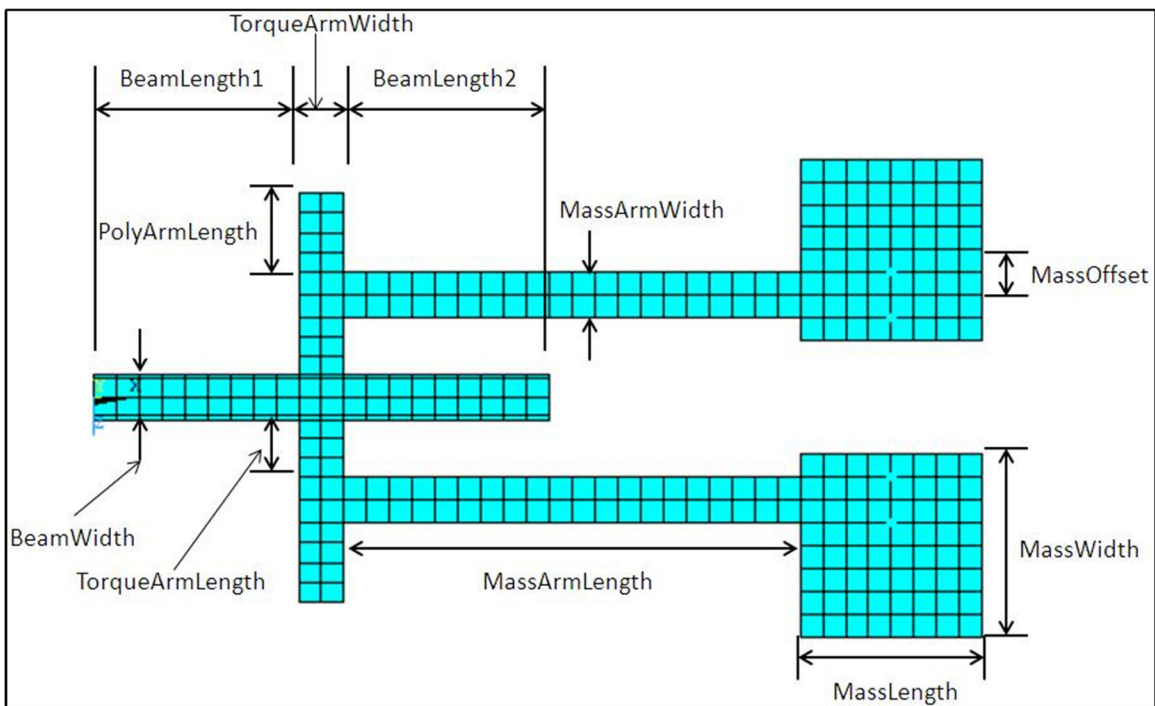


Figure 66. ANSYS model of prototype with script file geometric variables. The names given here have changed in later versions.

Selecting an optimal residual stress within the silicon nitride is done after discovering how much our prototype will deflect and how much force/torque it takes to actuate said device. This requires we guess a stress in MPa and then back out a ΔK from Eq 62 above. Once we know what temperature to set in the ANSYS model for our prototype, we simply load the model with a slight perturbing stress to promote the “S” buckling shape, then we set the ΔK on the compressed portion of the beam, set the

perturbing stress down to zero (eliminate it). The resulting state of the model will show the resting deformation magnitudes and shape for the device.

Table 11. Materials used in the ANSYS model.

Material	Young's Modulus (GPa)	Poisson's Ratio
Silicon Nitride (Si ₃ N ₄)	260	0.253
Chrome (Cr)	279	0.21
Polyimide (PI 2611)	8	0.17

A contour plot of the displacement in the y-direction is shown in figure 67 below. The stress in the nitride layer was ramped up to -360 MPa in 400 sub-steps. This induced buckling into the center constrained beam and should have another stable state if the arms are pushed upwards with enough force or acceleration. This will be the next step in the analysis and should give us an idea of how the device operates. Displacements for the stressed middle beam are shown in figure 68 below. Maximum upward deflection is about 11.25 μm while the minimum is about -6.67 μm .

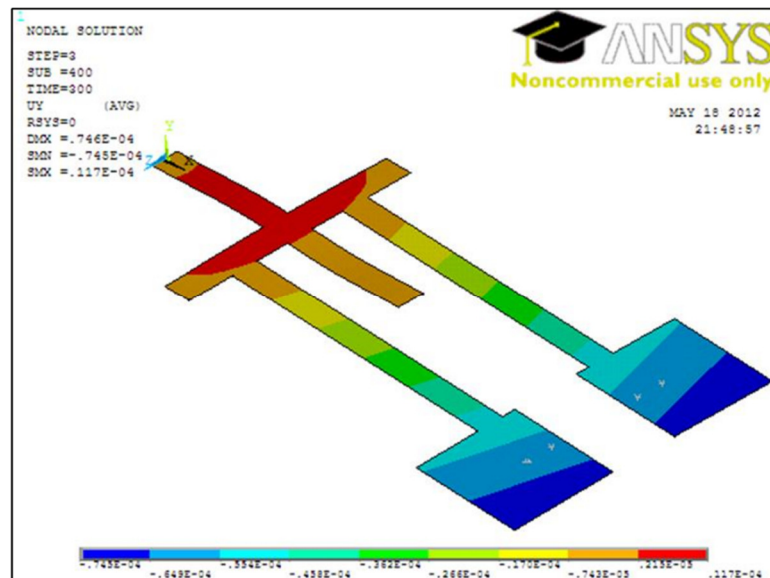


Figure 67. Contour plot of the y-displacement for the prototype with the stressed portion of the beam at -360 MPa. Units are in mm and color indicates displacement in the y-direction.

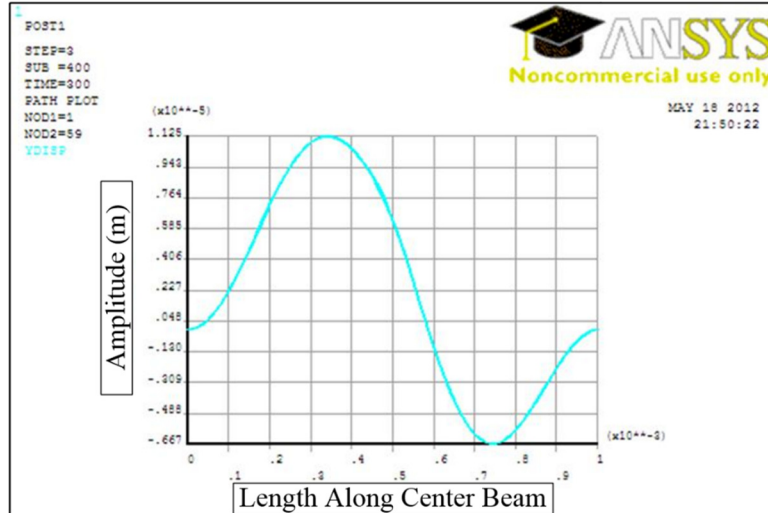


Figure 68. Y-displacement of the stressed middle beam.

C. ANSYS Snap-through Loads and Displacements

After the ANSYS model is loaded to its post buckled form it should describe our “as fabricated” device. Next, to determine the mechanical performance, a vertical force is applied to each of the proof mass centers. Force loading on the masses is done in two steps. The first step brings the model just to the tipping point of snap-through, while the second load causes the model to buckle into another stable position. Generally, the first load will be much larger than the second load because non-convergence is almost guaranteed if the load per substep is too large. Magnitudes for the first and second force loads are reassigned until a point of non-convergence is reached. At this point, the first load is set just slightly smaller than the load at non-convergence and the second load is set to about 10% of the first load to “step over” the snap through transition.

Unbalanced displacement of the masses is a problem encountered in the post snap-through model which is most likely due to the system finding a non-intuitive, but energetically stable equilibrium point. The displacements of the pre-stressed buckled beams after snap-through matches up with a reversed model in which the center beam is initially promoted out-of-plane in the opposite direction.

The complicated trial-and-error process for determining the appropriate first and second loads to perform a successful snap inhibits a full design optimization run at this point. Every iteration of the design optimization will need a modified geometry and applied loads to derive the best device with respect to certain output criteria such as natural

frequency or power density. Writing code that bypasses error and allows only converged solutions into the optimization routine would be required.

To determine the buckling load, the highest and lowest point on the center buckled beam is monitored while the load is varied from zero to some chosen buckling point. When we see a sharp transition in vertical displacement, this is an indicator that snap-through behavior has occurred at the respective load. Figure 69 below shows a snap-through behavior occurring at about 44 μN for an arbitrary ANSYS model of our device (center beam and mass arm length of around 1mm). Displacement of the tip masses give a good indication of when the center beam will start to buckle back and forth during energy harvesting, though hard to predict if the mass arms and center pre-stressed beam are out of phase.

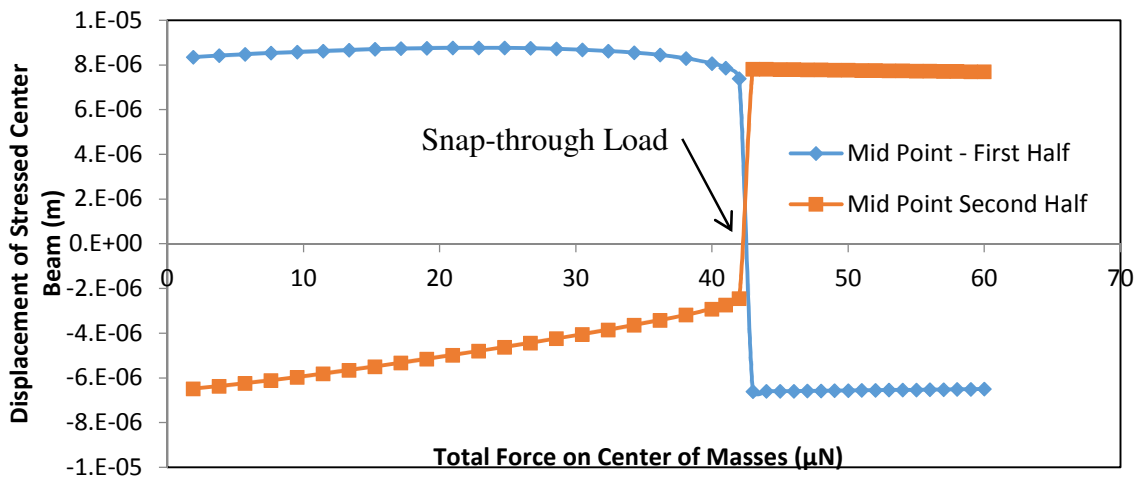


Figure 69. Displacement versus total load applied to center masses. Snap-through occurring at around 44 μN for a pre-stress of -300 MPa, stressed and unstressed nitride thickness of 0.5 and 0.5 μm respectively, and a beam length of 1,500 μm .

CHAPTER VI

MEMS ENERGY HARVESTER FABRICATION

A bi-stable buckled energy harvesting device is a not a completely novel concept in the electrical generation area. Devices with such a non-linear response have been shown to have a broader bandwidth response to varying frequencies and perform better under sporadic and random vibrations [34]. This is appealing to companies that wish to place sensors in areas where a forced vibration is not always constant. The majority of energy harvesting devices involve a single or multiple beam setup that utilize an end mass, chosen due to the simplicity of the structure. Another slight variation on this setup is a beam with a mass in the middle, which widens the frequency range slightly [30].

Our device takes the bi-stable buckled beam and pseudo constrains it in the middle using flexible outer torque arms pins that have stiff vertical constraints, but weaker torsional constraints. This allows effective torque transfer to the buckled center beam, which in turn, cause snap-through. From review of the field literature, nothing has been seen to operate like this thus far. It is our hope that the newly designed apparatus will lead to increased performance or additional benefits not shown by other devices in the energy harvesting community, mainly stability state switching and high energy orbital operation. Current prototypes that have been made are shown in figure 70 below. This chapter will primarily deal with fabricating a MEMS bi-stable buckled energy harvester with an active piezoelectric material.

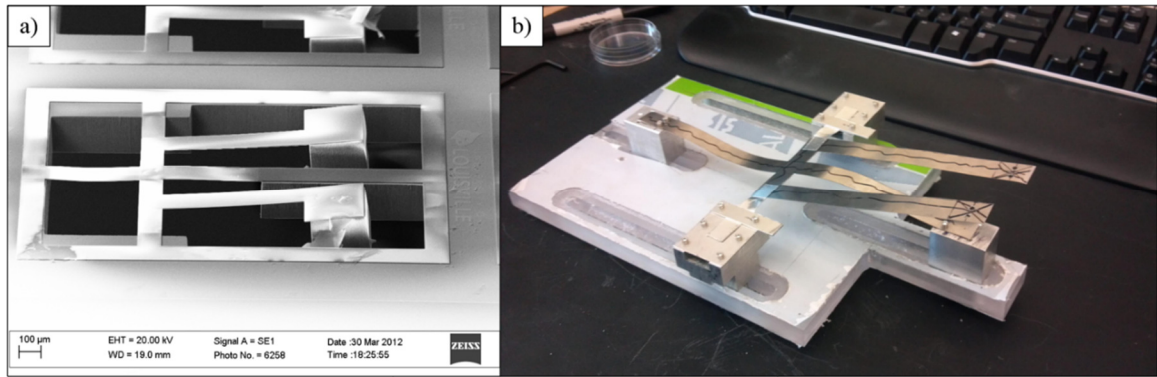


Figure 70. MEMS fabricated prototype (left) and a macro scale prototype (right) of our device. Both with no active piezoelectric layer.

ANSYS models have shown that our mass arms operate at a resonance frequency of 35 to 130 Hz with the lower end having arm lengths of 2 mm. These low resonance frequencies will help create large torques via mass displacement which should help induce snap-through of the center pre-stressed beam. Thus far determining the amplitude of driving acceleration needed to cause snap-through will be done experimentally.

A. Design and Planned Fabrication Steps

To fabricate an energy harvester from our prototype device a few things must be considered. One is that the device has to be tested so that its performance characteristics can be measured and quantified, allowing comparison with other devices reported in literature. This requires the ability to mechanically and electrically couple wires and force sensing probes to the device. While the macro scale prototype can be fitted quite easily with components such as force transducers and accelerometers, the MEMS based model will involve a more clever approach. The other consideration is the fabrication and monetary feasibility associated with the project. Construction in the cleanroom relating to MEMS is primarily a planar process so any solution to our energy scavenging idea must remain simple and cost effective.

Sol-gel based lead zirconate titanate is chosen to be our piezoelectric material for the device. This is primarily due to its power efficiency and ease of deposition, which involves spinning down a solution multiple times and then firing the wafer to a temperature of roughly 650 °C. PZT thin films are also capable of handling a great deal of strain when

compared to bulk crystalline PZT. While the method allows for small vertical step discrepancies for spin coating, it does come with a few downfalls that limit our ability to fabricate and theoretically model the device accurately. The d_{ij} coefficients vary widely depending on the consistency of the PZT mixture, how they are combined, coating method, firing temperature, etc. Also the d_{ij} coefficients for PZT are about half the magnitude of bulk PZT. Using sol-gel PZT reduces the potential types of material available to us for fabrication (pre PZT) due to the high firing temperatures.

If trouble arises from using the sol-gel based PZT then there is always the bulk PZT route that includes a thin layer of epoxy and a wet etch method to thin the material to a desired thickness. This method will require us to increase the size of the device because the dependability of thinning a bulk PZT wafer to 1 or 2 μm becomes troublesome. Benefits of bulk PZT is the high and relatively consistent d_{ij} coefficients while the downsides includes the need to epoxy it to a flat surface, more fabrication steps, and its overall lower tolerance for strain. Piezoelectric polymers represent additional alternatives, but will require development of MEMS compatible thin film processing.

Two ways of utilizing electrodes for our device are the d_{13} sandwich and the d_{33} inter-digitated methods. Literature articles and websites have argued that performance is about the same with the two setups but still ultimately depends on factors such as adhesion of the metal to the piezoelectric, electrode spacing through the material, inter-digitated electrode geometry, and the piezoelectric properties themselves. With this in mind, one must also weigh the additional pros and cons of executing such a fabrication method. The sandwich method will require designing and fabricating two photolithography masks which in turn will require an additional alignment and exposure step. If there are holes in the PZT layer then there also arises the possibility of a short between sandwich layers which would decimate the performance of our device. An upside to the sandwich method is that a small tear in the metal trace would not impede the performance by much. Interdigitated electrodes would only require one additional mask and exposure step during fabrication but requires better resolution for liftoff. We did court the possibility of using aqua regia to remove unwanted platinum but the risk of etching the underlying PZT was too great. There are studies that give optimum interdigitated electrode geometries for PZT actuators and composites; one of them being [18].

The new energy harvesting model will require the insertion of a piezoelectric layer between the silicon nitride and polyimide layer. In a planar sense, it will cover all the areas of the device minus the polyimide compliance arms. Electrodes will be inserted into the design process and will have wire bonding pads exposed on the outer areas of the chip/die. The die will be glued into a dual inline package (DIP) so that the wire bonds can electrically connect the device on the macro level. Once this is done, experimental tests can be carried out.

A schematic of the device with half symmetry is shown in figure 71 below. The parameters listed were assigned after evaluating FEA and non-piezo prototype characteristics. For the actual construction of the piezoelectrically active devices, values in table 12 below are assigned to the photomask. For simplicity and the fact that space is limited on the 4" silicon wafer being used, the widths for the center beam, brace arm, compliance arm, and torque arm will remain constant for each device. This means that when a value for width is set, it is set for all four of those variables.

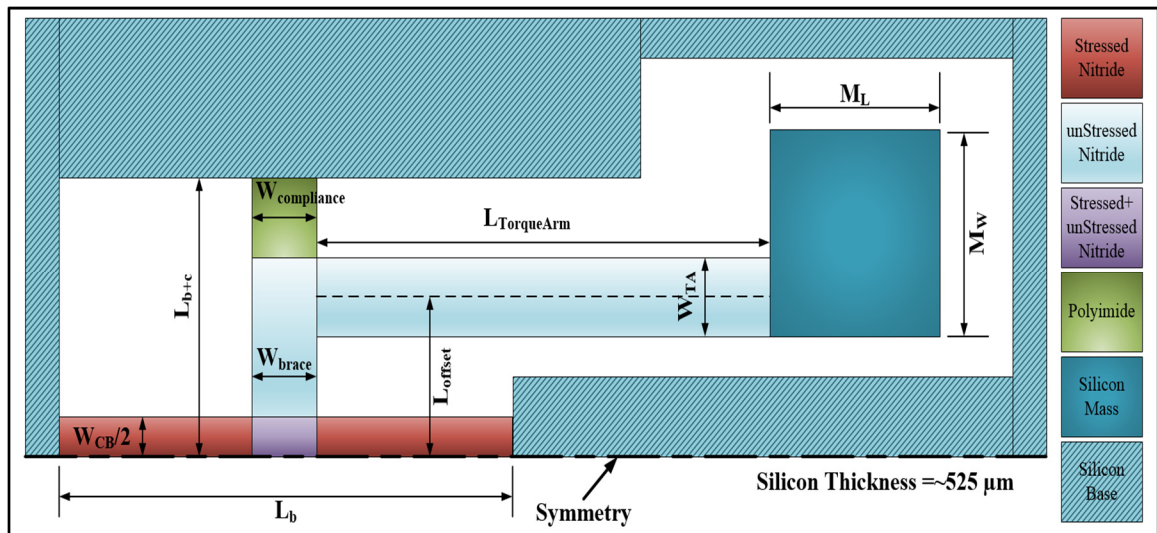


Figure 71. Half model MEMS device with PZT parameters.

Two 4” wafer thicknesses will be tried which will change the natural frequency of the device due to mass inertial difference. Typically a ~525 μm thick wafer with one side polished will be used which is the standard thickness for our stock wafer supply and cost about \$15 a piece. Another, more expensive, wafer which is the double side polished wafers that are 200 μm thick and cost about \$45 per wafer. Great care must be taken when using the thin 200 μm wafers because of their fragility. Cracking can occur with even the most minor mishandlings. As a first iteration of the device with piezoelectric material, the masses will be omitted to so that we can visualize the torque arm remnant stress.

Table 12. MEMS with PZT geometric variables and their assignments.

Variable	Values (μm)
L_b	2000, 3000
W_{cb}	100, 150
W_{brace}	100, 150
$W_{compliance}$	100, 150
L_{b+c}	550
L_{offset}	300
$L_{TorqueArm}$	2000
W_{TA}	100,150
M_L	500
M_W	500

Alignment markers for all 7 masks are shown in figure 72 below. This method was chosen so that the fabricator could go back and check to see how well each mask was aligned with respect to the others. Every brick in the alignment marker had seven teeth which were spaced 5, 10, and 15 μm apart from the middle so that an estimation of misalignment metric could be made. All masks (M1-7) have a minimum feature size of 5 μm .

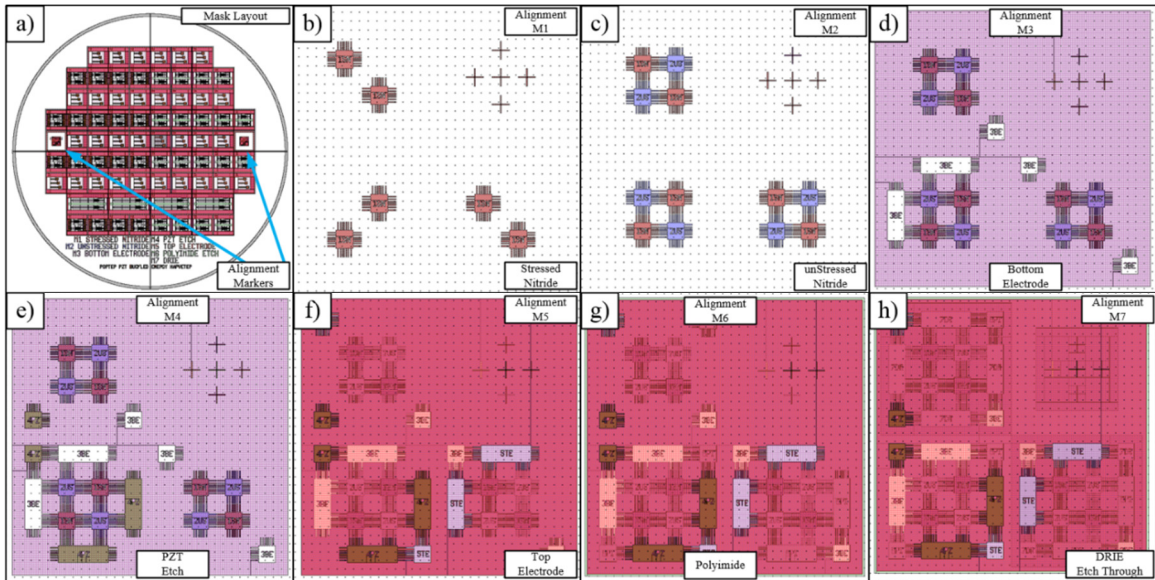


Figure 72. Piezoelectric capable device photomask design showing a) all masks and alignment markers with b) stressed nitride, c) unstressed nitride, d) bottom electrode, e) PZT etch, f) top electrode, g) polyimide, h) DRIE masks stacked on top of each other.

Masks for a single unit die are shown in figure 73 below. The first planned step is to deposit stressed silicon nitride, measure bi-axial stress, anneal in oven, measure stress again, and then etch it (M1) using RIE until the SiO_2 below is exposed. Next the wafer is cleaned before an unstressed nitride layer is deposited with annealing routines just like the one described above before then being etched (M2) in the RIE. The annealing routine was found to be a critical step in processing these devices due to the later PZT anneal step. More about this is found later in the chapter.

After cleaning the wafer again and washing it with dilute HF the bottom layer electrode is deposited via liftoff (M3) which should be a combination of titanium and platinum. Titanium forms an adhesion layer to the silicon nitride to which platinum can bond to. Platinum tends to be a good chemically inert metal to anneal PZT on because it doesn't react as much compared to chrome or aluminum. PZT is spun onto the wafer and dried on a hot plate multiple times before being fired at high temperatures. Once the wafer is fired it can be etched (M4) using a combination of BOE, HCL, and H_2O .

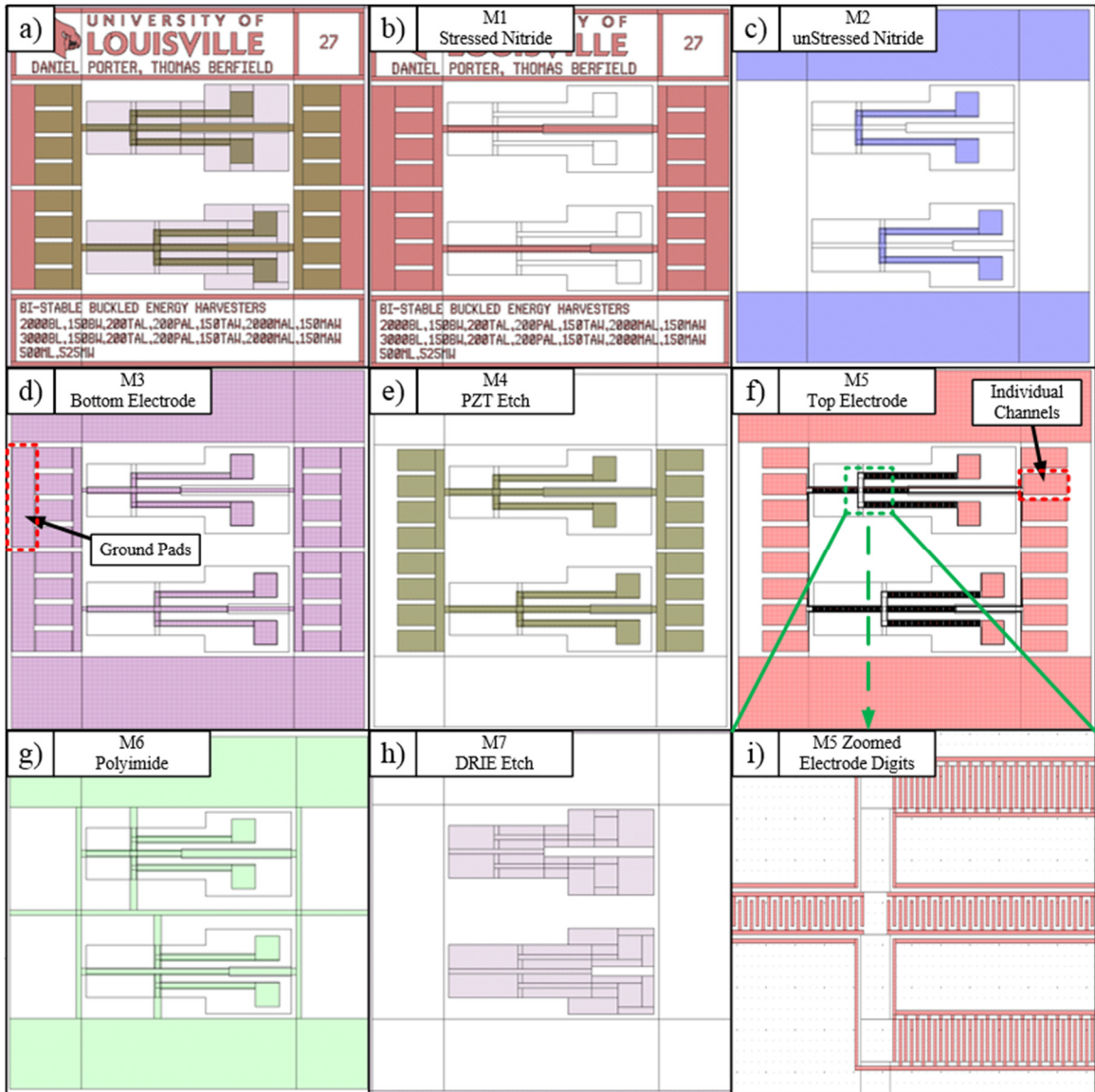


Figure 73. Mask designs for the bi-stable buckled beam MEMS device a) overview, b) stressed nitride, c) unstressed nitride, d) bottom electrode, e) PZT etch, f) top electrode, g) polyimide, h) DRIE etch, i) zoom in of top electrode showing interdigitated array.

Thorough cleaning will be needed after the PZT etch and possibly a nitric acid dip to remove residue on the wafer. A top electrode will be deposited using either chrome or gold and etched (M5). The top electrode is the most critical because there are interdigitated electrodes with $5\ \mu\text{m}$ gaps that need to be etched thoroughly but not under etched, which can be difficult using dark liquid etchants.

Polyimide is pretty straight forward in terms of application and processing. Once cleaned of residues the wafer will have an adhesion promoter liquid dispersed right before application of polyimide. The wafer will then be cured in a vacuum oven at an elevated temperature of 350 C for about 3 hours. A new layer of chrome or aluminum will be applied to the top of the cured polyimide as an extra masking layer. Photoresist will be patterned (M6) and the metal protective layer underneath it will etched. Removing the polyimide underneath the protective layers will require RIE etching using O₂ which will consequently eat the positive photoresist quickly, hence the extra metal protective layer.

Front side processing is finished at this point and will be protected with a thick layer of photoresist so that the backside can be operated on with minimal damage to the front. The backside of the wafer will be cleaned using the usual solvents before the application of a very thick photoresist layer that will be patterned using the DRIE etch mask (M7). Before etching windows into the SiO₂ the front side of the wafer will be adhered to a backing wafer via “Crystalbond”. Once bonding is complete the device substrate along with the backing wafer will be dipped in BOE to remove SiO₂, rinsed and dried, then promptly put into the DRIE. Etching all the way through the wafer (~525 μm) will generate heat and degrade the photoresist so it might be reasonable to stop the etching process and let the wafer cool down periodically. The DRIE will not only hollow out the backside of the devices but also separate the dies.

The device wafer will be put into a beaker of Acetone and left several days so that the die and backing wafer can separate. Each die will be taken out, cleaned using a sequence of solvents and then left to air dry. There should still be some top side SiO₂ layer so each die will be submersed in BOE to remove it. Potential problems include excess side etching of PZT, which if substantial, could short top and bottom electrodes.

Die can be imaged in an SEM to evaluate device quality at this point. Continuity checks using a probe station would also be beneficial to determine which candidates are the most likely to be 100% operational. Once a lot of die have been selected for packaging, the die will be epoxied into a DIP chip. Wire bonding from the pads to the DIP pins will complete the final product which should be left open to air at this point so high speed video can be obtained of bi-stable actuation. Other die will be simultaneously constructed with the proposed prototypes. One is of a simple cantilever beam structure which will test the

piezoelectric constants of the fired PZT while the other is of another proposed device utilizing multiple constraint nodes. These extra die are shown in figure 74 below.

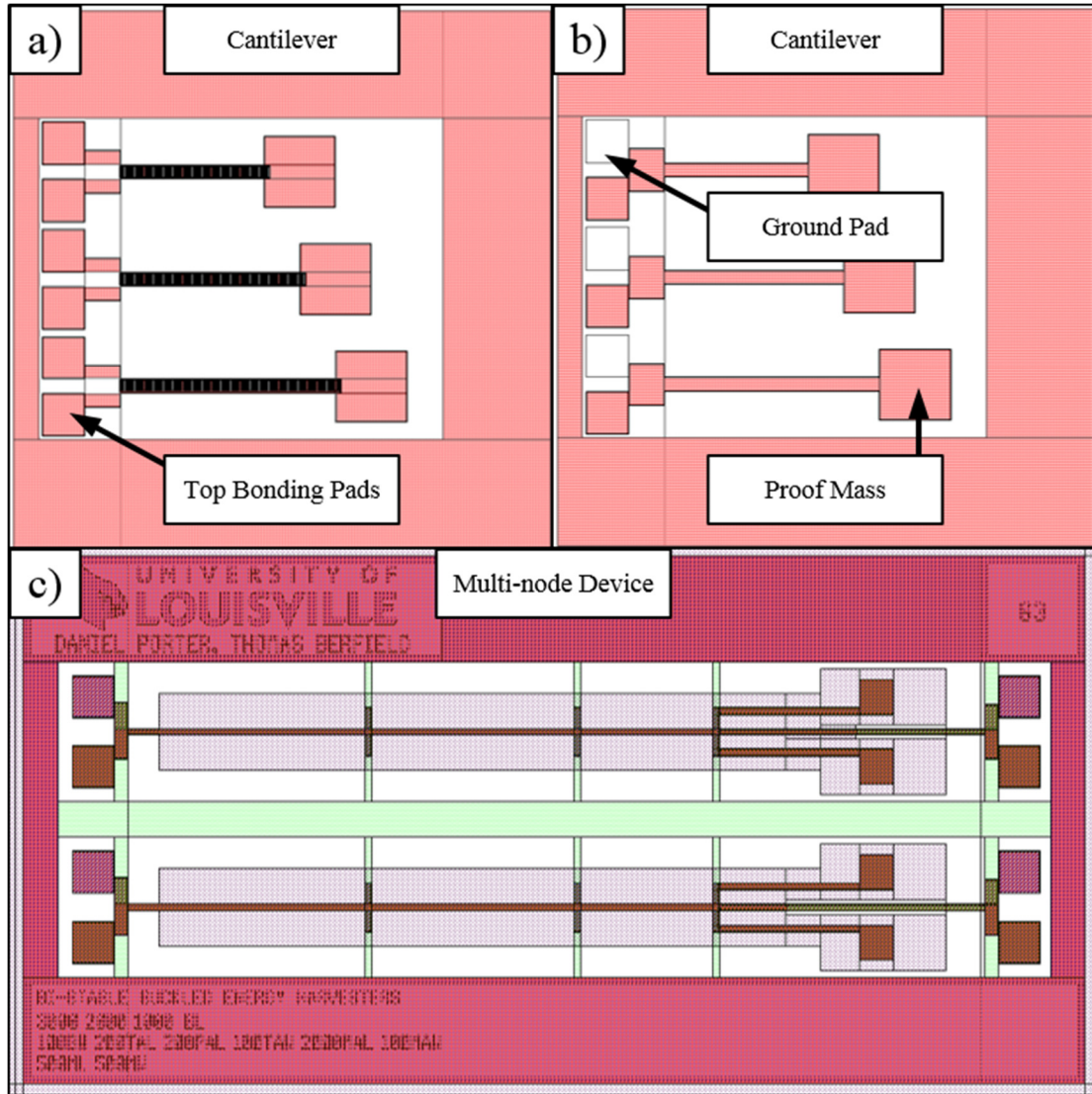


Figure 74. Other devices being fabricated with proposed device; cantilever beams with a) interdigitated and b) sandwiched electrodes, and c) a multi-node bi-stable snap-through device.

B. Bi-Stable Buckled Energy Harvester Utilizing PZT

The actual fabrication of these bi-stable energy harvesters was extremely difficult due to high temperature steps and the need to control stress. Operation of the device in the regime of bi-stable switching (and thus wider operating frequency) requires careful tuning

of the torque required to cause snap-through. If the stress on the center beam is too little, then it will not be bi-stable. Conversely, if the stress is too high then snap-through can only be achieved at high accelerations which could damage the device due to internal stress or the mass arms colliding with the base or roof of the DIP package.

Silicon wafer <100> ~525 μm thick are wet oxidized to create SiO_2 that is about 900 nm thick in a furnace using the recipe shown in table 13 below. The wafers were placed in the middle of the tube furnace so that the thicknesses would all be nearly the same. Five to eight wafers are done at a time with the SiO_2 thickness varying no more than 50 nm between all samples. Usual cleaning of the wafer is done with a multi-step process called AMI or acetone, methanol, then isopropyl solvent followed by a nitrogen gun drying finish.

Table 13. Tube furnace input parameters for UofL's cleanroom to get ~900 nm SiO_2 .

Variable	Type/Set
Oxidation Type	Wet
Target Temp (C)	1000
Ramp Rate (C/min)	20
Time at Target (hr)	4.5
Bubbler Temp (C)	98
Heater Tape (%Pot)	45
Flow Meter (ml/min)	1668
SiO_2 Thickness (nm)	900

Stressed silicon nitride is deposited in a PECVD using a standard recipe shown in table 14 below. References for the stress versus RF/LF ratio is shown in figure 13 at the beginning of this thesis. Since PZT tends to have a higher compressive stress, the target stress in the Si_3N_4 will need to be much higher. The first iterations of devices had 1 μm of stressed and unstressed silicon nitride but the final working ones needed to use thinner layers (~300 nm) due to reasons that will be obvious further on down.

Table 14. PECVD recipe to obtain ~-700 MPa stressed silicon nitride.

Variable	Value	Variable	Value
Chiller (C)	70	Heater (C)	350
Total Pulse Period (s)	20	Run Time (min)	17
RF On Time (s)	10	RF Power (W)	50
LF On Time (s)	10	LF Power (W)	50
5% SiH ₄ /Ar	400	Total Thickness (nm)	300
N ₂	600	Deposition Rate (Å/min)	18.33
NH ₃	20	Biaxial Stress (MPa)	-640

A protective layer of chrome is deposited and patterned with M1 so that the stressed nitride can be etched. Chrome deposition is done in the KJL PVD at 300 W for 372 seconds which produces a film thickness of about 100 nm. The patterning is done using Shipley Microposit 1827 at 4000 rpm which is detailed along with the chrome deposition rate in the recipe Appendix (MEMS FABRICATION RECIPES). Etching is done in a March RIE machine by first O₂ (50% of MFC) cleaning the chamber for 1 minute at 300 W and 300 mTorr without the wafer present. Once the chamber has been cleaned the silicon nitride is etched using the recipe shown in table 15 below. Etching rate is very non-linear at the start and usually converges on about 3000 Å/min if initial slow etching effects are ignored. These devices were etched a little longer which so that the outer portions could complete the 300 nm depth since the center always etches faster.

Table 15. Silicon nitride etching recipe using March RIE.

Variable	Value
O ₂ (% MFC)	5
CF ₄ (% MFC)	20
Power (W)	300
Pressure (mTorr)	300
Time (s)	90
Etch Depth (nm)	300
Etch Rate (Å/min)	3000*

*linear rate of etch

Hot Nanostrip at 95 C for 10 minutes was used to remove the rest of the photoresist. When evaluating the nitride etch from above it is discovered that the chrome protective mask at the center is penetrated about 20-50 nm. This protective layer is stripped using CEP200 and is usually entirely gone from the surface in about 6 minutes at room temperature. The wafer is cleaned then put into the PECVD for the unstressed nitride layer, which is done at the same specs as table 14 but with a RF/LF on time of 14/6 seconds respectively. This gave about 50 MPa of tensile stress for a 300 nm thick layer. Another protective layer of chrome was applied to the wafer and etching was done using M2 as it was for the first layer.

Liftoff of Ti/Pt was done to create the bottom electrode via Shipley Microposit 1813 and LOR-3A for which the recipe is in the Appendix under (MEMS FABRICATION RECIPES). The bottom electrode layer was about 75 nm thick and is considered well within geometric tolerance limits for these devices. A picture of one wafer after bottom electrode deposition is shown in figure 75 below. Inspection shows that the edges of the Ti/Pt metal is quite smooth so it is noted that liftoff of the top electrode could be used in future procedures should the need arise.

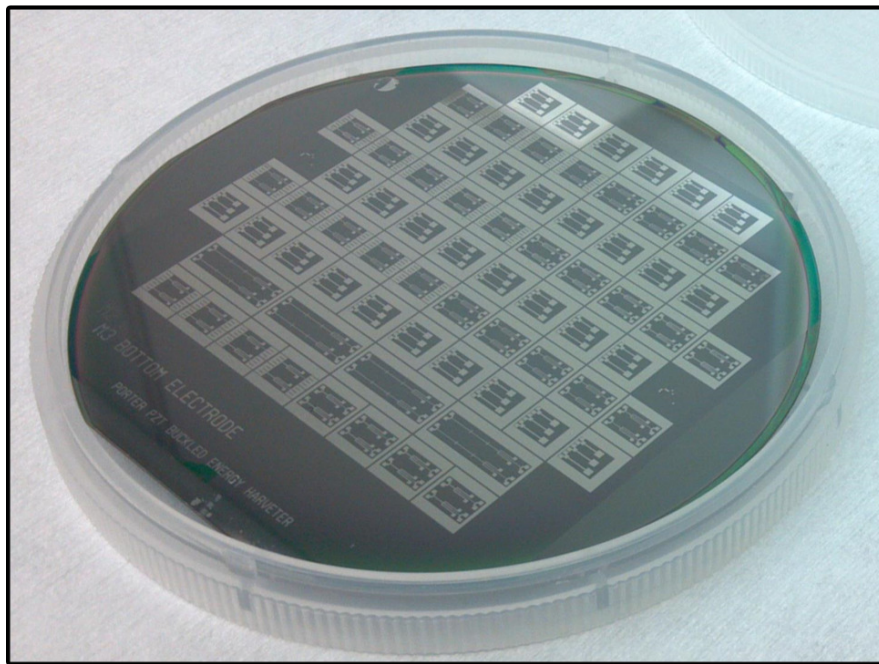


Figure 75. Device wafer with stressed nitride, unstressed nitride, and Ti/Pt bottom electrodes.

Deposition of (1:1:1) sol gel is done in a multistep process. Two hot plates set to 100 C and 200 C are allowed to reach their peak stable temperatures. The wafer is cleaned with AMI, blow dried, then exposed to UV light for five minutes to promote adhesion. About 3 mL of 1:1:1 PZT sol-gel solution is spread onto the wafer at 300 rpm for 15 seconds which is then rapidly ramped to 3000 rpm for 45 seconds. Putting the wafer on the 100C hotplate for five minutes allows solvent to evaporate out of the sol-gel without causing violent spallation of the film, which redeposit as flakes. Then the wafer is put on the 200 C hot plate to drive out even more solvent. Once the wafer is cool the coating process is repeated two more times to give a total of 3 coats. The device wafer is now ready for high temperature firing which will promote the piezoelectric β -phase in the PZT film.

Firing takes place in a “trash furnace” because the PZT outgases lead particles which tend to be bad for CMOS type processes. A wafer is put into the furnace at room temperature and is heated to 650 C at a rate of 20 C/min in an O₂ atmosphere (1668 mL/min) and held at 650 C for 12 minutes (0.2 hr). Ramping down is done at the same 20 C/min rate until the temperature is below 300 C which allows them to be removed from the furnace. The resulting thickness of PZT is 130 nm which is on par with previous tests. Though an interest result is found from the first batches of fired device wafers; they blistered as shown in figure 76 a) below.

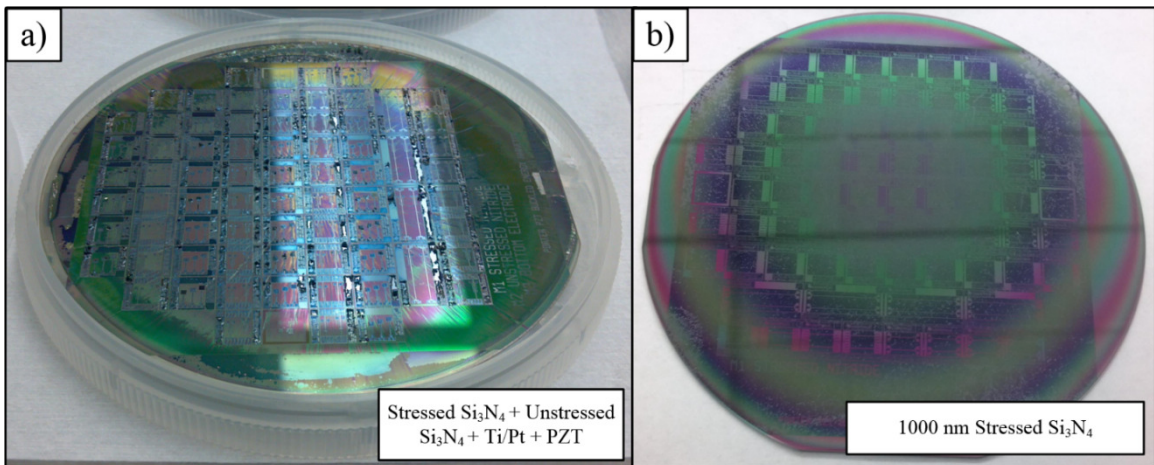


Figure 76. Blistered wafer after firing at 650 C with a) all layers up to PZT and b) just stressed silicon nitride.

Blistering of the device wafers renders them useless so time was spent to investigate the cause of this failure. Ramp rates and peak temperature of firing were the first suspects but that would also allude to poor adhesion between PZT and the underlying layers. It should be noted at this point that we have successfully annealed PZT (1:1:1) on SiO₂ and Ti/Pt coated substrates. Combinations of peak temperatures and ramp rates as low as 450 C and 2 C/min were done but blistering still persisted. This led to the Si₃N₄ layers being suspected and confirmed via annealing after the first two layers were deposited and tested, blistering the top Si₃N₄ layer.

Research into this failure revealed literature of outgassing in the PECVD Si₃N₄ layer due to incorporated H₂ [5]. The films in that research were only 100 nm thick and processed fine after a 600 C post deposition anneal for 1 hr. Repeating their anneal using our nitride thickness proved erroneous because blistering occurred during the “de-gassing” anneal. Figure 76 b) above shows the effects of blistering when the silicon nitride is 1000 nm in thickness and exposed to 650 C for 1 hr in an argon atmosphere. Another test using only 300 nm of stressed nitride (~-700 MPa) on top of a 100nm layer of chrome (550 MPa tensile) annealed at 650 C for 1 hr did not outgas and blister; but measuring the stress after anneal revealed that the nitride layer stress reduced to -30 MPa (assuming that the chrome stress state difference was minor). One last effort included using stressed nitride that is 570 nm thick (-400 MPa) on SiO₂ and annealing at the same parameters. The resulted in minor blistering and a stress state change to tensile 200 MPa. This effect is significant, as the compressive stress used to buckle the center beam would essentially disappear if a high temperature outgassing or β-phase growing process is used with silicon nitride. We theorize that annealing the thicker Si₃N₄ in incremental deposition steps would allow us to achieve thick films that would not outgas, but those films would have their stress pushed towards tensile values.

A new idea of fabricating a prestressed center beam is to use a thick SiO₂ as the compressive layer in the center beam. The SiO₂ is grown at 1000 C and the annealing process is 350 C below that. Young’s modulus for Si₃N₄ is about 270 GPa which is nearly four times as high as SiO₂ at 73 GPa and would mean that the out of plane buckling of the final device would be less. Device 18 (Dev18) was constructed using the same masks as

before but with SiO₂ at 935 nm thick and (-300 MPa). Figure 77 below shows the first two layers of SiO₂ and unstressed silicon nitride for Dev18.

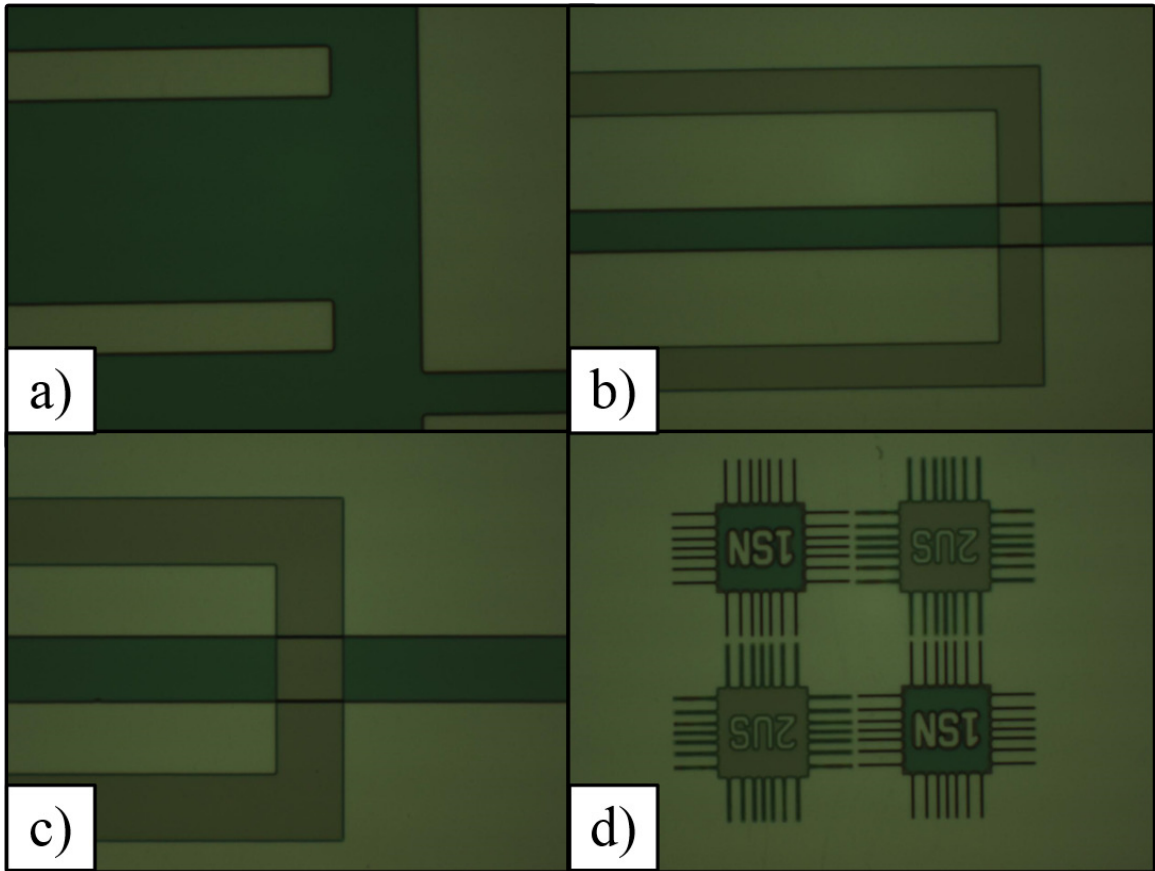


Figure 77. Microscope photos of Dev18 after the stressed and unstressed nitride etch a) electrode platform, b) center of buckled beam, c) center of buckled beam for wider device, and d) alignment markers.

Liftoff was done on Dev18 just like on the wafers before it and pictures showing the results are in figure 78 below. The titanium was not oxidized on any of these wafers to promote adhesion like in [5]. Instead the vacuum was never broken and platinum was sputtered immediately afterwards. Removing the liftoff photoresist involved ultrasonically sonicating the wafer for about 1 hour in acetone and then putting it into a solvent called NMP for about 10 minutes. The NMP was the only solvent we had to remove LOR-3A, which was quite inert to acetone.

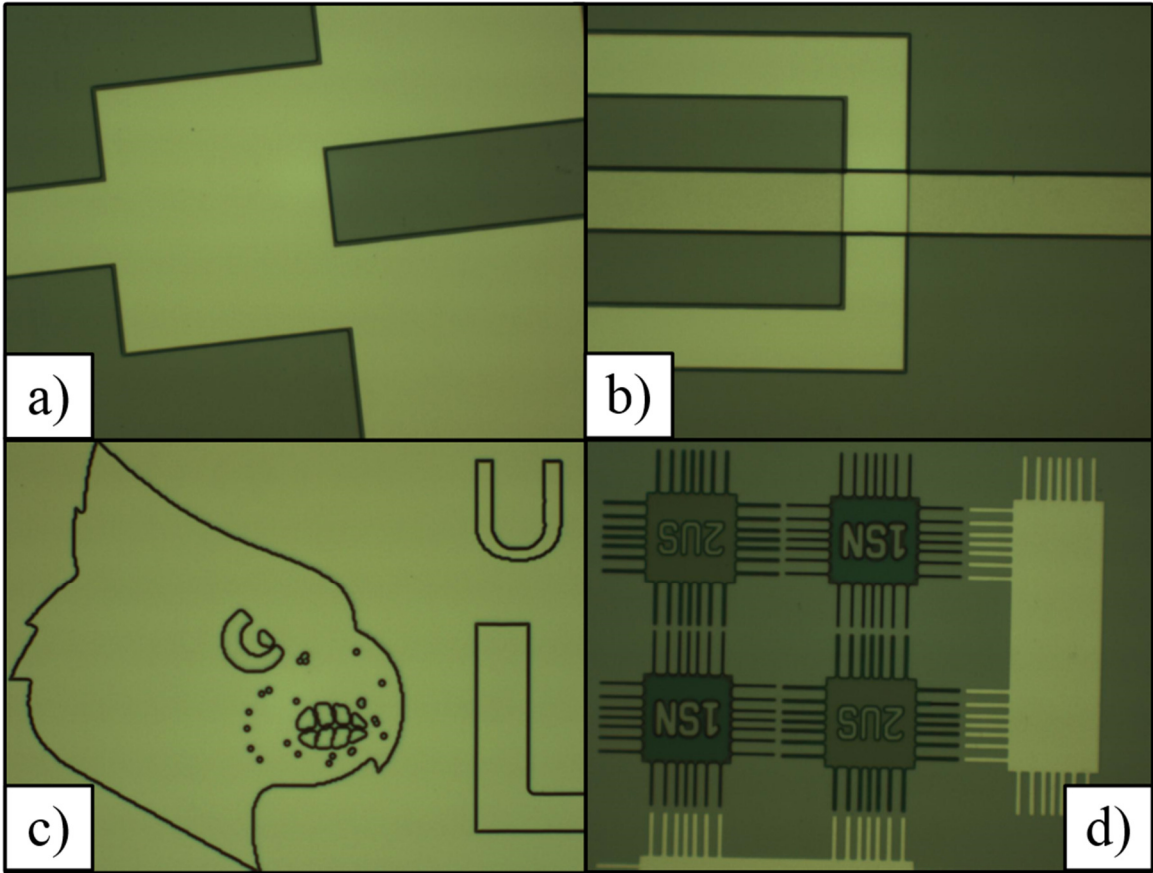


Figure 78. Microscope photos of Dev18 after bottom electrode platinum liftoff for a) buckled beam anchor section, b) center of buckled beam, c) UofL logo on all die, and d) alignment markers.

Our PZT spin recipe was applied after a quick UV wafer treatment. The annealing process revealed slight cracking in certain areas but was minimal on platinum surfaces. It is assumed that the abrupt surface topology caused large stress gradients and initiated crack sites. Adhesion of the Ti/Pt layer was compromised in about 50% of the etched locations as shown in figure 79 below which might be attributed to the PZT wet etching process. No Ti/Pt was delaminated under the remaining PZT patterns meaning the stress in the PZT ceramic film was not enough to completely fail the bottom electrode. Potential nano-pores in parts of the metal film may have exposed the SiO_2 and Si_3N_4 , causing it to be etched during the BOE dip. Other areas appeared to be fine, figure 79 d), but may be under a high state of residual stress.

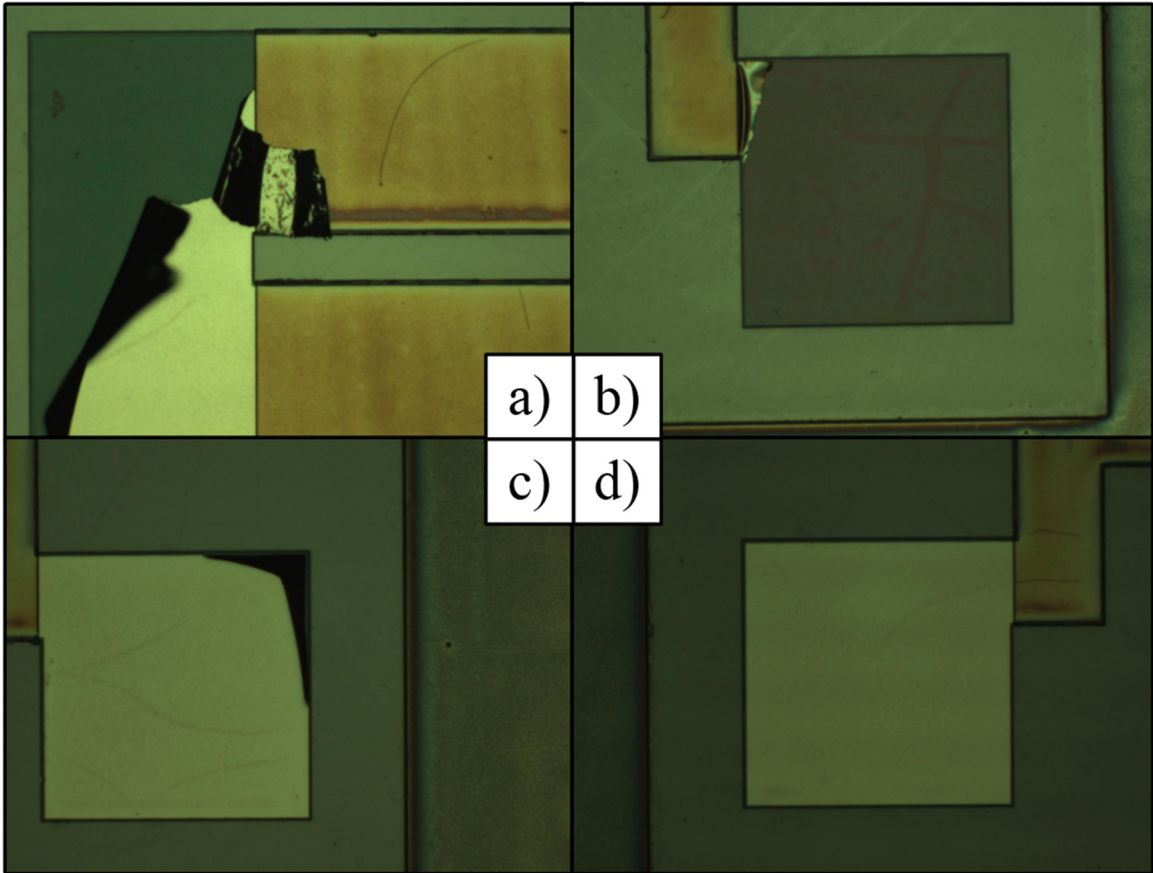


Figure 79. Microscope photos of Dev18 after PZT etching a) bottom electrode delaminating, b) bottom electrode completely, c) partially, and d) not delaminated.

Continuation of device 18 was done even though there was failure in certain places. The wafer was ultra-sonicated for two hours in a beaker of acetone as to attempt removal of any loose PZT or metal flakes. A 100 nm top electrode of chrome was deposited and patterned as shown in figure 80 below. There was slight over-etching which caused the interdigitated electrodes to become thinner than they should have. Breaks in electrodes were visually seen in about 10% of the devices and mostly occurred in the interdigitated devices.

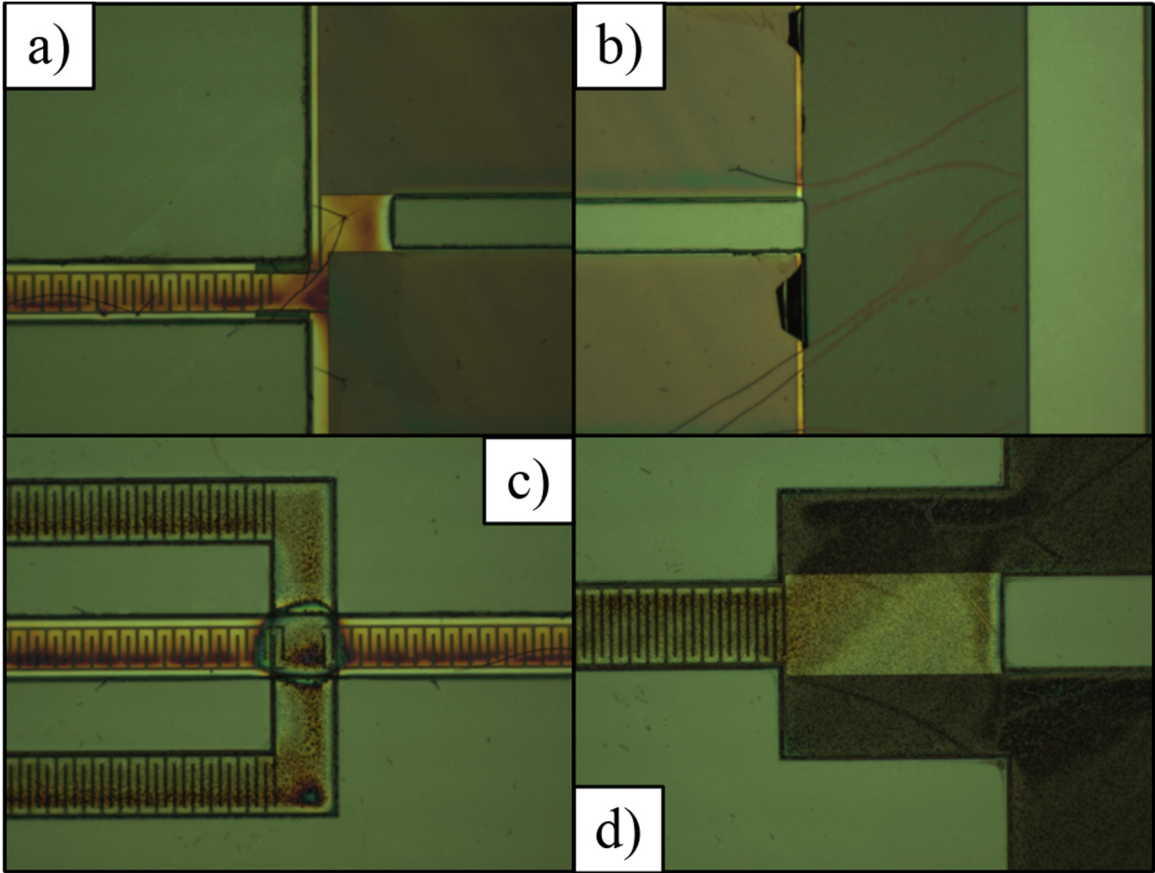


Figure 80. Microscope photos of Dev18 after top electrode etch for a) base of center buckled beam, b) top electrode next to delaminated bottom electrode, c) center of stressed beam, and d) base of cantilever interdigitated beam.

Polyimide provides the compliance arm mechanism which pseudo pins the center beam in this device iteration. The Appendix (MEMS FABRICATION RECIPES) in the back shows the application and etch recipe for PI2611 polyimide. For this device a spin speed of 4,900 rpm was used which gave 3.5 μm of polyimide after curing. Pictures of device 18 after the polyimide etch are shown in figure 91 below. The profile after etching was acceptable with no immediate flows being observed. While the curing for this process is 350 C max for three hours, it is not considered a high temperature step compared to the PZT anneal routine. It should be noted that PVDF, if used, will melt at 171 C so any polyimide processing would have to be done before PVDF application in future iterations.

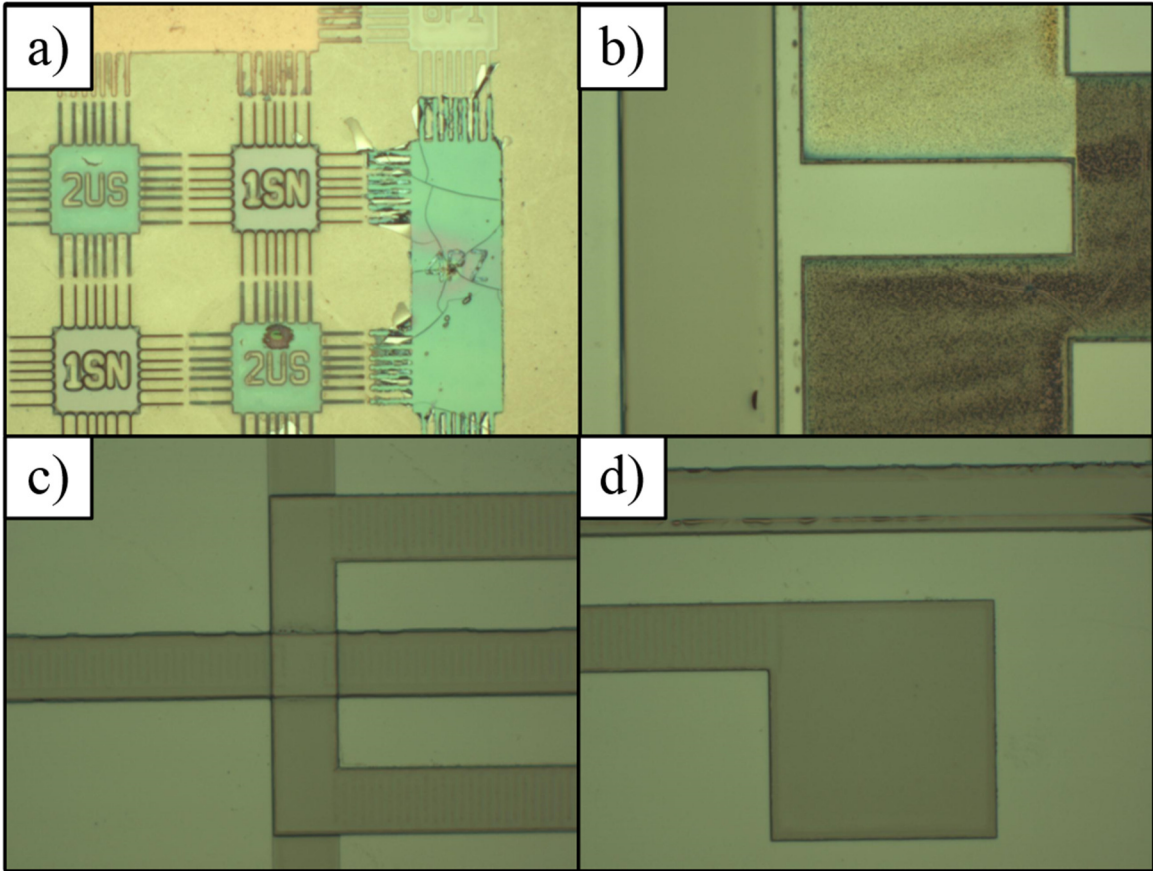


Figure 81. Microscope photos of Dev18 after polyimide etch for a) alignment markers, b) near base of cantilever beam electrodes, c) center of stressed buckled beam, and d) proof mass of a bi-stable device.

Satisfactory polyimide etching marks the end to top side processing. The last step involves etching a pattern through the silicon substrate which in turn will create our buckled beam and release our masses. Protecting the top side is a simple thick layer of Shipley 1827 photo-resist that is hard baked to seal the devices from damage that may occur. The patterning of the backside is done with SPR220 and should hold up for the majority of the DRIE etch. Backside SiO_2 will be a safeguard in case of PR failure. A backing wafer is adhered using Crystal Bond to give support so that the device substrate does not fracture into the DRIE chamber during processing.

The DRIE recipe used for Dev18 is shown in the Appendix (MEMS FABRICATION RECIPES). This recipe was successfully used to completely process all discussed device wafer iterations and test samples. Helium leak up rate, which keeps the

wafer cool, was the most significant control variable that fluctuated with DRIE etching. Maintaining a very smooth and clean backing wafer kept it under 10 mT/min which was acceptable. Two sets of 250 cycle etches were done on Dev18 that removed 220 μm of silicon. This meant that there was at least 305 μm of silicon left to be etched. Three more etching sets were done with cycles of 350, 350, and 100 to completely remove the silicon substrate pattern. It was immediately noticed that the DRIE mask alignment was off by one die because the backside cameras on the SUSS Aligner couldn't target the wide alignment die on the top side of the wafer. Thus the user had to rely on other features to align the front markers to the backside photo mask markers.

Images of Dev18's backside after DRIE etching, but before removing the backing wafer, are shown in figure 82 below. Heavy misalignment can be seen in figure 82 d) while fractured cantilever beams are shown in figure 82 f). The best dies were close to the correctly aligned alignment marker and are shown in figure 82 c) and zoomed in figure 82 b). A beaker with acetone was prepared and sealed after Dev18 was placed inside. After two days it was opened and each die was removed and cleaned using AMI without letting the acetone dry.

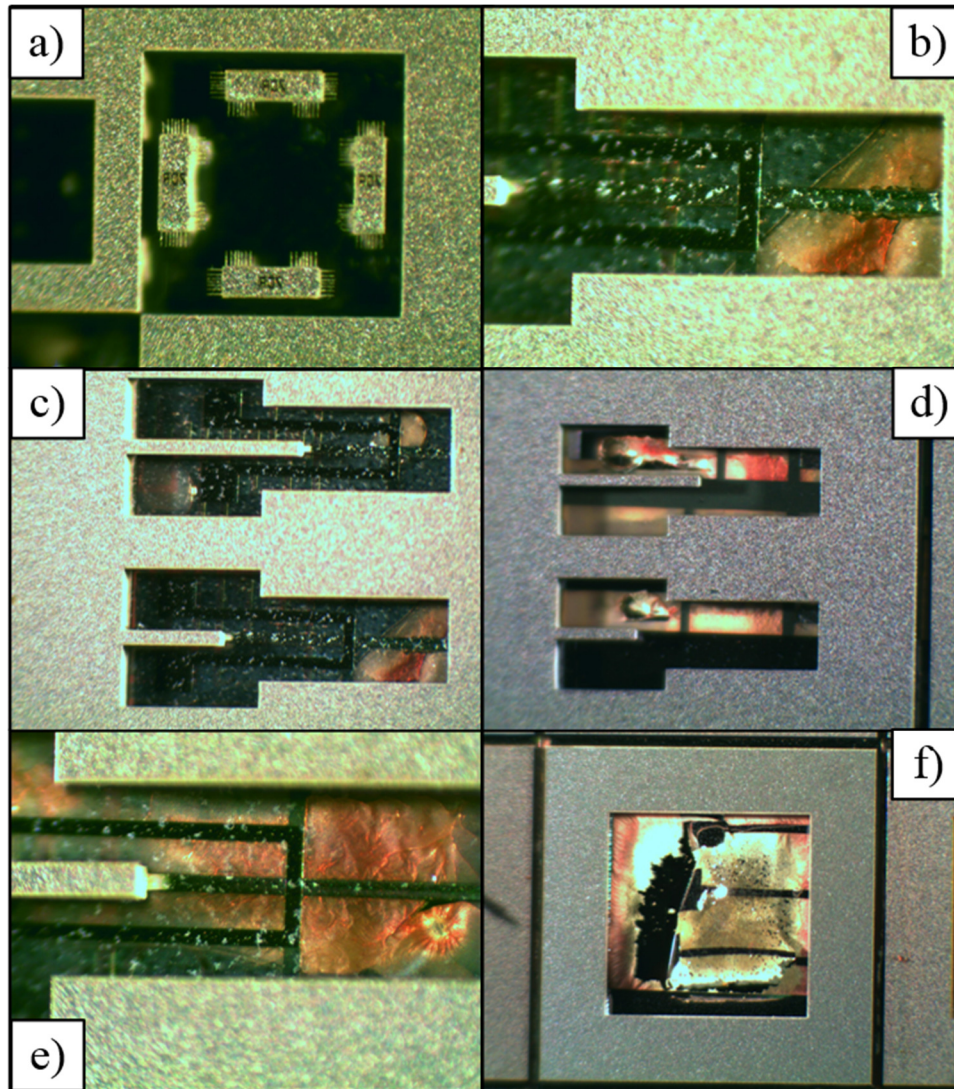


Figure 82. Backside microscope photos of Dev18 after DRIE etching but before being released a) alignment markers, b) acceptably aligned device, c) almost acceptable, d) very misaligned, e) close up of resist residue and crystal bond, and destroyed cantilever beams.

Only two die of the Dev18 wafer were really worth investigating due to the misalignment issue. Close up pictures of a die side showing DRIE separation technique are shown in figure 83 a) below while the rest of figure 83 shows to top sides with the focus on different areas. What was considered silicon nitride/chrome/PZT/polyimide torque arms with roughly zero stress has now bowed slightly out-of-plane after release. PZT annealing most likely induced a slight change in silicon nitride stress to tensile. The direction of buckling indicate that the top most portion is under more tensile load than the

bottom meaning the very thick polyimide layer is dominating the lower ones. PI 2611 polyimide is supposed to have a tensile stress of around 2 MPa at 2 μm thick. Testing of the electrodes of the released die showed that there was shorting meaning the PZT could not be poled.

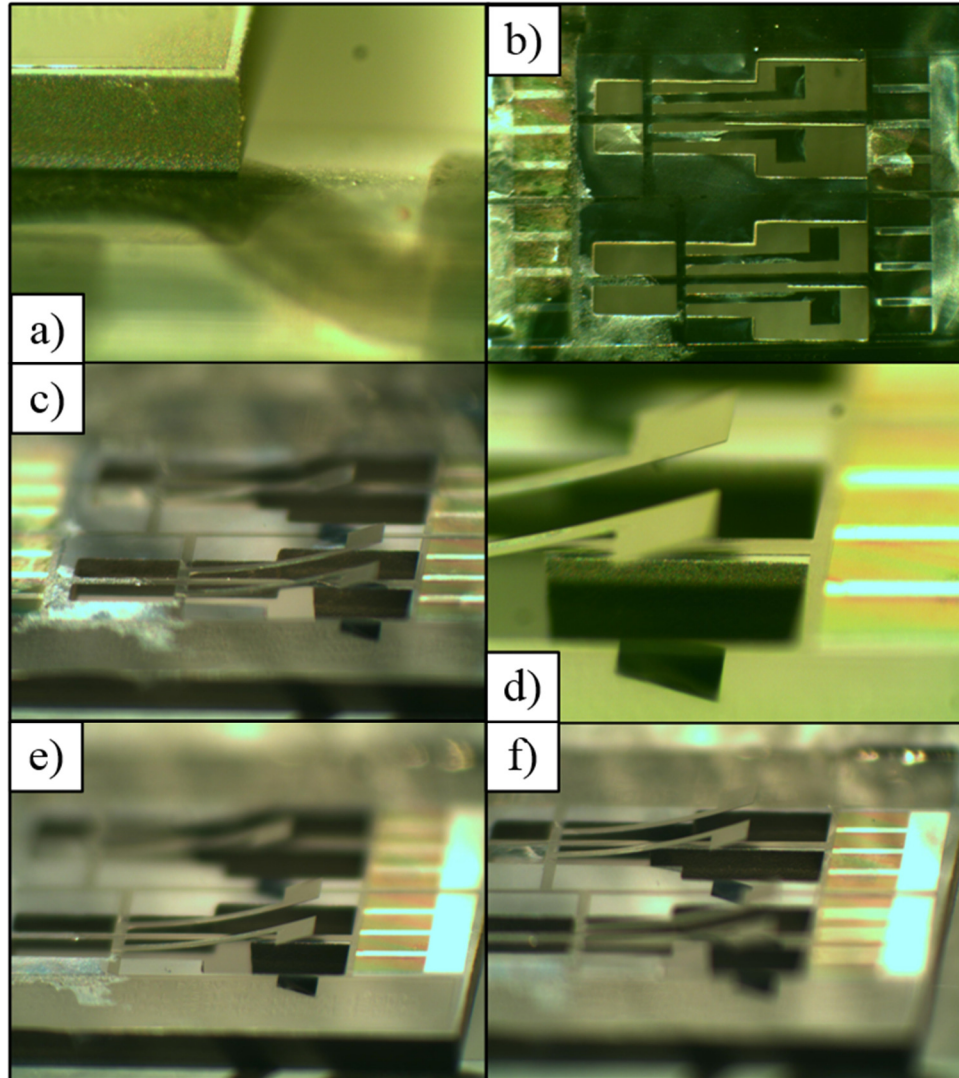


Figure 83. Microscope photos of released Dev18 die a) DRIE cut edge of die, b) top side, c) side view showing top electrode pads, d) close up of mass tips, e) long center beam device focus, and f) short center beam focus.

SEM images of the Dev18 die are shown in figure 84 below. It is apparent that there exists a film of what is most likely the residue of Crystal Bond and photoresist. The solvents acetone and isopropyl had no effect of removing it even after a few days of it sitting in a beaker and then being ultra-sonicated. Figure 84 c) shows that the center beam did not buckle out of plane into an s-shape like expected. It is most likely that the thin PZT film had enough tensile stress to nullify the SiO_2 's compress stress which would create a negligible deflection.

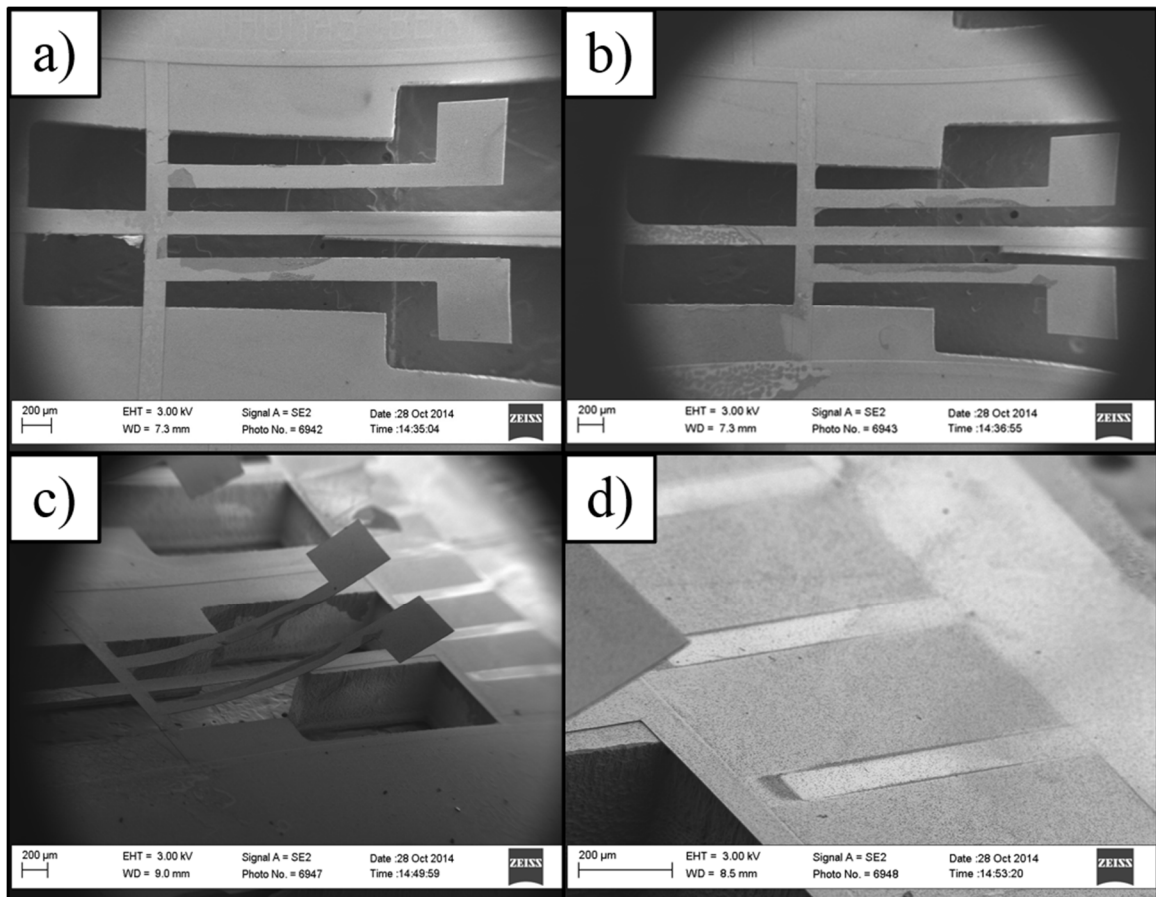


Figure 84. SEM images of Dev18 released die a) short center beam device, b) long center beam device, c) angled view of long device, and d) electrodes for long device.

Close-up images of the long center beam device die is shown in figure 85 below. This further emphasizes the fact that the center beam is indeed not buckled. Figure 85 c) indicates that there is some kind of sputtered/dried material adhered to the top of the

polyimide. It also shows the layering of 1.7 μm SiO_2 , nitride, chrome/Ti/Pt, and PZT stack plus the 3.5 μm of polyimide for the center beam and the center brace for the torque arms.

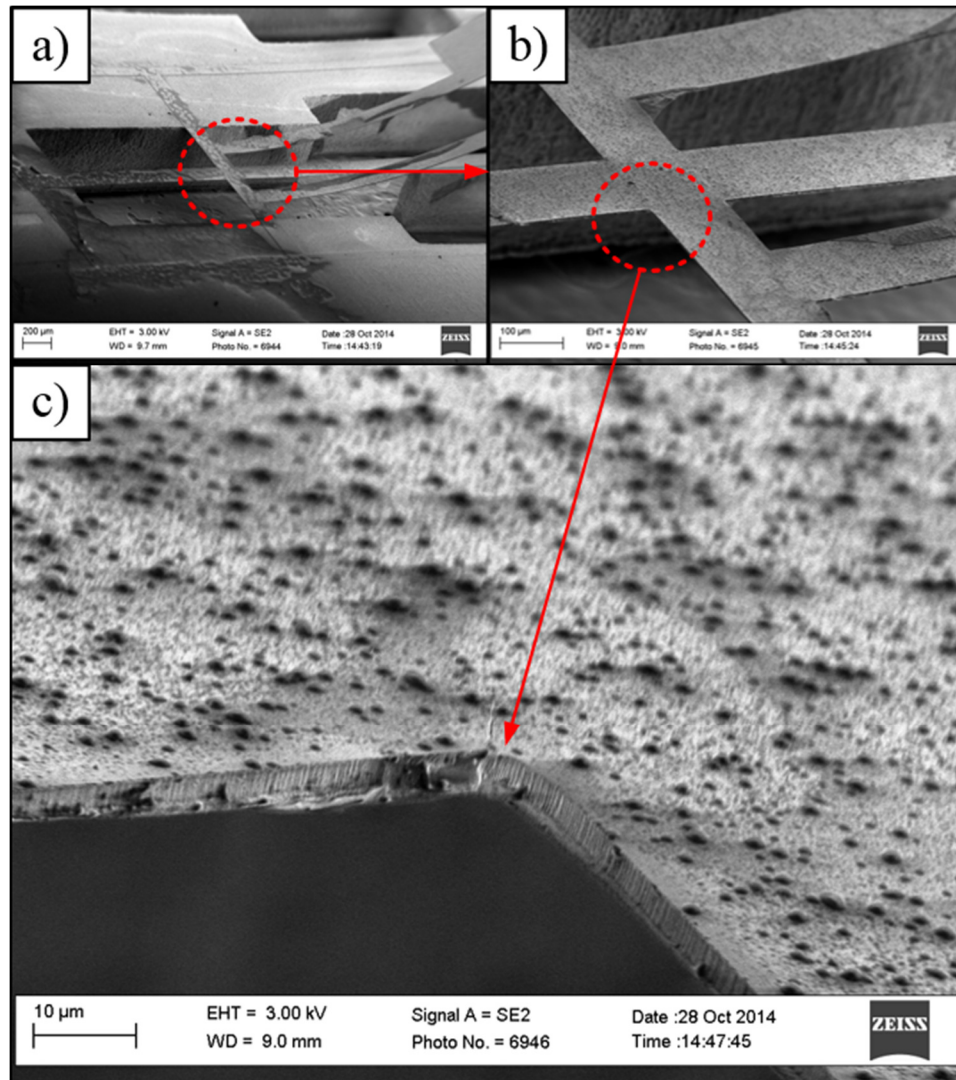


Figure 85. SEM images of Dev18 center beam showing a) device, b) close up of polyimide, and c) cross section of beam showing stressed SiO_2 , unstressed nitride, PZT, and polyimide.

At this point it is evident that PZT was a detriment for these first iteration buckled devices simply due to the high temperature step that changes the known stress states of the other materials and could still be causing bottom electrode delamination. PZT does have excellent piezoelectric coefficients but another alternative is AlN which has a lower

piezoelectric coefficient (x1/10) but also a lower processing temperature. AlN films stays chemically inert up to 2500 C [76] so they should be compatible with any other process the proposed device would encounter. PVDF homo or copolymer is another possible piezoelectric material to use in the MEMS field. This material will cause less tensile stress interference than the PZT and can easily be spread on thicker leading to more charge generation. It could also be used as the compliance arms and completely eliminate the polyimide. The one downside is that it will melt at 171 C and short term exposure to 80-100 C will cause it to lose its polarization.

CHAPTER VII

PIEZOELECTRIC ENERGY HARVESTING MODEL

Predicting the power generated from a newly designed energy harvester can be quite complicated as shown by [11], [105], [119], [121], [123] and also requires experimental work to be done before the theoretical prediction itself. Complex models that give theoretical power production as a function of time and driving acceleration is ultimately desired to determine optimal energy harvesting performance for future design iterations. As a starting point, a simple model will be used to make predictions of peak power production at different driving frequencies. A simple model to determine peak power as a function of frequency has been utilized by Renaud *et al.* and Berdy *et al.* [119], [11]. This model involves creating an equivalent circuit schematic and analyzing the output voltage across an optimal load resistor. The schematics for this type of setup are shown below in figure 86. A generalized model is shown in a) while the schematic in b) indicates that many modes may be incorporated into a single model. Assumptions for these models include: the natural frequency of the structure and the frequency of the input are close together, differing modes do not interfere with one another, the effective mass of the bending beams is negligible compared to the main proof mass, and electro-mechanical wave propagations can be ignored [118].

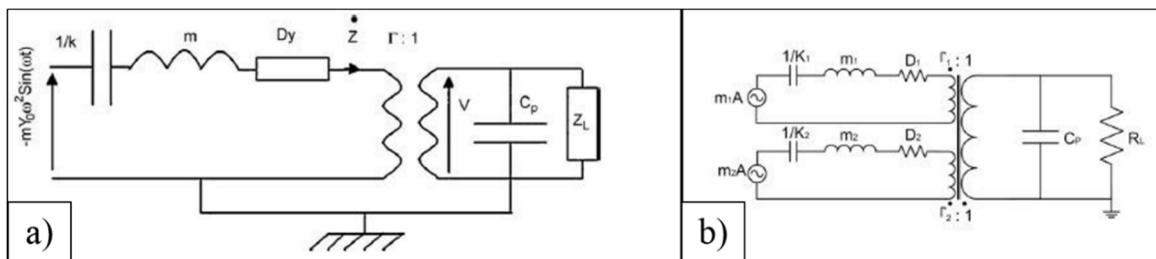


Figure 86. a) General equivalent circuit model [118], b) equivalent circuit model using the first two modes [11].

Inputs to these models are forces derived from accelerations. From Figure 86 above, the K 's are spring constants corresponding to the stiffness of the beam (not to be confused with the coupling coefficients k_{31} and $K_{coupling}$), D 's are the parasitic dissipations, m 's are the effective modal masses, Γ is the inverse of a perfect transformer ratio and is directly proportional to d_{31} for a beam, C_p is the electrical capacitance for the device, and R_L or Z_L is the resistance or impedance that uses the scavenged energy. This exact model will have to be adjusted for our proposed device, since it does not have the same boundary conditions as a cantilever beam. This requires resolving the complex equations and backing out a new optimum power expression.

A power versus frequency curve analysis starts out by the user performing a FEA modal analysis of the structure in first a short then open circuit configuration. This will reveal the first few natural resonant and anti-resonant frequencies (f_n in ANSYS) and also derive effective modal masses using the *Get command for each direction (*GET under the solution part). Next the generalized electromechanical coupling factor (GEMC) is derived using

$$K_{coupling} = \sqrt{\frac{f_{n,oc}^2 - f_{n,sc}^2}{f_{n,sc}^2}} \quad \text{Eq 63.}$$

where $f_{n,oc}$ is the open circuit natural frequency and $f_{n,sc}$ is the short circuit natural frequency without the effect of parasitic losses. Since charge is not allowed to flow as freely in the open circuit configuration as when compared to the short circuit setup, one expects $f_{n,oc}$ to be slightly higher due to increased stiffness of the piezoelectric material. The model's parameters are solved for using [11]

$$K_n = (2\pi f_{sc,n})^2 m_n \quad \text{Eq 64.}$$

$$D_n = \frac{m_n(2\pi f_{sc,n})}{Q} \quad \text{Eq 65.}$$

$$\Gamma_n = \sqrt{K_{coupling}^2 K_n C_p} \quad \text{Eq 66.}$$

where Q is the quality factor for the structure and must be determined experimentally. All other parameters for the simplified model can be extracted using the modal analysis. Capacitance for the piezoelectric layer is straight forward to calculate and utilizes the equation for a parallel plate capacitor which is

$$C_p = \frac{\varepsilon_{r,p}\varepsilon_0 A}{d} \quad \text{Eq 67.}$$

where $\varepsilon_{r,p}$ is the relative permittivity, A is the planar area, and d is the thickness for the piezoelectric layer. The term ε_0 is permittivity of free space and has a value of 8.854×10^{-12} Farad per meter.

Experimentally determining the quality factor Q will require a “ring-down” test. This requires that a test specimen is driven at its natural frequency while the displacement (preferably at a location where displacement is maximized) can be monitored via a macro sensor or laser interferometry. Immediately the input driving the system is cut off and the time constant τ is measured while the system peak to peak amplitude dies down. In a damped oscillator configuration, the quality factor can be described as

$$Q = \frac{1}{2\zeta} \quad \text{Eq 68.}$$

where ζ is the dampening ratio. Also for a damped oscillator, the value of the displacement at any given point can be characterized by the equation

$$x(t) = Ae^{-\zeta\omega_0 t} \sin \left[\sqrt{1 - \zeta^2} \omega_0 t + \varphi \right] \quad \text{Eq 69.}$$

where A is max amplitude of the oscillation at resonance, t is time, and φ is the phase offset of the signal. Most practitioners of this method tend to only look at the peak to peak amplitude values so that the sinusoidal term can be taken to unity. This allows for the measure of the time constant which is

$$\tau = \frac{1}{\zeta\omega_0} \quad \text{Eq 70.}$$

for the system described by Eq 69. Combining Eq 70 and Eq 68 gives the revealing relation between the time constant and the quality factor

$$Q = \pi f_0 \tau \quad \text{Eq 71.}$$

The meaning of the GEMC is the square root of the ratio of electrical energy derived divided by the dissipated mechanical energy or vice versa. This is different from the electromechanical coupling coefficient, k_{31} , which is the square root of the ratio of the electrical/mechanical energy divided by the total input energy for the piezoelectric ceramic. Figure 87 shows the direct meaning and element paths to define k_{31} . Starting from a point of no stress or strain, the piezo element is either pulled in tension or compressed in a short

circuited manner, which causes it to strain and allows free charges to neutralize. Then the leads are disconnected and the material is relieved of stress resulting in charges collecting on the top and bottom electrode but also leaving a residual strain. A resistor is then used to shunt these charges allowing for neutralization and the relief of strain. Areas under each curve represent the energy density for each process.

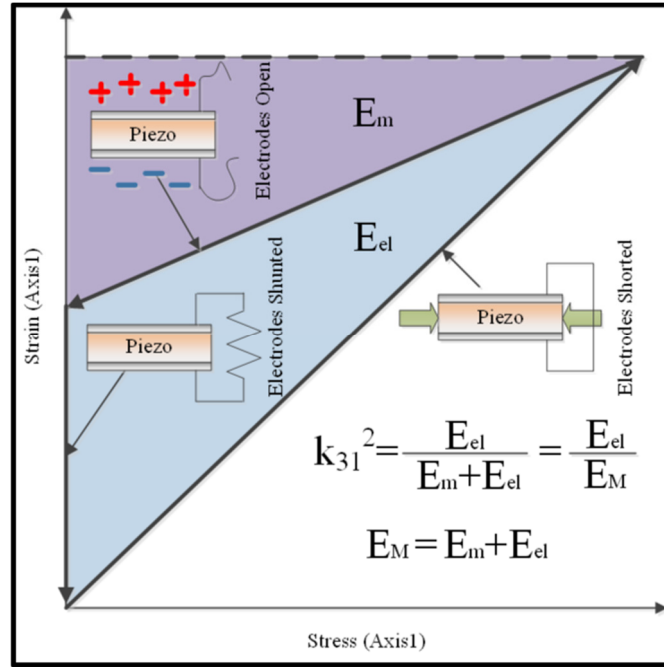


Figure 87. Definition of electromechanical coupling coefficient for a pure piezoelectric material using a thermodynamic cycle. Modified from [118].

To sum up the two coupling coefficient definitions for a pure piezoelectric element in a d_{31} setup, the equation for the electromechanical coupling coefficient is

$$\text{EMC } k_{31}^2 = \frac{E_{el}}{E_M} \quad \text{Eq 72.}$$

and the general electromechanical coupling coefficient is

$$\text{GEMC } K_{Coupling}^2 = \frac{E_{el}}{E_m} = \frac{k_{31}}{1-k_{31}} \quad \text{Eq 73.}$$

One important aspect to note about Eq 73 is that it only applies to a pure piezoelectric element. When a uni-morph or other structure which includes a non-piezoelectric material or material with differing k_{31} or s_{ij} coefficients then the value of the

GEMC will be much less than what is derived in Eq 73. Thus in this work, Eq 63 will be used to estimate the GEMC via a FEA modal analysis.

Once all of the parameters for the equivalent circuit in figure 86 are found, power values can be modeled in PSPICE as a function of frequency which can be compared to experimental data collected. PSPICE is a free program that has a multitude of functionality for electronic circuits and can be used as a model tool. Transient analyses can also be executed in PSPICE which opens the door to the possibility of a power analysis as a function of time or simply speaking, a devices response to a step or impulse input.

A simplified model that utilizes FEA packages like ANSYS requires only the dampening ratio to estimate “maximum” power generated for the device. This works by using a resistive element configured with a constant value R_{opt} , which is the optimum resistance. Without the dampening ratio, the optimum resistance is [162]

$$R_{opt} = \frac{1}{\omega_n C_p} \quad \text{Eq 74.}$$

where ω_n is the resonant frequency and C_p is the capacitance value of the piezoelectric material or, in other words, the amount of charge that can stay in the element. The value C_p is found from the simple capacitor formula in Eq 67. When dampening is present, Eq 74 becomes [123]

$$R_{opt} = \frac{1}{\omega_n C_p} \frac{2\zeta}{\sqrt{4\zeta^2 + k_{31}^4}} \quad \text{Eq 75.}$$

A harmonic analysis is done to determine maximum power generated as a function of driving frequency. This is accomplished by solving for the voltage generated on the electrodes for each frequency. Once this is known, the “maximum” power is simply

$$Power = \frac{V^2}{R_{opt}} \quad \text{Eq 76.}$$

Yang, *et al.* [154], compiled a multimode model that is more complex than method above but derives the admittance for an equivalent circuit model. This allows for the evaluation of circuit component values that can be incorporated into PSPICE for analysis various voltage input responses. The process still requires knowledge of the dampening ratio for an accurate prediction and is encompassed in the modal and harmonic FEA analysis. An outline of the method is shown below [154]

- Finite element static analysis to determine the static capacitances.
- Finite element modal analysis to determine the short-circuit resonance frequency of each vibration mode.
- Finite element harmonic analysis to obtain the charge response and then the admittance with a harmonic alternating voltage input. Identify the parameters for the admittance circles.
- Finite element harmonic analysis to obtain the charge response at each resonance, with base excitation applied, to determine the voltage input function (for PSPICE).
- Circuit modeling and simulation in the PSPICE software with the parameters identified from FEA to evaluate the performance of energy harvesters.

CHAPTER VIII

MACRO ENERGY HARVESTER CONCEPT AND DESIGN

A bi-stable switching energy harvester made from a buckled steel structure mounted with uni-axially poled piezoelectric polyvinylidene fluoride (PVDF) and 3D printed polylactic acid (PLA) components are constructed and tested. A data collection system and frequency sweeping program is built to drive the device using a custom compression rig fitted with an accelerometer. The energy harvester is tested with the center beam compressed to different degrees of buckling, as well in its unloaded state. Root mean square (RMS) accelerations are applied to the device in the range of 0.1 to 0.9g_{rms} by 0.2g steps. The device is driven with a frequency between 16 and 40Hz (by 0.5Hz) in both forwards and backwards sweeps. Finite element modeling program ANSYS is used to model the device and determine undamped pre-stressed modal frequencies, proof mass displacements to “snap-through”, and static buckled profiles for the center beam. As a comparison, a doubly constrained beam (DCB) with the same width and length is constructed and tested in the same manner as the torque arm (TA) device. RMS power density for the torque actuated device compressed by 0.13mm and frequency swept in reverse was 0.246μW/cm² (3.13μW) at 16.5Hz and 1.5g_{rms} using two 0.19g proof masses. The doubly constrained beam RMS power density swept in reverse was 1.287μW/cm² (6.18μW) at 59.5Hz and 1.5g_{rms} with a 1.38g proof mass.

A. Materials and Fabrication

The base layer of the TA actuated buckled beam energy harvesting device was fabricated from a 100μm thick stainless steel sheet (Precision Brand Carbon AISI/1008). Dimensions of the cut-out stainless steel section are in figure 89 a). An additional layer of polylactic acid (PLA) plastic was fabricated using a 3D printer to add stiffness to the torque

arms and overlapping center portion of the buckled beam, figure 89 b). Poly(lactic) acid, or PLA, is a thermoplastic polyester which is used in commercial and hobbyist 3D printing. The modulus of elasticity is around 1.7 to 3.6 GPa for directly extruded materials but can increase to 4.2 GPa with subsequent heat treatments [115] [107]. Information on the production and molecular structure of this polyester can be found in [82]. An industrial adhesive (JB-Weld Compound 8265-S) was used to bind the PLA layer to the bottom side of the stainless steel shim stock, figure 89 c). Simple proof masses consisting of 2-56 stainless steel hex nuts (0.19 g each) were then attached at the ends of the torque arms.

Four individual strips of a commercially purchased piezoelectric polymer of polyvinylidene fluoride (PVDF) were bound to the topside of the stainless steel using the same adhesive, as shown in figure 89 c) and d). PVDF is a ferroelectric material that, if processed correctly, can exhibit appreciable piezoelectric coefficients. While formed from a melt, PVDF usually will crystallize into the non-polar α phase which is undesirable for piezoelectric applications. The β phase of PVDF has the highest polarization potential of all the other phases and it is the most desirable in energy harvesting application. To promote the β phase from the other phases, the PVDF is drawn to about 300% of its original length while held at an elevated temperature. Gel deposition methods can also be used for MEMS scale fabrication but require polar solvents mixed in with dissolved PVDF solutions or specially catered processing parameters such as temperature, pressure, spin rates, etc. [102]. Molecular structures of the α and β phases are shown in figure 88 below. More information on the molecular chains of PVDF can be found in [130, 55, 35, 63, 45].

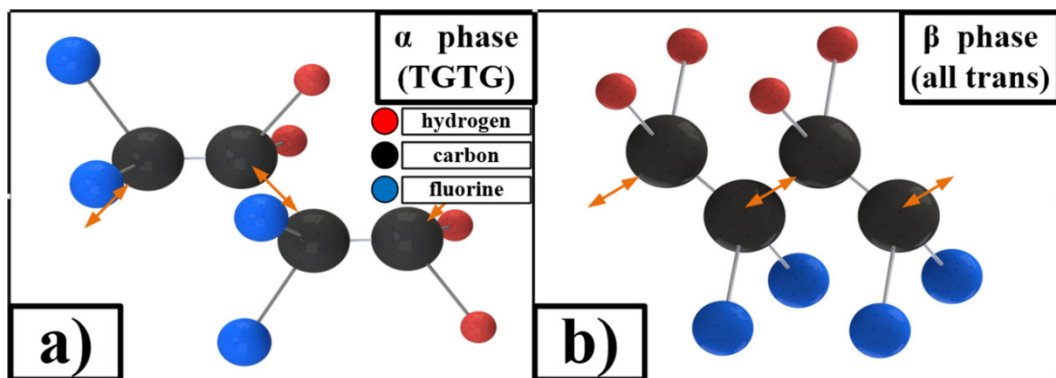


Figure 88. Molecular chain of PVDF in the a) non-polar α and b) polar β phase.

The aluminum metalized piezoelectric PVDF (GoodFellow FV301960/3, $d_{31}=19\text{pC/N}$, $d_{33}=-20\text{pC/N}$) strips were uni-axially oriented with the beam length and had a nominal thickness of $110\mu\text{m}$. Two PVDF strips were attached to the front and back sections of the center beam while the other two PVDF strips were each bonded to a separate torque arm. Silver epoxy (Circuit Works CW2400) was used to connect enameled 30 gauge copper wire to each of the PVDF strip electrodes. The final assembled structure is shown with the electrode labeling scheme figure 89 d).

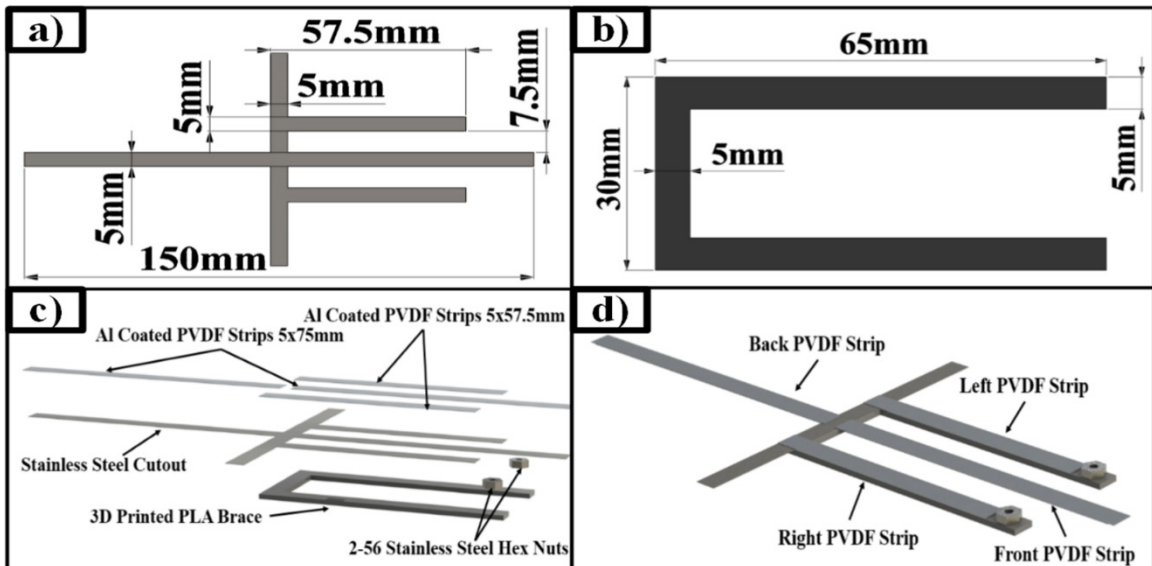


Figure 89. a) Stainless steel cutout dimensions, b) PLA planar dimensions, c) assembly exploded view, d) assembly collapsed view and associated PVDF beam section labeling scheme.

Critical to the operation of the bi-stable energy harvester is the constraint base, which provides adjustable levels of center beam compression and clamps the side arms pinning the center beam into the ‘S’ buckled mode shape. To provide feedback for the dynamic driving routines, a 3-axis accelerometer (MPU6050) was also attached near the centroid of the constraint base, figure 90 a). By adjusting the threaded rods within the constraint base, the compression of the center buckled beam could be controlled and locked. For this work three compressive loading cases were tested; uncompressed, 0.13 mm of compression, and 0.25 mm of compression. Under the latter two levels of

displacement constraint, the center buckled beam exhibited two dominant bi-stable buckled states. A visual of the device in the buckled up and down position is shown in figure 90 a) and b), respectively. This shows the bi-stability of the proposed device. Marks and symbols on the device are for digital image correlation.

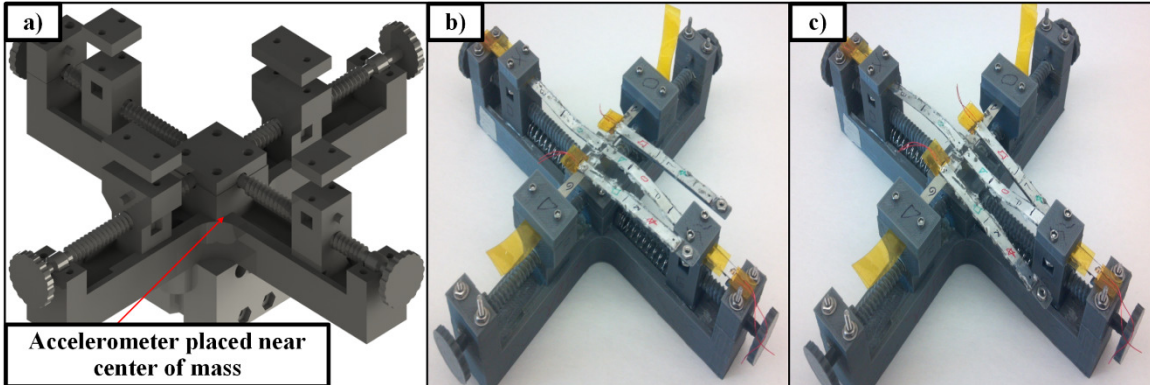


Figure 90. a) Base and clamping mechanisms to hold the device, b) device in buckled up state, and c) device in buckled down state.

To provide a quantitative comparison for the TA device performance, a single doubly constrained beam (DCB) device was also constructed and tested on the same shaker table setup. This simple device, consisted of only a single beam clamped at both ends and a proof mass placed at the midpoint of the beam. The beam length and width were kept the same as that used for the torque actuated model center beam (96mm and 5mm, respectively). Two PVDF strips were placed on the left and right side as to be consistent with the electrode placement of the previous device. A 10-32 nut weighing 1.38grams was adhered to the middle using thin Kapton tape.

B. Quasi-Static Behavior

Two experimental tests using quasi-static loading conditions were performed on the buckled energy harvester device. The first types of tests were simple load-deflection experiments to determine the effective stiffness response of the multi-layer structure, the results of which served as material parameters for later finite element modeling. The second set of quasi-static experimental tests probed the bi-stability switching conditions

for the buckled device. Both tests were performed using a specimen probe mounted on a 5 lb_f load cell (Sensotec Model 11) driven by a linear actuator stage.

Prior to rigging in the constraint base, the stacked layers of metalized PVDF/adhesive/stainless steel used for the center beam were clamped as a cantilever beam. The known stainless steel dimensions and parameters, table 16, were used to determine the material stiffness properties for the cured adhesive layer and the metalized PVDF, which were lumped and treated as a single layer (210 μm in thickness) for simplicity. The effective stiffness of the composite beam was determined through load deflection data and the classic beam end deflection

$$\delta_{tip} = \frac{FL^3}{3E_{eff}I_{eff}} \quad \text{Eq 77.}$$

where F is the force applied at the tip, L is the length of the cantilever beam, E_{eff} is the effective Young's Modulus of the composite beam, and I_{eff} is the effective moment of inertia for the composite beam cross section. From the experimental data the stiffness of the composite layer was estimated, the results of which are shown in table 16. A similar experiment was then performed on a PLA cantilever beam to determine the Young's Modulus of 3D printed PLA (JustPLA) with similar print characteristics.

Table 16. Material properties used in ANSYS analysis.

	Young's Modulus (GPa)	Poisson's Ratio	Density (kg/m ³)
AISI/1008	200	0.30	7872
PLA ¹	2.31 measured	0.30	1250
PVDF	2.66 measured ²	0.34	1760
J-B Weld	2.66 measured ²	0.30	1890

¹PLA present on torque arms only

²Measured as a composite with AISI/1008

The 2nd type of quasi-static experiment was performed on the entire energy harvesting device in its buckled configuration mounted within the constraint base. Tests were performed with the center beam under two different compression levels, 0.13mm and 0.25mm of axial displacement. At 0.13mm of compression, the center beam just began to exhibit bi-stable buckling behavior which meant that the energy well for this configuration

was the smallest that could be obtained. For 0.25mm of compression, the center beam was also bi-stable, but required a greater applied force to switch between stable buckled states, figure 91. The force and displacement required to induce switching between buckling stability states in each direction was determined by either pushing or pulling on the two proof masses simultaneously using a custom fixture connected to the same 5 lbf load cell and linear actuator stage as the previous experiments. The results of the quasi-static bi-stability switching tests are shown in table 17 below.

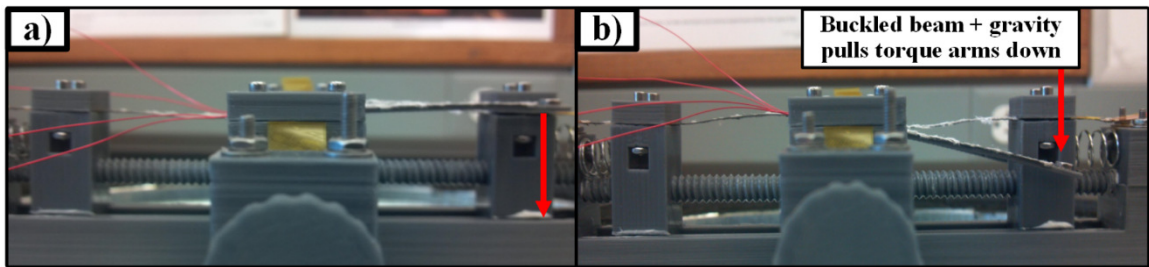


Figure 91. Side view of device in a bi-stable state a) buckled upwards and b) buckled downwards.

A finite element model of the buckled energy harvesting system was meshed using SHELL281 and MASS21 elements. Using the ANSYS simulation software, the buckled conditions were applied to discern the resting displacement profile, quasi-static stability switching displacements, and the pre-stressed undamped modal frequency of the structure. As shown in figure 92 a), the post-buckling displacement profile of the structure was determined for both stable states using an analysis which included the effects of gravitational forces. The displacement of the proof masses needed to induce switching between stable buckled states, or “snap-through”, was found from this FEA model. A plot of the typical load-displacement behavior to the snap-through load is shown in figure 92 b).

Table 17. Proof mass displacements from resting position required to induce stability state switching for both finite element analysis model and experimental tests.

Compression (mm)	FEA Disp. (mm)	Experimental Disp. (mm)	% Difference
0.13, push down	5.36	6.35	-18.50
0.25, push down	7.83	9.33	-19.12
0.13, push up	6.35	5.70	10.19
0.25, push up	8.71	10.28	-17.99

In addition to the buckled switching behavior, the static post-buckled profile of the beam found via the FEA model was compared with a 3-D experimental scan of the structure. The experimental buckled profile was measured by taking approximately 40 high resolution images of the structure from various angles and building a reconstruction of the specimen surface using software called 123D Catch. A comparison of the maximum and minimum out-of-plane displacements found for the buckled devices in their different configurations via both ANSYS and the experimental scan are included in table 18. A typical profile of the center buckled beam derived from ANSYS is shown in figure 92 c).

The ANSYS model results could also be used to determine the static axial strain state spatially throughout the center buckled beam. The results for the 0.25 mm compressed case, figure 92 d), show the location of strain sign change for the top (PVDF) surface. This information provides useful insights into electrode positioning to minimize charge neutralization.

Table 18. Maximum and minimum displacement points for FEA and experimental results.

Compression (mm)	ANSYS Simulation Results		Experimental Scan Measurements		% Back Ch. Difference	% Front Ch. Difference
	Back Ch. (mm)	Front Ch. (mm)	Back Ch. (mm)	Front Ch. (mm)		
0	0.04	-0.10	0.00	0.00	~	~
0.13, buckled up	-1.13	1.09	-1.35	1.26	-19.88	-15.31
0.25, buckled up	-1.56	1.53	-1.90	1.90	-21.63	-23.86
0.13, buckled down	1.09	-1.12	1.48	-0.97	-35.22	13.25
0.25, buckled down	1.53	-1.55	1.93	-1.85	-26.11	-19.27

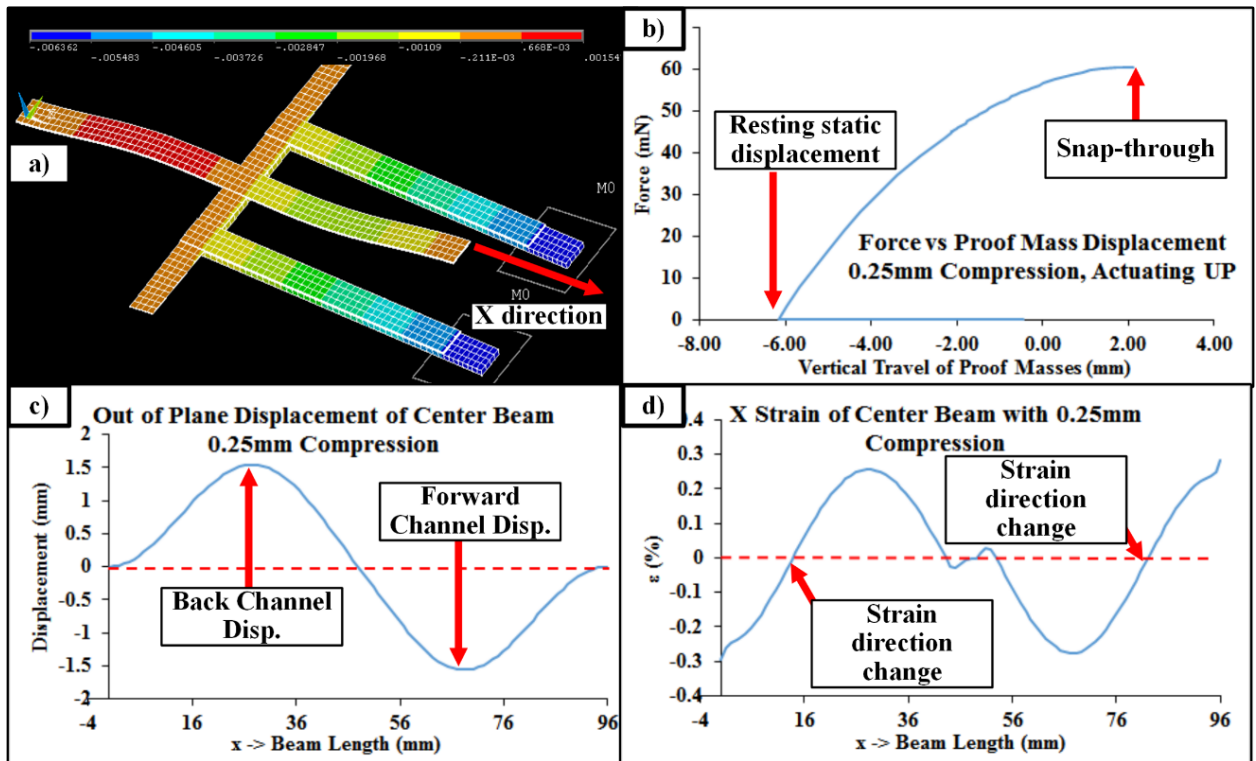


Figure 92. FEA model results for 0.25mm of center beam compression showing a) the mesh of the structure in the buckled "down" state, b) the vertical mass displacement through "snap-through", c) the center beam deflection profile, and d) the axial (x-direction) strain for the center beam.

C. Dynamic Behavior

The energy harvesting potential of the device was tested using a custom designed shaker system capable of both variable acceleration and frequency control. The shaker system consisted of an anchor platform mounted on a 42 watt speaker driven using an audio amplifier (Kinter MA-150) capable of delivering 30 watts of peak power. An Arduino Nano (V3.0) was used to read the accelerometer and send its value to a LabVIEW program. The LabVIEW program compared RMS acceleration values to a setpoint value and then adjusted input parameters for the proportional-integral-derivative (PID) controller so that the sine wave audio signal minimized the RMS acceleration input error. To perform constant acceleration sweeps, the LabVIEW program would adjust the frequency of the speaker while tuning the RMS value of the acceleration until an acceptable tolerance threshold was met ($< 2.5\%$). When this tolerance was met for a certain amount of time (~ 5 seconds), data was logged at that frequency and acceleration. Then the frequency was increased to the next increment and the stabilization process was repeated. During testing, the entire constraint base containing the buckled energy harvester device was mounted on the anchor platform and driven at various accelerations and frequencies.

All grounds (bottom portion) of the PVDF strips were connected together while the top portions of the four individual strips went to independent circuit inputs for logging. All four channels of the devices PVDF strips were fed into a unity gain amplifier (LM224) while driving a load of $3.3\text{ M}\Omega$. The output of this amplifier was then put into another op-amp (LM224) which converted a ± 10 volt signal to a 0-5 V which is utilized by the Arduino's 10 bit analog inputs. Calibration of the conversion circuit was done with an oscilloscope to verify that -10, 0, and 10 volts input produced 0, 2.5, and 5 volts output, respectively. The LabVIEW program along with the Arduino recorded the acceleration in the vertical direction and all four voltage channels at a frequency of 2,000 Hz.

Frequency sweeps at constant acceleration were performed on the uncompressed, 0.13mm compressed, and 0.25mm compressed beam configurations over the range of 16-40Hz using 0.5Hz increments, figure 93 and figure 94. From the experimental frequency sweeps, the natural frequency of the device was found and compared with the undamped natural frequencies found from the ANSYS models, table 19. Acceleration was controlled via a PID tuning method that modified the amplitude of the output audio signal. The

sweeps were performed at constant acceleration levels from 0.1 - 0.9g_{rms}, increasing by 0.2g increments. Though testing up to 1.5g_{rms} were performed on the 0.25mm compression case to evaluate the acceleration needed for bi-stable switching. The tolerance to determine acceptable acceleration to initiate data logging was 2.5% of the set point acceleration. Logged data included the acceleration of the rigid base structure with respect to time, the RMS value for the acceleration for ~1 second, the peak-peak value for the acceleration, an averaged peak-peak value for acceleration (2048 data points split into 10 sub arrays), and similar data for each voltage channel of the PVDF strips. After a forward (increasing) frequency run, a similar sweep of the setup was run in reverse (frequency descending from 40 to 16 Hz). All sweeps were run with the torque arms starting in the buckled down position, figure 91 b) and figure 90 c). When run in a compressed state, the device was actuated manually to ensure that it remained bi-stable both before and after each frequency sweep.

Table 19. Undamped FEA and experimental natural frequencies.

Compression (mm)	Mode 1, ANSYS, no damping (Hz)	Experimental Natural Frequency (Hz)						
		0.1g	0.3g	0.5g	0.7g	0.9g	Average (Hz)	% Diff
0	25.79	22.50	21.50	22.00	22.50	22.50	22.20	13.93
0.13, buckled up	24.48	19.50	19.00	18.50	18.00 ¹	17.75 ¹	19.00	22.37
0.13, buckled down	27.74				31.51			
0.25, buckled up	25.49	18.50	18.50	18.00	18.00	19.00	18.40	27.83
0.25, buckled down	27.89							34.01

¹bi-stable actuation, value reported is average of broadband frequency.

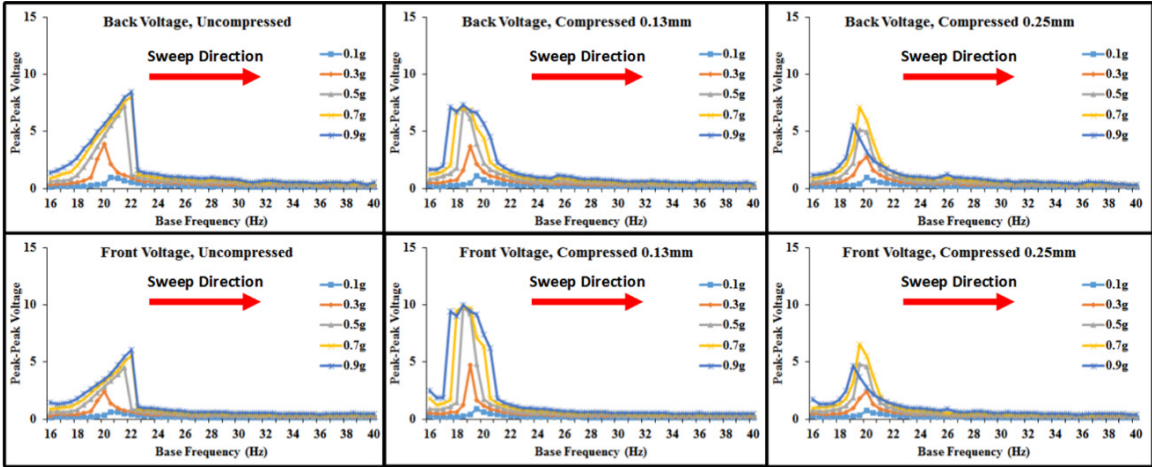


Figure 93. Peak-peak voltages for “forward” frequency sweeps of the “front” and “back” center beam PVDF sections under different constant RMS acceleration levels.

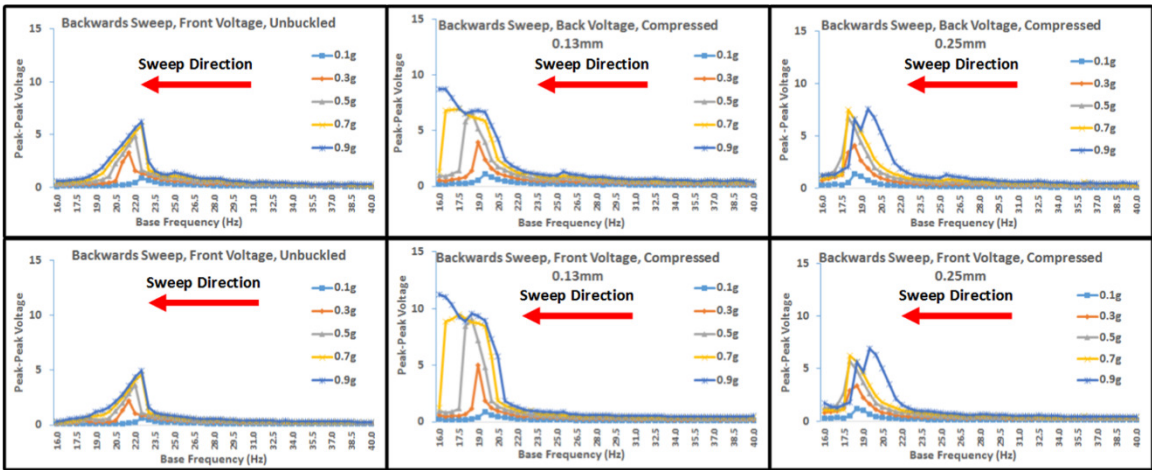


Figure 94. Peak-peak voltages for “backward” frequency sweeps of the “front” and “back” center beam PVDF sections at different constant RMS acceleration levels.

V_{rms} for all channels during $0.5g_{rms}$ and $0.9g_{rms}$ (before and after inter-well actuation threshold at 0.13mm compression level) are shown in figure 95 below. Snap-through was observed at about $0.7 g_{rms}$ for the 0.13mm compressed center beam state and about $1.3g_{rms}$ for the 0.25mm case. An observable benefit from the device at higher compression levels is the obvious reduction in operating frequency, which can be seen from figure 95. Once actuation between the two energy wells is reached, the operating frequency band is widened and the device can maintain high voltage operation as long as there is enough

energy in the system to continue snap-through actuation as the frequency is swept. The higher compression value causes the device to kick out of inter-well actuation because the stored energy during actuation is not enough to cause snap-through to perpetuate as the frequency meanders out of the resonance range. To widen the frequency band at this compression level, higher accelerations would have to be used. For all loading cases, the output from the torque arm PVDF strips (right and left channels) was comparatively low due to the higher structure stiffness provided by the thick PLA brace.

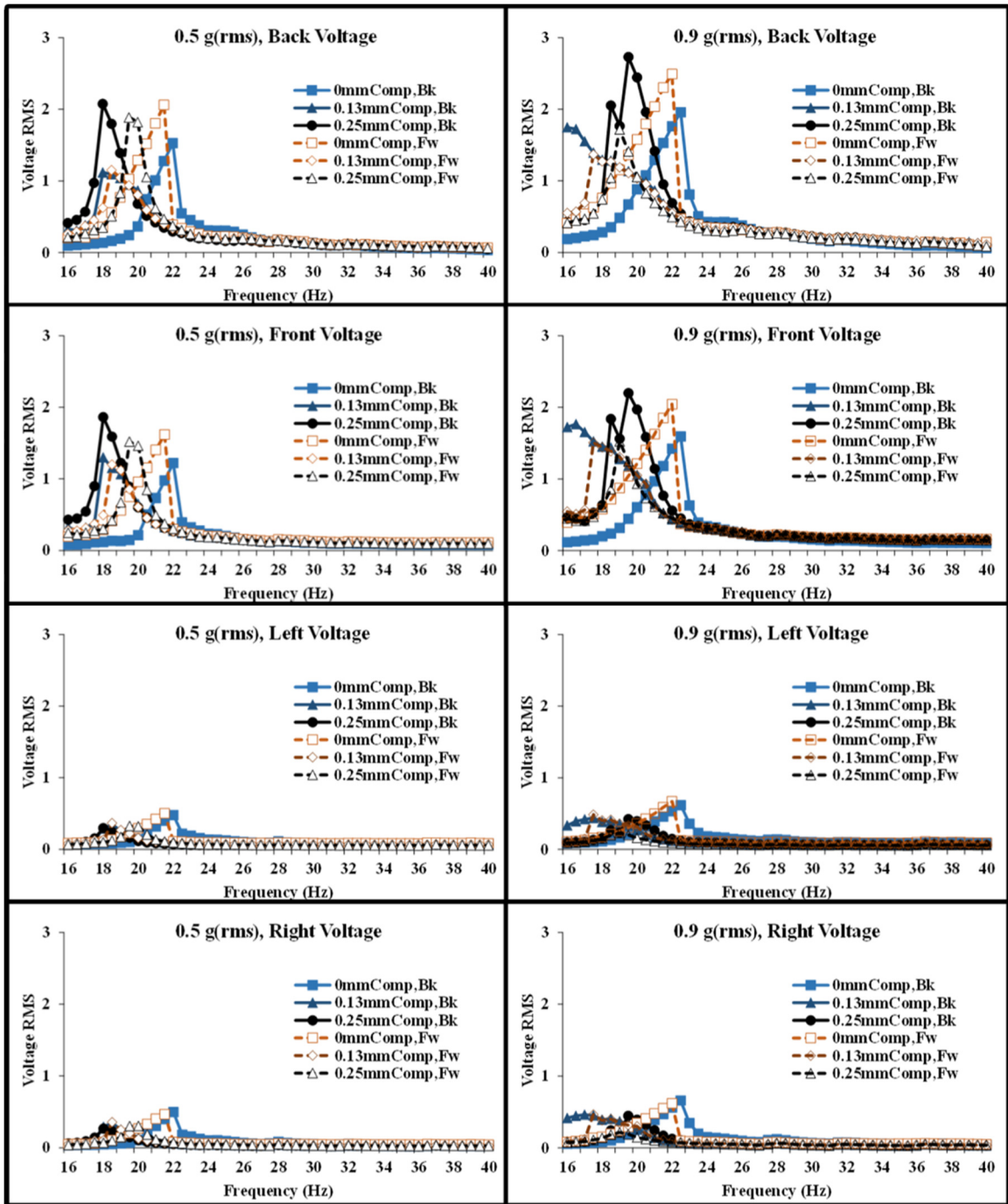


Figure 95. V_{rms} device output values for backward and forward sweeps of all channels at driving accelerations of 0.5 and 0.9 g_{rms} .

Time variant graphs of the acceleration and voltage for all four PVDF channels are shown in figure 96 below. The frequencies for each sub graph are picked to correspond to the highest RMS voltage in the back channel during a backwards sweep and a set point

acceleration of 0.5 and 0.9g_{rms}. From figure 96 it is seen that the front channel voltage (center beam part opposite the torque arm placement) is mostly 180° out of phase with the other channels. Given a little bit of compression, figure 96 c) and d), the device exhibits snap-through if the base acceleration is high enough. This causes higher frequency voltage content to appear in all of the channels post inter-well actuation. It also causes very high V_{p-p} as shown in figure 96 c) and d). The accelerometer mounted in constraint base detects reaction forces due to the bi-stability switching, which can also be seen in figure 96 c) and d).

It was also observed in preliminary experiments involving a single impulse acceleration applied over a baseline low-level acceleration that snap-through actuation could be induced and maintained, even when the baseline acceleration level was below the typical threshold to induce bi-stable switching. This is a similar effect to that seen in [44] and [91] where a perturbation or impulse could force the system into high energy orbits and allow it to output more power given the same vibrational power input. This behavior is desirable for chaotic vibration loading characteristics found for many real-life energy harvesting operating conditions.

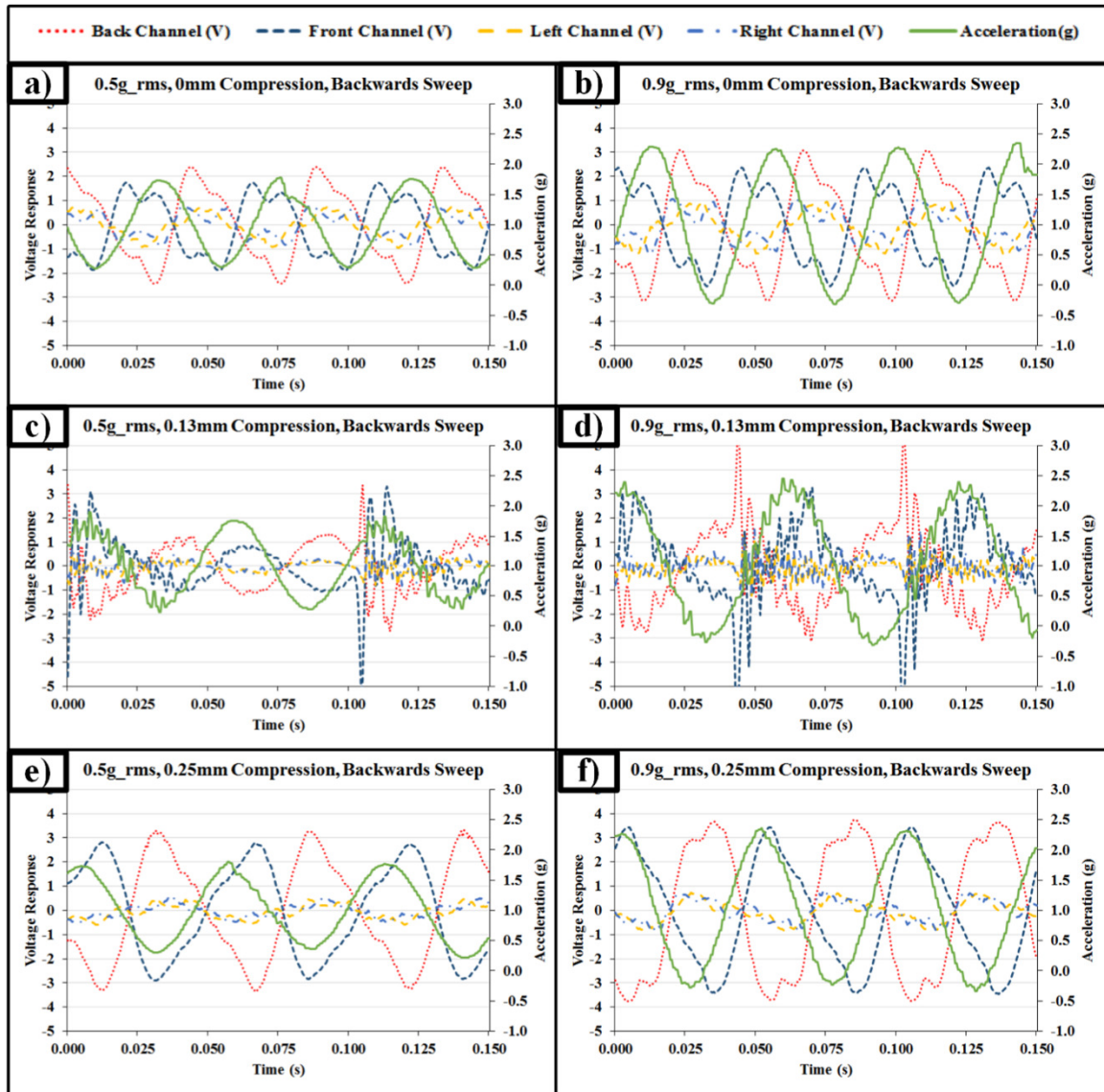


Figure 96. Time variant results at frequencies corresponding to the maximum back channel RMS voltage during backwards sweeps on the uncompressed beam at a) $0.5g_{\text{rms}}$ and b) $0.9g_{\text{rms}}$; the 0.13mm compressed beam at c) $0.5g_{\text{rms}}$ and d) $0.9g_{\text{rms}}$; and the 0.25mm compressed beam at e) $0.5g_{\text{rms}}$ and f) $0.9g_{\text{rms}}$.

The doubly constrained device, shown in figure 10a, was driven from 20 to 80 Hz by 0.5 Hz increments using accelerations similar as those used for the previous tests. Afterward testing the uncompressed state, the device was buckled until it was just bi-stable at 0.73mm of axial compression. Again the device was driven with a sinusoidal signal in the range of 20 to 80 Hz forwards and then backwards in frequency. Total RMS power

results from the compressed forward and reverse sweeps shown in figure 97 b) and figure 97 c). The setup for the doubly constrained beam was heavily biased in the buckled down position due to the weight of the proof mass. In the acceleration ranges tested, bi-stable snap-through did not occur continuously.

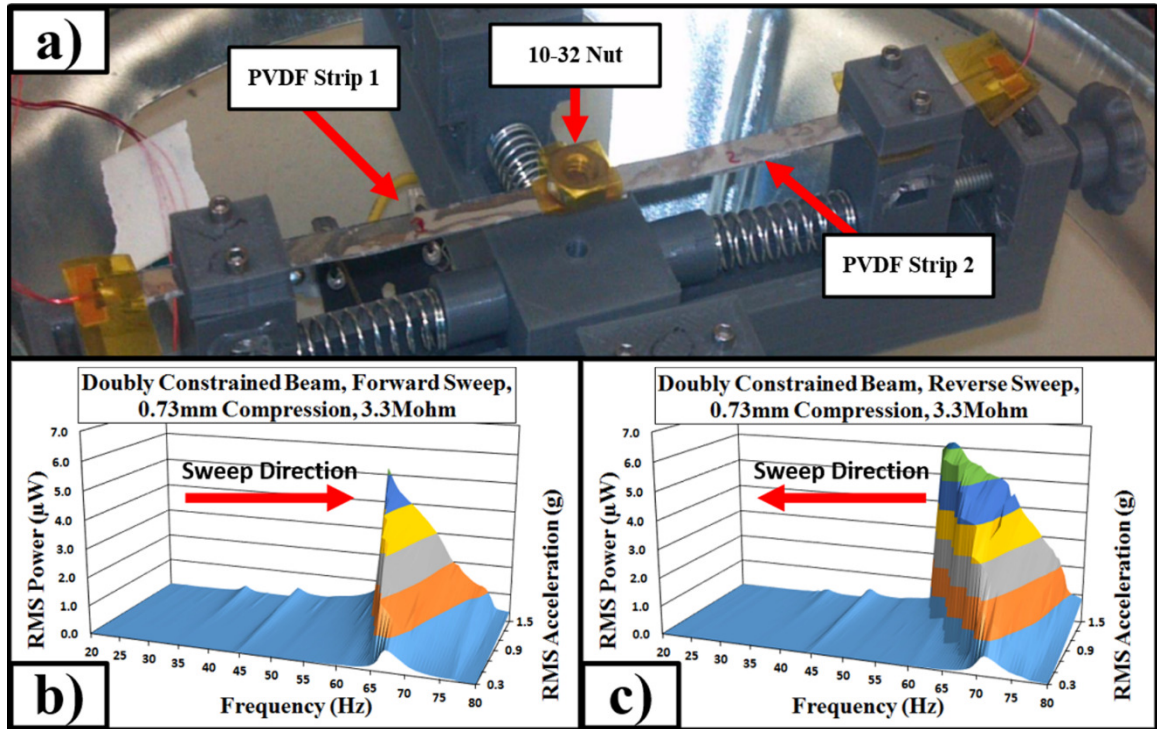


Figure 97. Doubly constrained beam in the unbuckled state a), and RMS power results from b) a forward sweep, and c) a backwards sweep.

A comparison of the power output results from the dynamic experiments is shown in table 20. The full-width half-max (FWHM) measurements are used to quantify the range of usability in the frequency spectrum. Peak power is calculated by taking the absolute maximum voltage generated during a frequency sweep at a given RMS acceleration and converting it to power using the 3.3Mohm load. Area used to construct the device was the factor governing power density. For the doubly constrained beam, it was simply the length multiplied by the width which came out to be 4.8cm^2 . The TA device required more space, 12.75cm^2 , for the elaborate geometry needed to transfer torque and create a pseudo pin. If the entire rectangular area was used to calculate power density, then a value of 58.56cm^2 should be used in the calculation of power density. FWHM measurements for the buckled

TA device could not be fully measured in some cases due to the operation of the device falling below the 16Hz limit of the shaker system. Below 16Hz the sinusoidal wave from the accelerometer begins to indicate distortions from the speaker. Thus the FWHM of these devices are almost certainly greater than indicated in table 20.

Table 20. Power comparison of the TA device and DBC.

	RMS Accel (g)	Resonance Freq RMS (Hz)	Peak RMS Power (μ W)	FWHM RMS Power (Hz)	Resonance Freq Vpp (Hz)	Peak Power (μ W)	FWHM Peak Power (Hz)	RMS Power Density, DevArea (μ W/cm ²)
DCB, 0mm Comp, Forward Sweep	0.7	61.5	0.45	4.76	61.5	1.29	4.16	0.094
	1.1	63.5	0.63	6.62	63.5	1.94	5.55	0.132
	1.5	68.0	1.71	5.02	68.0	6.42	4.35	0.356
DCB, 0.73mm Comp, Forward Sweep	0.7	64.0	2.75	5.44	64.0	6.08	5.46	0.572
	1.1	61.5	3.98	7.71	61.5	8.88	7.84	0.828
	1.5	59.5	5.24	9.73	59.5	14.99	8.03	1.091
DCB, 0.73mm Comp, Reverse Sweep	0.7	66.5	3.21	6.20	66.5	7.35	6.28	0.668
	1.1	62.5	4.85	11.33	62.0	10.94	11.72	1.010
	1.5	58.5	6.18	16.63	58.0	16.47	15.11	1.287
TA, 0mm Comp, Forward Sweep	0.7	22.0	2.98	1.70	18.0	7.43	1.30	0.233
	1.1	24.0	7.95	2.07	18.5	6.68	1.32	0.624
	1.5	24.5	10.09	2.36	18.0	24.64	1.98	0.791
TA, 0.13mm Comp, Forward Sweep	0.7	18.0	1.18	2.26	18.5	11.91	1.88	0.093
	1.1	17.0	2.04	2.70	17.0	17.58	3.51	0.160
	1.5	16.5	3.13	2.24+	16.5	26.35	1.95+	0.246
TA, 0.13mm Comp, Reverse Sweep	0.7	17.5	1.35	3.46	17.5	11.52	3.54	0.106
	1.1	17.0	2.13	3.45+	17.0	17.84	4.28+	0.167
	1.5	16.5	2.65	3.45+	17.5	26.70	1.94+	0.208

+ indicates that actual value may be greater due to limited frequency range tested

D. Experimental Discussion

The difference in mass displacement required to switch between bi-stable states, shown in table 17, can be attributed to imperfections in the constructed device. The device fabrication process involved cutting the steel using shearing forces, which could potentially leave residual stresses near these edges. The FEA models do not account for these effects, though the overall influence should be minimized due to the constraint on the thin steel layer provided by the PLA brace and the compression rig.

Another insight provided by the FEA model was the strain profile for the topside PVDF layers. Ideally, to minimize potential charge neutralization, the PVDF strips should be placed further in on the center beam starting at about 1/6th of the center beams constrained length and terminating at the center point. Our setup had the strips epoxied the full half length of the constrained beam; thus there will be charge neutralization due to

opposing strain. Future iterations will have four channels for the center beam and two for the outer torque arms. From figure 92 d), it is evident some charge neutralization will be occurring given our current electrode placement. Correction of this issue should only improve the device power output.

It should also be noted that the device in its unbuckled state generated large voltages at higher frequencies when compared to the buckled cases. Even uncompressed the device shows “hard” non-linear behavior and, eventually, “soft” non-linear behavior after the beam is compressed [162]. During the onset of a bi-stable compression (~0.13 mm) the device is actuated between states at low g levels and exhibits a wide frequency response range compared to the other configurations at the same g level. Lower compression levels allow the device to traverse between energy wells quite easily. Only a relatively small amount of energy is needed to “push” the device over the energy well even when the operation frequency is meandering past the natural frequency. At the 0.25 mm compressed state, the g level needed to onset a bi-stable actuation is much higher and the broadening effect is realized at higher g ranges such as 1.3 to 1.5 g_{rms} (not shown). This higher compression level gives impressive V_{p-p} but near the voltage limits of the constructed DAQ. Even more interesting is amount of energy needed to continue bi-stable oscillation in the 0.25 mm compressed state. If the device is perturbed in such a way during bi-stable actuation as to diminish energy in the system (post resonance), then the system will kick out of bi-stable oscillation and enter the mono-stable oscillation state. Conversely, if the system is near resonance in the mono-stable state and is perturbed (say, by a static spike applied in the audio line), the device will enter the bi-stable mode and often remains that way until the system goes out of the resonance region or is perturbed negatively as to diminish the systems overall energy. The higher compression level, 0.25 mm, allows the observer to see this behavior much more easily than the 0.13 mm state during large device oscillations.

Post-interwell actuation generates higher frequency content in the voltage signal as shown in figure 96 c) and d). Utilization of sub-harmonics has been seen in [88] to harvest energy off of lower frequencies for a bi-stable buckled harvester. The super harmonics seen in the present device post-actuation could lead to better performance given the right

conditions like ambient vibrations that match these sub/super harmonics to assist maintaining high energy orbits.

Comparison of the TA device to the DCB is difficult because the actuation mechanisms are very different. Ultimately it was decided to keep the beam length and width the same for the DCB but using the same mass value pushed the device into a higher frequency range ($>100\text{Hz}$). The larger 1.38 g mass was selected to help push the frequency down to the $\sim 60\text{Hz}$ region where it would be more comparable to the TA device. The DCB did provide more power than the torque arm device, but the resonance frequency was almost three times higher. When the DCB was compressed until just bi-stable the RMS power output, peak power, increased but the operating frequency decreased. Compression of the TA device tended to decrease the RMS power output and operating frequency of the entire device but increased the peak power generated. Both the TA and DCB seemed to favor reverse sweeps in generating the most power.

Two favorable outcomes from these experiments are low operating frequency of the TA device compared to the DCB and the increased peak power generation. Also, if high energy orbitals can be maintained then a frequency broadening effect for the TA device can be realized in the V_{pp} data as shown in figure 93 and figure 94. It is important to note that the load impedance used in these experiments are not optimal. In future iterations, an optimal load circuit using a digital pot will be created so that fast resistance and short band frequency sweeps can be used to target the driving load impedance.

Indeed, buckling tended to broaden the operating bandwidth of the devices. Even though the confirmation of frequency broadening on the TA device could not be realized at higher accelerations, it is evident from the voltage graphs that the peaks become broader as acceleration is increased. A solution to determine this for the TA device would be to remove the masses and drive it at much higher accelerations using a more powerful shaker table. Other improvements include replacing the PVDF strips with a more efficient piezoelectric material such as PZT or aluminum nitride.

E. ANSYS Non-linear Harmonic Analysis

ANSYS typically linearizes all loads in its own built-in harmonic analysis. This is a problem when evaluating a bi-stable device's performance to varying frequency inputs. Thus the only way to attempt a non-linear harmonic analysis is to run a transient module with a modified sinusoidal displacement input. This displacement amplitude must be tailored to the frequency so that it emulates a constant acceleration input. A shell model of the 3x1 mm macro device with 8mm long compliance arms, figure 98, was constructed using the multilayer method and two point masses.

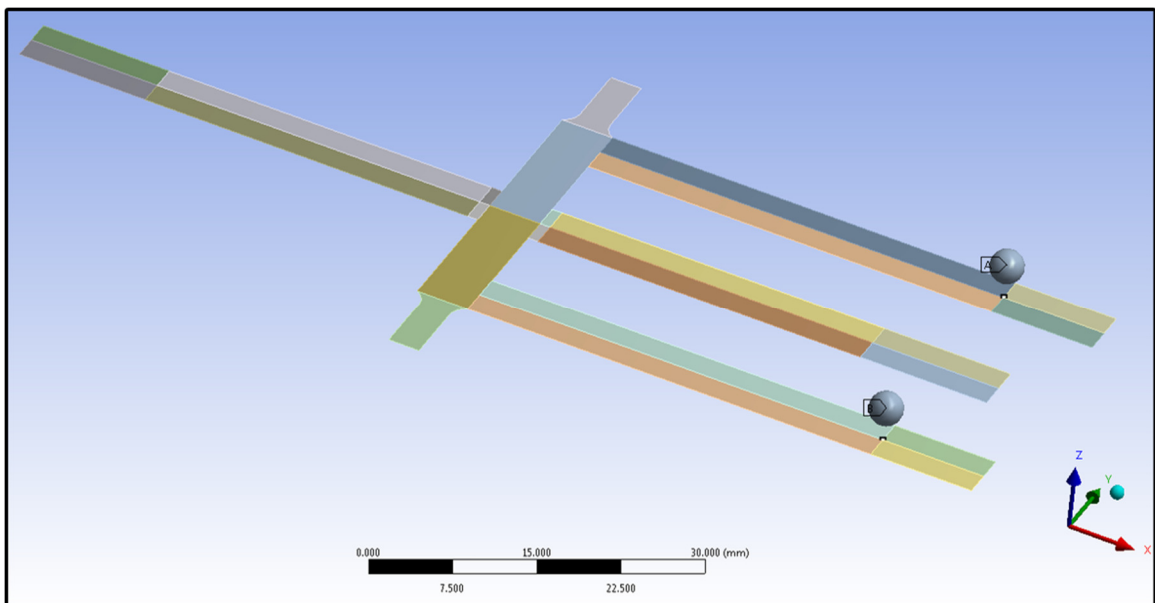


Figure 98. Point masses and areas for ANSYS non-linear harmonic sweep.

Meshing was done on the model with refinements and locations deemed to have larger stress gradients. Mid-side nodes were kept so that accuracy would be improved in this large displacement analysis. The mesh is shown in figure 99 below. In this model the effect of the PVDF strips are input as 0.11 mm thick layers on top of the steel with the assumption of perfect bonding. It is assumed that the effect of adhesives is minimal on the response of the structure.

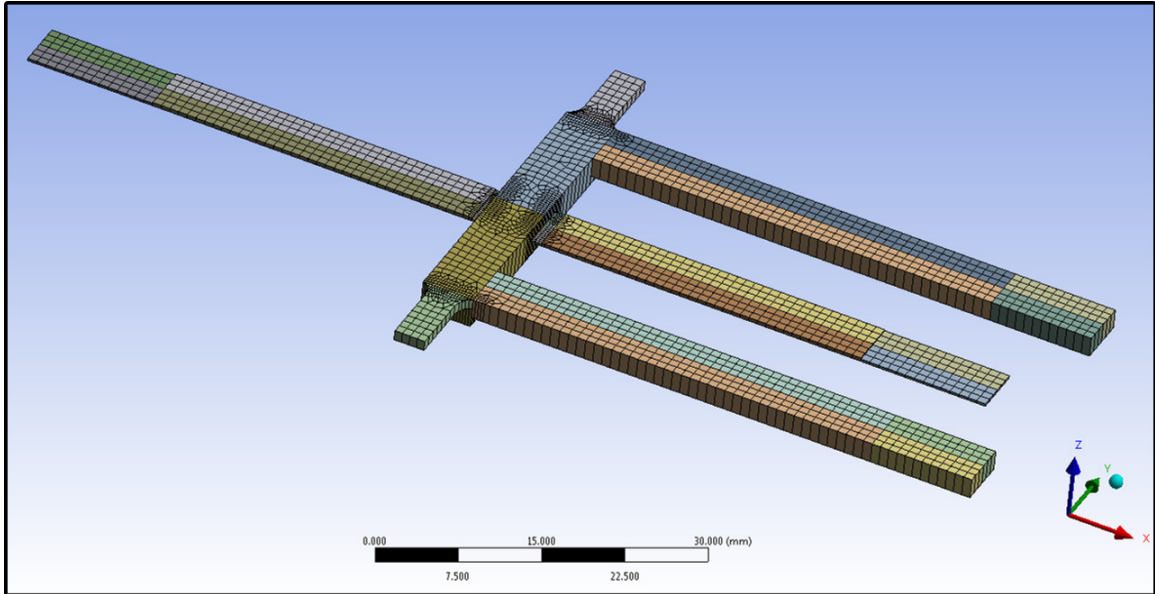


Figure 99. Mesh for ANSYS non-linear harmonic sweep.

Constraints and loading inputs for the model before applying the constant acceleration sweep is shown in figure 100 below. Preparing the device with a buckling stress is done in three steps. The first step applies the 1 g standard load and a slight perturbing pressure that gives the model a non-symmetric profile allowing the second step (displacement compression) to buckle the device with a 0.1 mm total compression. After buckling the device is relieved of the perturbing pressure during the third step and is ready for the displacement input which emulates a constant acceleration sweep.

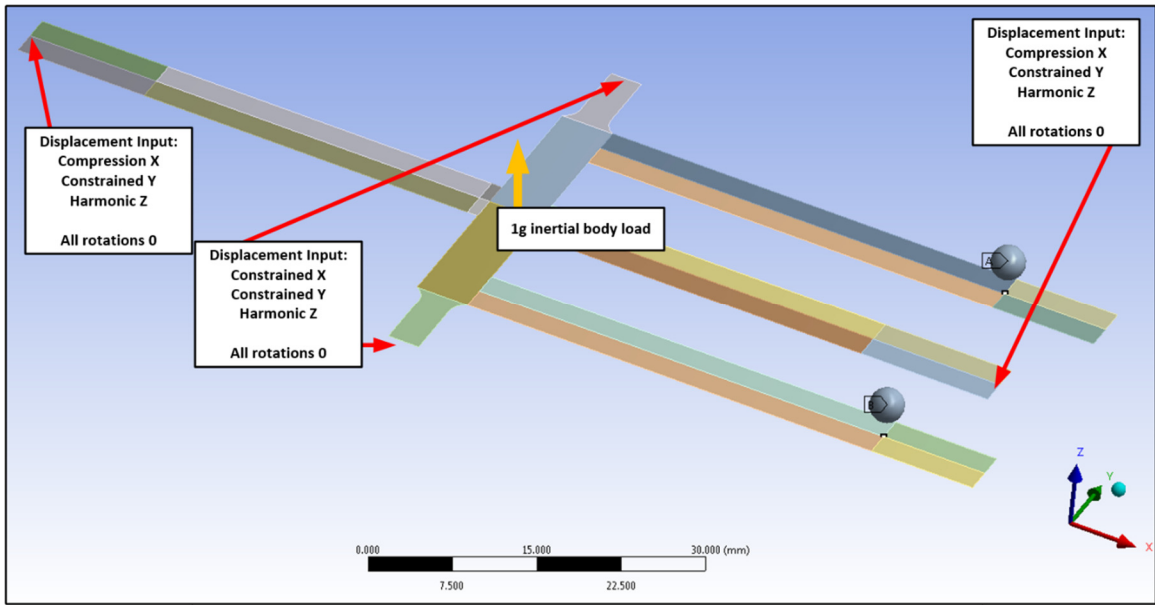


Figure 100. Loading conditions for a non-linear sweep in ANSYS.

ANSYS analysis settings for the non-linear harmonic sweep are shown in figure 101 below. Prepping each run with a compression before applying an input load took about 20 minutes on a 3.5 GHz i7-4770K with 16 GB of RAM. This is a small amount of time compared to the 4th load step which contained around 5000 sub-steps and may or may not run into a bifurcation which causes the model to snap-through to a more energy favorable state.

Analysis Settings				
Properties	Step 1	Step 2	Step 3	Step 4
Step Controls				
Step End Time	1.	2.	3.	8.
Auto Time Stepping	On	On	On	On
Define By	Substeps	Substeps	Substeps	Time
Carry Over Time Step	N/A	Off	Off	Off
Initial Substeps	100	100	100	N/A
Minimum Substeps	50	50	50	N/A
Maximum Substeps	200	200	200	N/A
Initial Time Step	N/A	N/A	N/A	1.e-003
Minimum Time Step	N/A	N/A	N/A	1.e-005
Maximum Time Step	N/A	N/A	N/A	1.e-003
Time Integration	Off	Off	Off	On
Nonlinear Controls				
Force Convergence	On	On	On	On
--Value	Calculated by solver	Calculated by solver	Calculated by solver	Calculated by solver
--Tolerance	5.e-003	5.e-003	5.e-003	5.e-003
--Minimum Reference	1.e-002	1.e-002	1.e-002	1.e-002
Moment Convergence	On	On	On	On
--Value	Calculated by solver	Calculated by solver	Calculated by solver	Calculated by solver
--Tolerance	5.e-003	5.e-003	5.e-003	5.e-003
--Minimum Reference	10.	10.	10.	10.
Displacement Convergence	On	On	On	On
--Value	Calculated by solver	Calculated by solver	Calculated by solver	Calculated by solver
--Tolerance	5.e-003	5.e-003	5.e-003	5.e-003
--Minimum Reference	0.	0.	0.	0.
Rotation Convergence	On	On	On	On
--Value	Calculated by solver	Calculated by solver	Calculated by solver	Calculated by solver
--Tolerance	5.e-003	5.e-003	5.e-003	5.e-003
--Minimum Reference	0.	0.	0.	0.
Line Search	Program Controlled	Program Controlled	Program Controlled	Program Controlled
Stabilization	Off	Off	Off	Off
Output Controls				
Stress	Yes	Yes	Yes	Yes
Strain	Yes	Yes	Yes	Yes
Nodal Forces	Yes	Yes	Yes	Yes
Contact Miscellaneous	Yes	Yes	Yes	Yes
General Miscellaneous	Yes	Yes	Yes	Yes
Store Results At	All Time Points	All Time Points	All Time Points	All Time Points

Figure 101. ANSYS settings for the non-linear sweep.

The damping ratio for this non-linear harmonic analysis is assumed to be 5% at 20 Hz for this analysis which comes from (the second journal article). Rayleigh damping is used in ANSYS and is modeled using

$$\zeta(\omega) = \frac{\alpha}{2\omega_i} + \frac{\beta\omega_i}{2} \quad \text{Eq 78.}$$

where ζ is the damping ratio as a function of angular frequency, α is the mass coefficient, β is the stiffness coefficient, and ω_i is the angular frequency of the modal response i . A limitation of the damping experiments is that we could only excite and measure the first mode amplitude gain thus for the non-linear harmonic analysis we assume that the higher modes are extremely damped using $\alpha=0$. If we assume $\zeta=0.05$ (or 5%) at 20 Hz then the stiffness coefficient β becomes about $7.957e-4$.

In ANSYS the transient governing dynamic analysis system is primarily

$$[M]\{\ddot{u}\} + [C]\{\dot{u}\} + [K]\{u\} = \{F\} \quad \text{Eq 79.}$$

where $[M]$ is the mass matrix, $[C]$ is the damping matrix, $[K]$ is the stiffness matrix, $\{\ddot{u}\}$ is the nodal acceleration, $\{\dot{u}\}$ is the nodal velocity, $\{u\}$ is the nodal displacement, and $\{F\}$ is

the load vector. Material properties and geometries set $[M]$ and $[K]$ but the matrix $[C]$ is set using proportional constants α and β from Eq 78. Damping is used via the damping matrix

$$[C] = \alpha[M] + \beta[K] \quad \text{Eq 80.}$$

which, in ANSYS, can be entered by simply applying α and β ; or stiffness damping can be applied by inputting a damping ratio and a frequency.

A Microsoft Excel spreadsheet was used to create a displacement profile with a continuous frequency sweep and constant acceleration. For a non-accelerating sinusoidal function and its integrals

$$Accel(t)_{\alpha=0} = A \sin(\theta(t)) \quad \text{Eq 81.}$$

$$Vel(t)_{\alpha=0} = Accel(t) = \frac{-A}{\omega} \cos(\omega t) \quad \text{Eq 82.}$$

$$Disp(t)_{\alpha=0} = Vel(t) = \frac{-A}{\omega^2} \sin(\omega t) \quad \text{Eq 83.}$$

where A is the amplitude of acceleration and is related to the g_{rms} value quoted throughout this dissertation by

$$A = 9.807 \left(\frac{g_{rms}}{0.707} \right) \text{ units } \left(\frac{m}{s^2} \right) \quad \text{Eq 84.}$$

The important part of Eq 83 is the overall amplitude $\frac{A}{\omega^2}$ which will be used to modify the varying frequency sine wave. If the frequency is to vary linearly then the time dependent equation for angular acceleration should look like

$$\alpha(t) = B \quad \text{Eq 85.}$$

where B and the angular velocity becomes

$$\omega(t) = B t + \omega_0 \quad \text{Eq 86.}$$

where ω_0 is the starting frequency. Given a total time run period of t_n and an ending frequency of ω_n , we can back out B and solve for our time dependent angular frequency

$$\omega(t) = \left(\frac{\omega_n - \omega_0}{t_n} \right) t + \omega_0 \quad \text{Eq 87.}$$

Integrating once more gives the angular displacement as a function of time which is

$$\theta(t) = \frac{1}{2} \left(\frac{\omega_n - \omega_0}{t_n} \right) t^2 + \omega_0 t \quad \text{Eq 88.}$$

Combining Eq 88 and the amplitude derived from Eq 83 will derive the constant acceleration, linearly varying frequency, sine function

$$Disp(t)_{Excel} = \frac{A}{\left(\left(\frac{\omega_n - \omega_0}{t_n}\right)t + \omega_0\right)^2} \sin\left(\frac{1}{2}\left(\frac{\omega_n - \omega_0}{t_n}\right)t^2 + \omega_0 t\right) \quad \text{Eq 89.}$$

which is used to generate inputs for a non-linear constant acceleration harmonic sweep in ANSYS and is easily checked by taking two derivatives using the finite difference method. Another check is to actually integrate the equation

$$Accel(t)_{\alpha=const} = A \sin(\theta(t)) \quad \text{Eq 90.}$$

assuming that α is constant which is actually more difficult than it would seem. Replacing $\theta(t)$ with Eq 88 gives

$$Accel(t)_{\alpha=const} = A \sin\left(\frac{1}{2}\left(\frac{\omega_n - \omega_0}{t_n}\right)t^2 + \omega_0 t\right) \quad \text{Eq 91.}$$

which, when integrated, requires the Fresnel function and has the solutions from Maple shown in figure 102 below. The trick to actually getting a tangible solution is to offset each solution by its average before integrating again. Code from Maple that derives and solves the constant acceleration, linear frequency, sinusoidal sweep is shown in the Appendix (CODE).

$\text{Acceleration}(t) = -\text{Amp} \sin\left(\frac{1}{2} \frac{(\omega_n - \omega_0) t^2}{t_n} - \omega_0 t\right)$
$\text{Velocity}(t) = \frac{\text{Amp} \sqrt{\pi} \cos\left(\frac{1}{2} \frac{\omega_0^2 t_n}{-\omega_n + \omega_0}\right) \text{FresnelC}\left(\frac{1}{\sqrt{\pi}} \sqrt{\frac{-\omega_n + \omega_0}{t_n}}\right) - \sin\left(\frac{1}{2} \frac{t(-\omega_n + \omega_0)}{t_n} - \frac{1}{2} \frac{\omega_0 t}{t_n}\right) \text{FresnelC}\left(\frac{1}{\sqrt{\pi}} \sqrt{\frac{-\omega_n + \omega_0}{t_n}}\right)}{\sqrt{\frac{-\omega_n + \omega_0}{t_n}}}$
$\text{Displacement}(t) = \frac{1}{\sqrt{\frac{-\omega_n + \omega_0}{t_n}}} \left[\frac{\text{Amp} \sqrt{\pi} \cos\left(\frac{1}{2} \frac{\omega_0^2 t_n}{-\omega_n + \omega_0}\right) \text{FresnelS}\left(\frac{1}{\sqrt{\pi}} \sqrt{\frac{-\omega_n + \omega_0}{t_n}}\right) - \cos\left(\frac{1}{2} \frac{t(-\omega_n + \omega_0)}{t_n} - \frac{1}{2} \frac{\omega_0 t}{t_n}\right) \text{FresnelS}\left(\frac{1}{\sqrt{\pi}} \sqrt{\frac{-\omega_n + \omega_0}{t_n}}\right)}{\sqrt{\frac{-\omega_n + \omega_0}{t_n}}} \right] + \frac{\cos\left(\frac{1}{2} \frac{\omega_0^2 t_n}{-\omega_n + \omega_0}\right) \text{FresnelC}\left(\frac{1}{\sqrt{\pi}} \sqrt{\frac{-\omega_n + \omega_0}{t_n}}\right) - \sin\left(\frac{1}{2} \frac{t(-\omega_n + \omega_0)}{t_n} - \frac{1}{2} \frac{\omega_0 t}{t_n}\right) \text{FresnelC}\left(\frac{1}{\sqrt{\pi}} \sqrt{\frac{-\omega_n + \omega_0}{t_n}}\right)}{\sqrt{\frac{-\omega_n + \omega_0}{t_n}}} + \frac{\sin\left(\frac{1}{2} \frac{t(-\omega_n + \omega_0)}{t_n} - \frac{1}{2} \frac{\omega_0 t}{t_n}\right) \text{FresnelS}\left(\frac{1}{\sqrt{\pi}} \sqrt{\frac{-\omega_n + \omega_0}{t_n}}\right) - \cos\left(\frac{1}{2} \frac{t(-\omega_n + \omega_0)}{t_n} - \frac{1}{2} \frac{\omega_0 t}{t_n}\right) \text{FresnelC}\left(\frac{1}{\sqrt{\pi}} \sqrt{\frac{-\omega_n + \omega_0}{t_n}}\right)}{\sqrt{\frac{-\omega_n + \omega_0}{t_n}}} - \frac{\omega_0}{\sqrt{\pi}} \left(\frac{(-\omega_n + \omega_0) t}{\sqrt{\frac{-\omega_n + \omega_0}{t_n}}} - \frac{\omega_0}{\sqrt{\pi}} \right)$

Figure 102. Maple solutions for a constant acceleration, linear frequency, sinusoidal sweep involving use of the Fresnel function.

By using Eq 89, a displacement profile is generated from 10 to 30 Hz or 30 to 10 Hz with a constant acceleration. This profile is shown in figure 103 below for the forward and reverse sweeps that are imported into ANSYS with a time step of 0.001 seconds. Comparing Eq 89 to the true solution shown in shows that there is a 2.5% max difference

at the beginning of the sweep which increases to about 12% at the end. The sweep comparison is shown in figure 104 below.

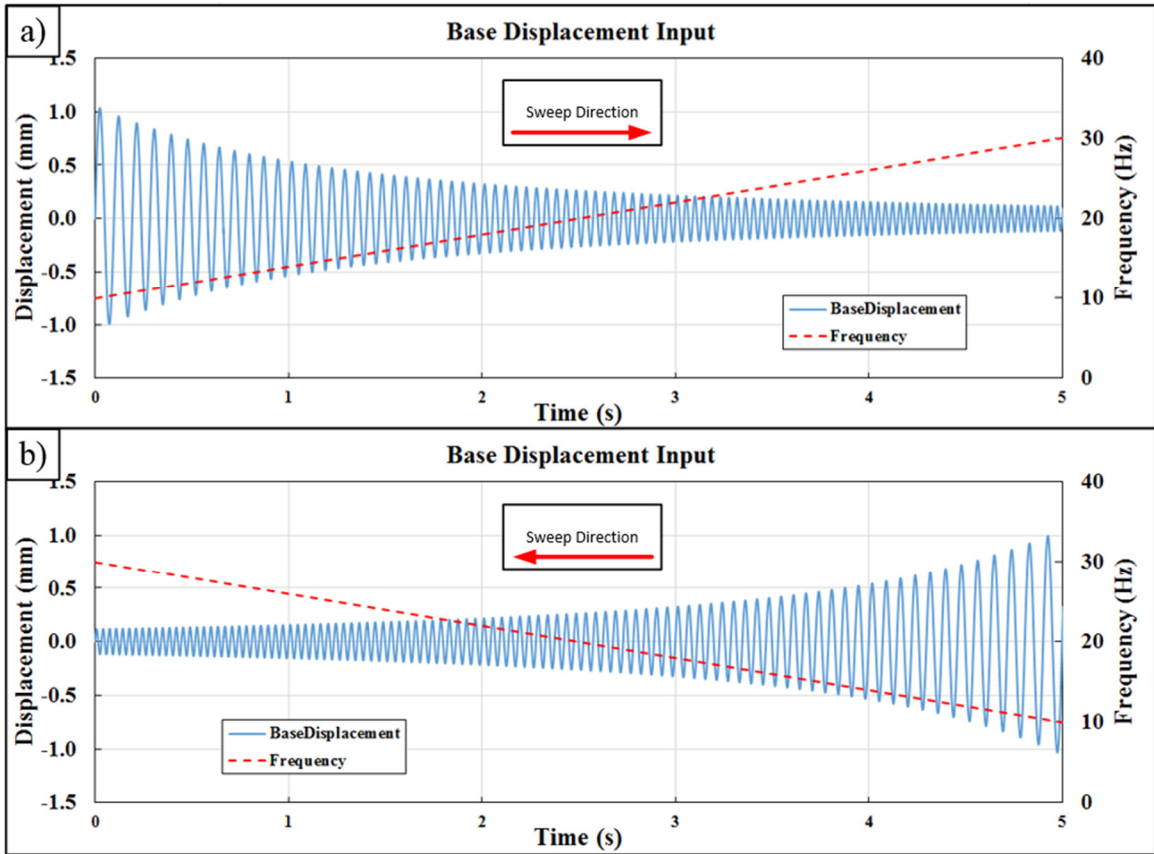


Figure 103. Base displacement inputs for the a) forward and b) reverse sweeps equivalent to a $0.3g_{rms}$ acceleration, time step is 0.001 seconds.

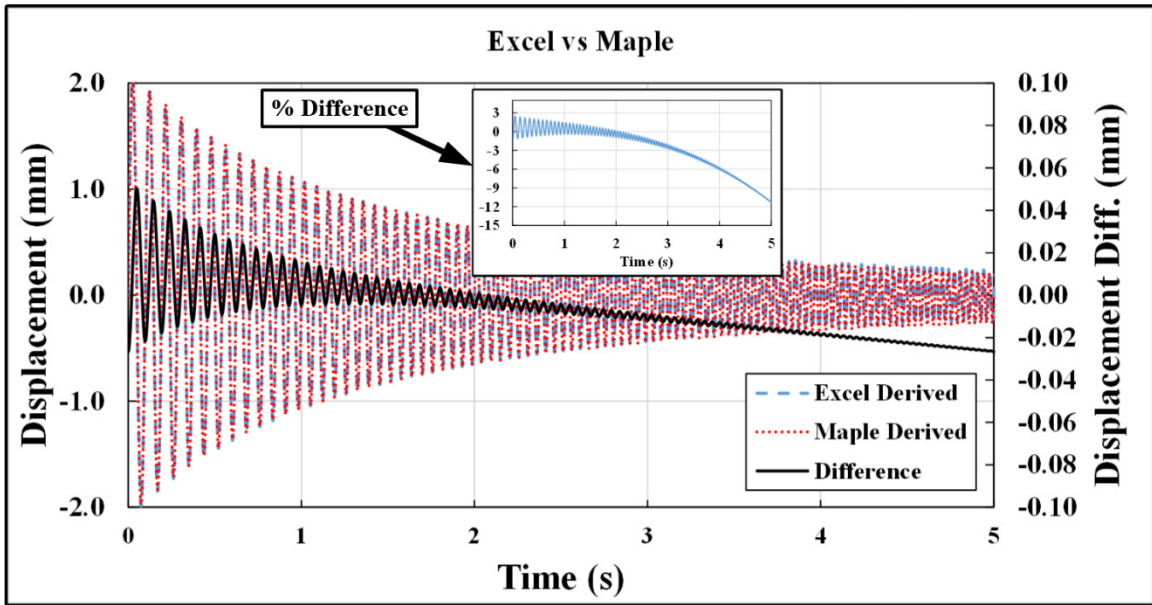


Figure 104. Difference between the derived Excel and the true Maple function.

The ANSYS transient problem results in a tip displacement profile that is, of itself, sinusoidal in nature. To extract a gain plot from the analysis, peak detection must be done on the tip displacement signal after a DC offset is removed. Rectifying the signal and using the logical expression

$$(Disp_t > Disp_{t-1} + hyst) \text{ AND } (Disp_t > Disp_{t+1} + hyst)$$

Eq 92.

Then $Disp_t$ is current peak

Else no peak found

will find the local peaks for a sinusoidal signal but must be filtered enough so that the hysteresis error is not overly high. For the results of this non-linear harmonic sweep the output signal did not need to be filtered. Peak detection for the output and input signals are shown in figure 105 below.

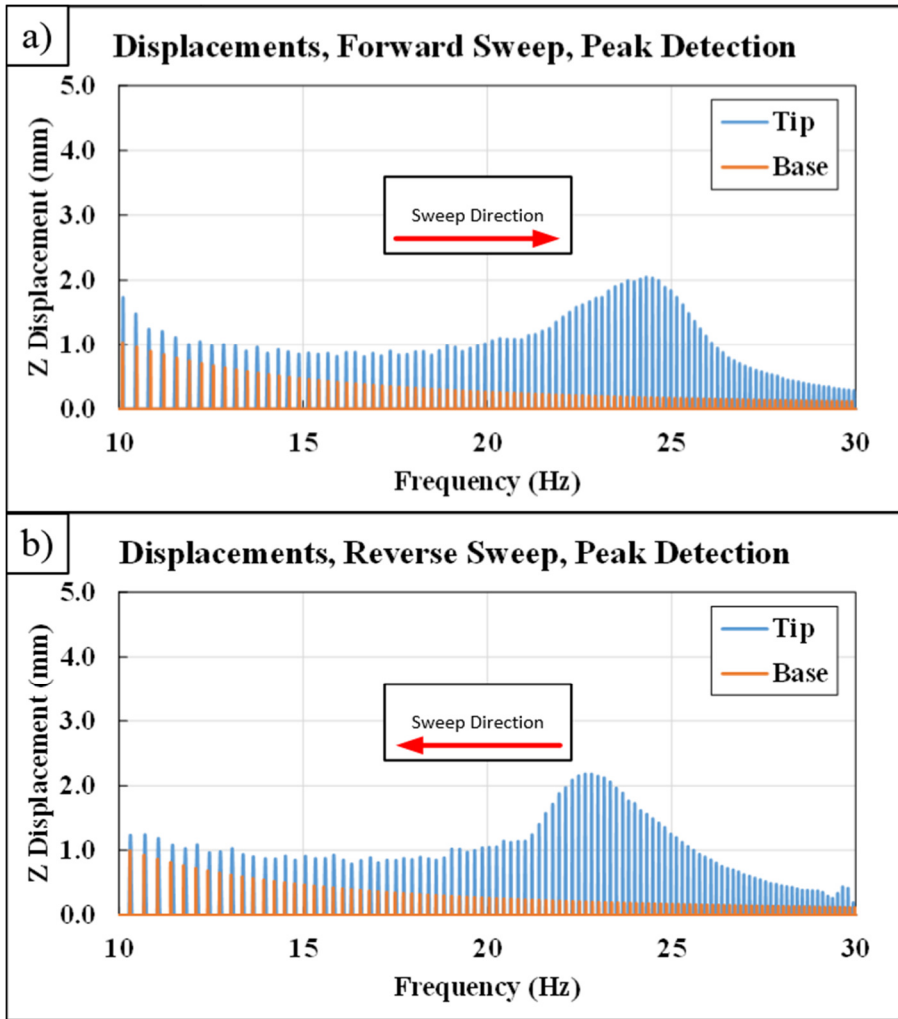


Figure 105. Displacement peak detection results for the base and tip of the 3x1 device in a) forward and b) reverse 0.3g_{rms} ANSYS sweep setup.

Outlines for the 0.3 g_{rms} sweeps are shown in figure 106 below which then are used to calculate the gains of the 3x1 device. This gain extraction routine works well for symmetrical responses to a sinusoidal signal but need modification if an extreme non-linear event occurs during the analysis, such as snap-through. Snap-through causes the DC offset to shift to a different neutral position which means a continuously changing DC shift algorithm or section will need to be used.

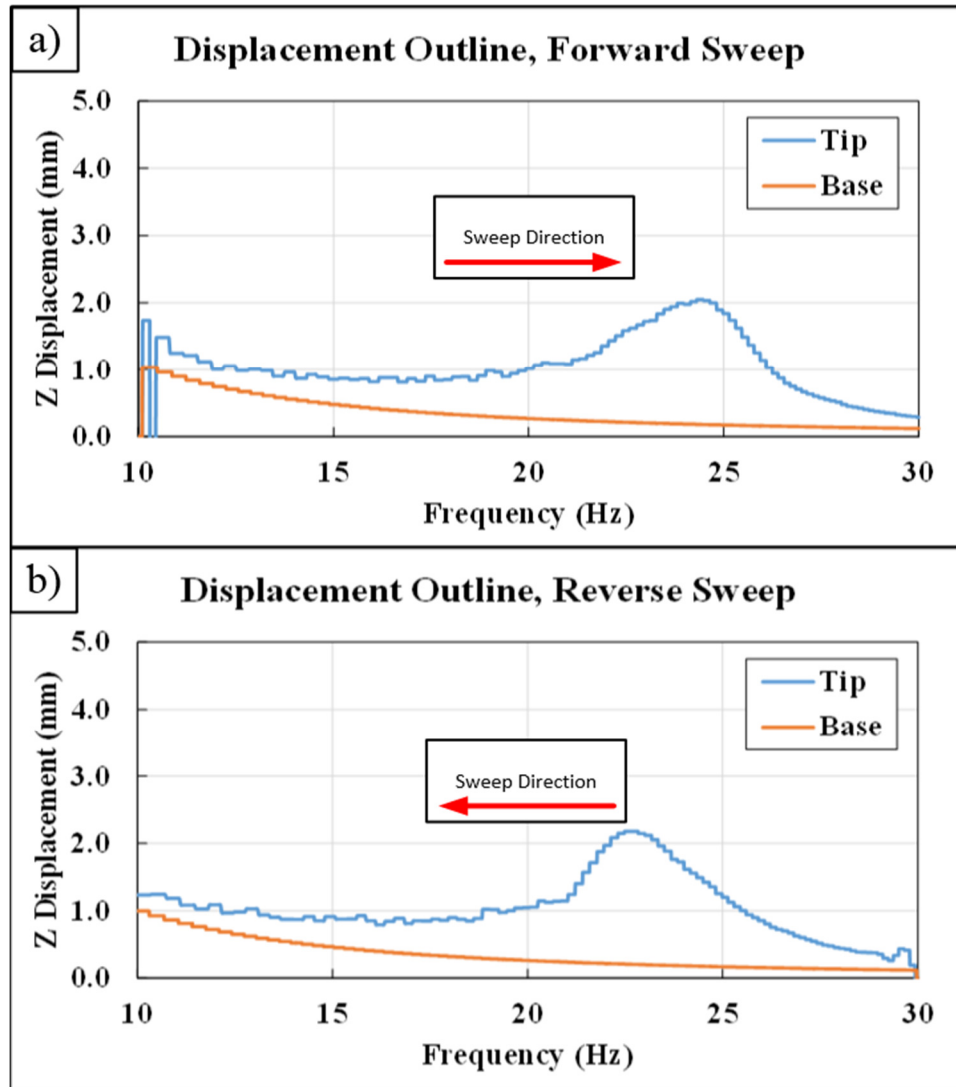


Figure 106. Peak outline results for the base and tip of the 3x1 device in a) forward and b) reverse 0.3 g_{rms} ANSYS sweep setup.

The amplification, or gain, for the 3x1 device with 8 mm arms is shown in figure 107 below for the unbuckled case. Harmonic analysis in ANSYS linearizes all effects of the model such as large displacement, contact, and material non-linearity's. Multiple methods exist to apply an acceleration in a harmonic analysis and include a direct acceleration, a large mass/force application, or a scripted displacement analysis. The displacement harmonic analysis is ideal but does not work for the pre-stressed modal superposition method. To pre-stress the structure a thermal load is applied to the steel beam. This thermal load was applied at different values until the x-directional stress is

approximately the same as the 0.1 mm displacement compression stress. At a ΔT of about 90 C the stresses matched the 0.1 mm compression load. After the static loading in ANSYS, a modal analysis is completed and the results are sent to a modal superposition analysis with an acceleration load. This is how a linearized pre-stressed structure is handled in ANSYS. Applying the harmonic displacement requires the script shown in the Appendix under (CODE).

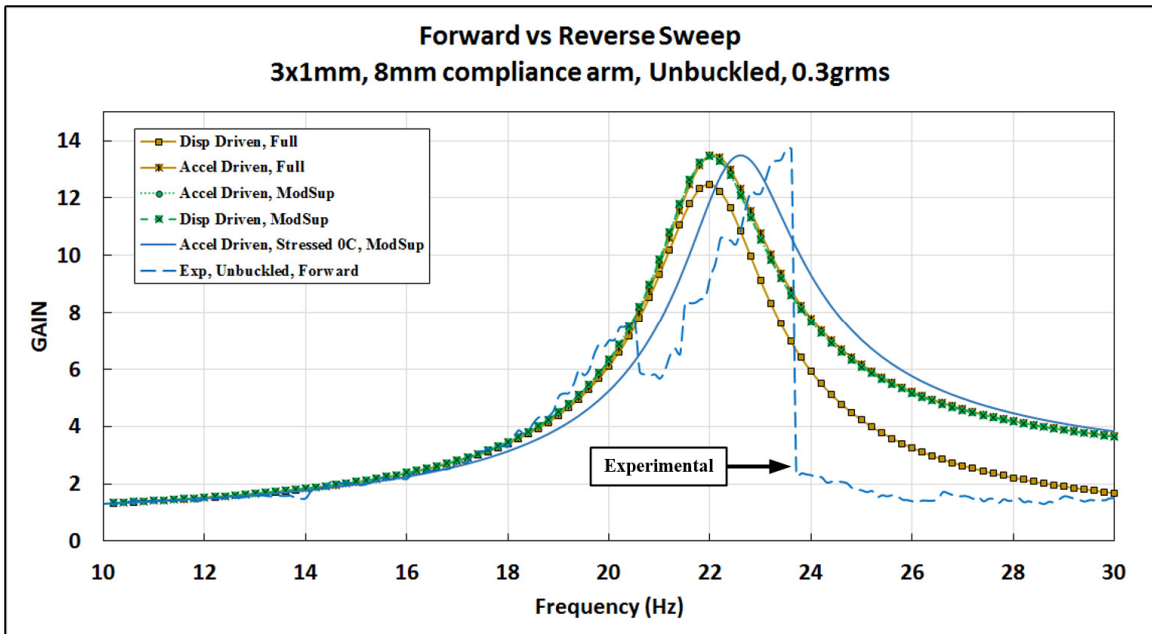


Figure 107. Comparison of the unbuckled harmonic sweep gains for the forward experimental, linear harmonic displacement driven, and linear harmonic acceleration driven at 0.3 g_{rms} .

Buckled results for the non-linear transient, pre-stress linear harmonic analysis, and the experimental gain data is shown in figure 108 below. It is interesting to note that the experimental buckled data did not match the non-linear transient data in gain amplitude and deviated by about 5 Hz in peak frequency. This could be due to non-ideal boundary conditions when buckled or a potential driving detriment that dampens the device at low accelerations.

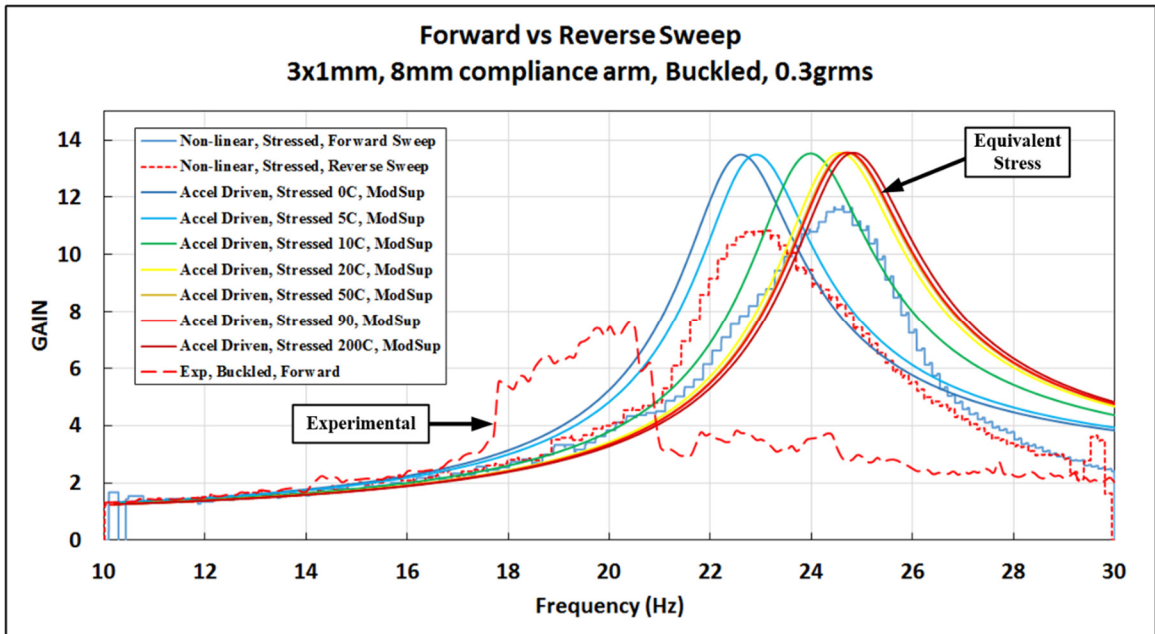


Figure 108. Comparison of the buckled harmonic sweep gains for the non-linear harmonic transient, forward experimental, linear harmonic displacement driven, and linear harmonic acceleration driven (with temperature induced buckling stress) $0.3 g_{rms}$ analysis.

When driven at higher accelerations, the non-linear behavior of the buckled device stands out, especially in the case of snap through. The non-linear harmonic transient analysis driven at $0.6 g_{rms}$ for the $3 \times 1 \times 8$ mm device is shown in figure 109 below. The forward sweep does not actuate in a bi-stable state for this simulation but makes two snap-through movements when swept in the reverse direction. At first it looks as though the actual rectified displacement is smaller in the bi-stable snap-through regime but if the device is driven in this frequency area there should be continuous actuation which would broaden the bandwidth between the two black lines shown in figure 109.

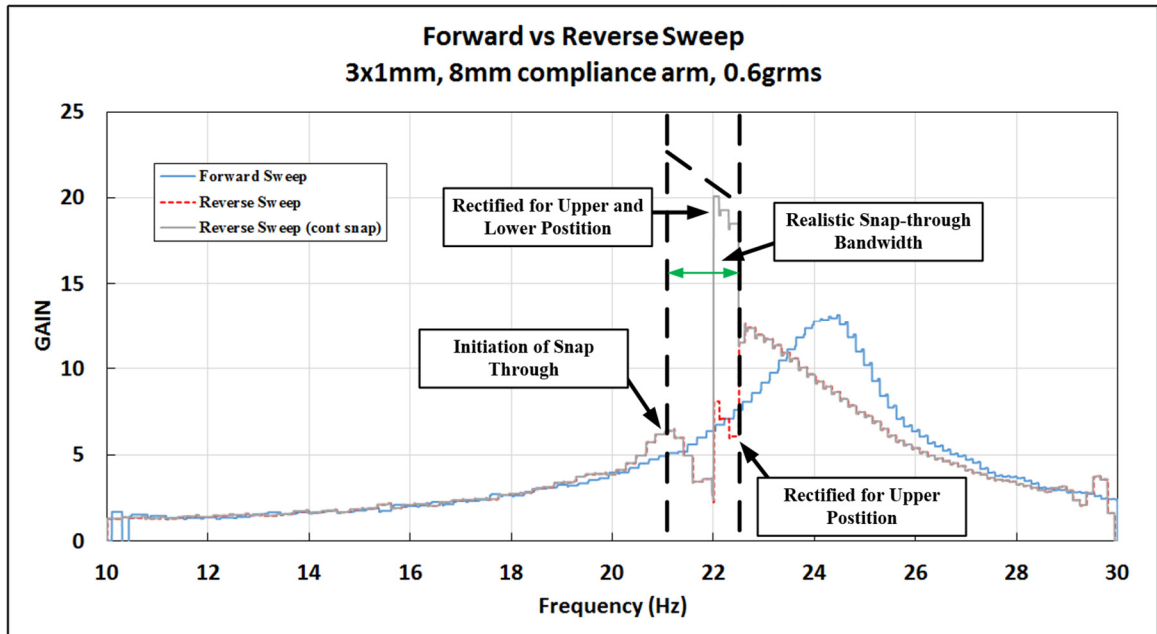


Figure 109. Forward and reverse non-linear harmonic transient runs at 0.6g_{rms}.

A simple cantilever beam was analyzed in ANSYS using the non-linear harmonic sweep to see what non-linear effects would come up using the routines described above and a dampening ratio of 5% at 20 Hz. Figure 110 below shows the effect of allowing the frequency to change slower by going from a 5 to 10 second transient run. This essentially allows more oscillations which trends towards the linear harmonic response. It would make sense that the bi-stable buckled beam above would have the same trend except that the snap-through bandwidth would most likely increase. Also, the overall system performance due to state switching would be different due to sweep direction.

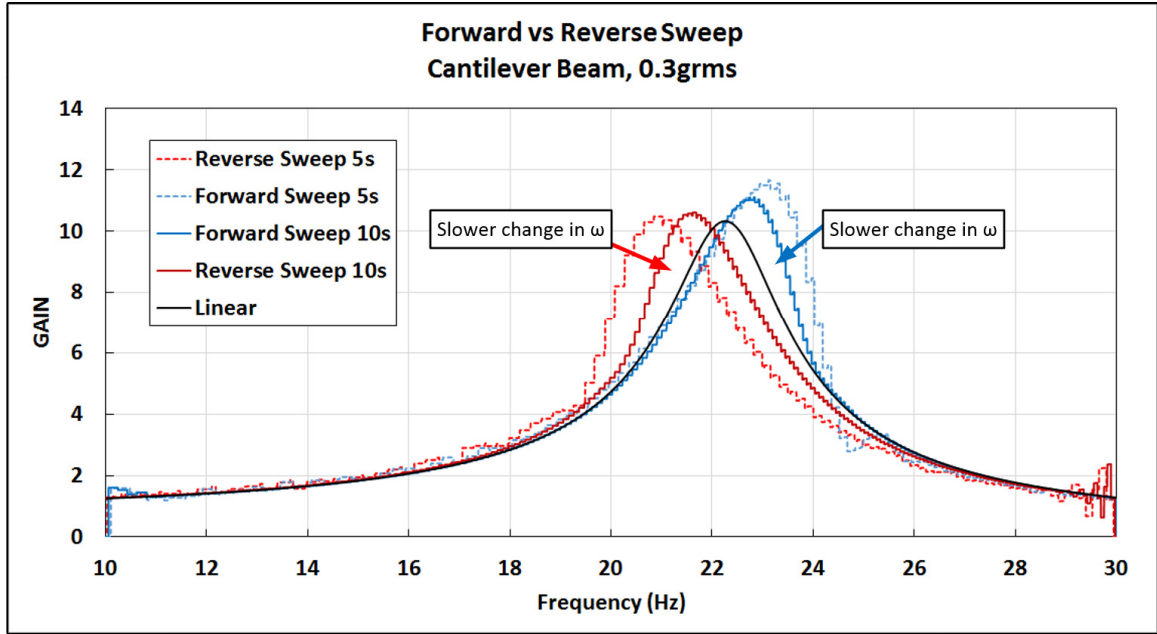


Figure 110. Cantilever beam response for a 80x10x0.75mm steel beam with a 10 gram mass at the end. The displacement load emulates a 0.3 g_{rms} acceleration.

F. ANSYS Voltage and Power Estimation

Actuating a model in ANSYS via piezoelectric elements is quite straightforward with either scripting or using the “Piezo ACT extension”. Estimating the voltage generated during dynamic motion requires some knowledge about the strain in the PVDF strips at different points in time coupled with the motion of charge through-out the system it’s hooked up to.

The electric displacement on a piezoelectric plate that is stressed with no external applied electric fields is

$$\begin{bmatrix} D_1 \\ D_2 \\ D_3 \end{bmatrix} = \begin{bmatrix} 0 & 0 & 0 & 0 & d_{15} & 0 \\ 0 & 0 & 0 & d_{15} & 0 & 0 \\ d_{31} & d_{31} & d_{33} & 0 & 0 & 0 \end{bmatrix} \begin{bmatrix} \sigma_1 \\ \sigma_2 \\ \sigma_3 \\ \tau_{23} \\ \tau_{31} \\ \tau_{12} \end{bmatrix} \quad \text{Eq 93.}$$

where the parameter of interest in our case is D_3 which is the charge per area on the top and bottom of the PVDF film. The total charge generated at an instant is

$$q_{piezo} = \iint [D_1 \quad D_2 \quad D_3] \begin{bmatrix} dA_1 \\ dA_2 \\ dA_3 \end{bmatrix} \quad \text{Eq 94.}$$

Assuming that D_1 , D_2 , and σ_3 are minimal and have no effect on the charge generated onto the electrode plates the above equation becomes

$$\begin{aligned} q_{piezo} &= \iint D_3 dA_3 = \iint (d_{31}\sigma_1 + d_{31}\sigma_2) dx dy \\ &= d_{31}E \iint (\varepsilon_1 + \varepsilon_2) dx dy \end{aligned} \quad \text{Eq 95.}$$

where E , ε_1 , and ε_2 are the stiffness, strain in the x, and strain in the y direction of the PVDF respectively. Using Poisson's ratio, ν , to account for transverse effects the above equation becomes

$$\begin{aligned} q_{piezo} &= d_{31}E \iint (\varepsilon_1 - \nu\varepsilon_1) dx dy \\ &= d_{31}E(1 - \nu) \iint \varepsilon_1 dx dy \end{aligned} \quad \text{Eq 96.}$$

The instantaneous voltage generated over the piezoelectric element is the charge divided by the capacitance of the PVDF where the capacitance is equivalent to Eq 67.

$$V_{piezo} = \frac{q_{piezo}}{C_p} = \frac{d_{31}E t(1 - \nu) \int_L \varepsilon_1 dx}{\varepsilon_{r,p} \varepsilon_0 L} \quad \text{Eq 97.}$$

where L is the length of the PVDF strip and t is the thickness. Since we are discretely evaluating the strain in ANSYS with each time step the integral changes to a numerical integration where we will know the area of an element and the strain

$$V_{piezo} = \frac{q_{piezo}}{C_p} = \frac{d_{31}Et(1 - \nu)}{\varepsilon_{r,p} \varepsilon_0 WL} \sum_{i=0}^n \varepsilon_{1,i} A_{element,i} \quad \text{Eq 98.}$$

where $\varepsilon_{1,i}$ is the x-direction strain and $A_{element,i}$ is the associated local area associated with node i and n is the total number of nodes. Taking out the state variable from Eq 98 gives

$$q_{piezo} = d_{31}E t(1 - \nu) \sum_{i=0}^n \varepsilon_{1,i} A_{element,i} = d_{31}E (1 - \nu) \sum (\varepsilon_1 A) \quad \text{Eq 99.}$$

The model used in ANSYS is the same shown in figure 100. Damping for the power estimate runs was also the same at 5% (20 Hz) lending to a β of 7.96×10^{-4} . Application of a static frequency displacement (5 seconds long) in the harmonic analysis gave a steady state response after about three to four cycles. At 0.6 g_{rms} the input, static

frequency, displacements did not cause snap-through. This is interesting because a reverse sweep of the same model does create buckled state switching.

After ANSYS finishes its transient analysis it gives the quantity $\sum(\epsilon_1 A)$ for each PVDF strip and at each time step. There is a problem using Eq 98 in its current form to evaluate voltage and power because the performance while driving a load is highly dependent on the state variable, charge. A proposed model for the piezoelectric strips which will handle charge generation and depletion is shown in figure 111 below.

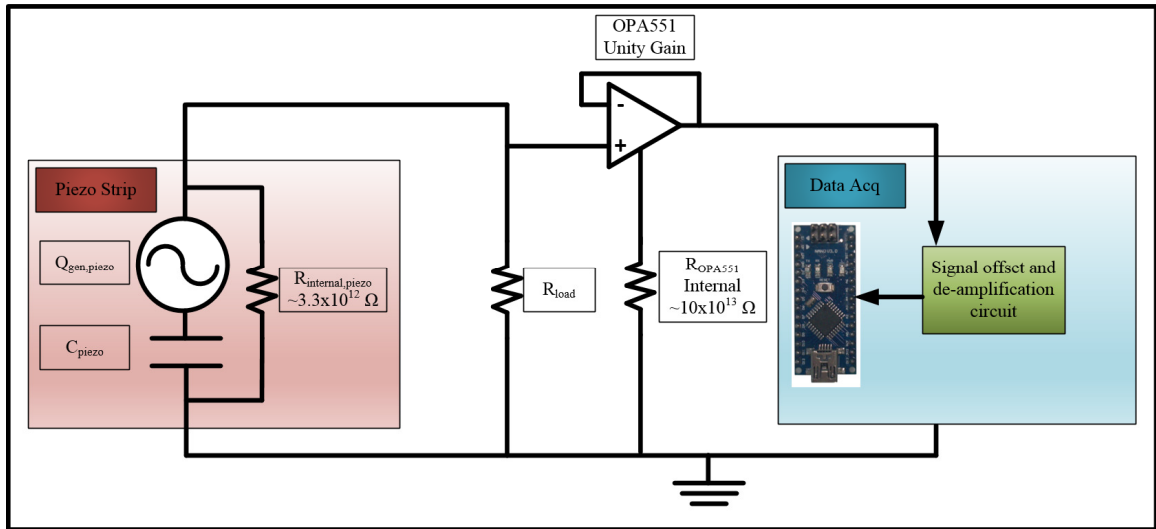


Figure 111. Circuit components to consider in the FEA power estimation model.

The resistance between the piezoelectric material electrodes is about $3.3 \times 10^{12} \Omega$ when not connected to anything else and is derived from the resistivity of PVDF which is about $5 \times 10^{14} \Omega \text{ cm}$. As mentioned before in earlier sections, the OPAA551 op amp has an input impedance of about $10^{14} \Omega$, and when combined with the PVDF resistance makes the above circuit a simple RC loop with a charge generator that applies charge directly to the capacitor. The circuit shown below, figure 112, has two components of interest which are the load resistor and the PVDF capacitance. New charge is introduced onto the capacitor every time the piezoelectric element changes strain state while the resistive element drains charge over time.

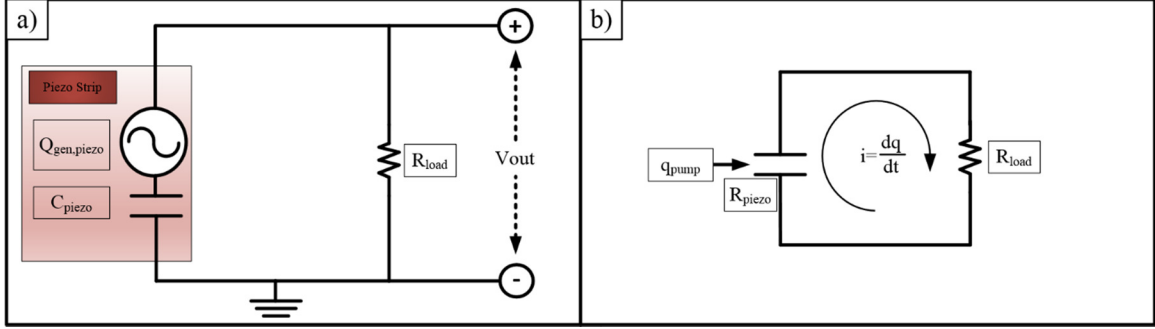


Figure 112. a) Circuit used in calculating power output from FEA model with negligible components removed and b) simplified circuit.

A script was written to obtain the x-direction strain integral from ANSYS at each time step for both of the PVDF strip shell layers. This script is placed after the solution phase and is shown in the appendix (CODE). The output of that script is then imported to excel where further calculations can be made. Essential equations for the two components are the

$$i_{cap} = \frac{dq}{dt} \quad \text{Eq 100.}$$

for the capacitor and

$$i_{resistor} = \frac{V}{R} \quad \text{Eq 101.}$$

for the resistor which are equal since the current has to be conserved for these elements. Setting Eq 100 and Eq 101 equal while realizing that they also share the same voltage gives

$$\frac{dq}{dt_{drain}} = \frac{\Delta q}{\Delta t_{drain}} = -\frac{V}{R} = -\frac{q}{C_p R} = -\frac{q}{\tau} \quad \text{Eq 102.}$$

where τ is the time constant. The important thing to note about Eq 102 is that no matter what sign the charge is on the capacitor, it will always tend towards zero. Extra charge is induced onto the capacitor every time a change in strain occurs within the PVDF strips and has the form

$$\frac{q_t - q_{t-1}}{\Delta t} = \frac{\Delta q}{\Delta t_{induced}} = \frac{d_{31}E(1-\nu)}{\Delta t} \left(\sum (\epsilon_1 A)_t - \sum (\epsilon_1 A)_{t-1} \right) \quad \text{Eq 103.}$$

meaning that it is the incremental change in charge given a reference strain that is important in time and not the charge generated at one given strain point. This change in charge effect

has the potential to neutralize opposite charges on the capacitor and is the sole cause of creating \pm voltages.

There are two time step regimes to worry about using this method which determine convergence of an iterative solution. These regimes are the ANSYS transient Δt and the electric modeled circuit Δt . Depending on the resistance load used, the RC time constant of the circuit in figure 112 b) will be modified, meaning that a smaller resistance loads lend to faster transients, which in-turn require a small Δt on the electric circuit modeling method. For this reason, the first thing that is done in excel is the interpolation of the ANSYS Δt to a different (most likely smaller) Δt to accommodate the RC circuit.

After voltage on the PVDF elements is established at each time step the power over the load resistor is calculated as

$$P_{load} = \frac{V_{cap}^2}{R} = \frac{V_{load}^2}{R} \quad \text{Eq 104.}$$

where R is the value of the load resistor. Summing the squares of power over the steady state region for ten cycles and then taking the square root gives the RMS power estimation for our 3x1 8mm device (which is introduced in the next section) at that frequency. Different runs were done at varying frequencies to evaluate the power generated. Results are shown in figure 113 below with experimental data at the same acceleration as a comparison. The buckled devices are compressed a total of 0.1mm.

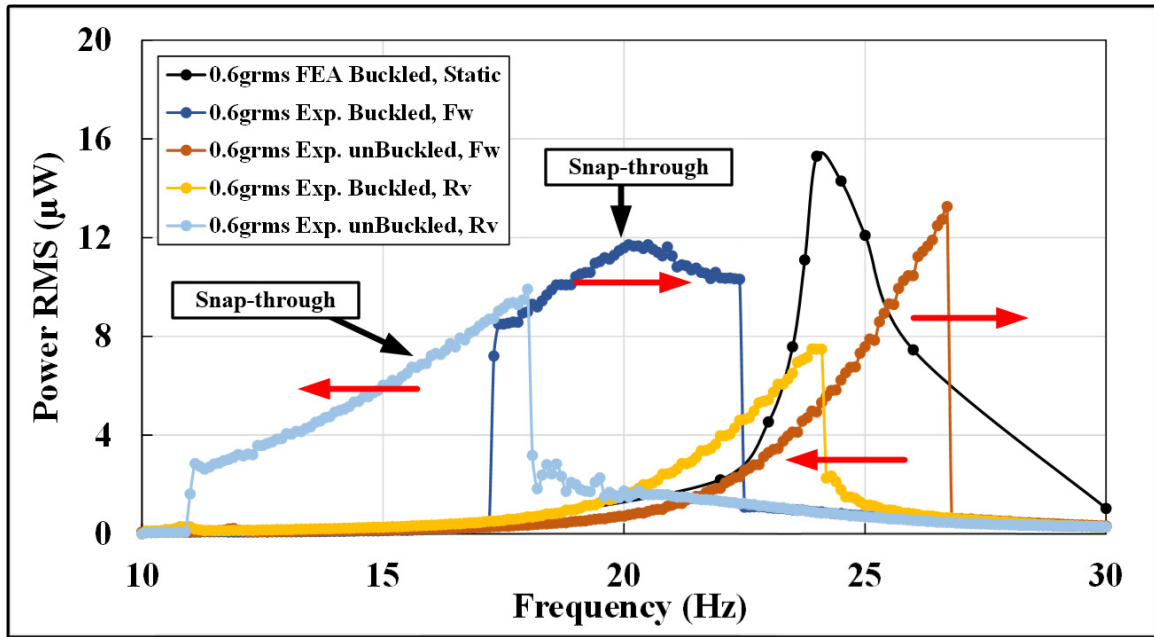


Figure 113. FEA buckled RMS power results at static driving frequencies compared to experimental sweeps for a 3x1 device with 8mm long compliance arms.

The current model in FEA was unable to mimic the dramatic drop in resonant frequency for the buckled case which may be due to the device being perturbed into HEOs via small imperfections in our driving system. Imperfect boundary conditions could also be an issue that allows for a more compliant structure. Non-linearity's in material properties could also change the simulation results. It is expected that the buckled devices exhibit a softening non-linearity when compressed.

CHAPTER IX

EFFECT OF COMPLIANCE ARM CONSTRAINTS

The effect of boundary conditions of a bi-stable device that buckles into an “S” shape and utilizes polyvinylidene fluoride is evaluated via a custom built shaker table and data collection system. Four permutations with different center constraints are named after their respective cross sections and are the perfectly pinned circular steel, rigid glued circular steel, 3x1 and 5x1 3D printed rectangle polylactic acid prototypes. Using a load of 30 M Ω , which was close to the optimal load resistance, frequency sweeps in the forward and reverse directions indicated different non-linearities depending on if the device is buckled or not. Peak resonant frequencies for the devices are around 18 to 30 Hz with bi-stable actuation occurring as low as 0.3 g_{rms}.

Damping was measured using the logarithmic decrement method as well as the linear and non-linear half-power methods. Results showed that the devices have an average damping ratio of 4.1% and that damping of buckled devices tends to be higher than non-buckled. The highest power generating device was the buckled 3x1 mm device with 3 mm compliance arms and resulted in 12.6 μ W at 21.1 Hz and 0.4 g_{rms} excitation. Higher accelerations for this device were actually a detriment to its performance. Unbuckled devices tended to exhibit a spring stiffening non-linearity while buckled devices obtained higher power outputs in the forward direction but could have their operating frequencies significantly lowered if swept backwards. All buckled devices tested during a chirp input could be promoted to high energy orbitals for increased performance while being driven with the same acceleration input.

A. Design Considerations and Specifications of Fabricated Devices

The energy harvester of interest operates on the basic premise that proof masses mounted on cantilevered arms transfer torque to the mid-section of a central compressively buckled beam with piezoelectric polyvinylidene fluoride (PVDF) strips adhered. A schematic of the device is shown in figure 114 below. Upon compression of the center beam, quasi-pinned compliance arm supports induce ‘S’ shaped buckled deflection profiles of the center beam. Transverse motion (vibration) of the structure base introduces a moment at the center of the ‘S’ shape, and can induce switching between buckled states for sufficiently large accelerations. Snap-through (switching between buckled stable states) is desirable for potentially generating large strains within the central piezoelectric strips and maximizing power output.

Ideally, compliance arms that act as a perfect pin constraint would provide optimal torque transfer to the center and allow snap-through to be exhibited at the lowest possible accelerations levels. However, mimicking a perfectly pinned condition at the center beam adds fabrication cost/difficulty and is not feasible for planned MEMS scale versions of the device. Using anything but a perfectly pinned method to constrain the deflection of the center beam will add both torsional and potential out-of-plane compliance. Torsional stiffness of the compliance arm will reduce the amount of force transferred to the center beam, increasing the energy threshold to be overcome to create stability state switching. Vertical compliance can change the buckling force needed to make the device bi-stable, increasing the acceleration needed to induce snap-through or pushing the center beam into 1st buckled mode deflection profile (dome shape) rather than the ‘S’ shaped 2nd mode.

To test the effects of the compliance arm constraint and geometrical parameters, four device variations were constructed. The first device was a pinned beam that used a greased 20 gauge steel rod running through the entire center body width that allowed nearly free rotation at the compliance arm supports (figure 114 c). The second device was nearly identical to the first with the exception of the compliance arm constraint. In this case, the compliance arm rod was locked to the central beam using an industrial adhesive (JB-Weld Compound 8265-S), in addition to clamping at the base supports. The result was a clamped-clamped compliance arm made of steel with a round cross section. The third and fourth devices used 3x1 mm and 5x1 mm cross-section polylactic acid (PLA) compliance

arms, respectively, with 2mm fillets near the brace structure (figure 114 d-e). In all cases, 5/16” steel nuts (4.62 grams) were used as proof masses and were adhered 10 mm from the tip of the brace as shown in figure 114.

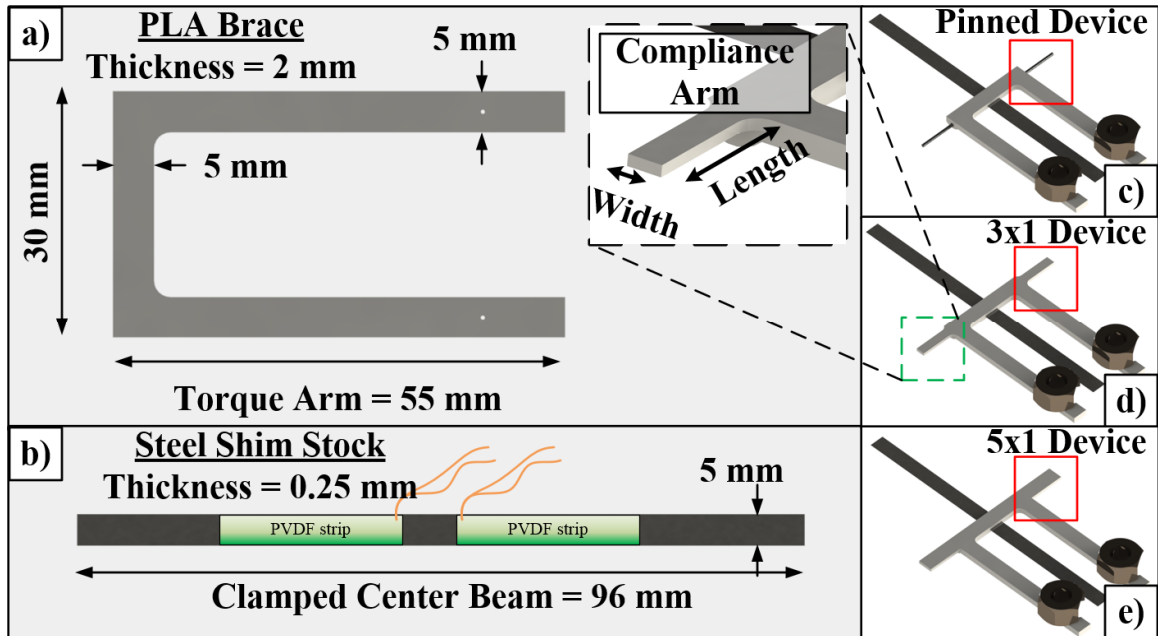


Figure 114. Main components of energy harvesting device, including the (a) torque arm PLA brace, the (b) steel shim stock center beam with PVDF strips, and the compliance arms constructed in the (c) pinned, (d) 3x1, and (e) 5x1 configurations.

Piezoelectric strips of 0.11 mm thickness (GoodFellow FV301960/3, $d_{31}=19 \text{ pC N}^{-1}$, $d_{33}=-20 \text{ pC N}^{-1}$) were cut to a width and length of 5 and 33 mm respectively. Previous FEA results on the buckled center beam [111] show that a strain sign change occurs at about 16% of the beam length from the end constraints and at the middle for these devices. Thus, to minimize charge neutralization, two separate strips of PVDF are adhered to the center beam on spans of $1/6^{\text{th}}$ to $1/2$ along the length of the beam, and again on a span from $1/2$ to $5/6^{\text{th}}$ of the beam (figure 114 b).

B. Shaker Table Setup

A custom-built shaker table setup was construed to test the devices under sinusoidal driving conditions. The shaker consisted of a 250 W_{p-p} (peak to peak) speaker, a 200 W_{rms} (root mean squared) amplifier, Arduino Nana v3.0 micro controller, MPU-6050 accelerometer, and an op-amp signal buffer and conditioning circuit. The buffer and conditioning circuit are needed to accept a moderately high voltage response and provide a high input impedance so that the power generated can be accurately measured. To accommodate the large impedance loads that accompany single layer element PVDF strips [66, 150] a two stage op-amp buffer circuit was used with an input impedance over 1 GΩ (OPA551PA). Driving specifications used in this work for the system were 10-500 Hz and 0.1 to 3 g_{rms} while the logging specifications for the Arduino utilized four voltage channels running 2048 S/s.

A compression rig mounted atop the shaker plate allowed for each device to have variable length compliance arms and the ability to fine tune a compression displacement by turning 8-32” push rods and then locking down the rig by tightening M3 bolts. Compression displacement measurements for the system were performed via calipers. A render of the designed shaker table and the as-fabricated system with the 3x1 mm device and 8 mm compliance arms in the uncompressed state are shown in figure 115 below. Great care was taken to buckle the device symmetrically as the shape of the potential energy function (specifically the maximum deflection point of the center beam which must be traversed to exhibit snap-through) must be within a certain range to provide energy harvesting benefits [89]. Near the critical buckling load, the resonant frequency of the center beam should theoretically approach zero and afterwards stiffen up as more compression is applied [90].

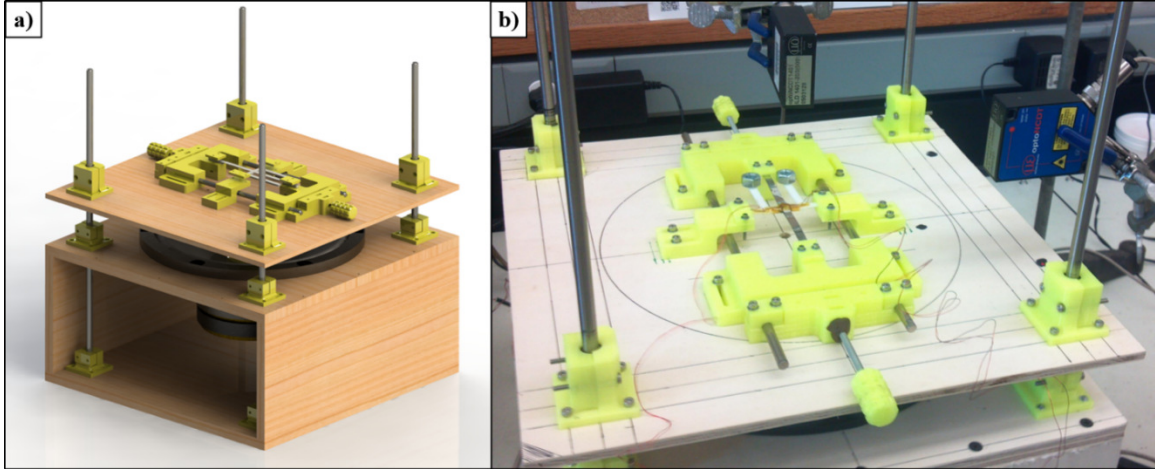


Figure 115. (a) Render of designed shaker table, and (b) the as-fabricated shaker table.

C. Optimum Load

To evaluate devices at peak power performance conditions, the optimum load was determined. PVDF strips with single electrodes tend to have high optimum resistance driving loads. This can introduce difficulties as the input impedance on standard laboratory testing equipment can be on the same scale as the devices being tested, which in turn, can create power sharing that diminishes the signal. To reduce the optimum load of PVDF, multiple stacked PVDF and electrode layers can be used but the amount of layers needed would be very costly.

Four test cases were run at different impedance loads to determine the optimum load conditions for which all other tests would be performed. Three of the cases included the uncompressed pinned, 3x1 mm, and 5x1 mm devices while the last test case was a compressed 3x1 mm device. All optimum load cases were run at 0.5 *grms* and near resonance.

A plot of normalized voltage response versus load impedance is shown in figure 116 below. Optimum values ranged from around 20 to 40 M Ω . Since all tests showed minimal drop-off in power performance around 30 M Ω , 30 M Ω was chosen as the driving resistance load for all devices and testing cases.

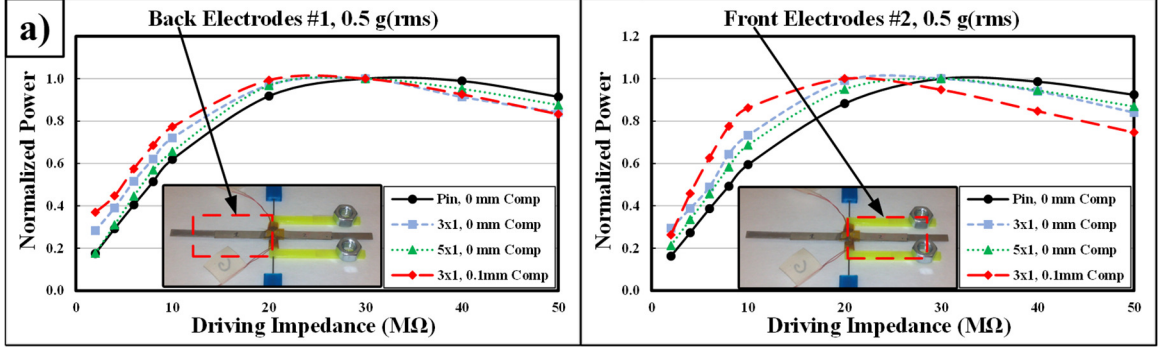


Figure 116. Normalized voltage response versus load impedance for the (a) back and (b) front electrode, all tested using 8mm compliance arms.

D. Evaluation of Damping

Viscous damping was evaluated for the device using three different methods: free, linear forced, and non-linear forced. Free vibration analysis works well for decaying responses, but can be a poor representation of damping in energy harvesting structures that have a constant input function exerted upon them. Despite this limitation, values for free damping were extracted using the voltage response to a mono-pulse chirp sent to the shaker table and using the logarithmic decrement method in equation (1) [7]

$$\zeta_{\text{free}} = \frac{1}{\sqrt{1 + \left(\frac{2\pi}{\ln(x_0/x_1)} \right)^2}} \quad \text{Eq 105.}$$

where x_0 and x_1 is the amplitude of the decaying sine wave at the beginning and end of each successive cycle, respectively.

A more realistic evaluation of linear viscous damping is to use the half-power bandwidth method (HPB) which evaluates the quality and damping ratio for a linear system [7]. This process requires the displacement measurement of the base shaker table and the tip of the torque arms, which was performed using two micro-epsilon laser displacement sensors (Micro-Epsilon NCDT1401). The gain, which is the ratio of the tip displacement to the base displacement, can be plotted against frequency to form a bode plot. From this plot, the linear quality factor can be determined using [7]

$$Q_{\text{forced},l} = \frac{f_r}{f_2 - f_1} \quad \text{Eq 106.}$$

where f_r is the resonant frequency, f_1 is the first -3 dB drop down point, and f_2 is the second. The damping ratio can then be determined from $\zeta = 1/2Q$. The buckled energy harvester device tested here was found to be non-linear in both the uncompressed and compressed states, exhibiting a spring-stiffening or spring-softening effect characterized by a jump discontinuity. Physically, this means the frequency response depends on the direction of frequency sweeping. An even better estimate of the damping for a non-linear system is to use a modified version of the HPB from [36]

$$Q_{forced,nl} = \frac{f_p}{f_{jd2} - f_{jd1}} \sqrt{n^2 - 1} \quad \text{Eq 107.}$$

where f_p is the peak gain frequency, f_{jd1} is the frequency of the jump down point, f_{jd2} is the frequency of the jump down point that has the same gain as f_{jd1} . The value n is the ratio of the gain of f_p and f_{jd1} . It is important to know which type of non-linearity, stiffening or softening, the system falls under because one peak will be larger than the other during the directional sweep.

Free vibration tests were performed for the majority of the VEH devices. After a monopulse was applied to the stationary device, the output voltage recorded typically appeared to be similar to a decaying sine wave. In the logarithmic decrement method, only peaks in the signal obtained after the base accelerometer had come to rest are used to determine damping behavior. Conversely, the non-linear half power method analysis is slightly more complicated due to deviations in devices performance based on sweep direction. Graphs for the logarithmic decrement and half-power method are shown in figure 117 below for the 3x1 mm device with 8 mm compliance arms. Sweeps for a few of the devices in their various configurations are shown table 21 below. An additional compressed case for the 5x1 mm device was also performed to investigate effects of damping on an over-compressed prototype. As seen below, over-compression tends to increase damping which is highly detrimental to device power performance. If the over-compressed case is neglected, the average dampening for all of the non-linear devices combined is approximately 4.1%.

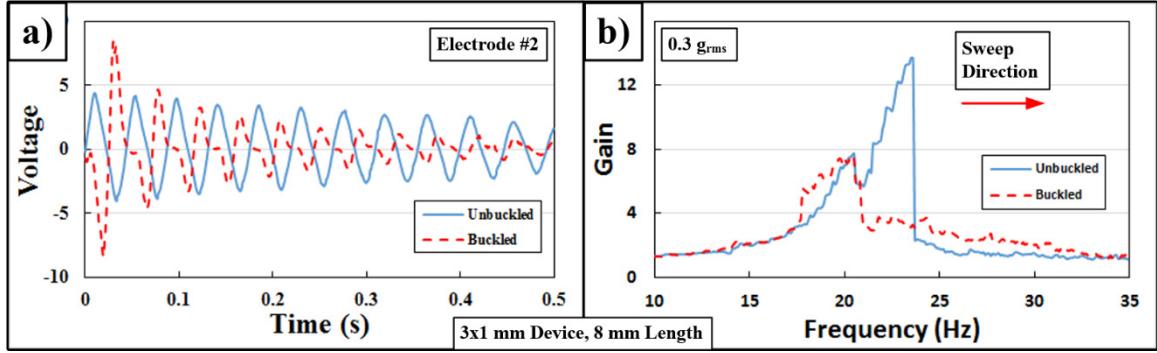


Figure 117. (a) Voltage output and (b) gain response plots for the 3x1 mm device with 8 mm compliance arms.

Table 21. Damping ratios for the tested compressed and uncompressed devices using different methods.

	Compliance length=8mm	Forward, Compliance length=8mm		Reverse, Compliance length=8mm		Forward, Compliance length=12.5mm		Reverse, Compliance length=12.5mm	
	Free	Forced Linear	Forced Non-linear	Forced Linear	Forced Non-linear	Forced Linear	Forced Non-linear	Forced Linear	Forced Non-linear
Glue, 0mm comp		0.056	0.042	0.037	0.035	0.029	0.026	0.016	0.025
Glue, 0.1mm comp		0.059	0.041	0.078	0.050	0.095	0.080	0.075	0.054
Pin, 0mm comp	0.023	0.037	0.045			0.034	0.041		
Pin, 0.1mm comp	0.040	0.051	0.053			0.045	0.039		
3x1 0mm comp	0.009	0.034	0.035	0.066	0.050	0.022	0.026	0.060	0.059
3x1 0.1mm comp	0.061	0.071	0.048			0.047	0.028		
5x1 0mm comp	0.015	0.039	0.032			0.033	0.038		
5x1 0.1mm comp	0.046	0.032	0.029			0.032	0.046		
5x1 0.2mm comp		0.095	0.066			0.067	0.056		

E. Parametric Evaluation of Compliance Arms

A parametric evaluation of the effect of compliance arm geometry on device behavior was performed using the length and the width of the arms as parameters. For clarity, a naming scheme was selected based on the arm width, with devices named as 3x1 and 5x1 referring to 3mm x 1 mm cross-section and 5 mm x 1 mm cross-section, etc. The other two device variations were named for their free pinned or completely glued 20 gauge steel support. For the pinned, glued, 3x1, 5x1 the compliance length was varied between 8 and 12.5 mm. The 3x1 device was also tested in a 3 mm length setup as an additional run. Each device was frequency swept both forwards and backwards from 0.2 to 0.6 g_{rms} with a frequency range of 10 to 35 Hz.

F. ANSYS Modal Frequency Simulations

To get a rough estimate of the resonant frequencies for the fabricated devices, an ANSYS modal analysis was used. ANSYS linearizes all contact and non-linear effects when estimating a modal frequency or harmonic sweep response. To capture more accurate, non-linear responses for the devices, a transient analysis would be needed with a linearly varying frequency acceleration load. If the device exhibits snap-through under the simulated driving conditions, then the model would require a very small time step increment to capture this large displacement event. Due to the large computational times required to perform resonant frequency estimates under such snap-through conditions, these cases were not considered.

The model consisted of 8 node SHELL281 elements for the center beam and 20 node SOLID95 elements for the PLA brace and proof masses. Two cases were run for each device in which one had no compression and the other had a total of 0.1 mm of compression for the pre-stressed state. One item of great interest was the proximity of the second mode (each torque arm being 180° out of phase) to the first mode in terms of frequency, as the second mode tends to be detrimental to the power output of the device.

G. Power Generation

Forward and reverse sweeps of all devices were performed while recording V_{pp} and V_{rms} voltages. Another interesting parameter is the full width at half max (FWHM) value of the sweep, and is calculated by measuring the width of the peak (in Hz) at half of the maximum resonant value. This parameter provides an indication of device operating bandwidth. Data from the sweeps of the 3x1 mm device with the 8 mm compliance arm length configuration are shown in figure 118 below. It should be noted that the V_{rms} amplitude increases greatly once snap-through behavior initiates for the buckled cases, and that the response of the unbuckled devices looks inherently non-linear. Such behavior can be caused by large out-of-plane displacements or imperfect boundary conditions [136]. Graphs for all of the tested devices can be shown in figure 134 - figure 151 in (FIGURES AND TABLES) at the back of this dissertation. Also in the appendix is a graph (figure 142 and figure 151) of the RMS and peak power output of the unbuckled and

buckled 3x1 device with 12 mm compliance arms taken at two different times to show repeatability.

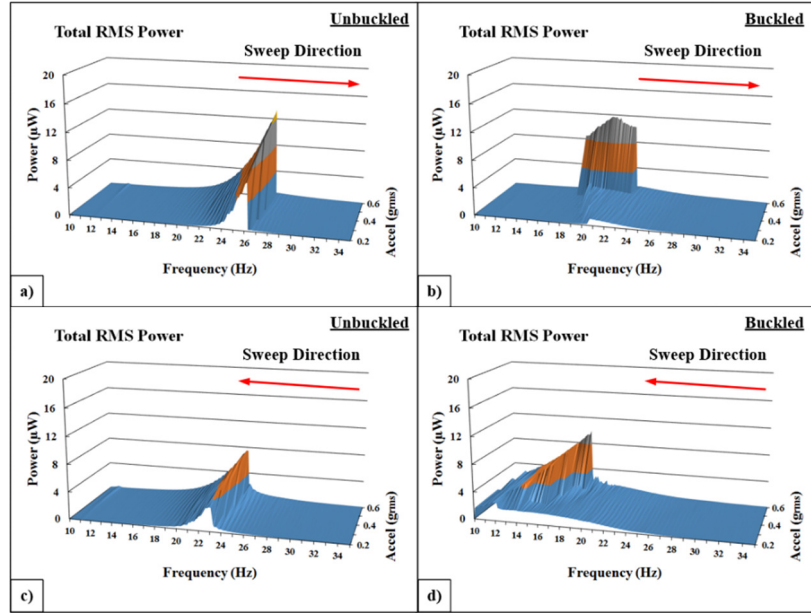


Figure 118. Power results for the 3x1 mm device in the (a) unbuckled forward sweep (b) buckled forward sweep (c) unbuckled reverse sweep and (d) buckled reverse sweep case. Compliance arms are 8 mm long.

Power output is one of the critical, useful metrics for evaluating energy harvesting device performance. The rms power (P_{rms}) from the PVDF strip voltage is

$$P_{rms} = \frac{V_{rms}^2}{R} \quad \text{Eq 108.}$$

peak resonant frequency, the linear modal frequencies, and P_{rms} are shown in table 22 and table 23 below. Bold and superscript (a) elements show the acceleration and sweep cycles where snap-through behavior was identified.

Table 22. Forward sweep data for all devices tested.

Forward Sweep ---->	Total Width (mm)	Compliance Length (mm)	Compression (mm)	Fr Peak Avg (Hz)	FEA Fn (Hz), $\zeta=0$	% Diff	RMS Power (μ W)				
							0.2	0.3	0.4	0.5	0.6
Glued Pin Device	46	8	0	28.58	31.29	-8.70	0.77	1.15	1.53	2.07	2.57
Glued Pin Device	55	12.5	0	28.08	29.68	-5.40	1.41	2.20	2.93	3.62	4.26
Glued Pin Device	46	8	0.1	27.62	31.17	-11.4	0.94	1.44	2.03	2.22	2.66
Glued Pin Device	55	12.5	0.1	23.02	29.93	-23.1	1.48	3.40	5.05^a	5.92^a	6.63^a
Pure Pin Device	46	8	0	23.76	22.82	4.10	4.22	5.61	7.19	6.31	5.54
Pure Pin Device	55	12.5	0	23.06	22.41	2.90	3.79	5.00	6.41	5.62	6.10
Pure Pin Device	46	8	0.1	18.26	23.41	-22.0	1.25	1.40	1.50	10.40^a	11.20^a
Pure Pin Device	55	12.5	0.1	17.98	23.20	-22.5	1.09	1.37	1.69	9.46^a	10.10^a
3x1 mm Device	36	3	0	24.70	25.43	-2.90	5.87	7.75	9.54	10.50	12.00
3x1 mm Device	46	8	0	26.5	20.89	26.90	6.77	8.81	10.90	11.70	13.30
3x1 mm Device	55	12.5	0	24.54	19.85	23.70	6.69	8.36	10.20	11.30	12.80
3x1 mm Device	36	3	0.1	18.70	25.27	-26.00	0.82	1.23	12.60^a	12.30^a	12.00^a
3x1 mm Device	46	8	0.1	19.74	22.57	-12.50	0.95	1.36	1.58	2.39	11.70^a
3x1 mm Device	55	12.5	0.1	20.46	21.80	-6.10	0.97	1.37	1.73	2.02	3.03
5x1 mm Device	46	8	0	29.08	22.96	26.70	2.46	3.42	4.16	4.84	5.69
5x1 mm Device	55	12.5	0	26.88	23.20	15.90	2.41	3.75	4.24	5.00	5.71
5x1 mm Device	46	8	0.1	23.08	23.46	-1.60	0.47	0.49	0.59	0.82	1.03
5x1 mm Device	55	12.5	0.1	24.14	21.07	14.60	0.32	0.27	0.38	0.82	0.93

^a indicates that device exhibited snap-through.

Table 23. Reverse sweep data for all devices tested.

Reverse Sweep <---	Total Width (mm)	Compliance Length (mm)	Compression (mm)	Fr Peak Avg (Hz)	FEA Fn (Hz), $\zeta=0$	% Diff	RMS Power (μ W)				
							0.2	0.3	0.4	0.5	0.6
Glued Pin Device	46	8	0	28.38	31.29	-9.31	1.28	1.75	2.02	2.32	2.66
Glued Pin Device	55	12.5	0	27.96	29.68	-5.80	2.23	2.94	3.50	3.93	4.30
Glued Pin Device	46	8	0.1	24.52	31.17	-21.33	1.29	1.95	2.42	3.00	3.54^a
Glued Pin Device	55	12.5	0.1	23.30	29.93	-22.14	3.28	4.59	5.27^a	5.91^a	6.60^a
Pure Pin Device	46	8	0	21.22	22.82	-7.02	2.06	2.92	3.44	3.84	4.57
Pure Pin Device	55	12.5	0	20.52	22.41	-8.43	1.94	2.56	3.41	3.73	4.64
Pure Pin Device	46	8	0.1	16.32	23.41	-30.29	1.01	1.32	1.36	5.03^a	6.16^a
Pure Pin Device	55	12.5	0.1	13.82	23.20	-40.43	1.42	2.44^a	3.56^a	4.62^a	5.71^a
3x1, mm, Device	36	3	0	21.82	25.43	-14.20	3.05	3.97	4.97	5.52	6.34
3x1, mm, Device	46	8	0	23.40	20.89	12.03	3.46	4.97	5.74	6.82	7.49
3x1, mm, Device	55	12.5	0	22.02	19.85	10.96	3.21	4.67	5.03	6.06	6.68
3x1, mm, Device	36	3	0.1	17.16	25.27	-32.10	1.62	1.70	1.70	2.50	9.20^a
3x1, mm, Device	46	8	0.1	15.24	22.57	-32.48	2.72	4.50^a	6.73^a	7.82^a	9.91^a
3x1, mm, Device	55	12.5	0.1	17.78	21.80	-18.43	2.01	2.00	2.00	2.09	9.89^a
5x1 mm Device	46	8	0	27.24	22.96	18.67	1.53	2.30	3.01	2.89	3.34
5x1 mm Device	55	12.5	0	24.84	23.20	7.07	1.46	1.86	2.54	2.95	3.28
5x1 mm Device	46	8	0.1	17.72	23.46	-24.48	1.75	2.69^a	3.22^a	3.54^a	3.91^a
5x1 mm Device	55	12.5	0.1	16.40	21.07	-22.16	0.85	2.14^a	2.84^a	3.73^a	4.53^a

^a indicates that device exhibited snap-through.

Snap-through action almost always tended to increase P_{rms} values for the devices when compared to their unbuckled states. Improvements as high as 102.2% for the forward sweeps and 53.5% for the reverse sweeps are obtained using the data in table 22 and table 23 above when compared to the same device in the unbuckled state. With the exception of the glued pinned device (which buckling always increased power in both sweep directions) buckling was a detriment until intra-well actuation was achieved. Forward sweep performance without snap-through was almost always around 80% lower than their unbuckled counterparts.

There are many different ways to characterize the performance of an energy harvester [106], some of which are quite complicated due to the many different variables that can be involved. Ideally, the performance metrics should be dimensionless but that cannot always be accomplished while maintaining an intuitive meaning. One of the most common metrics used for linear energy harvesters is the normalized power density (NPD) which is defined as

$$NPD = \frac{P_{rms}^{max}}{a_{rms}^2 V} \quad \text{Eq 109.}$$

where V is the swept volume required to operate the energy harvester and a_{rms} is the input acceleration. This does not take into account the bandwidth of the device. Another metric is called the volume figure of merit (FoM_V) [95] and normalizes the output by a proof mass made of gold that occupies half the same volume as the compared energy harvester. It is defined as

$$FoM_V = \frac{16P_{rms}^{max}}{Y_0 \rho_{gold} V^{4/3} \omega^3} \quad \text{Eq 110.}$$

where Y_0 is the input amplitude, ρ_{gold} is the density of gold, and ω is the peak frequency in rad/s. To account for bandwidth the FoM_V is modified by

$$FoM_{BW} = FoM_V \frac{BW_{1dB}}{\omega_m} \quad \text{Eq 111.}$$

where BW_{1dB} is the bandwidth measured -1 dB from the maximum power generated. The creator of the metric wanted to favor flatter frequency curves, thus measuring down from the peak power by about ~80%.

An interesting metric to use for this non-linear device is called the performance index [106] and is defined for a particular frequency as

$$I = \frac{P_{rms}f}{ma_{rms}^2} \quad \text{Eq 112.}$$

where m is a specified mass of the oscillator. The entire mass of the device was used in evaluation and not just the proof mass due to the rest of the system making up a considerable amount of the system mass. This would yield a conservative estimate of the performance index. To get the total performance index, all performance index values are integrated over a set range as

$$I_{a-b} = \frac{\int_a^b I df}{b-a} \quad \text{Eq 113.}$$

where a and b are picked by the user. A value of -3dB (~50%) from the peak power generated was selected for the new bi-stable devices since that is where the FWHM is usually measured. I_{a-b} is typically thought of as a mean index value. The standard deviation for this metric which specifies how the index varies from the mean is determined from

$$\sigma_{I_{a-b}} = \sqrt{\frac{\int_a^b I^2 df}{b-a} - (I_{a-b})^2} \quad \text{Eq 114.}$$

Two plots showing this power metric under forward and reverse sweeps for each device are given in figure 119 below. Snap-through behavior in the forward sweep direction was observed to increase this power metric for the buckled glued device with long compliance arms and the buckled pinned device, but only at higher input acceleration. In the reverse direction, only the buckled glued device with long compliance had a metric consistently higher during snap-through.

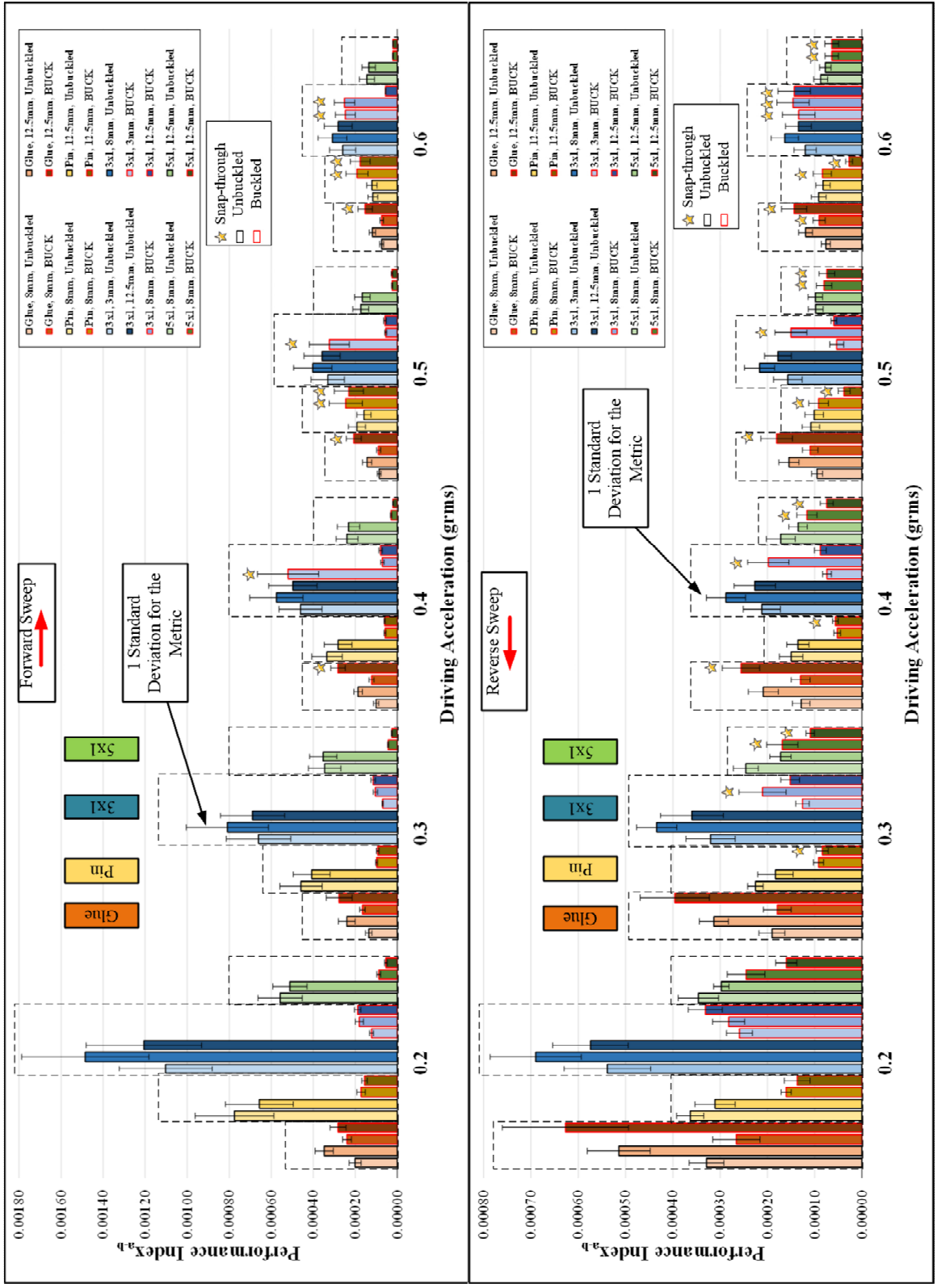


Figure 119. Power generation performance index metric for the forward (left) and reverse (right) cases.

The metric in Eq 114 is very sensitive to the placement of a and b for these devices and selecting the -3 dB point gives the benefit to very high narrow peaks. Also Eq 112 shows that the incremental metric increases as f increases. The buckled devices are skewed with the highest content near the upper frequency range. Thus any “added” content due to HEO operation tends to increase the difference $b-a$ and lower the metric even though there is more power volume under the graph.

A common observation in HEO operation is that it extends the operating range if it can be promoted. Actually evaluating this enhancement requires a stitching of the forward and reverse sweep. Figure 120 below shows what this stitching looks like. It is equivalent to merging the two sweeps. This shows that HEO operation broadens the devices operating bandwidth when compared to the non-buckled setup.

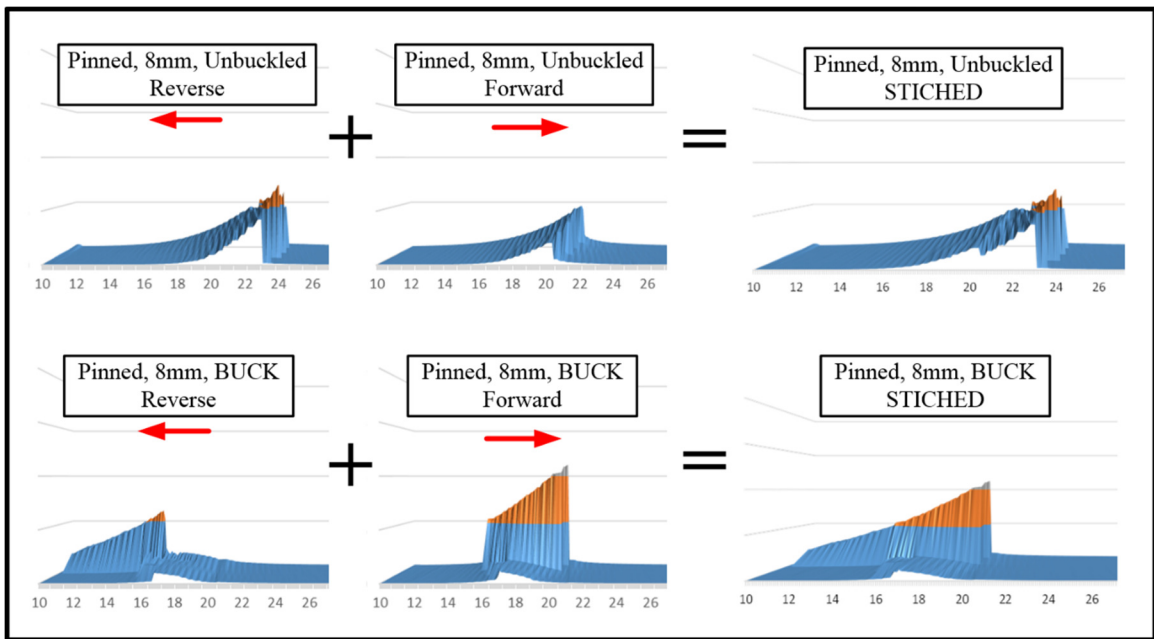


Figure 120. Stitching method for the pinned device with 8mm compliance arms combining bandwidths.

Evaluating new performance indices for the stitched pinned device with 8mm compliance arms shows increased performance when HEO is achieved. Once stitched, it is independent of sweep direction and shows the devices full potential in a HEO state.

Figure 121 below shows the stitched performance metric for the pinned device with 8mm compliance arms.

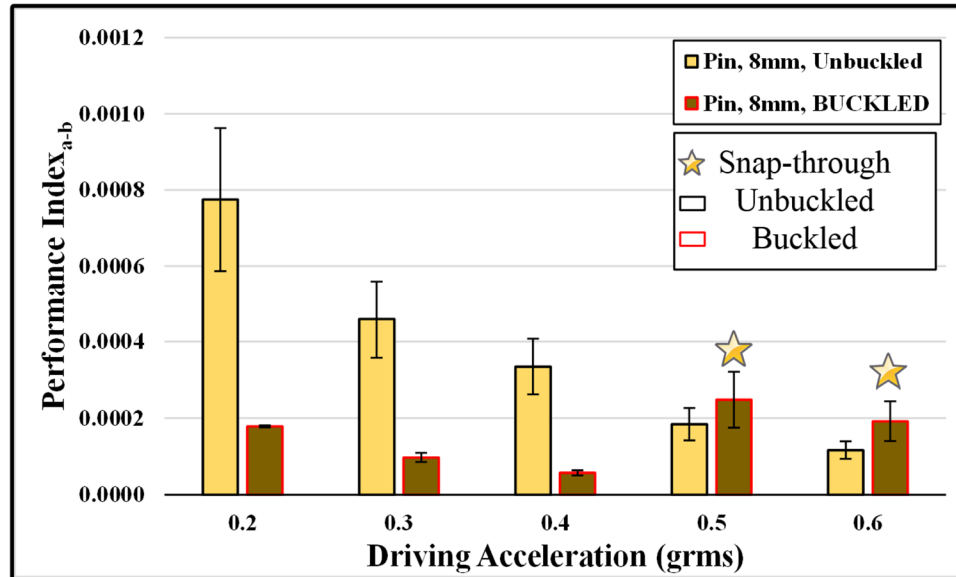


Figure 121. Performance index from stitching for the pinned device with 8mm compliance arms.

Nothing really useful is gained from the NPD metric because the operation of the bi-stable buckled energy harvesters gives broader bandwidths and lowered operating frequency (higher P_{rms} values were not a generally noticeable trend). The results for FOM_{BW} shows that the metric did increase during HEO when compared to the unbuckled cases for the same device. Though the overall FOM_{BW} metric is small compared to others, it does give us a way to compare the devices to each other and see what benefits buckling and snap-through can have. The FoM_{BW} metrics are shown in figure 122 below for the forward and reverse cases. Increasing these metrics to a scale comparable with the better performing devices in literature will require material refinement, optimized geometry, and extensive testing. Numerical values for the metrics are shown in the Appendix (ENERGY HARVESTER METRICS) along with geometry and mass values used to calculate them. Common metric values and power outputs are reported in literature and can be found in [4], [161], [8], [9], [98]. The mass was essentially the same for all energy harvesters because changing compliance are geometry did not change induce a significant change in that parameter and was verified using a scale.

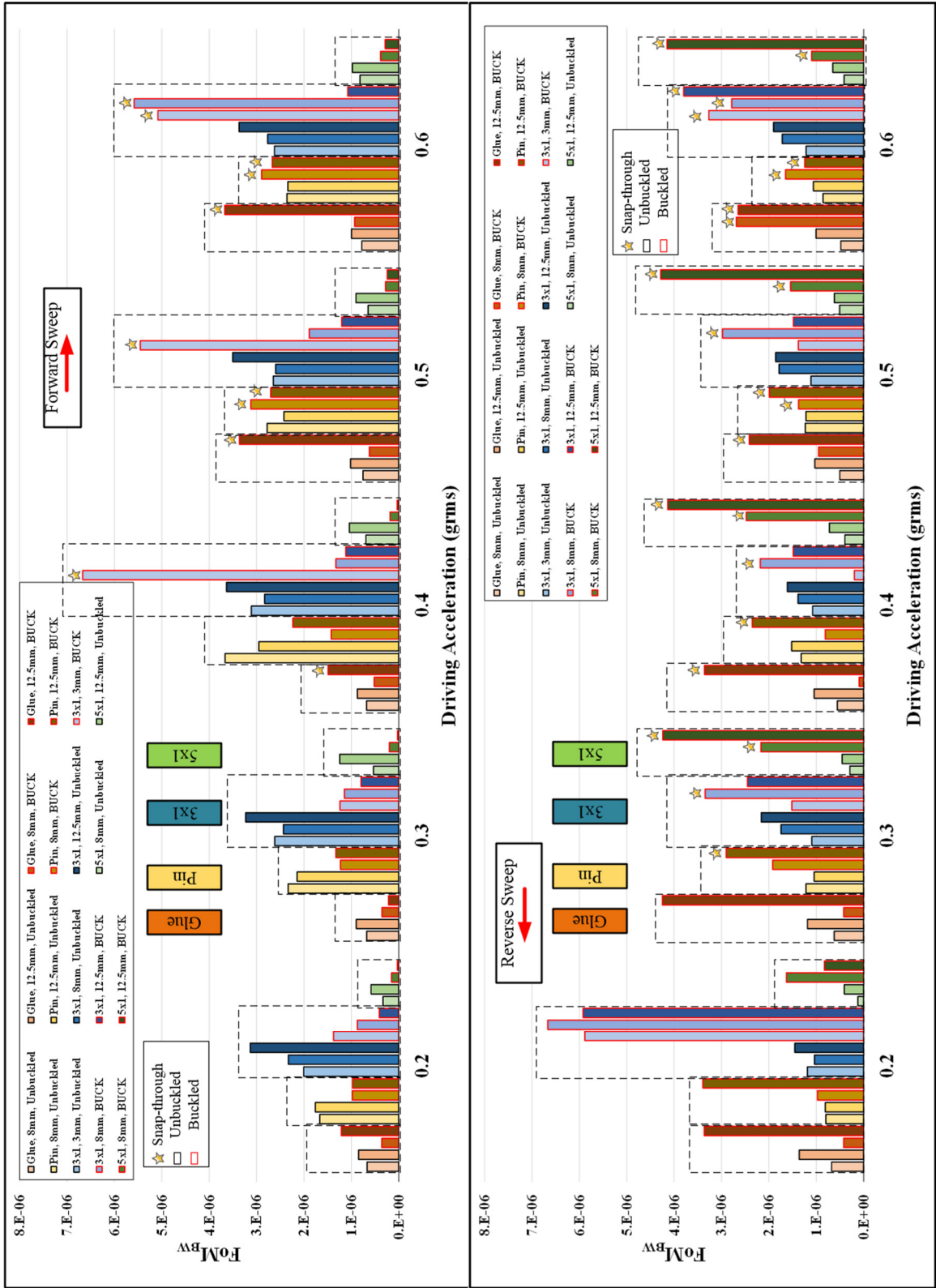


Figure 122. FoM_{BW} metric for the bi-stable buckled energy harvesters in the forward (left) and reverse (right) sweep direction.

H. Promotion into High Energy Orbits

Non-linear buckled devices such as the prototypes evaluated in this article generally exhibit chaotic behavior in response to an acceleration input. Normal, low energy, snap-through behavior is governed by strange attractors that demonstrate stochastic voltage responses and provide little benefit in terms of peak rms power generation. However, if extra energy is put into the system, the device investigated herein can be pushed into a more periodic, high energy orbital state that can be maintained. Associated with these high energy orbitals are very large displacement amplitudes that can greatly increase power performance for a given input acceleration.

The buckled devices probed in this work were promoted into high energy orbitals by generating a Gaussian input monopulse three times as high as the driving sinusoidal audio wave and superimposing it onto this signal in phase. The result created a rapidly decaying acceleration chirp or impulse that momentarily pushed the device at a higher acceleration. Based on previous works [44], it was theorized that this impulse would provide sufficient additional energy into the structure to enter a high energy orbital state and increase device power production.

Determining what frequency to drive the devices at while imposing a monopulse was done by using the value found at peak performance in swept forward experiments from prior prototypes of the same geometry but swept at a faster rate. Data analysis on the power generation had not been done so it was not known whether the devices would exhibit spring stiffening or softening. To judge the stability and ease of promotion, experiments were performed at f_p and ± 2 Hz. Acceleration for the experiments ranged from 0.1 to 0.8 g_{rms} . Chirp tests were not performed on the glued pin version of the device. A plot of the pinned devices undergoing a chirp excitation is shown in figure 123 below.

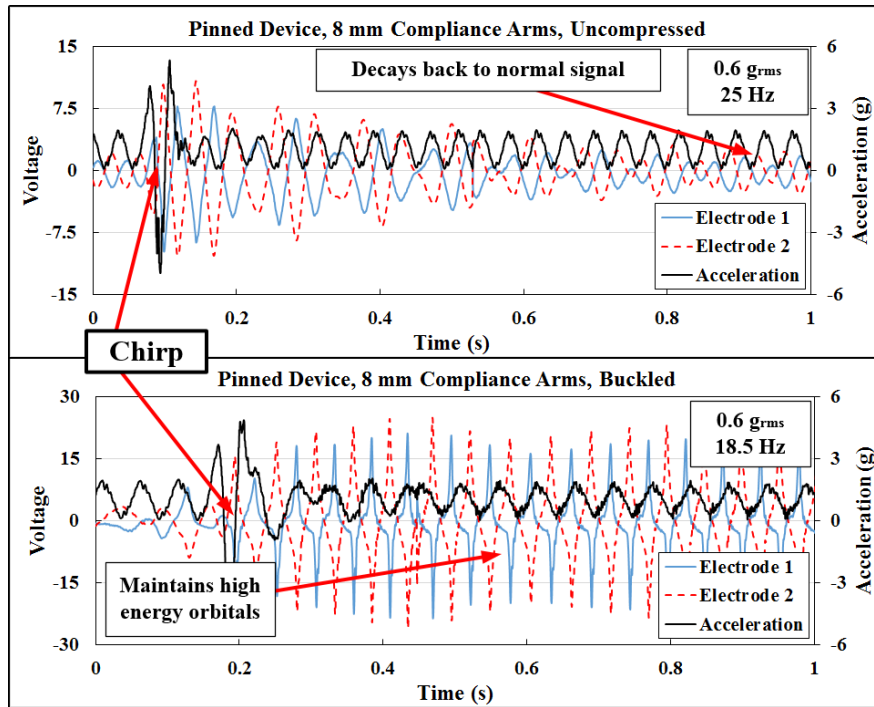


Figure 123. Chirp response of the pinned device in the unbuckled (above), compared to the maintained high-energy orbital in the buckled configuration (below).

All experiments for the chirp excitation are shown in table 24 below. Values in bold and blue exhibited high energy orbital (HEO) operation after an in-phase chirp and either temporarily or constantly maintained that state. During HEO operation the proof mass displacement amplitude greatly increases as well as the voltage output. Some devices would exhibit HEO for 1 to 3 seconds until ultimately going back to their normal oscillation state which could be a non-snap-through or a continuous snap-through state.

Table 24. Chirp results for the 8 mm length compliance arm devices. Bold indicates devices that can be induced into high energy orbitals.

Base Accel (g _{rms})	Pinned			3x1 mm			5x1 mm		
	Fr-2 (Hz)	Fr (Hz)	Fr+2 (Hz)	Fr-2 (Hz)	Fr (Hz)	Fr+2 (Hz)	Fr-2 (Hz)	Fr (Hz)	Fr+2 (Hz)
0.1	18.5	20.5	22.5	22.5	24.5	26.5	22.5	24.5	26.5
0.2	17.0	19.0	21.0	22.0	24.0	26.0	21.5	23.5	25.5
0.3	15.5	17.5	19.5	21.5	23.5	25.5	21.0	23.0	25.0
0.4	14.5	16.5	18.5	21.0	23.0	25.0	20.0	22.0	24.0
0.5	14.0	16.0	18.0	20.5	22.5	24.5	19.5	21.5	23.5
0.6	18.5	20.5	22.5	21.0	23.0	25.0	18.5	20.5	22.5
0.7	18.0	20.0	22.0	20.0	22.0	24.0	16.0	18.0	20.0
0.8	18.0	20.0	22.0	19.5	21.5	23.5	18.0	20.0	22.0

High energy orbits may be identified by large displacement/velocity operation curves plotted against voltage or power. Erturk et al. identified high energy orbits of a bi-stable energy harvester by using a velocity vs voltage plot and a velocity as a function of time plot [44] as shown below in figure 124. Data for low-energy versus high-energy states for the bi-stable buckled device can similarly be deduced from figure 123 above.

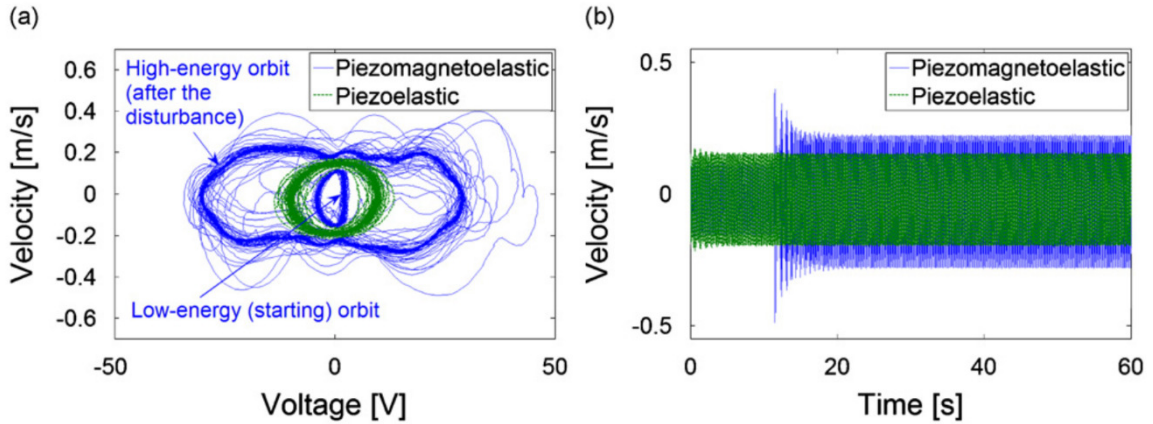


Figure 124. High energy orbit operation of a non-linear VEH [44].

I. Discussion of Compliance Arm Effect and HEO

Power generation for the devices above is not very impressive compared to other constructed VEHS when considering the size of the prototypes. This is because PVDF in a single d_{31} electrode arrangement is not very efficient at generating and collecting enough charge on a per unit strain bases. These piezoelectric elements were chosen due to their cost efficiency and design convenience (can cut any PVDF strip you like with scissors). One way to improve power output is to choose a more efficient medium like PZT or AlN.

Optimum load resistance was quite high for the PVDF strips but that was to be expected. This is the primary reason the custom data acquisition system was built; so as to not allow a parasitic load drop through the internals of the DAQ and only through the chosen load resistors. The selected optimum load resistance of $30\text{ M}\Omega$ was within 10% of the maximum power generating performance given a constant input acceleration for all tested devices in load resistance testing.

Free damping experiments usually led to greatly different damping ratios. This is due to the sensing mechanism used, which was the PVDF electrode signal that is essentially

the average strain effect of the sensing area. It is assumed that the structure buckles as if it were pinned in the middle giving no charge neutralization points over the electrodes but there still can be out of plane movement due to the geometry of the compliance arms. The damping linear and non-linear models give interesting results. While it is entirely appropriate to say the non-linear model does not give an accurate damping ratio, it is worthwhile to mention that some of the buckled gain plots are not necessarily perfect representations of a spring stiffening/softening behavior. This can be seen in figure 117 b above and also deduced from the fact that the non-linear model should almost always give a lower damping ratio value than the linear model given an ideal gain plot. From the outcomes, compression almost always increases the damping ratio for these VEH. It would seem that a value of 3 to 6% is a good estimate for the damping ratio in future FEA analysis given the data presented here.

It is interesting to note that the uncompressed devices mostly exhibited a stiffening non-linearity due to their voltage outputs. On the other hand all of the buckled devices had a softening non-linearity where their response was largest and broadest when swept in a reverse direction. This of course only applies to the region where snap-through is not occurring. One reoccurring aspect of snap-through and HEOs is that it seems to extend the frequency response of the device on the lower end during a reverse sweep as seen in figure 118 d). Snap-through action of the devices almost always improves the maximum P_{rms} value obtained compared to the unbuckled case and does broaden the higher power FWHM operating condition. The downside is that these benefits are only obtained at a sufficient input acceleration to achieve intra-well actuation. After a sufficient amount of time in the bi-stable regime, devices such as the 3x1 mm and pinned setup tend to kick into HEO's quite easily and can be audibly heard and seen. These performance improvements come from the fact that the device can generate higher voltages (given the same acceleration input) in HEO actuation then it can in the stochastic snap-through actuation.

The performance index shows that stitching together frequency content in the forward and reverse sweeps during HEO may only slightly improve the metric, if at all. Since the performance of the given devices during HEO increase the lower frequency content, the added benefit is only achieved if the extra content is significantly above the measured bandwidth region. Using the FoM_{BW} shows that HEO operation does increase

the metric for all buckled devices when compared to their unbuckled state with the exception of the buckled 3x1 devices at 0.2 g_{rms} . This device had an interestingly large bandwidth even though HEO was not achieved. In the forward direction, the 3x1 device with 3mm compliance arms had an 82.1% higher FoM_{BW} metric than any other device. In the reverse direction, excluding the 3x1 devices at 0.2 g_{rms} , all buckled devices tended to have much higher FoM_{BW} metrics.

Promotion into high energy orbitals is a fascinating aspect of bi-stable devices and can be induced in these prototypes at driving accelerations as low as 0.3 g_{rms} . As stated above the frequency regime chosen to do the chirp experiments was done before a full sweep data analysis so the frequencies of the chirp analysis tended to be slightly higher than the stability region for HEO. An example of this is that the 5x1 mm device would only exhibit HEOs momentarily at 18 Hz and 0.6 g_{rms} which was the lower frequency end of the experiment but going back and repeating the 0.6 g_{rms} experiments at 16 Hz resulted in the device maintaining HEOs. Looking back at the 5x1 mm devices reverse frequency sweep chart indicated that 18 Hz was just on the cusp of the power drop off point for that prototype.

J. Torque Arm Effect Conclusion

The effects of compliance arms on bi-stable buckled devices actuated via torque are quantified. Optimum load resistance for all devices is around 30 M Ω . Peak operating frequencies are between 18 to 30 Hz and snap-through actuation occurring as low as 0.3 g_{rms} . Damping ratios are produced for free and driven scenarios with an average damping ratio of 4.1%. Non-buckled devices generally had lower damping ratios but not by much if the devices are not overly compressed. The buckled 3x1 mm device with the shortest compliance arms generated 12.6 μ W at 21.1 Hz and was the highest rms power of all devices tested.

Snap-through behavior increases power output (up to 102.2%) in almost all devices. Buckled glued devices outperformed all unbuckled glued devices. Devices that are buckled but do not exhibit snap-through perform significantly worse than their unbuckled counterparts (except the buckled glued device). Too much compressive stress (applied beyond the threshold for inducing buckling) increased the snap-through acceleration

threshold to an unrealistic level. These bi-stable devices can be promoted into HEOs by applying a perturbing force. HEOS increased power output while being driven by the same input sine wave before the monopulse was applied.

The glued pinned devices performed poorly in the forward sweep direction but had comparable power results in the reverse sweep. Pinned devices were the easiest to promote into HEOs. The 3x1 devices generated the most power than all other devices. 5x1 devices performed poorly compared to the 3x1 which shows that an optimum width of the PLA compliance arms exists. Compliance arm length functioned as a snap-through performance modifier which could increase torsional resistance but prevent out of plane deflection thus creating a shallower energy well hump. Compliance arm length for the glued devices did increase power as length increased because the steel rod essentially disallowed out of plane deflection for the lengths tested.

CHAPTER X

SUMMARY

A new bi-stable buckled device actuated via torque arms has been fabricated and tested. Expectations for this new device is that it will operate with a wide bandwidth. Multiple macro size prototypes that test bi-stability and switching actuation feasibility were constructed. This gave insight into how the different levels of compressive stress affected snap-through performance. Prototyping without a piezoelectric material on the MEMS scale was also done with an 'S' shaped center buckled beam. ANSYS models predicting and the beams out of plane displacement matched up well.

Piezoelectric materials such as PZT and PVDF are investigated as possible candidates for the energy harvester. Spin on sol-gel PZT required high temperatures to promote the highly piezoelectric β -phase. It also has a high tensile stress which opposes the desired compressive stress needed in the MEMS device. Processing parameters for a desired thickness of PZT are derived. Saturated hysteresis loops show that the thin films are indeed piezoelectric. PVDF films do not require high processing temperatures or result in highly stressed structural layers. FTIR tests show that β -phase is present in almost all hydrated salt samples but requires vacuum annealing to promote a viable poled sample. Simple macro film testing using large electrodes was prone to shorting via flaws in the film. Corona poling did not have this problem.

Modeling the center compressed beam using the finite difference method was done which showed the deflection, angle, moment, and shear force given geometric, material properties, and compress inputs. Due to the complexities of the device, a numerical model is quite difficult knowing the dynamic PDE equations governing the structure. Thus the FEA package ANSYS was used to determine buckled behavior. Snap through force and displacement values are estimated and match up well with experimental results. Linear

pre-stressed modal analyses are accomplished to estimate resonance frequencies on the micro scale.

After a successful MEMS prototype was accomplished, a new device with active piezoelectric materials is attempted. Die containing d_{31} and d_{33} electrode configurations are designed with variable geometry bi-stable buckled beam devices. Also fabricated are cantilever beam harvesters which allow for PZT film piezoelectric coefficient measurements. Execution of the fabrication process revealed delamination between the bottom electrodes and the SiO_2 which occurred after the high temperature PZT anneal step. Some devices survived the high temperature process but a misalignment on the last etching step meant that only three die remained possibly aligned. Interesting SEM images revealed that no buckling occurred in the center beams of the surviving devices. Tensile stress from the PZT and electrode layers combined with stress relaxation during the high temperature PZT annealing phase were determined to be the cause. Further progress on the MEMS device will require a redesign with the PZT step done first or selecting a piezoelectric material that has low processing temperatures and favorably compressive stress.

A macro version of the VEH was constructed with commercial PVDF strips to have a better understanding of the operation and potential benefits. It consisted of stainless steel shim stock as the buckled 'S' beam and compliance arms. A 3D printed brace made of PLA constituted the torque arms and used 2-56 nuts as proof masses. The device is buckled by different amounts to show the effect of a "just bi-stable" device and an overly compressed device. Quasi-static behavior was estimated using ANSYS and then compared to experimental data collected via a custom mini MTS machine and 123D catch 3D DIC software. Higher compression resulted in higher forces and thus larger mass displacements to cause switch into another state.

Dynamic testing of the macro concept was accomplished on a custom shaker table using an input impedance of $3.3 \text{ M}\Omega$ and four channels. Two strips are placed on the center beam while the other two are on the torque arms. Constant acceleration frequency sweeps in the forward and reverse direction are done on the 0, 0.13, and 0.25 mm compressed devices. In-between certain compression levels the device operates at a significantly lowered frequency and wider bandwidth when continuous inter-well operation is achieved. Too much compression requires much higher acceleration values to exhibit this behavior.

Voltage responses from the torque arms accounted for about 25% of the total power generated. Perturbing the system when below the threshold of inter-well actuation can cause the system to go into high energy orbital operation, thus increasing power output while maintain the same input driving force. Peak power output was also highest during high energy orbitals.

Non-linear harmonic sweeps in ANSYS are done using a transient analysis with sinusoidal input displacements that represent constant accelerations. Damping from experimental tests are input using Rayleigh coefficients. Emulating linearly increasing frequency sweeps with constant accelerations via displacements required the use of the Fresnel function for a closed form solution and was not simple. Actual input displacements for ANSYS were calculated using Excel and some simplified assumptions which agreed well with the closed form solutions. Experimental gain sweep data agreed well for the unbuckled case using a linear harmonic analysis and was best estimated using a displacement input and a full modal solution method. The buckled case sweep was not estimated well using a linear harmonic analysis and only slightly improved on matching amplitude with the non-linear harmonic sweep. Snap-through operation evaluation using ANSYS will require significant computing power due to the large amount of time steps needed.

A method of simulating the power generated using ANSYS was devised and compared with experimental data. Since the PVDF strips were more compliant than the steel center beam we could assume that the charges generated did not affect the stiffness of the system by much. Thus a script was written to compute the summation of longitudinal strain through the center of each PVDF strip. That data was taken to excel and used as a charge generation source in a RC electrical circuit. Amplitudes for the power estimation were appreciable to the experimental data, though frequency broadening and shifting could not be simulated.

Since the MEMS devices require simple planar constructed constraints, the effects of the compliance arms on the VEH are evaluated. Four cases were evaluated and are the steel gauge wire that is perfectly pinned, steel gauge wire that is firmly glued, 3x1 mm PLA rectangular cross section, and 5x1 mm PLA rectangular cross section. Compliance arm lengths are also evaluated. Optimum driving electrical loads were evaluated for the

PVDF piezoelectric strips which didn't seem to change by much given buckled and unbuckled states. Non-linear damping ratios are evaluated using a modified equation for the half power bandwidth method. From this a rough estimate of a damping ratio to use in ANSYS was obtained.

P_{rms} for all setups was evaluated in the forward and reverse sweeps experiments as well as snap-through and high energy orbital operation identification. Given a set acceleration value, HEO operation can significantly improve the power output when compared to the same setup in the unbuckled state. If HEO was not obtained then the buckled devices always performed lower than their unbuckled counterparts. Peak RMS power generation was not necessarily higher during HEO when compared to devices in the unbuckled state but bandwidth and lower frequency power extension did increase the area under the operational frequency curve.

Comparing the device with normalized metrics proved difficult. Since the VEH in question is being evaluated for potential performance characteristic increases and not necessarily being optimized to compete with other VEHS at this time, it did not compare well with other energy harvesters on a metric scale. It could, however, be compared to the other torque actuated bi-stable energy harvesters in this research. The performance index and FoM_{BW} metric was evaluated for all cases in the compliance arm effect cases. HEO operation of this device increases the bandwidth if said device is induced into HEO. Performance index metrics evaluated at -3 dB did not show much improvement even when the bandwidths were stitched to give a true evaluation of the device. This is because the performance index does not weight the extra lower frequency content when the -3 dB bandwidth stays the same. The FoM_{BW} metric of HEO operation did show improvements to the metric when compared to devices that did not or were not buckled except for one case. That case was the 3x1 devices at the lowest acceleration. It tended to have a low P_{rms} but an interestingly broad bandwidth when buckled.

High energy orbital operation could be achieved by adding additional energy into the buckled system. This had the overall effect of generating higher P_{rms} while keeping the continuous driving force the same. Not all devices stayed in HEO if outside a given frequency range and driving acceleration.

Macro VEH evaluation has shown that a perfectly pinned constraint will not necessarily give better performance. In fact a rectangular compliance arm could outperform the perfectly pinned scenario, assuming these results scale well. Another observation is that compliance arm length should be short and flexible to prevent out-of-plane movement but allow some torsional flexibility.

CHAPTER XI

FUTURE WORKS

Advancing this concepts performance will require more understanding of the FEA model in the buckled state, realizing a working MEMS fabrication routine, and incorporation of the device into a VEH application. As of now the buckled experimental data is frequency shifted with the FEA modeling capability. The reason for this needs to be investigate and ameliorated if any optimization routine is to be accomplished; especially in the snap-through acceleration range. The MEMS devices fabricated so far have fractured PZT layers resulting from thermal stress development, thus generating voltage from them is unlikely. Moving to a lower processing temperature piezoelectric like AlN should fix this problem. Lastly, fabricating the MEMS or macro device into a useful package with rectification and storage circuitry would give insight into real world performance proof of concept data.

A. Design Optimization Feasibility

Eventually, an optimized energy harvesting beam will be created with emphasis placed on power density. ANSYS has an optimum design routine built into it and incorporates such things as design, state, and objective variables. Design variables are parameters that you specify at the beginning of model construction such as geometry, loads, and material properties. State variables are the specific outcomes of the solution such as stress, strain, weight, and voltage. Only one objective variable is defined which is the one that is minimized for the ANSYS analysis. If multiple variables need to be minimized, then a scheme which incorporates both variables into one quantifying factor should be used; then that one quantifying factor will be the objective variable.

Power estimation methods like the one used in this dissertation are very appropriate for FEA models. Even more so in the case of default ANSYS (14.5) because it does not have piezoelectric SHELL elements. The RC discrete circuit solutions used in Excel can be incorporated into an ANSYS APDL post script that would evaluate power after each iteration is solved. Parameter variables like RMS power, peak power, RMS voltage, peak voltage, HWFM bandwidth could feasibly be extracted using a sweeping window that is 2 to 3 times the longest period of the input sine wave. Of course the downside of this method is the length of time per iteration.

Other optimal design paths that would reduce processing time include constructing an equivalent circuit model. Models like these can be solved via OrCAD or MATLAB quite easily. Cantilever beam simulation is straightforward because the force transferred to the piezoelectric material via a tip displacement is linear in the small deflection regime. This makes the transduction value a constant in the circuit diagram. It is unknown at this point how the center pre-stressed beam for the concepts will be incorporated into the lumped parameter optimization model because its function as an oscillator is complex in nature. Snap-through behavior will not be exhibited until a proper amount of torque is transferred to the mid-section of the device. If the value of the torque is too small, then only small vibrational effects will be seen by the center beam.

B. High Energy Orbital Stitched Bandwidth

As stated before, the bandwidth of the devices in the high energy orbital switching state should be evaluated for all future devices. Perturbance schemes which induce HEO actuation at different accelerations and frequencies should be incorporated so that additional benefits can be evaluated. The author suggests finding the peak resonance point at a given acceleration level, inducing HEO, then moving the frequency forward at a known rate. Repeat the experiment while moving backwards and stitch the two P_{rms} regimes together. This can be done for all acceleration levels to give insight into the true frequency band of operation during HEO.

C. Potential Additional Advancements

A multiple node type device (multiple constrained buckled beam) is being fabricated alongside the main devices being researched in this proposal. We would like to investigate if it can snap-through multiple compressed areas of a beam with a single input. The hope is that whatever benefits that is realized from the normal bi-stable energy harvesters may be amplified in this device. If a mathematical model can be derived for the normal devices then it can be extended to these; hopefully without too much trouble. A picture of the multi-node device is shown below in figure 125.

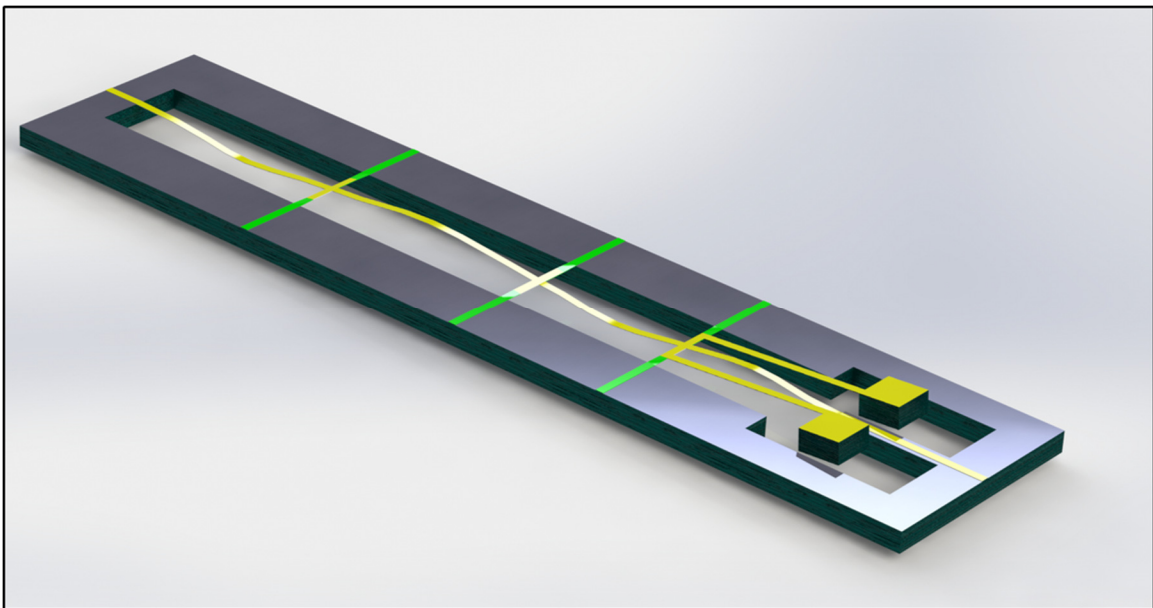


Figure 125. Multiple node bi-stable device being fabricated.

Actuating our device is of real interest for future research. Using the proposed mechanism as a latching actuator allows for things such as low power electrical switches, memory modules, precision stages, and optical switches. Tough obstacles to overcome are the percent strain that piezoelectrics can achieve without electrical breakdown. Outcomes for this part of the project are switching voltages and achievable displacements with voltage applied.

Semi-crystalline piezoelectrics like PVDF have lower piezo coefficients but are capable of larger strains. This is also a possible solution to make the device more compliant by removing material such as polyimide and replacing it with PVDF. Though it would

replace the polyimide layer it would also require a new set of electrode photomasks. PVDF can be spun on by using a solvent dissolving method and is reported in multiple literatures. There is no high temperature firing step required for this fabrication path but a high voltage poling step must be done. The poling routine exposes the device to a high electric field with some literature using two copper electrodes sandwiching a μm thick film and using 3,000 volts [25].

One of the most interesting things to accomplish with this project is the implementation of the energy harvester into an actual accumulation circuit. This would allow for the charging of a capacitor and possibly the activation of a sensor to transmit data. We would require a rectifier, a DC-DC amplifier, and a control circuit to run the accumulator circuit. Usually a full bridge rectifier is considered costly in terms of efficiency because of the voltage drop associated with the diodes.

REFERENCES

- [1] IEEE standard on piezoelectricity (ANSI-IEEE std 176-1978), 1978. IEEE, New York, NY.
- [2] PZT Wet Etching. Website, 2004. Last accessed 2/4/2015. <http://ssel-sched.eecs.umich.edu/wiki/Public.PZT%20Wet%20Etching.ashx>.
- [3] Ningli An, Hongzhong Liu, Yucheng Ding, Min Zhang, and Yiping Tang. Preparation and electroactive properties of a PVDF/nano- TiO_2 composite film. *Applied Surface Science*, 257(9):3831 – 3835, 2011.
- [4] B Ando, S Baglio, C Trigona, N Dumas, L Latorre, and P Nouet. Nonlinear mechanism in mems devices for energy harvesting applications. *Journal of Micromechanics and Microengineering*, 20(12):125020, 2010.
- [5] S Arscott, N Smith, R Kurchania, S J Milne, and R E Miles. Sol-gel derived $Pb(Zr, Ti)O_3$ thin films on GaAs. *Semiconductor Science and Technology*, 13(2):244, 1998.
- [6] H Bardaweel, O Al Hattamleh, R Richards, D Bahr, and C Richards. A Comparison of piezoelectric materials for MEMS power generation. In *Proc. 6th Int. Workshop Micro and Nanotechnology for Power Generation and Energy Conversion Applications*, pages 207 – 210, 2006.
- [7] C. F. Beards. *Engineering Vibration Analysis with Application to Control Systems*. Butterworth-Heinemann, 1995.
- [8] S P Beeby, R N Torah, M J Tudor, P Glynn-Jones, T O'Donnell, C R Saha, and S Roy. A micro electromagnetic generator for vibration energy harvesting. *Journal of Micromechanics and Microengineering*, 17(7):1257, 2007.
- [9] S P Beeby, M J Tudor, and N M White. Energy harvesting vibration sources for microsystems applications. *Measurement Science and Technology*, 17(12):R175, 2006.
- [10] Ferdinand P. Beer, E. Russell Johnston, Jr., and John T. DeWolf. *Mechanics of Materials*. MCGraw Hill, 4th edition, 2006.

- [11] D. Berdy, B. Jung, J. Rhoads, and D. Peroulis. Increased-bandwidth, meandering vibration energy harvester. In *Solid-State Sensors, Actuators and Microsystems Conference*, pages 2638 – 2641, 2011.
- [12] D.F. Berdy, P. Srisungsitthisunti, Byunghoo Jung, Xianfan Xu, J.F. Rhoads, and D. Peroulis. Low-frequency meandering piezoelectric vibration energy harvester. *Ferroelectrics and Frequency Control, IEEE Transactions on Ultrasonics*, 59(5):846 – 858, 2012.
- [13] A. Bertacchini, S. Scorcioni, D. Dondi, L. Larcher, P. Pavan, M.T. Todaro, A. Campa, G. Caretto, S. Petroni, A. Passaseo, and M. De Vittorio. AlN-based mems devices for vibrational energy harvesting applications. pages 119 – 22, Piscataway, NJ, USA, 2011.
- [14] V Bharti, T Kaura, and R Nath. Ferroelectric hysteresis in simultaneously stretched and corona-poled PVDF films. *Dielectrics and Electrical Insulation, IEEE Transactions on*, 4(6):738 – 741, 1997.
- [15] Vivek Bharti and R Nath. Piezo-, pyro- and ferroelectric properties of simultaneously stretched and corona poled extruded poly(vinyl chloride) films. *Journal of Physics D: Applied Physics*, 34(5):667, 2001.
- [16] Jeremie Bouchaud. High Value MEMS Market Overview. 2011. Last Accessed 3/21/2012. http://cmp.imag.fr/conferences/dtip/dtip2011/ppt/DTIP_highvalueMEMS_iSuppli_hando ut.pdf.
- [17] Jeremie Bouchaud. MEMS Market Tracker, 2011. Last Accessed 3/21/2012. http://www.isuppli.com/Abstract/P13577_20120117095302.pdf.
- [18] C. R. Bowen, L. J. Nelson, R. Stevens, M. G. Cain, and M. Stewart. Optimisation of interdigitated electrodes for piezoelectric actuators and active fibre composites. *Journal of Electroceramics*, 16(4):263 – 269, 2006.
- [19] L. Bu, X.M. Wu, X.H. Wang, and L.T. Liu. A packaged electrostatic energy harvester with micro-molded bulk electrets. In *Micro Electro Mechanical Systems (MEMS), 2013 IEEE 26th International Conference on*, pages 853 – 856, 2013.
- [20] Louis Bucciarelli, Jr. Engineering Mechanics of Structures, Chapter 8, 2002. Last Accessed 3/18/2012. <http://web.mit.edu/emech/dontindex-build/>.

- [21] Changlong Cai, Jing Huang, Yujia Zhai, Weihong Ma, and Weiguo Liu. Patterning of pzt thin films. *Chinese Optics Letters*, 8(s1):210 – 212, 2010.
- [22] V F Cardoso, G Minas, C M Costa, C J Tavares, and S Lanceros-Mendez. Micro and nanofilms of poly(vinylidene fluoride) with controlled thickness, morphology and electroactive crystalline phase for sensor and actuator applications. *Smart Materials and Structures*, 20(8):087002, 2011.
- [23] E Cattan, A Mollier, G Velu, and D Remiens. Effect of poling treatment on e_{31} piezoelectric constant of sputtered PZT thin films. *Le Journal de Physique IV*, 8(PR9):Pr9–229, 1998.
- [24] V. Challa, M. Prasad, Y. Shi, and T. Fisher. A vibration energy harvesting device with bidirectional resonance frequency tenability. *Smart Material Structures*, 17(1):10, January 2008.
- [25] Kiran Kumar Chatrathi. Microfabrication and characterization of PVDF copolymer thin films suitable for integrating into optical microsystems. Master's thesis, Concordia University, 2006.
- [26] Qin Chen, Don Natale, Bret Neese, Kailiang Ren, Minren Lin, QM Zhang, Matthew Pattom, KW Wang, Houfei Fang, and Eastwood Im. Piezoelectric polymers actuators for precise shape control of large scale space antennas. In *The 14th International Symposium on: Smart Structures and Materials & Nondestructive Evaluation and Health Monitoring*, pages 65241 – 65241. International Society for Optics and Photonics, 2007.
- [27] Shuting Chen, Xue Li, Kui Yao, Francis Eng Hock Tay, Amit Kumar, and Kaiyang Zeng. Self-polarized ferroelectric PVDF homopolymer ultra-thin films derived from Langmuir-Blodgett deposition. *Polymer*, 53(6):1404 – 1408, 2012.
- [28] Shuting Chen, Kui Yao, Francis Eng Hock Tay, and Chung Lee Liow. Ferroelectric poly(vinylidene fluoride) thin films on Si substrate with the β phase promoted by hydrated magnesium nitrate. *Journal of Applied Physics*, 102(10):104108, 2007.
- [29] Jinrong Cheng and Zhongyan Meng. Thickness-dependent microstructures and electrical properties of PZT films derived from sol-gel process. *Thin Solid Films*, 385(1-2):5 – 10, 2001.
- [30] Jennifer Chu. Shake, rattle and ... power up? Last Accessed 2/4/2015. <http://web.mit.edu/newsoffice/2011/power-from-vibrations-0914.html>, September 2011.

- [31] J. Chug and H.H. Yoo. Dynamic analysis of a rotating cantilever beam by using the finite element method. *Journal of Sound and Vibration*, 249(1):147 – 164, 2002.
- [32] T G Cooney and L F Francis. Processing of sol-gel derived PZT coatings on non-planar substrates. *Journal of Micromechanics and Microengineering*, 6(3):291, 1996.
- [33] F. Cottone, P. Basset, R. Guillemet, D. Galayko, F. Marty, and T. Bourouina. Bistable multiple-mass electrostatic generator for low-frequency vibration energy harvesting. In *Micro Electro Mechanical Systems (MEMS), 2013 IEEE 26th International Conference on*, pages 861 – 864, 2013.
- [34] F. Cottone, L. Gammaitoni, H. Vocca, M. Ferrari, and V. Ferrari. Piezoelectric buckled beams for random vibration energy harvesting. *Smart Materials and Structures*, 21(3):035021 (11 pp.), 2012.
- [35] Tim R Dargaville, Mathias C Celina, Julie M Elliott, Pavel M Chaplya, Gary D Jones, Daniel M Mowery, Roger A Assink, Roger L Clough, and Jeffrey W Martin. *Characterization, performance and optimization of PVDF as a piezoelectric film for advanced space mirror concepts*. Sandia National Laboratories, 2005.
- [36] W.O. Davis. Measuring quality factor from a nonlinear frequency response with jump discontinuities. *J Microelectromech S*, 20(4):968 – 75, 2011.
- [37] Young Ho Do, Woo Suk Jung, Min Gyu Kang, Chong Yun Kang, and Seok Jin Yoon. Preparation on transparent flexible piezoelectric energy harvester based on PZT films by laser lift-off process. *Sensors and Actuators A: Physical*, 200(0):51 – 55, 2013.
- [38] Hugo Durou, G.A. Ardila-Rodriguez, A. Ramond, X. Dollat, C. Rossi, and D. Esteve. Micromachined bulk PZT piezoelectric vibration harvester to improve effectiveness over low amplitude and low frequency vibrations. 2010.
- [39] R Elfrink, T M Kamel, M Goedbloed, S Matova, D Hohlfeld, Y van Andel, and R van Schaijk. Vibration energy harvesting with aluminum nitride-based piezoelectric devices. *Journal of Micromechanics and Microengineering*, 19(9):094005, 2009.
- [40] Samir A. Emam. *A Theoretical and Experimental Study of Nonlinear Dynamic of Buckled Beams*. PhD thesis, Virginia Polytechnic Institute and State University, 2002.
- [41] Samir A. Emam and Ali H. Nayfeh. Nonlinear responses of buckled beams to subharmonic-resonance excitations. *Nonlinear Dynamics*, 35(2):105–122, 2004.

- [42] Samir A. Emam and Ali H. Nayfeh. On the nonlinear dynamics of a buckled beam subjected to a primary-resonance excitation. *Nonlinear Dynamics*, 35(1):1–17, 2004.
- [43] C.C. Enz, A. El-Hoiydi, J. D. Decotignie, and V. Peiris. Wisenet: an ultralow-power wireless sensor network solution. *Computer*, 37(8):62 – 70, 2004.
- [44] A. Erturk and D.J. Inman. Broadband piezoelectric power generation on high-energy orbits of the bistable Duffing oscillator with electromechanical coupling. *Journal of Sound and Vibration*, 330(10):2339 – 2353, 2011.
- [45] Daniel M. Esterly. Manufacturing of poly(vinylidene fluoride) and evaluation of its mechanical properties. Master's thesis, Virginia Polytechnic Institute and State University, 2002.
- [46] S. Ezhilvalavan and V.D. Samper. Ferroelectric properties of wet-chemical patterned $PbZr_{0.52}Ti_{0.48}O_3$ films. *Applied Physics Letters*, 86(7):72901 – 1.
- [47] Long-Shen Fan, Yu-Chong Tai, and R. S. Muller. IC-processed electrostatic micromotors. *Sensors and Actuators*, 20(1-2):41 – 7, 1989.
- [48] W. Fang and J. A. Wickert. Post buckling of micromachined beams. *Journal of Micromechanics and Microengineering*, 4(3):116 – 22, 1994.
- [49] Micheal Friswell, S Faruque Ali, Onur Bilgen, Sondipon Adhikari, Arthur W Lees, and Grzegorz Litak. Non-linear piezoelectric vibration energy harvesting from a vertical cantilever beam with tip mass. *Journal of Intelligent Material System*, 23:1505 – 1521, 2012.
- [50] NS Gajbhiye, PK Pandey, and P Smitha. Low-temperature synthesis of nanostructured PZT for dielectric studies. *Synthesis and Reactivity in Inorganic, Metal-Organic, and Nano-Metal Chemistry*, 37(6):431 – 435, 2007.
- [51] David Yang Gao. Finite deformation beam models and triality theory in dynamical post-buckling analysis. *International Journal of Non-Linear Mechanics*, 35(1):103 – 131, 2000.
- [52] José A Giacometti, Sergei Fedosov, and Mauro M Costa. Corona charging of polymers: recent advances on constant current charging. *Brazilian Journal of Physics*, 29(2):269 – 279, 1999.
- [53] U. R. Gowrishetty, K. M. Walsh, and D. Jackson. No-power vacuum actuated bistable MEMS SPDT switch. pages 1745 – 9, Piscataway, NJ, USA, 2010.

- [54] D. Guillou. New Manufacturing Methodology Substantially Reduces Smart MEMS Costs, 2003. Last Accessed 2/4/2015. <http://archives.sensorsmag.com/articles/1203/20/main.shtml>.
- [55] H Han, Y Nakagawa, Y Takai, K Kikuchi, S Tsuchitani, and Y Kosimoto. Microstructure fabrication on a β -phase PVDF film by wet and dry etching technology. *Journal of Micromechanics and Microengineering*, 22(8):085030, 2012.
- [56] R L Harne and K W Wang. A review of the recent research on vibration energy harvesting via bistable systems. *Smart Materials and Structures*, 22(2):023001, 2013.
- [57] Xujiang He and Kui Yao. Crystallization mechanism and piezoelectric properties of solution-derived ferroelectric poly(vinylidene fluoride) thin films. *Applied physics letters*, 89(11):112909, 2006.
- [58] Xiao Hui Xu, Bao Qing Li, Yan Feng, and Jia Ru Chu. Design, fabrication and characterization of a bulk-PZT-actuated MEMS deformable mirror. *Journal of Micromechanics and Microengineering*, 17(12):2439 – 2446, 2007.
- [59] iFixit. iPhone 4 Gyroscope Teardown, 2010. Last Accessed 2/4/2015. <http://www.ifixit.com/Teardown/iPhone-4-Gyroscope-Teardown/3156/1>.
- [60] K. Ikeda, H. Ishizuka, and A Sawada and K. Urushiyama. Vibration acceleration magnitudes of hand-held tools and workpieces. *Industrial Health*, 36(0019-8366):197 – 208, 1998.
- [61] Nathan Jackson, Rosemary O’Keeffe, Finbarr Waldron, Mike O’Neill, and Alan Mathewson. Influence of aluminum nitride crystal orientation on MEMS energy harvesting device performance. *Journal of Micromechanics and Microengineering*, 23(7):075014, 2013.
- [62] Madhusudhanan Jambunathan, Koray Karakaya, Rene Elfrink, Ruud Vullers, and Rob Van Schaijk. Influence of poling on RF and pulsed DC sputtered PZT thin films. In *Applications of Ferroelectrics (ISAF/PFM)*, 2011 International Symposium on Piezoresponse Force Microscopy and Nanoscale Phenomena in Polar Materials, pages 1 – 4. IEEE, 2011.
- [63] Sang-Soo Je, Tushar Sharma, Youngkyu Lee, Brijesh Gill, and John Xiaojing Zhang. A thin-film piezoelectric PVDF-TrFE based implantable pressure sensor using

- lithographic patterning. In *Micro Electro Mechanical Systems (MEMS), 2011 IEEE 24th International Conference on*, pages 644 – 647. IEEE, 2011.
- [64] Y. Jia and A.A. Seshia. Directly and parametrically excited bi-stable vibration energy harvester for broadband operation. In *Solid-State Sensors, Actuators and Microsystems 2013 Transducers Eurosensors XXVII: The 17th International Conference*, pages 454 – 457, 2013.
- [65] Yadong Jiang, Yun Ye, Junsheng Yu, Zhiming Wu, Wei Li, Jianhua Xu, and Guangzhong Xie. Study of thermally poled and corona charged poly(vinylidene fluoride) films. *Polymer Engineering & Science*, 47(9):1344 – 1350, 2007.
- [66] Yonggang Jiang, Syohei Shiono, Hiroyuki Hamada, Takayuki Fujita, Kohei Higuchi, and Kazusuke Maenaka. Low-frequency energy harvesting using a laminated PVDF cantilever with a magnetic mass. *Power MEMS*, pages 375 – 378, 2010.
- [67] Seok-Min Jung and Kwang-Seok Yun. A wideband energy harvesting device using snap-through buckling for mechanical frequency-up conversion. In *Micro Electro Mechanical Systems (MEMS), 2010 IEEE 23rd International Conference on*, pages 1207 – 1210, 2010.
- [68] T Kaura, R Nath, and MM Perlman. Simultaneous stretching and corona poling of PVDF films. *Journal of Physics D: Applied Physics*, 24(10):1848, 1991.
- [69] James M Kenney and Steven C Roth. Room temperature poling of poly (vinylidene fluoride) with deposited metal electrodes. *J. Res. Nat. Bur. Stand*, 84:447 – 453, 1979.
- [70] Dong-Won Kim, Gwang-Geun Lee, and Byung-Eun Park. The ferroelectric and electrical properties of P(VDF-TrFE) copolymer film. *Journal of the Korean Physical Society*, 51(2):719 – 722, August 2007.
- [71] Gi-Woo Kim and Jaehwan Kim. Compliant bistable mechanism for low frequency vibration energy harvester inspired by auditory hair bundle structures. *Smart Materials and Structures*, 22, 2013.
- [72] Vaden Komkov. Euler’s buckling formula and wirtinger’s inequality. *International Journal of Mathematical Education in Science and Technology*, 14(6):661 – 668, 1983.
- [73] A.N. Kounadis, C. Gantes, and G. Simitses. Nonlinear dynamic buckling of multi-DOF structural dissipative systems under impact loading. *International Journal of Impact Engineering*, 19(1):63 – 80, 1997.

- [74] Walter Lacarbonara, AliH. Nayfeh, and Wayne Kreider. Experimental validation of reduction methods for nonlinear vibrations of distributed-parameter systems: Analysis of a buckled beam. *Nonlinear Dynamics*, 17(2):95 – 117, 1998.
- [75] Brian Leclerc. Process optimization for solfilms PZT films. Master's thesis, Queen's University, 1999.
- [76] N. G. Ledermann. *Piezoelectric Acoustic Sensors and Ultrasonic Transducers Based on Textured PZT Thin Films*. Eacute, 2003.
- [77] Ching-Chich Leu, Ching-Pin Hsu, Cin-Guan Hong, and Chen-Ti Hu. Photochemical-induced self-seeding effect on lead zirconate titanate thin film. *J. Mater. Chem.*, 21:12991 – 13000, 2011.
- [78] Xue Li, Shuting Chen, Kui Yao, and Francis Eng Hock Tay. Ferroelectric poly(vinylidene fluoride) PVDF films derived from the solutions with retainable water and controlled water loss. *Journal of Polymer Science Part B: Polymer Physics*, 47(23):2410 – 2418, 2009.
- [79] J. M. Liu, B. Pan, H. L. W. Chan, S. N. Zhu, Y. Y. Zhu, and Z. G. Liu. Piezoelectric coefficient measurement of piezoelectric thin films: An overview. volume 75, pages 12 – 18, Singapore, Singapore, 2002.
- [80] W Q Liu, A Badel, F Formosa, Y P Wu, and A Agbossou. Novel piezoelectric bistable oscillator architecture for wideband vibration energy harvesting. *Smart Materials and Structures*, 22(3):035013, 2013.
- [81] Malik Loudini. *Timoshenko Beam Theory based Dynamic Modeling of Lightweight Flexible Link Robotic Manipulators*. InTech, 2010.
- [82] James Lunt. Large-scale production, properties and commercial applications of polylactic acid polymers. *Polymer Degradation and Stability*, 59:145 – 152, 1998. Issues 1-3.
- [83] Suresha K Mahadeva, John Berring, Konrad Walus, and Boris Stoeber. Effect of poling time and grid voltage on phase transition and piezoelectricity of poly(vinylidene fluoride) thin films using corona poling. *Journal of Physics D: Applied Physics*, 46(28):285305, 2013.

- [84] M. Majer and M. Husak. Bistable system for energy harvesting. In *Advanced Semiconductor Devices Microsystems (ASDAM), 2012 Ninth International Conference on*, pages 311 – 314, 2012.
- [85] JM Marshall, Q Zhang, and RW Whatmore. Corona poling of highly (001)/(100)-oriented lead zirconate titanate thin films. *Thin Solid Films*, 516(15):4679 – 4684, 2008.
- [86] Julia Vivian Martinez. Fabrication, materials, and characterization for efficient MEMS power generation. Master’s thesis, Washington State University, 2004.
- [87] Marcin Marzencki, Yasser Ammar, and Skandar Basrour. Integrated power harvesting system including a MEMS generator and a power management circuit. *Sensors Actuators A: Physical*, 145:363 – 70, 2008.
- [88] R. Masana and M. F. Daqaq. Energy harvesting in the super-harmonic frequency region of a twin-well oscillator. *Journal of Applied Physics*, 111(4), 2012.
- [89] Ravindra Masana and Mohammed F. Daqaq. Relative performance of a vibratory energy harvester in mono- and bi-stable potentials. *Journal of Sound and Vibration*, 330(24):6036 – 6052, 2011.
- [90] Ravindra Masana and Mohammed F. Daqaq. Response of duffing-type harvesters to band-limited noise. *J Sound Vib*, 332(25):6755 – 6767, 2013.
- [91] C.R. McInnes, D.G. Gorman, and M.P. Cartmell. Enhanced vibrational energy harvesting using nonlinear stochastic resonance. *Journal of Sound and Vibration*, 318(4-5):655 – 662, 2008.
- [92] S. Meninger, J. O. Mur-Miranda, R. Amirtharajah, A. P. Chandrakasan, and J. H. Lang. Vibration-to-electric energy conversion. *IEEE Transactions on Very Large Scale Integration (VLSI) Systems*, 9(1):64 – 76, 2001.
- [93] Tristan Miller. *Design of Corona Poling Apparatus*. UBC Electrical Engineering, September 2011.
- [94] Ioanna G. Mina. High frequency transducers from PZT films. Master’s thesis, Pennsylvania State University, 2007.
- [95] Paul D. Mitcheson, Eric M. Yeatman, G. Kondala Rao, Andrew S. Holmes, and Tim C. Green. Energy harvesting from human and machine motion for wireless electronic devices. *Proceedings of the IEEE*, 96(9):1457 – 1486, 2008.

- [96] Peter Moeck. X-ray diffraction (XRD). PDF online, March 2004. Portland State University.
- [97] Behzad Mohammadi, Ali Akbar Yousefi, and Samad Moemen Bellah. Effect of tensile strain rate and elongation on crystalline structure and piezoelectric properties of PVDF thin films. *Polymer Testing*, 26(1):42 – 50, 2007.
- [98] K. Najafi, T. Galchev, E.E. Aktakka, R.L. Peterson, and J. McCullagh. Microsystems for energy harvesting. In *Solid-State Sensors, Actuators and Microsystems Conference (TRANSDUCERS), 2011 16th International*, pages 1845–1850, June 2011.
- [99] A. Nisar, Nitin Afzulpurkar, Banchong Mahaisavariya, and Adisorn Tuantranont. MEMS-based micropumps in drug delivery and biomedical applications. *Sensors and Actuators B. Chemical*, 130(2):917 – 942, 2008.
- [100] T. Omori, H. Makita, M. Takamatsu, K. Hashimoto, M. Yamaguchi, and M. Sato. Preparation of piezoelectric PZT micro-discs by sol-gel method. *Tech Dig Sens Symp*, 17:69 – 72, 2001.
- [101] Tatsuya Omori, Hirofumi Makita, Mutsumi Takamatsu, Ken-ya Hashimoto, Masatsune Yamaguchi, and Manabu Sato. Preparation of piezoelectric PZT micro-discs by sol-gel method. *The transactions of the Institute of Electrical Engineers of Japan. A publication of Sensors and Micromachines Society*, 121(9):496 – 500, 2001.
- [102] Kenji Omote, Hiroji Ohigashi, and Keiko Koga. Temperature dependence of elastic, dielectric, and piezoelectric properties of "single crystalline" films of vinylidene fluoride trifluoroethylene copolymer. *Journal of Applied Physics*, 81(6):2760 – 2769, 1997.
- [103] Oxford Instruments. *Basic PECVD Plasma Processes (SiH4 based)*, 2003. Last Accessed 2/4/2015. <http://wcam.engr.wisc.edu/Public/Reference/Deposition/PECVD%20of%20silicon%20nitride%20and%20oxide.pdf>.
- [104] J. H. Park, H. Y. Bae, Y. R. Oh, Y. J. Kim, H. Y. Kim, and Y. H. Huh. Tensile test of lead zirconate titanate (PZT)/Platinum (Pt) thin film. *Materialwissenschaft und Werkstofftechnik*, 42(5):478 – 484, 2011.

- [105] Jong Cheol Park, Jae Yeong Park, and Yoon-Pyo Lee. Modeling and characterization of piezoelectric d_{33} - mode MEMS energy harvester. *Microelectromechanical Systems, Journal of*, 19(5):1215 – 1222, October 2010.
- [106] Sergio P Pellegrini, Nima Tolou, Mark Schenk, and Just L. Herder. Bistable vibration energy harvesters: A review. *J Intel Mat Syst Str*, (11):1045389 – 12444940, 2013.
- [107] Gabriele Perego, Gian Domenico Cella, and Catia Bastioli. Effect of molecular weight and crystallinity on poly(lactic acid) mechanical properties. *Journal of Applied Polymer Science*, 59(1):37 – 43, 1996.
- [108] Kris Pister. On the limits and applications of MEMS sensor networks. Technical report, UC Berkeley, 2001. Defense Science Study Group Report.
- [109] D. S. Popescu, D. C. Dascalu, M. Elwenspoek, and T. Lammerink. Silicon active microvalves using buckled membranes for actuation. volume 2, pages 305 – 8, Stockholm, Sweden, 1995.
- [110] D. S. Popescu, T. S. J. Lammerink, and M. Elwenspoek. Buckled membranes for microstructures. pages 188 – 92, New York, NY, USA, 1994.
- [111] D.A. Porter and T.A. Berfield. A bi-stable buckled energy harvesting device actuated via torque arms. *Smart Mater Struct*, 23(7):075003 (12 pp.), 2014.
- [112] Khaled S Ramadan, D Sameoto, and S Evoy. A review of piezoelectric polymers as functional materials for electromechanical transducers. *Smart Materials and Structures*, 23(3):033001, 2014.
- [113] Subramaniyan Ramasundaram, Sun Yoon, Kap Jin Kim, and Jong Soon Lee. Direct preparation of nanoscale thin films of poly(vinylidene fluoride) containing β -crystalline phase by heat-controlled spin coating. *Macromolecular Chemistry and Physics*, 209(24):2516 – 2526, 2008.
- [114] Hemanta Kumar Rana. Dynamic analysis of fixed-fixed beams. Master's thesis, Rourkela National Institute of Technology, 2012.
- [115] Sahas Rathi, Xiaolang Chen, E. Bryan Coughlin, Shaw Ling Hsu, Charles S. Golub, and Michael J. Tzivanis. Toughening semicrystalline poly(lactic acid) by morphology alteration. *Polymer*, 52(19):4184 – 4188, 2011.

- [116] V.T. Rathod, D. Roy Mahapatra, Anjana Jain, and A. Gayathri. Characterization of a large-area PVDF thin film for electro-mechanical and ultrasonic sensing applications. *Sensors and Actuators A: Physical*, 163(1):164 – 171, 2010.
- [117] E. Reilly, L. Miller, R. Fain, and P. Wright. A study of ambient vibrations for piezoelectric energy conversion. *PowerMEMS*, pages 1 – 4, December 2009.
- [118] M. Renaud, P. Fiorini, and C. Van Hoof. Optimization of a piezoelectric unimorph for shock and impact energy harvesting. *Smart Materials and Structures*, 16(4):1125 – 1135, 2007.
- [119] M. Renaud, K. Karakaya, T. Sterken, P. Fiorini, C. Van Hoof, and R. Puers. Fabrication, modelling and characterization of MEMS piezoelectric vibration harvesters. *Sensors and Actuators A: Physical*, 145 and 146(0):380 – 386, 2008.
- [120] Ivo B Rietveld, Kei Kobayashi, Takuya Honjo, Kenji Ishida, Hirofumi Yamada, and Kazumi Matsushige. Electrospray induced ferroelectricity in poly (vinylidene fluoride) thin films. *Journal of Materials Chemistry*, 20(38):8272 – 8278, 2010.
- [121] S. Roundy. On the effectiveness of vibration-based energy harvesting. *Journal of Intelligent Material Systems and Structures*, 16(10):809 – 23, 2005.
- [122] S. Roundy, E. S. Leland, J. Baker, E. Carleton, E. Reilly, E. Lai, B. Otis, J. M. Rabaey, P. K. Wright, and V. Sundararajan. Improving power output for vibration-based energy scavengers. *IEEE Pervasive Computing*, 4(1):28 – 36, 2005.
- [123] S. Roundy and P. K. Wright. A piezoelectric vibration based generator for wireless electronics. *Smart Materials and Structures*, 13:1131, 2004.
- [124] S. Roundy, P. K. Wright, and J. Rabaey. A study of low level vibrations as a power source for wireless sensor nodes. *Computer Communications*, 26(11):1131 – 1144, 2003.
- [125] Salem Saadon and Othman Sidek. A review of vibration-based MEMS piezoelectric energy harvesters. *Energy Conversion and Management*, 52(1):500 – 504, 2011.
- [126] A. Salimi and Yousefi A. A. Ftir studies of β -phase crystal formation in stretched pvdf films. *Polymer Testing*, 22:699 – 704, 2003.
- [127] S Satapathy, Santosh Pawar, PK Gupta, and KBR Varma. Effect of annealing on the phase transition in poly (vinylidene fluoride) films prepared using polar solvent. *Bulletin of Materials Science*, 34(4):727 – 733, 2011.

- [128] J F Scott. Ferroelectrics go bananas. *Journal of Physics: Condensed Matter*, 20(2):021001, 2008.
- [129] V. Sencadas, S. Lanceros-Mendez, R.G. Filho, D.L. Chinaglia, and A.S. Pouzada. Influence of the processing conditions and corona poling on the morphology of β -PVDF. In *Electrets, 2005. ISE-12. 2005 12th International Symposium on*, pages 161 – 164, Sept 2005.
- [130] Tushar Sharma, Sang-Soo Je, Brijesh Gill, and John X.J. Zhang. Patterning piezoelectric thin film PVDF-TrFE based pressure sensor for catheter application. *Sensors and Actuators A: Physical*, 177(0):87 – 92, 2012.
- [131] D. Shen, J. H. Park, J. Ajitsaria, S. Y. Choe, H. C. Wickle, and D. J. Kim. The design, fabrication and evaluation of a MEMS PZT cantilever with an integrated si proof mass for vibration energy harvesting. *Journal of Micromechanics and Microengineering*, 18(5), 2008.
- [132] Tatiana Smelova-Reynolds and Earl H. Dowell. The role of higher modes in the chaotic motion of the buckled beam i. *International Journal of Non-Linear Mechanics*, 31(6):931 – 939, 1996. A Selective Perspective on Non-linear Mechanics: Problems and Techniques.
- [133] Tatiana Smelova-Reynolds and Earl H. Dowell. The role of higher modes in the chaotic motion of the buckled beam ii. *International Journal of Non-Linear Mechanics*, 31(6):941 – 950, 1996. A Selective Perspective on Non-linear Mechanics: Problems and Techniques.
- [134] R. Solecki and E. Conant. *Advanced Mechanics of Materials*. Oxford Press, 2003. New York.
- [135] Rui Song, Guangmei Xia, Xueqing Xing, Linghao He, Qiaoling Zhao, and Zhi Ma. Modification of polymorphisms in polyvinylidene fluoride thin films via water and hydrated salt. *Journal of colloid and interface science*, 401:50 – 57, 2013.
- [136] D. Spreemann, B Folkmer, and Y. Manoli. Realization of nonlinear hardening springs with predefined characteristic for vibration transducers based on beam structures. Darmstadt, Deutschland, 2011.
- [137] Gang Tang, Jing-quan Liu, He-sheng Liu, Yi-gui Li, Chun-sheng Yang, Dan-nong He, Viet Dzung Dao, Katsuhiko Tanaka, and Susumu Sugiyama. Piezoelectric mems

- generator based on the bulk PZT/silicon wafer bonding technique. *physica status solidi (a)*, 208(12):2913 – 2919, 2011.
- [138] R. N. Torah, S. P. Beeby, M. J. Tudor, T. O'Donnell, and S. Roy. Development of a cantilever beam generator employing vibration energy harvesting. pages 181 – 4, Piscataway, NJ, USA, 2006.
- [139] H. R. Trankler and O. Kanoun. Recent advances in sensor technology. volume 1, pages 309 – 16, Piscataway, NJ, USA, 2001.
- [140] Supreya Trivijitkasem and Krit Koyvanich. Characterization of lead lanthanum zirconate titanate (PLZT) ceramics sintered at various temperatures. *Kasetsart J.(Nat. Sci.)*, 41:192 – 197, 2007.
- [141] Hong-Jie Tseng, Wei-Cheng Tian, and Wen-Jong Wu. P(VDF-TrFE) polymer-based thin films deposited on stainless steel substrates treated using water dissociation for flexible tactile sensor development. *Sensors*, 13(11):14777 – 14796, 2013.
- [142] W. Y. Tseng and J. Dugundji. Nonlinear vibrations of a buckled beam under harmonic excitation. *Journal of Applied Mechanics*, 38:467 – 476, 1971.
- [143] Y.L. Tu and S.J. Milne. A study of the effects of process variables on the properties of PZT films produced by a single-layer sol-gel technique. *Journal of Materials Science*, 30(10):2507 – 2516, 1995.
- [144] Louis Van Blarigan, Per Danzl, and Jeff Moehlis. A broadband vibrational energy harvester. *Applied Physics Letters*, 100(25), 2012.
- [145] Benedetto Vigna. Mems epiphany. pages 1 – 6, Sorrento, Italy, 2009.
- [146] B. A. Walmsley, Y. Liu, X. Z. Hu, M. B. Bush, J. M. Dell, and L. Faraone. Poisson's ratio of low-temperature PECVD silicon nitride thin films. *Journal of Microelectromechanical Systems*, 16(3):622 – 627, 2007.
- [147] K. M. Walsh and U. R. Gowrishetty. No-power mems devices using buckled diaphragms and engineered stress. page 2 pp., Piscataway, NJ, USA, 2010.
- [148] Susan Walter, Thomas Herzog, Henning Heuer, Hagen Bartzsch, and Daniel Gloess. Smart ultrasonic sensors systems: potential of aluminum nitride thin films for the excitation of the ultrasound at high frequencies. *Microsystem Technologies*, 18(7-8):1193 – 1199, 2012.

- [149] William Weaver, Stephen Timoshenko, and Donovan Young. *Vibration Problems in Engineering, 5th Edition*. Wiley Interscience, 1990.
- [150] Liu Wen, Han MengDi, Meng Bo, Sun XuMing, Huang XianLiang, and Zhang HaiXia. Low frequency wide bandwidth MEMS energy harvester based on spiral-shaped PVDF cantilever. *Sci China Ser E*, 57(6):1068 – 72, 2014.
- [151] M. Williams, B. Griffin, B. Homeijer, B. Sankar, and M. Sheplak. The nonlinear behavior of a post-buckled circular plate. pages 349 – 52, Piscataway, NJ, USA, 2007.
- [152] K. J. Winchester and J. M. Dell. Nano-indentation characterisation of PECVD silicon nitride films. pages 117 – 20, Piscataway, NJ, USA, 2000.
- [153] S. Yagnamurthy, I. Chasiotis, J. Lambros, R. Polcawich, J. Pulskamp, and M. Dubey. Mechanical properties of PZT films and their composites for RF-MEMS. volume 3, pages 1253 – 1259, Orlando, FL, United states, 2008.
- [154] Yaowen Yang and Lihua Tang. Equivalent circuit modeling of piezoelectric energy harvesters. *Journal of Intelligent Material Systems and Structures*, 20(18):2223 – 35, 2009.
- [155] Li-Ren Yao and Fu-Hsing Lu. Low vacuum deposition of aluminum nitride thin films by sputtering. *International Journal of Applied Ceramic Technology*, 10(1):51 – 59, 2013.
- [156] G. Yi and M. Sayer. An acetic acid/water based sol-gel PZT process. i. modification of Zr and Ti alkoxides with acetic acid. *Journal of Sol-Gel Science and Technology*, 6(1):65 – 74, 1996.
- [157] G. Yi and M. Sayer. An acetic acid/water based sol-gel PZT process ii. modification of Zr and Ti alkoxides with acetic acid. *Journal of Sol-Gel Science and Technology*, 6:75 – 82, 1996.
- [158] H. Zhang, Q. Xie, C. Qin, and L. Cai. Optimal design of piezoelectric cantilever for micro power. In *5th International Conference on e-Engineering & Digital Enterprise Technology*, 2006.
- [159] Jian Zhao, J. Jia, Xiaoping He, and Hongxi Wang. Post-buckling and snap-through behavior of inclined slender beams. *Journal of Applied Mechanics*, 75(4):041020 – 1, 2008.
- [160] Ke-lu Zheng, Jia-ru Chu, J., Jian Lu, and Heng LI. Study on wet-etching of PZT thin films. *Piezoelectrics & Acoustooptics*, 27:209, 2005.

[161] Dibin Zhu, Michael J Tudor, and Stephen P Beeby. Strategies for increasing the operating frequency range of vibration energy harvesters: a review. *Measurement Science and Technology*, 21(2):022001, 2010.

[162] Meiling Zhu, E. Worthington, and J. Njuguna. Analyses of power output of piezoelectric energy-harvesting devices directly connected to a load resistor using a coupled piezoelectric-circuit finite element method. *IEEE Transactions on Ultrasonics, Ferroelectrics and Frequency Control*, 56(7):1309 – 17, 2009.

APPENDIX A
(SYMBOLS AND ABBREVIATIONS)

List of Symbols

α	Rayleigh Mass Coefficient or Crystalline Phase
β	Rayleigh Stiffness Coefficient, Torsional Stiffness, or Crystalline Phase
c_{ij}	Elastic Stiffness Constant
C_p	Equivalent Capacitance
δ	Crystalline Phase
d_{ij}	Piezoelectric Strain Coefficient
D	Electric Displacement
$[e]$	ANSYS Piezoelectric Matrix
e_{ie}	Piezoelectric Constant
E	Electric Field or Young's Modulus
ε	Dielectric Permittivity, Strain, or Crystalline Phase
ε_0	Permittivity in a Vacuum
γ	Crystalline Phase
I	Second Moment of Inertia
k_{ij}, k	Coupling Factor or Spring Stiffness
λ	Wavelength or Eigen Factor
M	Moment
ν	Poisson's Ratio
ω_n	Angular Frequency of Mode n
P	Polarization, Power, or Compression Force
P_{rms}	Root Mean Square Power
Π	System Energy
R_{opt}	Optimal Resistance Load
s_{ij}	Elastic Compliance Constant
S	Strain Tensor
σ	Stress
T	Stress Tensor
τ	Time Constant
q	Charge Generated
Q	Charge or Quality Factor
V	Shear
V_{p-p}, V_{pp}	Peak to Peak Voltage
V_{rms}	Root Mean Square Voltage
W_{p-p}	Peak to Peak Watts
ζ	Damping Ratio

List of Abbreviations

ADC	Analog to Digital Converter
AMI	Acetone – Methanol – Isopropyl Cleaning Routine
ASIC	Application Specific Integrated Circuit
ATR	Attenuated Total Reflectance
BHF	Buffered Hydrofluoric Acid
BOE	Buffered Oxide Etch
CCFL	Cold-cathode Fluorescent Lamp
CMOS	Complementary Metal-Oxide Semiconductor
CVD	Chemical Vapor Deposition
DAQ	Data Acquisition
DBC	Doubly Constrained Beam
DCB	Doubly Constrained Beam
DIC	Digital Image Correlation
DIP	Dual Inline Package
DMA	Dimethylacetamide
DMF	Dimethylformamide
DRIE	Deep Reactive Ion Etching
FEA	Finite Element Analysis
FTIR	Fourier Transform Infrared Spectroscopy
FWHM	Full Width at Half Max
GEMC	Generalized Electromechanical Coupling Factor
HEO	High Energy Orbitals
ICP	Inductively Coupled Plasma
IEEE	Institute of Electrical and Electronics Engineers
LOC	Lab on a Chip
MEMS	Microelectromechanical Systems
MFC	Mass Flow Controller
NMP	N-Methyl-2-Pyrrolidone
PECVD	Plasma Enhanced Chemical Vapor Deposition
PID	Proportional-Integral-Derivative (controls)
PLA	Polylactic Acid
PVD	Physical Vapor Deposition
PVDF	Polyvinylidene Fluoride
PZT	Lead Zirconate Titanate
RIE	Reactive-Ion Etching
RMS	Root Mean Square
SCCM	Standard Cubic Centimeter per Minute
TA	Torque Arm (device)
TB	Timoshenko Beam
TBT	Timoshenko Beam Theory
VEH	Vibrational Energy Harvester
XRD	X-ray Diffraction

APPENDIX B (FIGURES AND TABLES)

Table 25. PZT samples setup and results.

Sample	SR-IPA-H20	Substrate	Coats Per Hopplate Treatment	Total Hopplate Treatments	Fired Coats	Spread (mm)	Spread Time (s)	Spin (rpm)	Spin Time (s)	Hot Plate 1 (°C)	Hot Plate 1 (min)	Hot Plate 2 (°C)	Hot Plate 2 (min)	Fire Temp (°C)	Ramp Rate (°C/min)	Hold Time (min)	Gas Flow	Caudy A	Caudy B	Thickness (mm)	Etch Thk (mm)	Peroxysulf? From XRD	Notes
Misc 1	11:1	S/S/O2	1	1	0	300	15	3000	45	100	5	300	5	N/A	N/A	N/A	N/A	1.971	0.0191	114.9	109.8		Heated
Misc 2	11:1	S/S/O2	1	0	0	300	15	3000	45	N/A	N/A	N/A	N/A	N/A	N/A	N/A	N/A	1.620	0.0137	378.0			Unheated
1a	11:1	S/S/O2	2	0	0	300	15	3000	30	N/A	N/A	N/A	N/A	N/A	N/A	N/A	N/A	1.579	0.0193	374.5			Unheated
1b	11:1	S/S/O2	2	0	0	300	15	3000	30	N/A	N/A	N/A	N/A	N/A	N/A	N/A	N/A	1.600	0.0124	314.5			Unheated
1c	11:1	S/S/O2	2	0	0	300	15	3000	30	N/A	N/A	N/A	N/A	N/A	N/A	N/A	N/A	1.585	0.0132	312.9			Unheated
2a	11:1	S/S/O2	2	0	0	300	15	3000	30	N/A	N/A	N/A	N/A	N/A	N/A	N/A	N/A	1.616	0.0132	296.9			Unheated
2b	11:1	S/S/O2	2	0	0	300	15	3000	30	N/A	N/A	N/A	N/A	N/A	N/A	N/A	N/A	1.613	0.0120	291.1			Unheated
2c	11:1	S/S/O2	2	0	0	300	15	3000	30	N/A	N/A	N/A	N/A	N/A	N/A	N/A	N/A	1.607	0.0127	289.4			Unheated
2d	11:1	S/S/O2	2	0	0	300	15	3000	30	N/A	N/A	N/A	N/A	N/A	N/A	N/A	N/A	1.617	0.0119	285.3			Unheated
2e	11:1	S/S/O2	2	0	0	300	15	3000	30	N/A	N/A	N/A	N/A	N/A	N/A	N/A	N/A	1.609	0.0125	294.8			Unheated
1a	11:1	S/S/O2	2	1	0	300	15	3000	30	100	1	300	2	N/A	N/A	N/A	N/A	1.752	0.0197	196.7			Heated
2a	11:1	S/S/O2	2	1	0	300	15	3000	30	100	1	300	2	N/A	N/A	N/A	N/A	1.752	0.0172	172.9			Heated
3a	11:1	S/S/O2	2	1	0	300	15	3000	30	100	1	300	2	N/A	N/A	N/A	N/A	1.937	0.0166	181.0			Heated
4a	11:1	S/S/O2	2	1	0	300	15	3000	30	100	1	300	2	N/A	N/A	N/A	N/A	1.734	0.0163	181.1			Heated
2a	11:1	S/S/O2	2	1	0	300	15	3000	30	100	1	300	2	N/A	N/A	N/A	N/A	1.759	0.0141	158.3			Heated
3a	11:1	S/S/O2	2	1	0	300	15	3000	30	100	1	300	2	N/A	N/A	N/A	N/A	1.762	0.0154	158.3			Heated
4a	11:1	S/S/O2	2	1	0	300	15	3000	30	100	1	300	2	N/A	N/A	N/A	N/A	1.736	0.0160	169.8			Heated
2a	11:1	S/S/O2	2	1	0	300	15	3000	30	100	1	300	2	N/A	N/A	N/A	N/A	1.736	0.0156	173.4			Heated
2b	11:1	S/S/O2	2	2	0	300	15	3000	30	100	1	300	2	N/A	N/A	N/A	N/A	1.782	0.0216	391.6			Heated
2c	11:1	S/S/O2	2	2	0	300	15	3000	30	100	1	300	2	N/A	N/A	N/A	N/A	1.800	0.0175	370.5			Heated
3a	11:1	S/S/O2	2	3	0	300	15	3000	30	100	1	300	2	N/A	N/A	N/A	N/A	1.775	0.0222	606.1			Heated
3b	11:1	S/S/O2	2	3	0	300	15	3000	30	100	1	300	2	N/A	N/A	N/A	N/A	1.751	0.0207	588.6			Heated
4a	11:1	S/S/O2	2	4	0	300	15	3000	30	100	1	300	2	N/A	N/A	N/A	N/A	1.809	0.0162	815.9			Heated
4b	11:1	S/S/O2	2	4	0	300	15	3000	30	100	1	300	2	N/A	N/A	N/A	N/A	1.785	0.0213	793.7			Heated
1a	11:1	S/S/O2	2	1	1	300	15	3000	30	100	1	300	2	550	5	30	None						No Crack
2a	11:1	S/S/O2	2	2	1	300	15	3000	30	100	1	300	2	550	5	30	None						No Crack
3a	11:1	S/S/O2	2	3	1	300	15	3000	30	100	1	300	2	550	5	30	None						No Crack
4a	11:1	S/S/O2	2	4	1	300	15	3000	30	100	1	300	2	480	5	30	None	2.086	0.0429	79.2			No Crack
1b	11:1	S/S/O2	2	1	1	300	15	3000	30	100	1	300	2	450	5	30	None	2.092	0.0351	183.9			No Crack
2b	11:1	S/S/O2	2	2	1	300	15	3000	30	100	1	300	2	450	5	30	None						No Crack
3b	11:1	S/S/O2	2	3	1	300	15	3000	30	100	1	300	2	450	5	30	None						No Crack
4b	11:1	S/S/O2	2	4	1	300	15	3000	30	100	1	300	2	450	5	30	None						No Crack
1c	12:1	S/S/O2	2	1	1	300	15	3000	30	100	1	300	2	550	5	30	None	1.872	0.0067	116.4			No Crack
1d	12:1	S/S/O2	2	1	1	300	15	3000	30	100	1	300	2	450	5	30	None	2.094	0.0391	79.5			No Crack
2c	12:1	S/S/O2	2	2	1	300	15	3000	30	100	1	300	2	550	5	30	None						No Crack
2d	12:1	S/S/O2	2	2	1	300	15	3000	30	100	1	300	2	450	5	30	None	2.141	0.0415	146.5			No Crack
3c	12:1	S/S/O2	2	3	1	300	15	3000	30	100	1	300	2	550	5	30	None						No Crack
3d	12:1	S/S/O2	2	3	1	300	15	3000	30	100	1	300	2	450	5	30	None	2.043	0.0384	233.0			No Crack
4c	12:1	S/S/O2	2	4	1	300	15	3000	30	100	1	300	2	550	5	30	None						No Crack
4d	12:1	S/S/O2	2	4	1	300	15	3000	30	100	1	300	2	450	5	30	None	2.098	0.0559	293.7			No Crack
Misc 3	11:1	S/S/O2/Ti/Pk	2	1	0	300	15	5000	60	100	1	400	2	N/A	N/A	N/A	N/A	2.149	0.0313	77.2			Heated
Misc 4	11:1	S/S/O2/Ti/Pk	2	1	0	300	15	4000	60	100	1	400	2	N/A	N/A	N/A	N/A	2.389	0.0122	86.1			Heated
1e	11:1	S/S/O2/Ti/Pk	2	1	1	300	15	3000	60	150	5	450	10	650	20	30	O2	2.27	0.0335	59.4			No Crack
2e	11:1	S/S/O2/Ti/Pk	2	2	1	300	15	3000	60	150	5	450	10	650	20	30	O2	2.632	0.1645	112.79			No Crack
1f	11:1	S/S/O2/Ti/Pk	2	1	0	300	15	4000	60	150	5	450	10	650	20	30	O2						No Crack
2f	11:1	S/S/O2/Ti/Pk	2	2	0	300	15	4000	60	150	5	450	10	650	20	30	O2						No Crack
1g	11:1	S/S/O2/Ti/Pk	2	1	0	300	15	5000	60	150	5	450	10	650	20	30	O2						No Crack
2g	11:1	S/S/O2/Ti/Pk	2	2	0	300	15	5000	60	150	5	450	10	650	20	30	O2						No Crack
perov1	11:1	S/S/O2/Ti/Pk	2	2	1	300	15	3000	60	175	5	N/A	N/A	450 then 650	20	30 then 60	O2	2.532	0.04976	165.84			Yes
perov2	11:1	S/S/O2/Ti/Pk	2	2	1	300	15	3000	60	175	5	N/A	N/A	450 then 650	20	30 then 60	O2	2.548	0.031	151.39			Yes
perov3	11:1	S/S/O2/Ti/Pk	2	2	1	300	15	3000	60	175	5	N/A	N/A	450 then 650	20	30 then 60	O2	2.57	0.042	149.91			Yes
perov4	11:1	S/S/O2/Ti/Pk	2	2	1	300	15	3000	60	175	5	N/A	N/A	450 then 650	20	30 then 60	O2	2.53	0.047	153.64			Yes

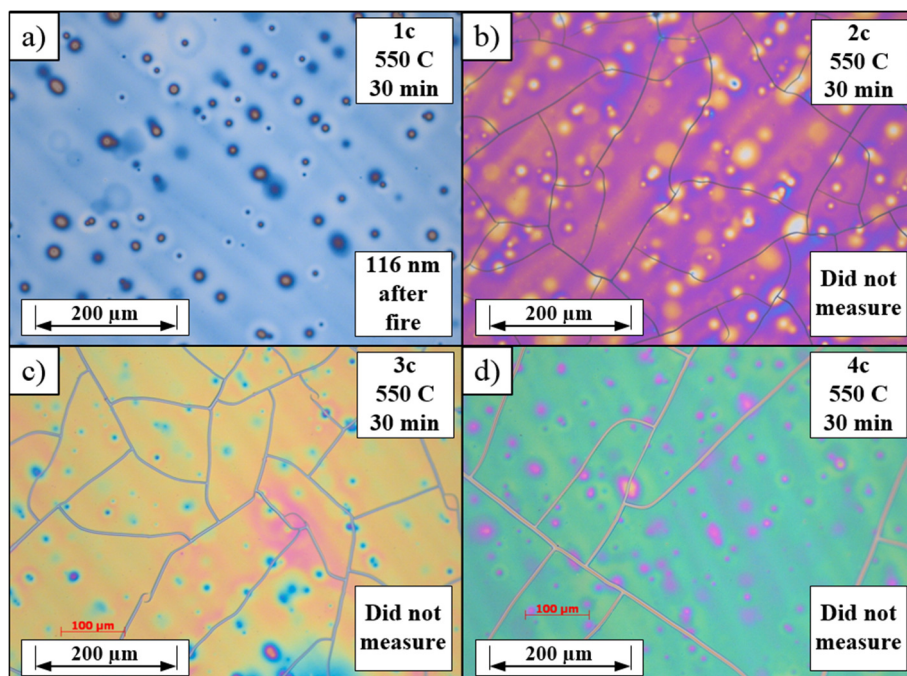


Figure 126. PZT (1:2:1) on SiO₂ annealed at 450 C in an ambient atmosphere for samples a) 1c, b) 2c, c) 3c, and d) 4c.

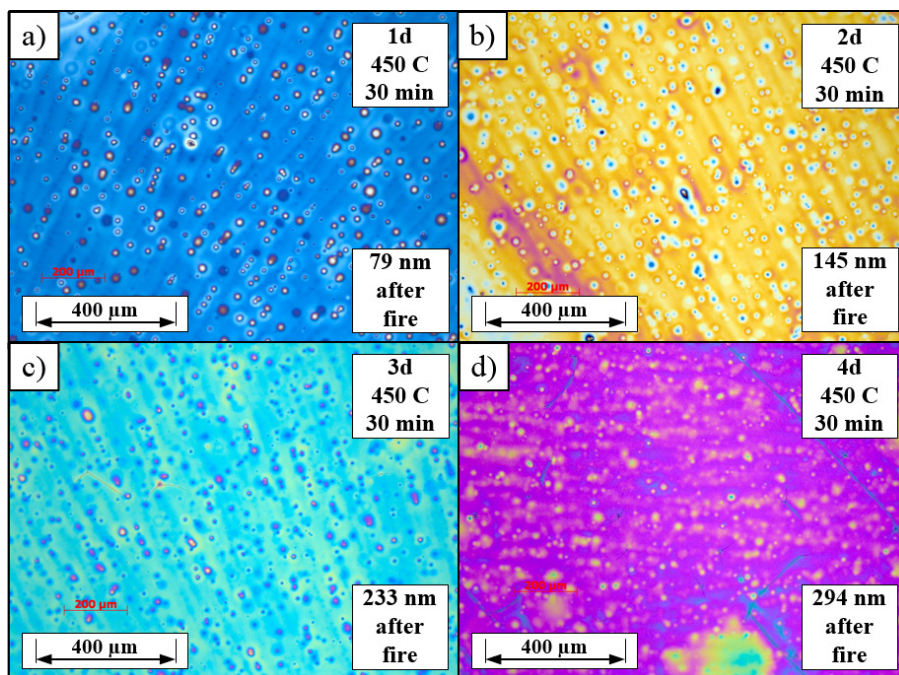


Figure 127. PZT (1:2:1) on SiO₂ annealed at 550 C in an ambient atmosphere for samples a) 1d, b) 2d, c) 3d, and d) 4d.

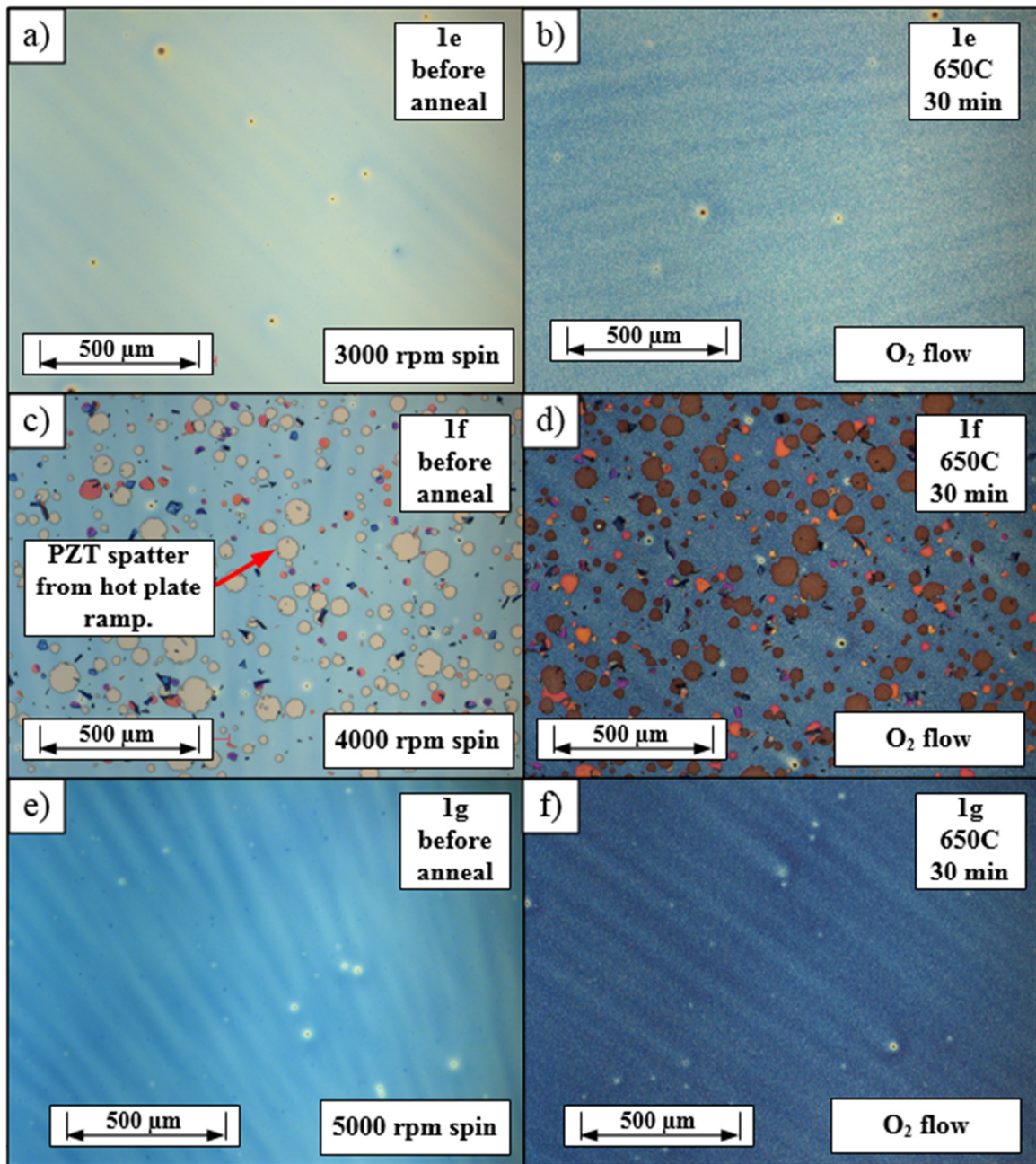


Figure 128. One coat of PZT (1:1:1) on platinum before and after being annealed at 650 C in an O₂ atmosphere for samples a) 1e, b) 1e, c) 1f, d) 2f, e) 1g, and f) 1g.

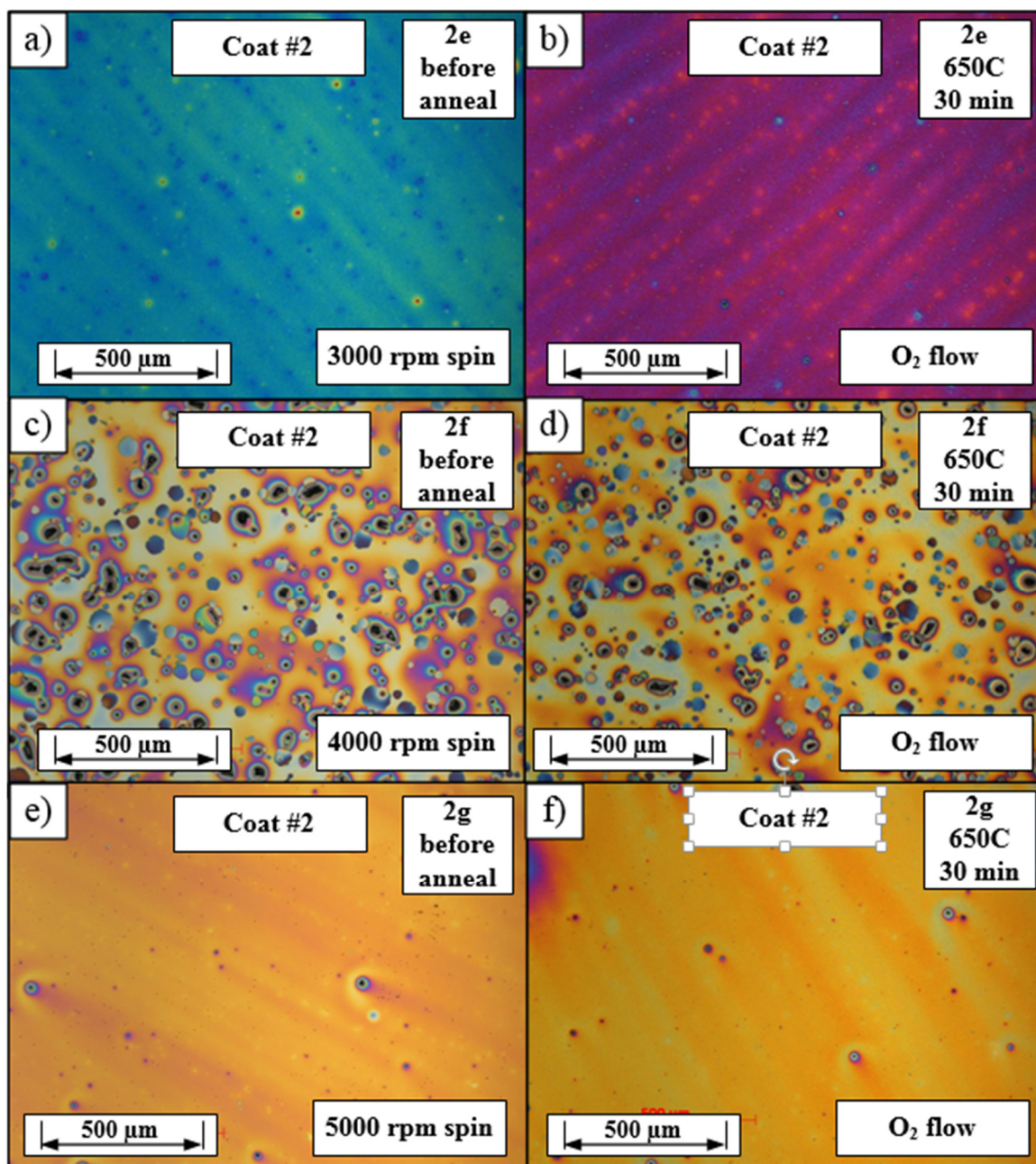


Figure 129. Two coat of PZT (1:1:1) on platinum before and after being annealed at 650 C in an O₂ atmosphere for samples a) 1e, b) 1e, c) 1f, d) 2f, e) 1g, and f) 1g.

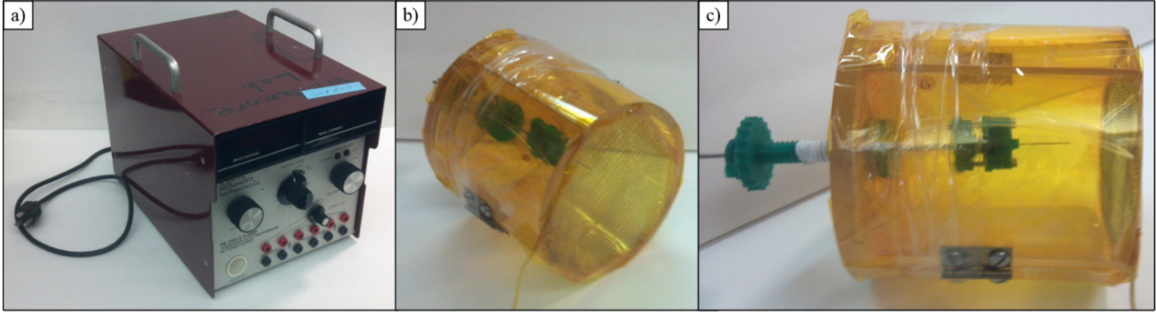


Figure 130. a) 250V DC power supply used for contact poling, b), c) prototype corona poling mechanism.

Table 26. A few results from the PVDF gel experiments.

Name	PVDF (wt%)	PVDF (MW)	Mg(NO ₃) ₂ 6H ₂ O (wt%)	Acetone (vol%)	DMF (vol%)	Solution Temp (C)	Spread Speed (rpm)	Spread Time (s)	Spin Speed (rpm)	Spin Time (s)	# of Coats	Hotplate Temp (C)	Anneal Temp (C)	Anneal Time (hr)	Film Thickness (µm)	Poling Voltage (V)	Poling Field (MV/cm)	Poling Time (Hr)	Poling Temp (C)	Rating	Notes
PVDF Film 1	20	534000	0	50	50	90	300	15	3000	60	1	90	90	5	7.1	150	21.12676	1	85	fair	Annealed on digital hot plate, no vent blowing. Film looks a little ununiform, can pole at 150V, broke down at 250V, Pt sub, did not check with FTIR
PVDF Film 2	20	534000	0	50	50	90	300	15	5000	60	1	90									
Samp1	20	534000	0	50	50	25	300	15	3000	60	1	120	135	2	5						
Samp2	20	534000	0	50	50	25	300	15	4000	60	1	120	135	2	4.3						
Samp3	10	275000	0	50	50	25	0	0	500	20	2	120	135	4	7						
Samp4	10	275000	0	50	50	25	0	0	500	20	3	120	135	4	7						
Samp5	5	275000	0.2	50	50	25	0	0	500	20	2	120	135	4	2						
Samp6	5	275000	0.2	50	50	25	0	0	500	20	4	120	135	4	3 to 10						
Samp7	10	275000	0	50	50	25	0	0	500	20	2	120	135	4	4.8						
Samp8	5	275000	0.2	50	50	25	0	0	500	20	2	120	135	4	1.9						
Samp9	10	275000	0	50	50	25	0	0	500	20	1	120	0	0	2.5						
Samp10	10	275000	0	50	50	90	300	15	1000	30	1	90	0	0							
Samp11	20	534000	0	50	50	90	0	0	5000	20	1	0	0	0		250					
Samp12	20	534000	0	50	50	90	0	0	5000	20	1	90	0	0							
Samp13	20	534000	0	50	50	0	0	0	5000	20	1	90	0	0							
Samp14	20	534000	0	50	50	0	0	0	5000	20	1	90	90	0.5							
Samp15	20	534000	0	50	50	0	0	0	2000	20	1	90	0	0							
Samp16	20	534000	0	50	50	0	0	0	2000	20	1	90	0	0							
Samp17	20	534000	0	50	50	0	0	0	2000	20	1	90	0	0							
Samp18	20	534000	0	50	50	0	0	0	3000	20	1	90	0	0							
Samp19	20	534000	0	50	50	90	300	15	3000	60	1	90									half BETA, half ALPHA
Samp20	10	534000	0.2	50	50	0	0	0	3000	10	3	120	120	0.5							
Samp21	10	534000	0.2	50	50	0	0	0	3000	10	1	120	120	0.5							
Samp22	10	534000	0.2	50	50	0	0	0	500	20	1	120	120	0.35							
Samp23	10	534000	0.2	50	50	0	0	0	500	20	1	140	140	0.9							
Samp24	10	534000	0.2	50	50	0	0	0	1000	20	1	140	140	0.2							
Samp25	10	534000	0.2	50	50	0	0	0	1000	20	1	25	90	0.333							
Samp26	10	534000	0.2	50	50	0	0	0	1000	20	1	140	140	0.2							
Samp27	10	534000	0.2	50	50	0	0	0	1000	20	1	90	90	0.333							
Samp28	10	534000	0.2	50	50	0	0	0	1000	20	1	90	90	2							
Samp29	10	534000	0.2	50	50	0	0	0	1000	20	1	90	90	0							
Samp30	10	534000	0.2	50	50	0	0	0	1000	20	1	90	0	0							
Samp31	10	534000	0.2	50	50	0	0	0	500	20	1	90	0	0							
Samp32	20	534000	0	50	50	0	0	0	4000	20	1	50	50	5							
Samp33	20	534000	0	50	50	0	0	0	2000	20	1	65	0	0		100		5	80	beta (none at 1275)	si sub, blow on, no beta at 1275, voltage response is about 20 to 40mV. Broke down at 150V. Might need to do a sinusoidal poling.

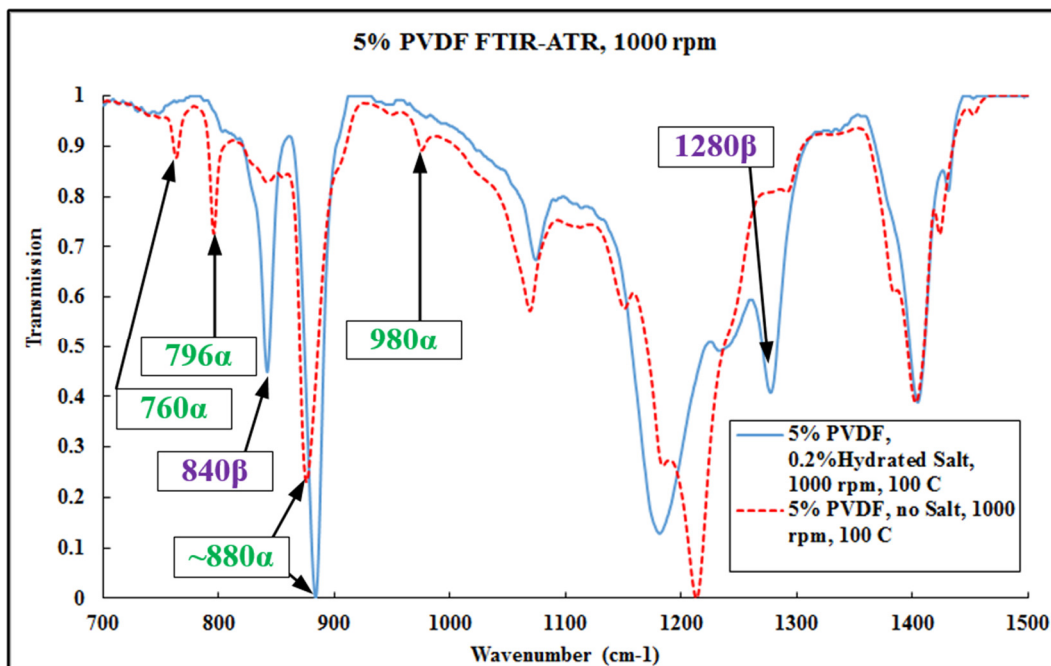


Figure 131. FTIR-ATR results for 5% PVDF with and without hydrated salt. Gel spun on individual die at 1000 rpm.

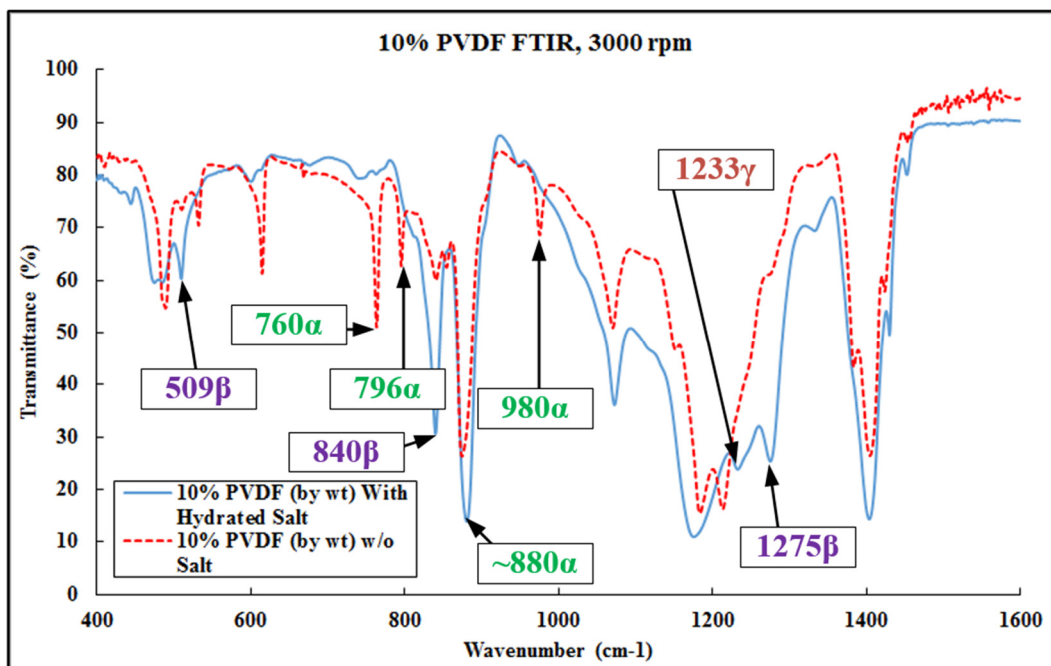


Figure 132. FTIR results for 10% PVDF with and without hydrated salt spun at 3000 rpm.

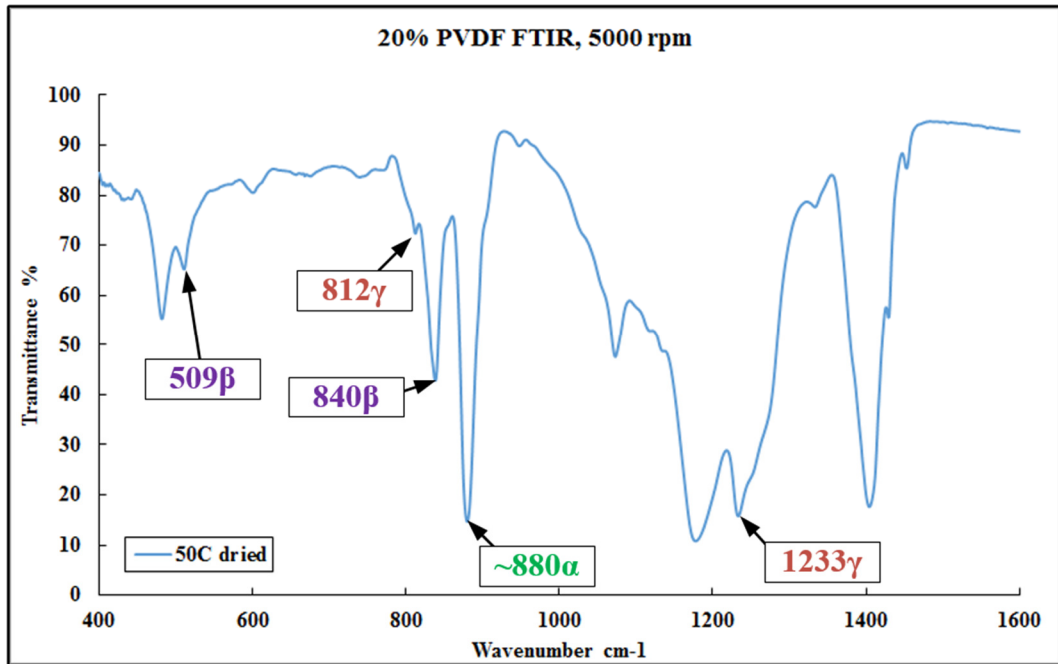


Figure 133. FTIR results for 20% PVDF without hydrated salt spun at 5000 rpm.

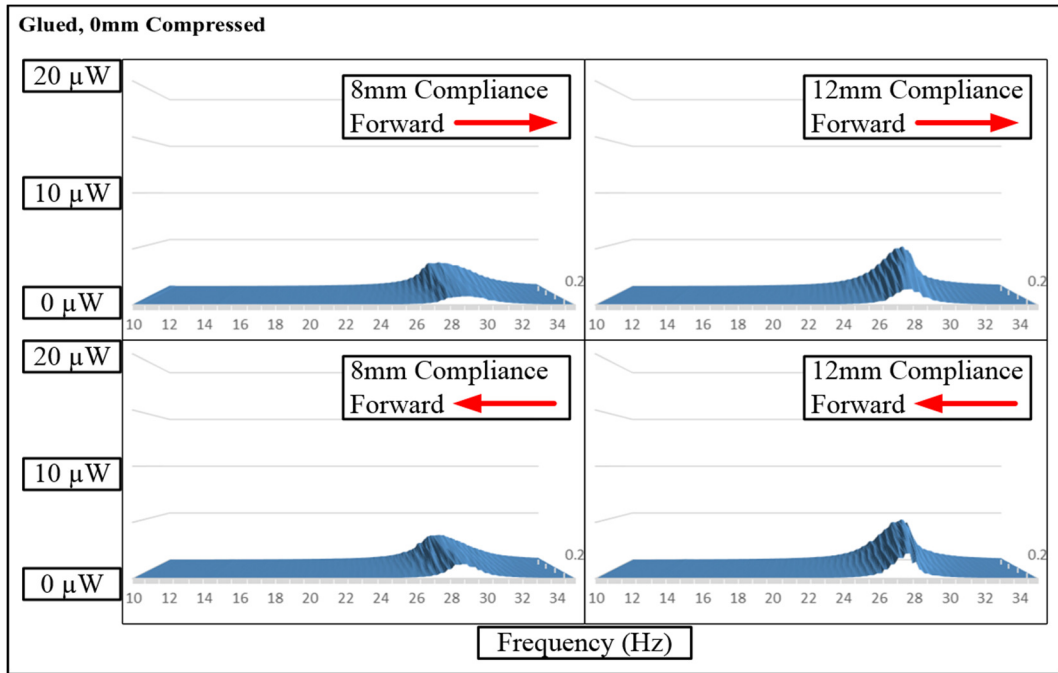


Figure 134. RMS power vs frequency for the uncompressed glued pin device. Acceleration from 0.2 to 0.6 g_{rms} .

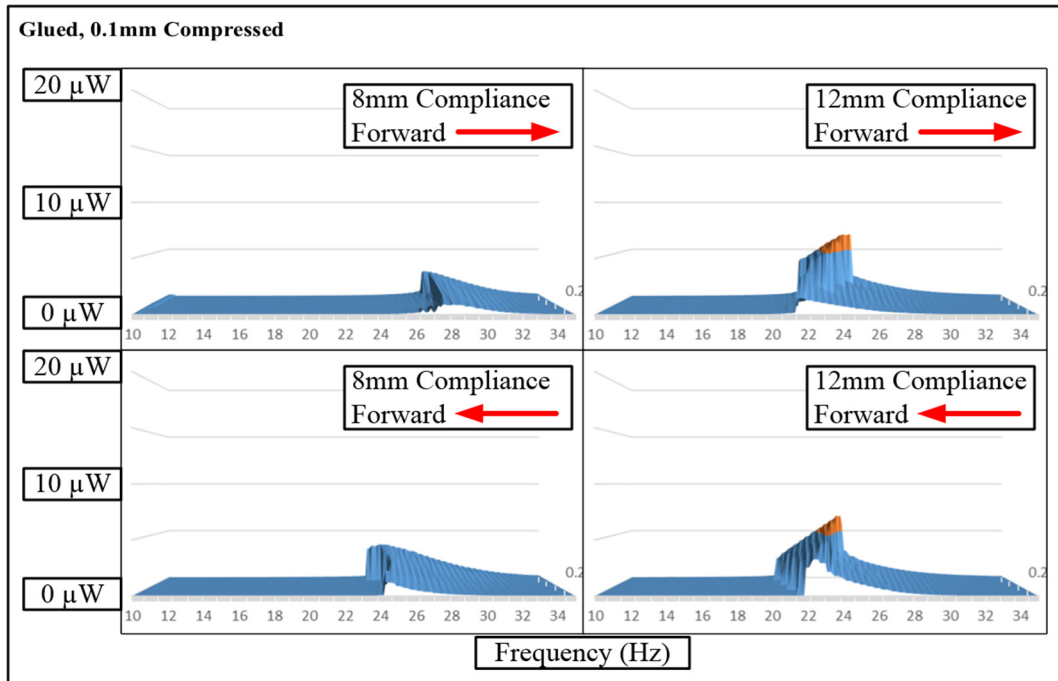


Figure 135. RMS power vs frequency for the compressed glued pin device. Acceleration from 0.2 to 0.6 g_{rms} .

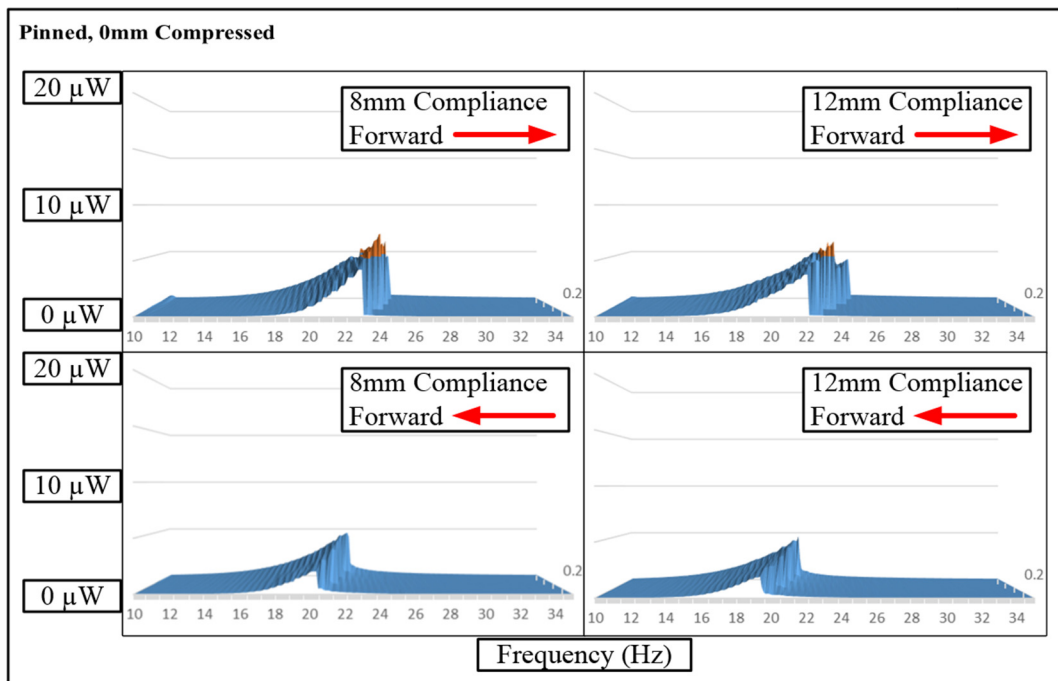


Figure 136. RMS power vs frequency for the uncompressed pinned device. Acceleration from 0.2 to 0.6 g_{rms} .

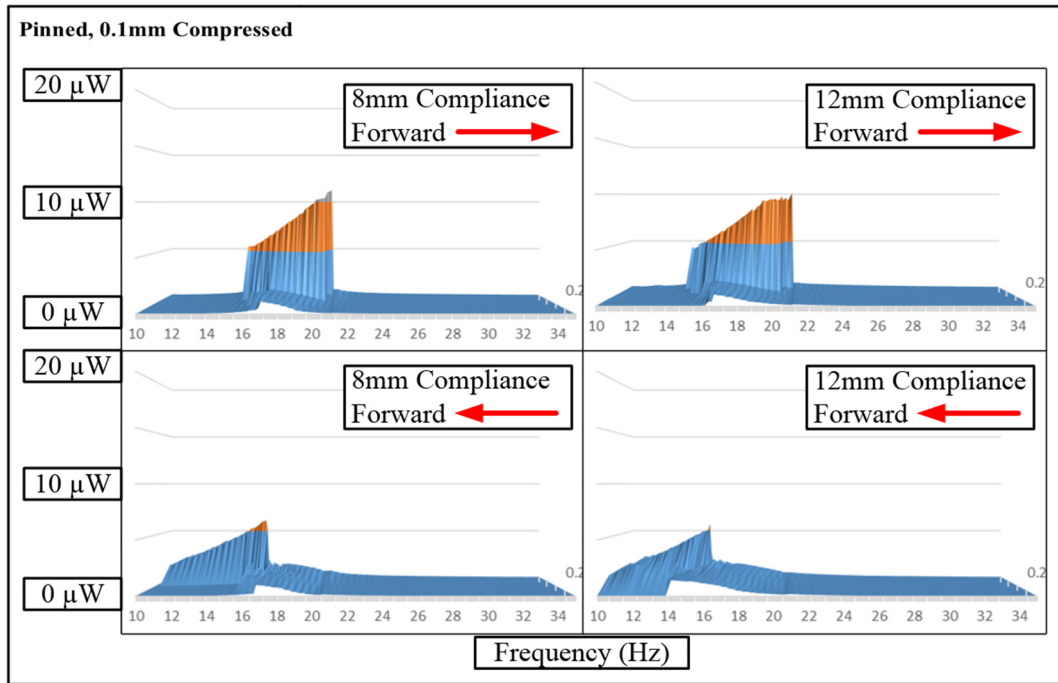


Figure 137. RMS power vs frequency for the compressed pinned device. Acceleration from 0.2 to 0.6 g_{rms} .

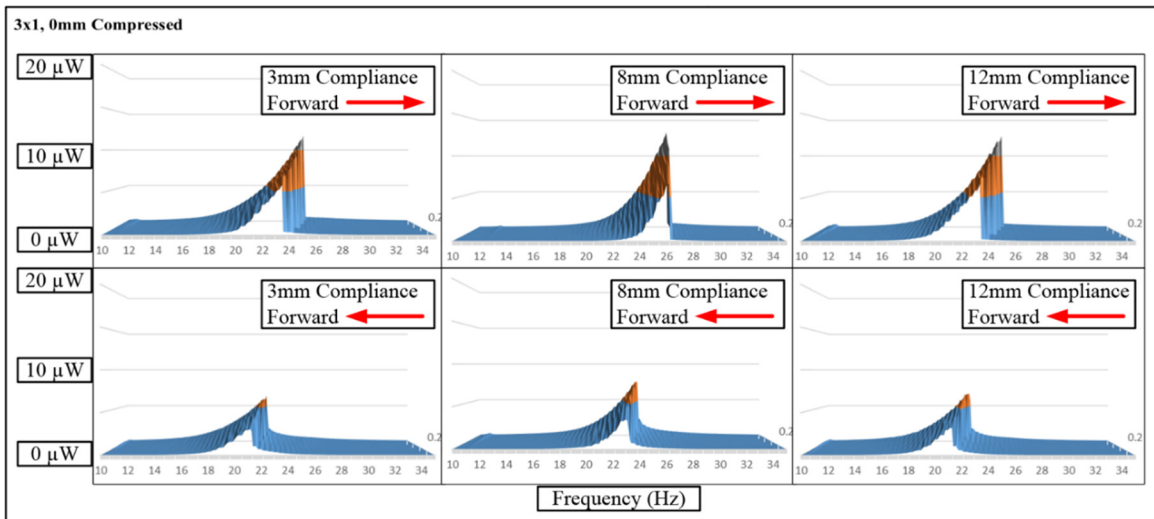


Figure 138. RMS power vs frequency for the uncompressed 3x1 device. Acceleration from 0.2 to 0.6 g_{rms} .

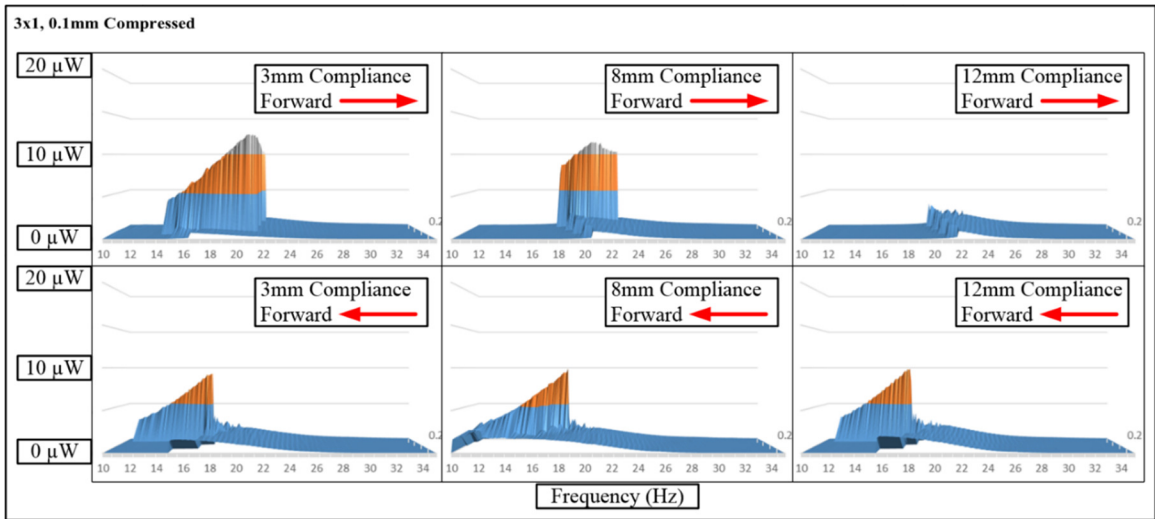


Figure 139. RMS power vs frequency for the compressed 3x1 device. Acceleration from 0.2 to 0.6 g_{rms} .

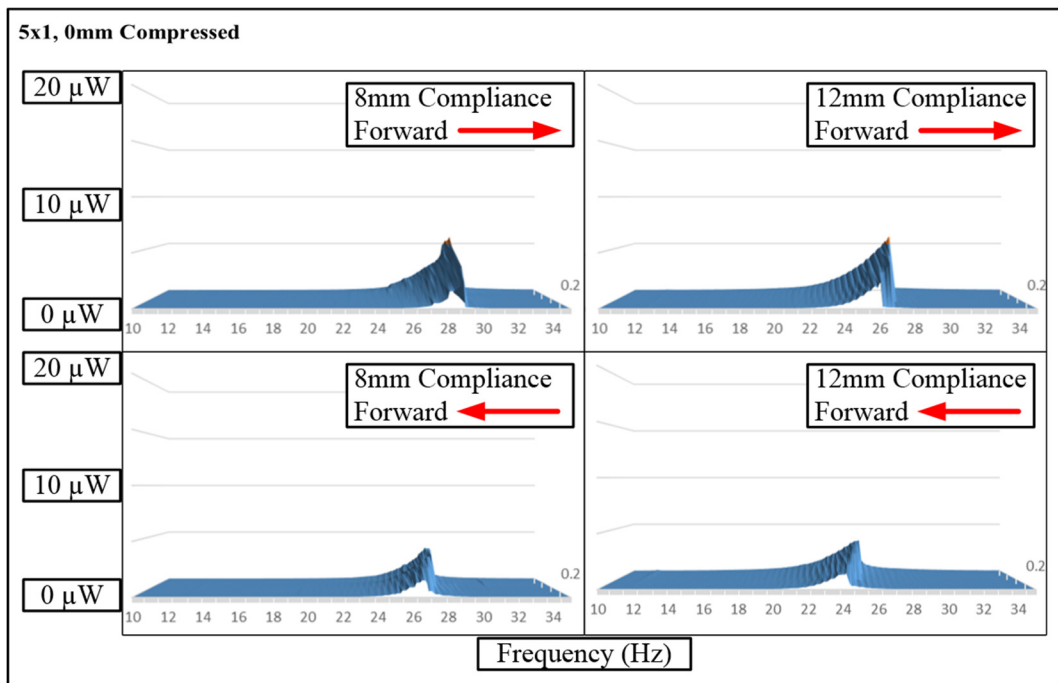


Figure 140. RMS power vs frequency for the uncompressed 5x1 device. Acceleration from 0.2 to 0.6 g_{rms} .

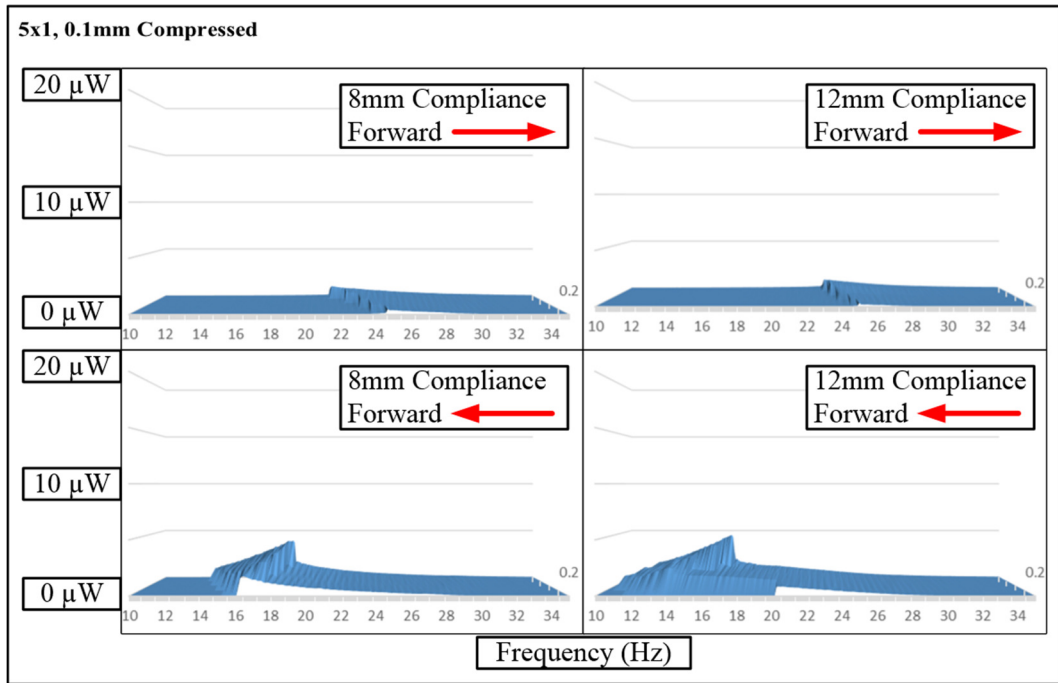


Figure 141. RMS power vs frequency for the compressed 5x1 device. Acceleration from 0.2 to 0.6 g_{rms}.

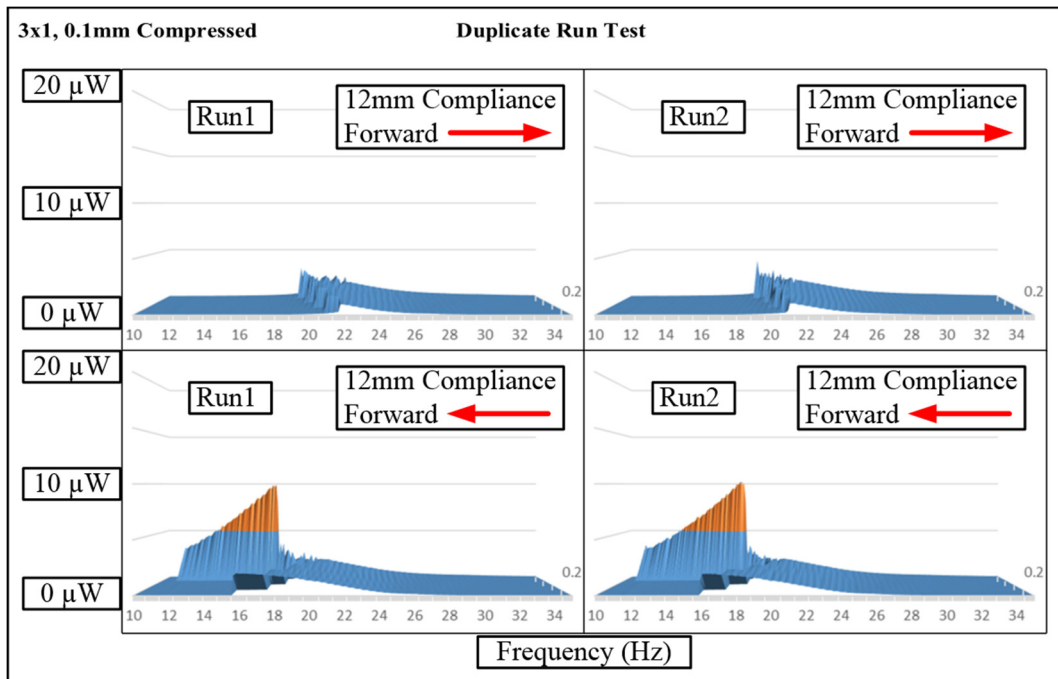


Figure 142. Separate RMS power vs frequency runs for the compressed 3x1 device taken before and after the 5x1 device sweeps to show repeatability. Acceleration from 0.2 to 0.6 g_{rms}.

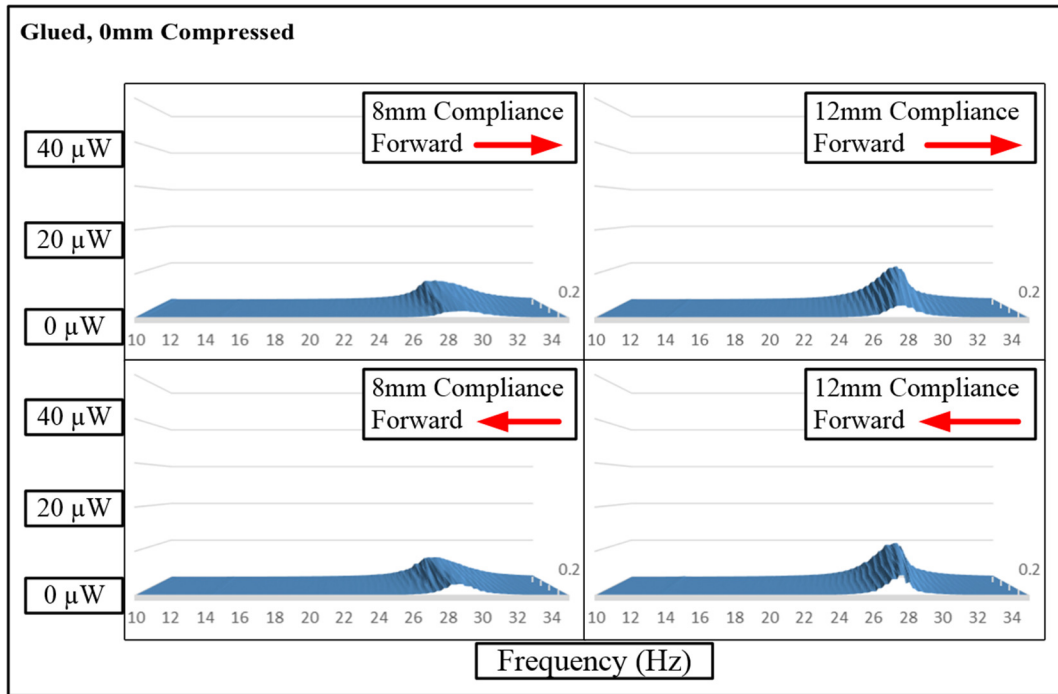


Figure 143. Peak power vs frequency for the uncompressed glued pin device.
Acceleration from 0.2 to 0.6 g_{rms}.

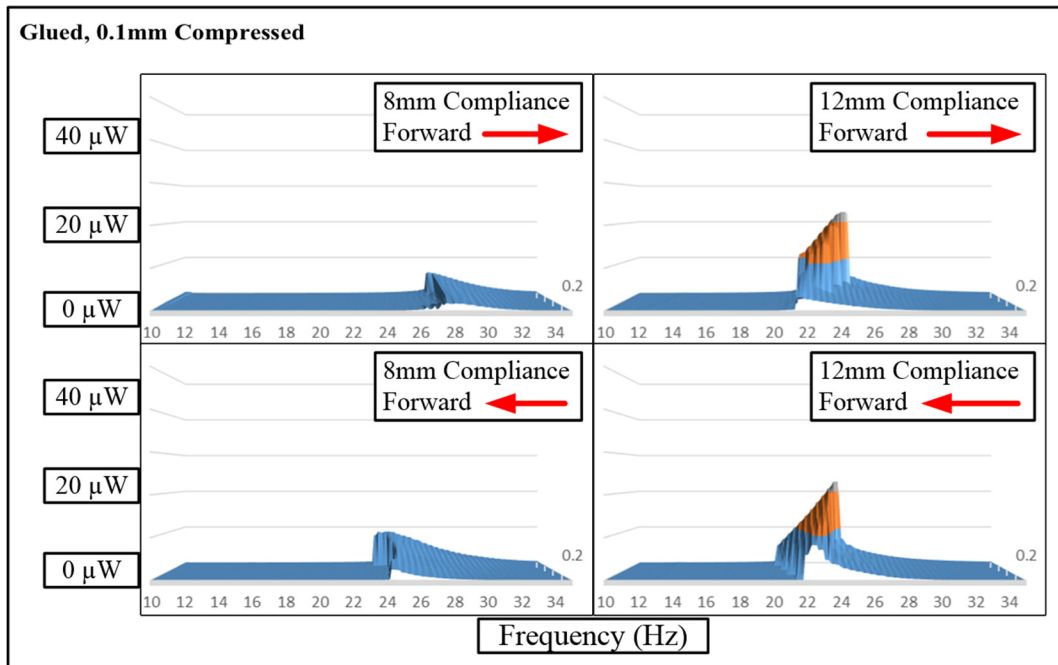


Figure 144. Peak power vs frequency for the compressed glued pin device. Acceleration from 0.2 to 0.6 g_{rms}.

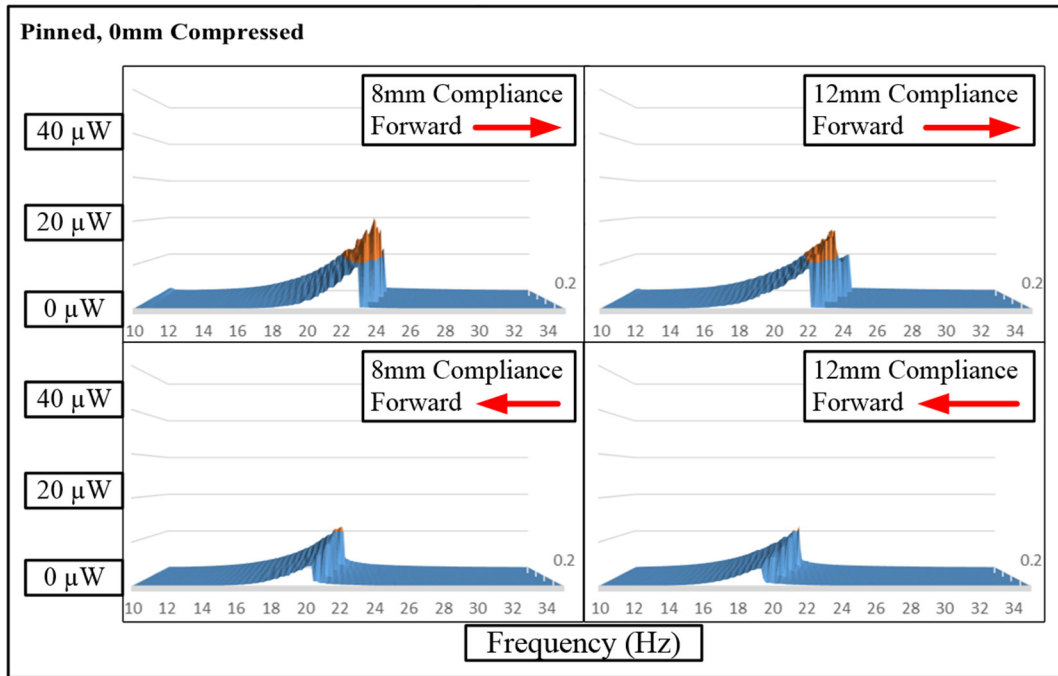


Figure 145. Peak power vs frequency for the uncompressed pinned device. Acceleration from 0.2 to 0.6 g_{rms} .

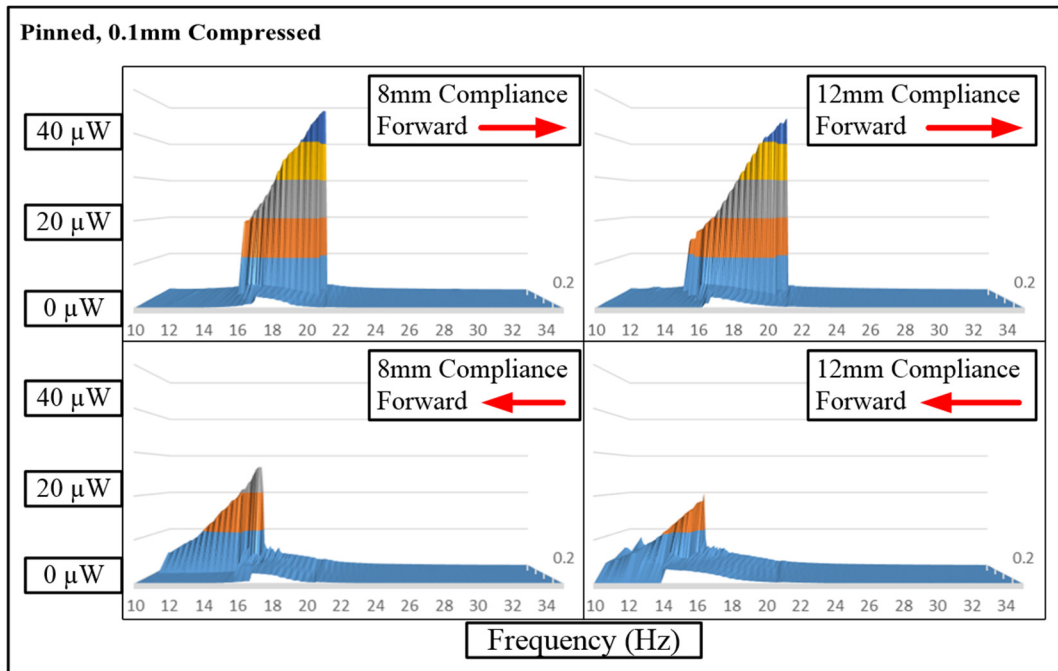


Figure 146. Peak power vs frequency for the compressed pinned device. Acceleration from 0.2 to 0.6 g_{rms} .

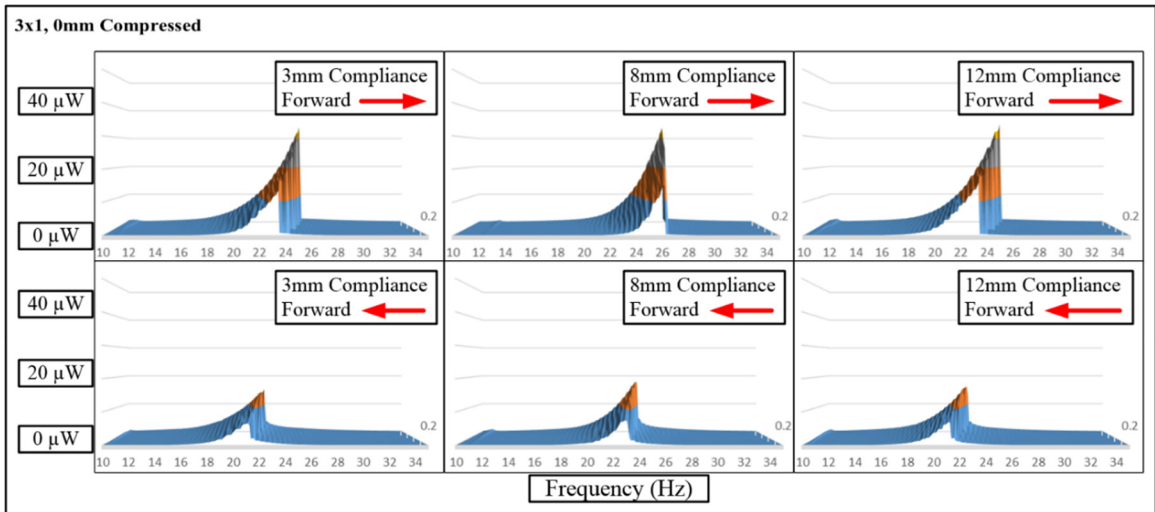


Figure 147. Peak power vs frequency for the uncompressed 3x1 device. Acceleration from 0.2 to 0.6 g_{rms} .

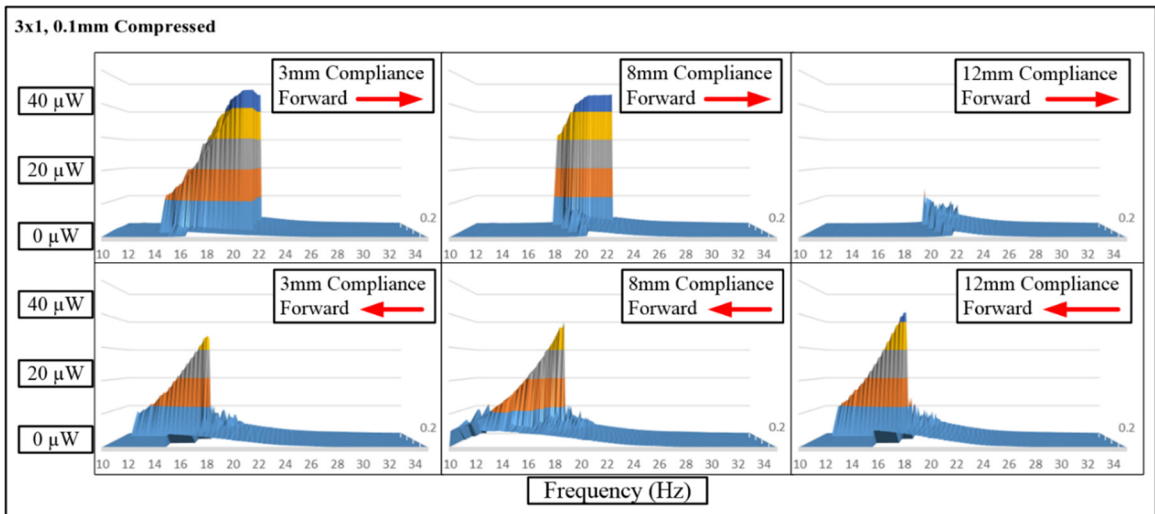


Figure 148. Peak power vs frequency for the compressed 3x1 device. Acceleration from 0.2 to 0.6 g_{rms} .

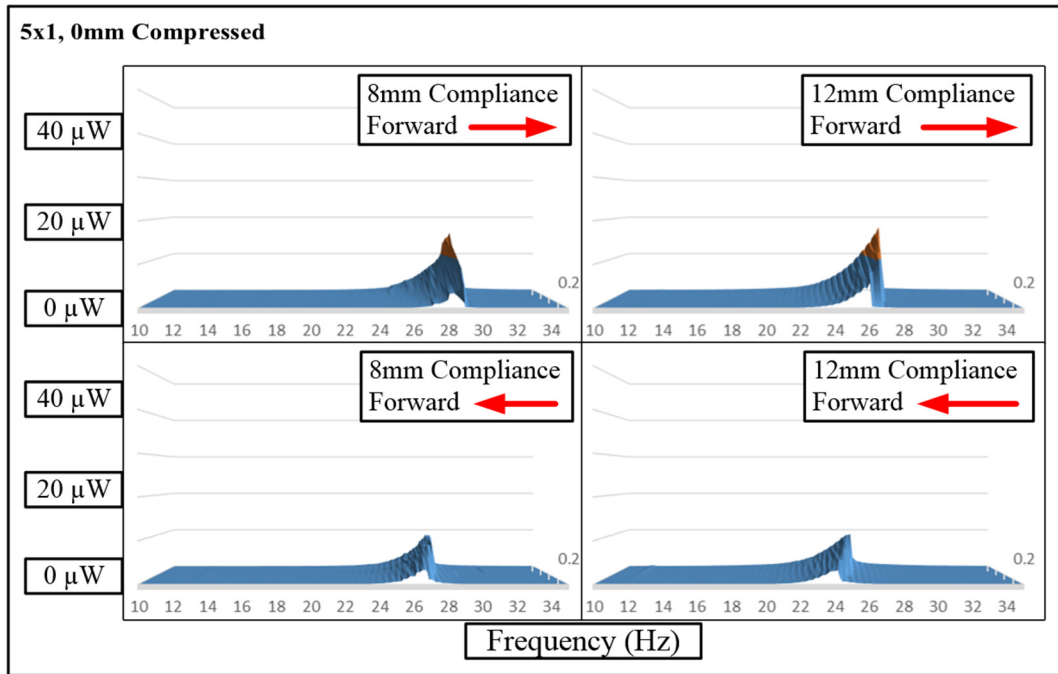


Figure 149. Peak power vs frequency for the uncompressed 5x1 device. Acceleration from 0.2 to 0.6 g_{rms} .

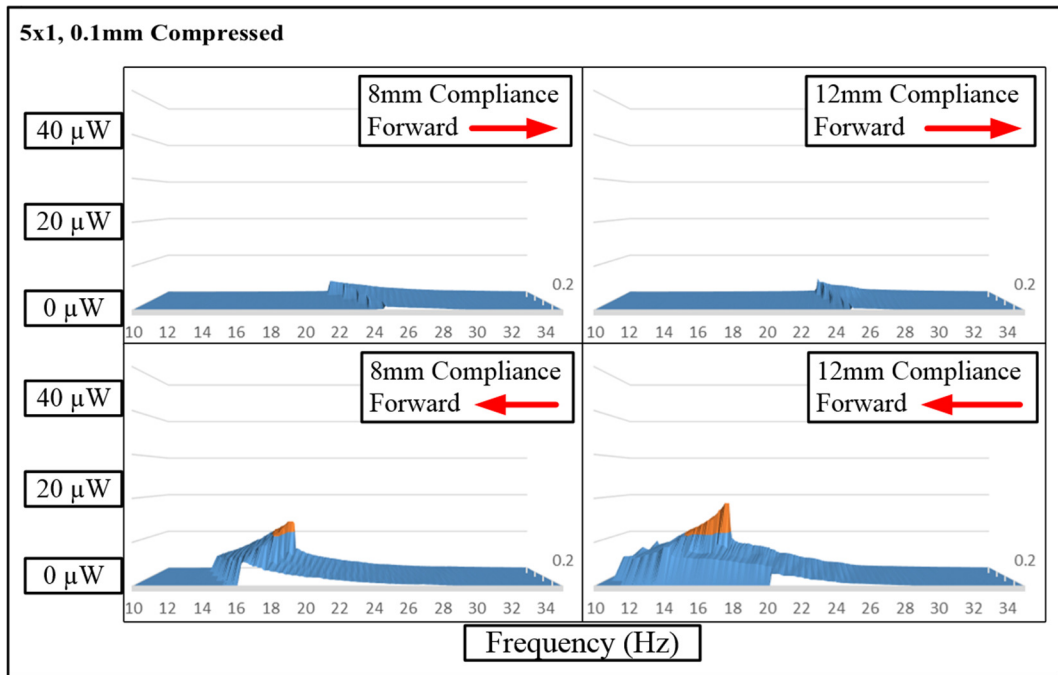


Figure 150. Peak power vs frequency for the compressed 5x1 device. Acceleration from 0.2 to 0.6 g_{rms} .

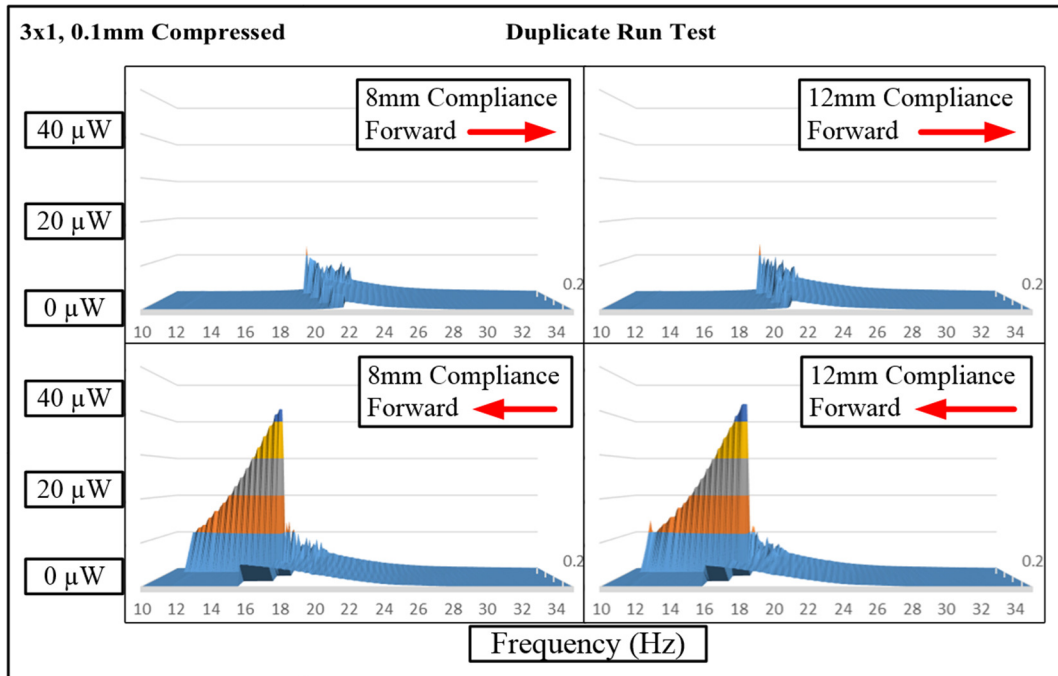


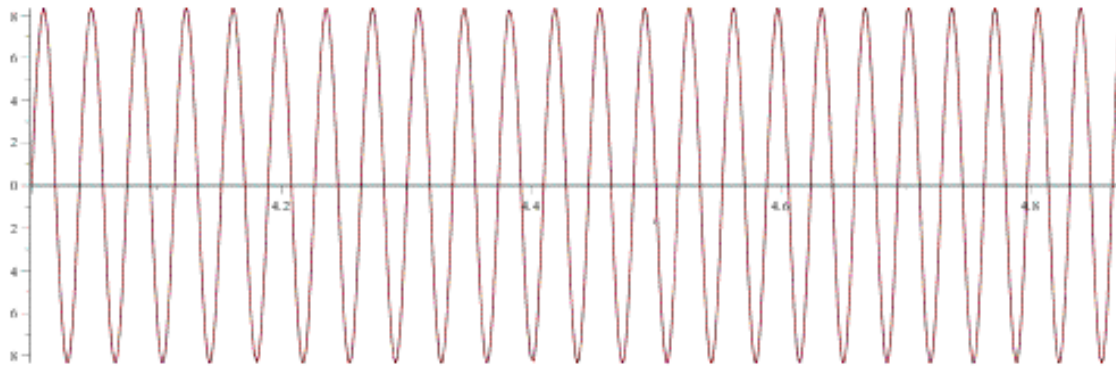
Figure 151. Separate peak power vs frequency runs for the compressed 3x1 device taken before and after the 5x1 device sweeps to show repeatability. Acceleration from 0.2 to 0.6 g_{rms} .

APPENDIX C

(CODE)

Maple 18 code to generate a constant acceleration, linear variable frequency, sine wave displacement input.

```

> #To integrate Fresnel function properly, you must remove the dc offset!
> restart;
> with(LinearAlgebra) :
>  $\omega_n := 188.496$ 
 $\omega_n := 188.496$ 
>  $\omega_0 := 62.832$ 
 $\omega_0 := 62.832$ 
>  $t_n := 5$ 
 $t_n := 5$ 
>  $Amp := 8.3253$ 
 $Amp := 8.3253$ 
>  $\alpha := t \rightarrow \frac{(\omega_n - \omega_0)}{t_n}$ 
 $\alpha := t \rightarrow \frac{\omega_n - \omega_0}{t_n}$ 
>  $\omega := t \rightarrow \alpha(t) * t + \omega_0$ 
 $\omega := t \rightarrow \alpha(t) t + \omega_0$ 
>  $\theta := t \rightarrow \left(\frac{1}{2}\right) \cdot \alpha(t) \cdot t^2 + \omega_0 \cdot t$ 
 $\theta := t \rightarrow \frac{1}{2} \alpha(t) t^2 + \omega_0 t$ 
>  $accel1 := t \rightarrow Amp \cdot \sin(\theta(t))$ 
 $accel1 := t \rightarrow Amp \sin(\theta(t))$ 
>  $accel1(t)$ 
 $8.3253 \sin(12.56640000 t^2 + 62.832 t)$ 
>  $plot(accel1(t), t = 4 .. 5)$ 

>  $vell := t \rightarrow \int(accel1(t), t)$ 

```

$$vell := t \rightarrow \int accel(t) dt$$

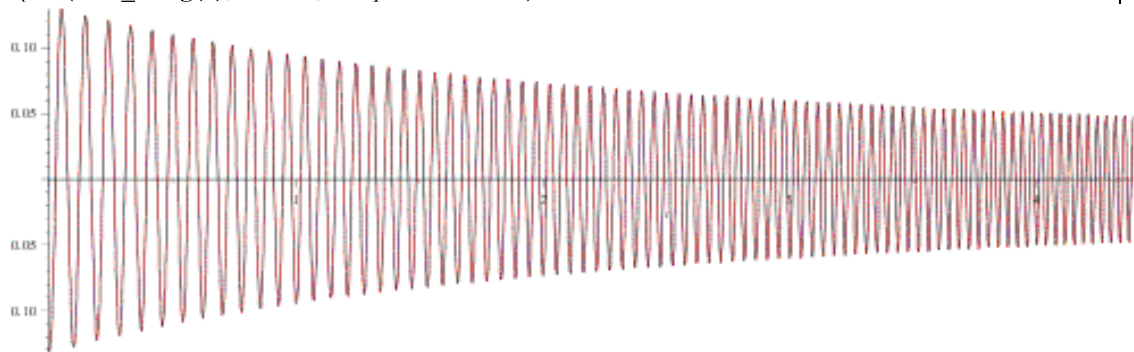
> $vell(t)$
 $-2.943434552 \text{FresnelS}(2.828430432 t + 7.071076079)$
 $+ 0.0005405919469 \text{FresnelC}(2.828430432 t + 7.071076079)$

> $vell_avg := \text{FunctionAverage}(vell(t), t = 0..5)$
 $vell_avg := -1.471454993$

> $vell_wAvg := t \rightarrow vell(t) - vell_avg$
 $vell_wAvg := t \rightarrow vell(t) - vell_avg$

> $vell_wAvg(t)$
 $-2.943434552 \text{FresnelS}(2.828430432 t + 7.071076079)$
 $+ 0.0005405919469 \text{FresnelC}(2.828430432 t + 7.071076079) + 1.471454993$

> $plot(vell_wAvg(t), t = 0..5, numpoints = 1000)$



> $displ := t \rightarrow \text{int}(vell_wAvg(t), t)$
 $displ := t \rightarrow \int vell_wAvg(t) dt$

> $displ(t)$
 $0.0005405919469 t \text{FresnelC}(2.828430432 t + 7.071076079)$
 $- 2.943434552 t \text{FresnelS}(2.828430432 t + 7.071076079)$
 $+ 0.001351479867 \text{FresnelC}(2.828430432 t + 7.071076079)$
 $- 7.358586379 \text{FresnelS}(2.828430432 t + 7.071076079)$
 $- 0.3312523818 \cos(1.570796327 (2.828430432 t + 7.071076079)^2)$
 $- 0.00006083789763 \sin(1.570796327 (2.828430432 t + 7.071076079)^2)$
 $+ 1.471454993 t$

> $displ_avg := \text{FunctionAverage}(displ(t), t = 0..5)$
 $displ_avg := -3.678603868$

> $displ_wAvg := t \rightarrow displ(t) - displ_avg$
 $displ_wAvg := t \rightarrow displ(t) - displ_avg$

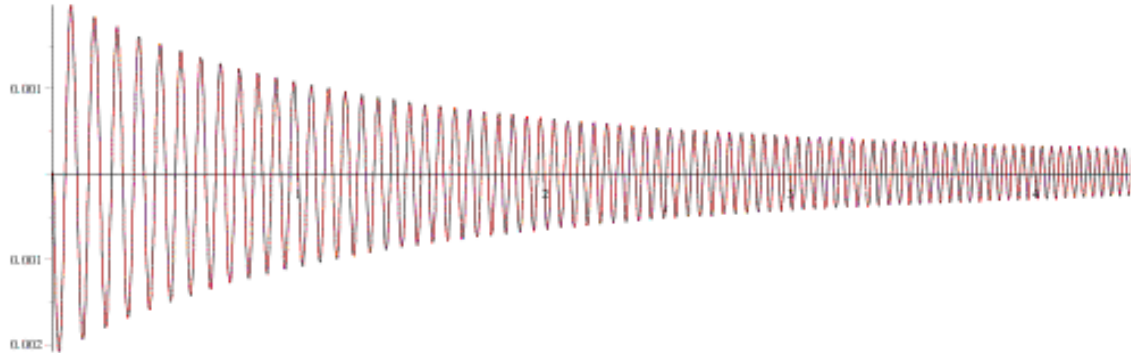
> $displ_wAvg(t)$

```

0.0005405919469t FresnelC(2.828430432t + 7.071076079)
- 2.943434552t FresnelS(2.828430432t + 7.071076079)
+ 0.001351479867 FresnelC(2.828430432t + 7.071076079)
- 7.358586379 FresnelS(2.828430432t + 7.071076079)
- 0.3312523818 cos(1.570796327 (2.828430432t + 7.071076079)^2)
- 0.00006083789763 sin(1.570796327 (2.828430432t + 7.071076079)^2)
+ 1.471454993t + 3.678603868

```

```
> plot(displ_wAvg(t), t=0..5, numpoints = 1000)
```



ANSYS code to apply a displacement (Commands APDL before solution)

```

!Applying a harmonic displacement in ANSYS "Harmonic Response" module
cmsel,s,Anchors      !Have to use named selections here
myaccel=4162         !0.3grms in mm/s^2
points=100           ! more points for better accuracy
start_freq=10        !start frequency in Hz
end_freq=30          !ending frequency in Hz
twopi=2*acos(-1)    !radians
stepsize=(end_freq-start_freq)/(points-1)
*dim,my_uz,table,points,,TIME,n      !TIME=frequency
*do,ii,1,points
  freq=start_freq+stepsize*(ii-1)    !frequency value
  my_uz(ii,0)=freq                    !put freq into array
  omegasq=(twopi*freq)**2              !amplitude of load
  my_uz(ii,1)=-myaccel/omegasq         !put amplitude into array
*enddo

d,all,uz,%my_uz%      ! Apply the load and frequency
allsel                 !select all nodes

```

ANSYS code to integrate x-strain over a shell layer area (Command APDL after solution)

```

!ONLY NEED TO EXPORT STRAIN*AREA

finish
/post1

!Set shell results to the 2nd (PVDF layer)
!get the results from the middle point-----

```

```

LAYER,2!select PVDF layer
SHELL,MID      !select shell middle

!might need to get number instead of SteelPVDF

!find out how many substeps there are-----
SET,4          !set load step 4
*GET, my_substeps1, ACTIVE, 0, SOLU, NCMSS!get the number of load steps in LS1
my_TotalSubsteps=my_substeps1

!Create Time and Strain*Area array
!-----
i=1
*DIM, my_TimeArray, ARRAY, my_TotalSubsteps
*DIM, my_StrainArray1, ARRAY, my_TotalSubsteps
*DIM, my_StrainArray2, ARRAY, my_TotalSubsteps

!calculate values throughout the substeps-----
*DO, i, 1, my_TotalSubsteps, 1

      SET, 4, i

      !TIME-----
      *GET, CurrentTime, ACTIVE, 0, SET, TIME
      my_TimeArray(i) = CurrentTime

!BACK
Electrode=====
      cmsel,s,SteelPVDFback          ! select nodes on face(s)
      !Get Strain*Area-----
      *stat

      *get,n_nodes1,node,,count      ! how many nodes in component
      *dim,node_arnode1,array,n_nodes1 ! associated elements surface area
each node
      *dim,node_Strain_Areal,array,n_nodes1 ! product of strain*area at each
node

      node_next=0

      *DO,ii,1,n_nodes1
          node_next=NDNEXT(node_next) !
work through all the nodes
          node_arnode1(ii)=ARNODE(node_next) !
associated area on element faces
          *GET, my_current_strain1, NODE, node_next, EPEL, X
          ! grab x direction strain
          node_Strain_Areal(ii)=ARNODE(node_next)*my_current_strain1 !
product
      *ENDDO

      *vscfun, sum_node_Strain_Areal, SUM, node_Strain_Areal(1) ! sum of
strain*area products
      *vscfun, sum_Areal, SUM, node_arnode1(1) ! sum of
areas

      my_sum_node_Strain_Areal = sum_node_Strain_Areal
      my_sum_Areal = sum_Areal
      my_StrainArray1(i) = my_sum_node_Strain_Areal

      allsel

```

```

!FRONT
Electrode=====
cmsel,s,SteelPVDFfront          ! select nodes on face(s)
!Get Strain*Area-----
*stat

*get,n_nodes2,node,,count      ! how many nodes in component
*dim,node_arnode2,array,n_nodes2  ! associated elements surface area
each node
*dim,node_Strain_Area2,array,n_nodes2 ! product of strain*area at each
node

node_next=0

*DO,ii,1,n_nodes2
  node_next=NDNEXT(node_next)      !
work through all the nodes
  node_arnode2(ii)=ARNODE(node_next) !
associated area on element faces
  *GET, my_current_strain2, NODE, node_next, EPEL, X
  ! grab x direction strain
  node_Strain_Area2(ii)=ARNODE(node_next)*my_current_strain2 !
product
*ENDDO

*vscfun, sum_node_Strain_Area2, SUM, node_Strain_Area2(1)      ! sum of
strain*area products
*vscfun, sum_Area2, SUM, node_arnode2(1)      ! sum of
areas

my_sum_node_Strain_Area2 = sum_node_Strain_Area2
my_sum_Area2 = sum_Area2
my_StrainArray2(i) = my_sum_node_Strain_Area2

*ENDDO

!write data to file-----
*CFCOPEN,AllData,txt

*VWRITE,
(' ', 6x, 'BackElectrodeArea', 6x, 'FrontElectrodeArea', 6x,)

*VWRITE,my_sum_Area1,my_sum_Area2      ! Write array in given format to file
"disp.dat"
(f16.9, 6x, f16.9, 6x, f16.9, 6x)

*VWRITE,
(' ', 6x, 'Time', 6x, 'StrainArray', 6x,)

*VWRITE,my_TimeArray(1),my_StrainArray1(1),my_StrainArray2(1)      ! Write array
in given format to file "disp.dat"
(f16.9, 6x, f16.9, 6x, f16.9, 6x, f16.9, 6x)

*CFCLOSE
!-----

allsel
set,last

```

APPENDIX D
(MEMS FABRICATION RECIPES)

<div style="background-color: yellow; text-align: center; padding: 5px; font-weight: bold;">1813 PR Spin Profile</div> <ul style="list-style-type: none"> Using Microposit 1813 photo-resist Use clean drop bottle and cover 2/3 of wafer <ul style="list-style-type: none"> – Spread at 500 rpm, 500 rpm/s, 1 sec. – Spin at 4000 rpm, 1000 rpm/s, 30 sec. Pre-bake at 115 C for 1 minute. Let sit and air dry for 5 minutes (so it doesn't stick to mask). Align and expose for 14 sec with a 50 μm gap, soft exposure. <ul style="list-style-type: none"> – 12 mW/cm² on power supply or 4 mW/cm² using intensity meter. Develop in fresh MF-319 for about 60 sec while agitating. Inspect: if good hard bake for 5 min at 115 C. Let sit and air dry for 5 minutes. <p style="text-align: right; font-size: small;">7</p>	<div style="background-color: yellow; text-align: center; padding: 5px; font-weight: bold;">1813 Liftoff Using LOR-3A</div> <ul style="list-style-type: none"> Clean wafer using AML. Put on hotplate at 150C for 3 to 5 min to remove moisture. Apply LOR-3A: <ul style="list-style-type: none"> – Spread, 500 rpm, 100 rpm/sec, 2 sec – Spin, 3000 rpm, 1000 rpm/sec, 10 sec – Soft bake 5min at 150C, contact (2um undercut) Let cool for about 1 min Apply Shipley 1813 (spin profile #2): <ul style="list-style-type: none"> – Spread, 500 rpm, 500 rpm/sec, 1sec – Spin 4000 rpm, 1000 rpm/sec, 30 sec – Soft bake 1min 115C Let cool for about 1 min Expose 14 sec (12, 4 mW/cm²) <ul style="list-style-type: none"> – Pattern PR using Mask#3 Develop ~1min Hard bake 3min at 115C Ready for sputtering. LOR itself must be removed with NMP or maybe and O2 plasma. <p style="text-align: right; font-size: small;">10</p>
--	--

Figure 152. Microposit 1813 photoresist processing parameters for a 1.3 μm thickness (left) and a liftoff recipe using 1813 and LOR-3A (right).

<div style="background-color: yellow; text-align: center; padding: 5px; font-weight: bold;">1827 PR (Thin) Spin Profile</div> <ul style="list-style-type: none"> Using Microposit 1827 photo-resist Use clean drop bottle and cover 2/3 of wafer <ul style="list-style-type: none"> – Spread at 500 rpm, 500 rpm/s, 1 sec. – Spin at 4000 rpm, 1000 rpm/s, 30 sec. Pre-bake at 90-115 C for 1 minute. Let sit and air dry for 5 minutes (so it doesn't stick to mask). Align and expose for 24 sec with a 50 μm gap, hard exposure. <ul style="list-style-type: none"> – 12 mW/cm² on power supply or 4 mW/cm² using intensity meter. Develop in fresh MF-319 for about 75 sec while agitating. Inspect: if good hard bake for 5 min at 90-115 C. Let sit and air dry for 5 minutes. <p style="text-align: right; font-size: small;">9</p>	<div style="background-color: yellow; text-align: center; padding: 5px; font-weight: bold;">1827 PR (Thick) Spin Profile</div> <ul style="list-style-type: none"> Using Microposit 1827 photo-resist Use clean drop bottle and cover 2/3 of wafer <ul style="list-style-type: none"> – Spread at 500 rpm, 1800 rpm/s, 10 sec. – Spin at 2500 rpm, 1800 rpm/s, 30 sec. – Edge Bead Removal at 4000 rpm, 1800 rpm/s, 0.1 sec. Pre-bake at 90-115 C for 1 minute. Let sit and air dry for 5 minutes (so it doesn't stick to mask). Align and expose for 40 sec with a 50 μm gap, hard exposure. <ul style="list-style-type: none"> – 12 mW/cm² on power supply or 4 mW/cm² using intensity meter. Develop in fresh MF-319 for about 75 sec while agitating. Inspect: if good hard bake for 5 min at 90-115 C. Let sit and air dry for 5 minutes. Working March 18th 2014. <p style="text-align: right; font-size: small;">8</p>
---	--

Figure 153. Microposit 1827 photoresist processing parameters for a 2.7 μm thickness (left) and for a 3.8 μm thickness (right).

<div style="background-color: yellow; text-align: center; padding: 5px; font-weight: bold;">PI2611 Polymer Spin&Cure</div> <ul style="list-style-type: none"> Put 1 or 2 drops of VM-651 in a 400mL beaker of DiH2O. Ratio should be roughly (1:999). Spin profile <ul style="list-style-type: none"> – Spread 100rpm, 100rpm/sec, 10sec – Spin 5,000rpm, 100rpm/sec, 30sec Bake at 90C for 2min Put in YES oven for 7hrs. <ul style="list-style-type: none"> – Use 350C bake Should get roughly 3.65um of polyimide. October 9th 2012 recipe. <p style="text-align: right; font-size: small;">12</p>	<div style="background-color: yellow; text-align: center; padding: 5px; font-weight: bold;">PI2611 Polymer Etching</div> <ul style="list-style-type: none"> Use chrome mask layer (~200nm) Spin 1827 PR (~2.7um) Using MARCH RIE <ul style="list-style-type: none"> – 300W, 300mTorr, 50% O2, 85mTorr base – ~7min etch. MARCH might stop after 5min. Photoresist should be gone after the 7 min etch. Strip chrome in CEP200 for about 2 min. Nov 17th 2012 recipe. <p style="text-align: right; font-size: small;">13</p>
---	---

Figure 154. Polyimide application (left) and etching recipes (right).

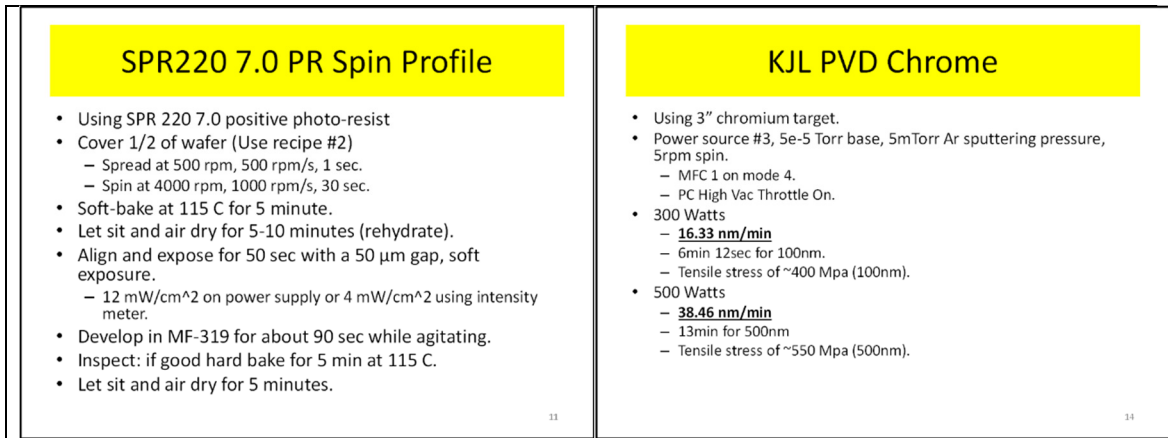


Figure 155. SPR220 7.0 photoresist recipe (left) and deposition rates of chrome in the physical vapor deposition KJL machine (right).

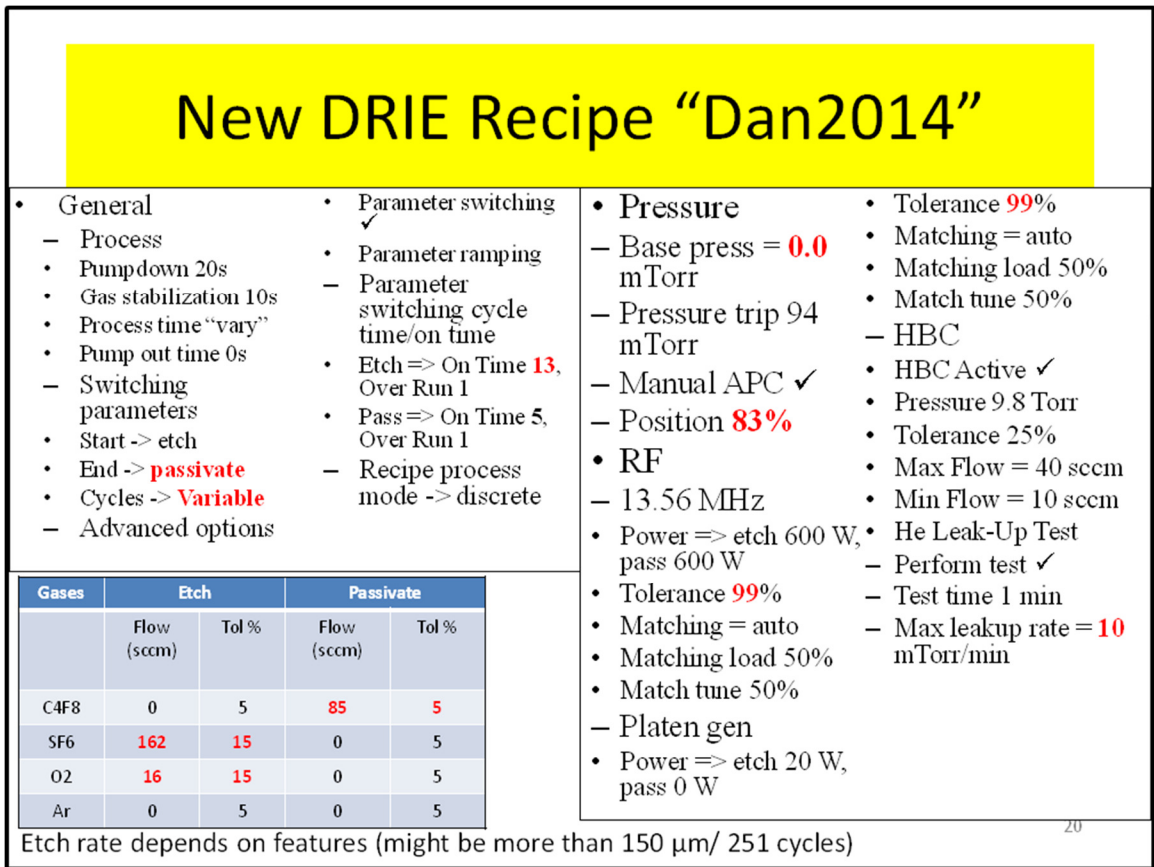


Figure 156. DRIE recipe used to etch silicon.

APPENDIX E
(ENERGY HARVESTER METRICS)

*grey boxes that are bold and underlined indicate snap-through/HEO operation.

Table 27. Performance index evaluation for forward swept experiments.

Forward Sweep -->	I					SD					CV				
	0.2	0.3	0.4	0.5	0.6	0.2	0.3	0.4	0.5	0.6	0.2	0.3	0.4	0.5	0.6
Forward															
Glue, 8mm, Unbuckled	0.00020	0.00014	0.00010	0.00009	0.00007	2.86E-05	1.52E-05	1.28E-05	8.97E-06	9.51E-06	0.14	0.11	0.13	0.10	0.13
Glue, 12.5mm, Unbuckled	0.00035	0.00024	0.00019	0.00014	0.00012	4.35E-05	3.96E-05	2.00E-05	2.19E-05	1.51E-05	0.13	0.17	0.11	0.15	0.13
Glue, 8mm, BUCK	0.00024	0.00017	0.00012	0.00009	0.00007	2.10E-05	1.29E-05	1.17E-05	9.76E-06	8.45E-06	0.09	0.08	0.10	0.11	0.11
Glue, 12.5mm, BUCK	0.00028	0.00028	0.00028	0.00021	0.00015	3.79E-05	6.17E-05	3.45E-05	3.58E-05	3.43E-05	0.13	0.22	0.12	0.17	0.22
Pin, 8mm, Unbuckled	0.00077	0.00046	0.00033	0.00019	0.00012	1.88E-04	1.01E-04	7.26E-05	4.06E-05	2.34E-05	0.24	0.22	0.22	0.21	0.20
Pin, 12.5mm, Unbuckled	0.00066	0.00041	0.00028	0.00016	0.00012	1.61E-04	8.76E-05	6.56E-05	3.38E-05	2.41E-05	0.25	0.22	0.23	0.21	0.20
Pin, 8mm, BUCK	0.00017	0.00010	0.00006	0.00025	0.00019	1.99E-05	4.78E-06	4.69E-06	7.89E-05	5.23E-05	0.12	0.05	0.08	0.32	0.27
Pin, 12.5mm, BUCK	0.00016	0.00009	0.00006	0.00023	0.00018	1.31E-05	5.94E-06	2.57E-06	6.93E-05	4.70E-05	0.08	0.06	0.04	0.30	0.27
3x1, 3mm, Unbuckled	0.00110	0.00066	0.00046	0.00033	0.00026	2.21E-04	1.54E-04	1.02E-04	7.98E-05	6.22E-05	0.20	0.23	0.22	0.24	0.24
3x1, 8mm, Unbuckled	0.00148	0.00081	0.00058	0.00040	0.00031	3.03E-04	1.95E-04	1.27E-04	9.10E-05	6.84E-05	0.20	0.24	0.22	0.23	0.22
3x1, 12.5mm, Unbuckled	0.00121	0.00069	0.00050	0.00036	0.00028	2.75E-04	1.53E-04	1.15E-04	8.56E-05	6.63E-05	0.23	0.22	0.23	0.24	0.24
3x1, 3mm, BUCK	0.00012	0.00007	0.00052	0.00032	0.00025	9.07E-06	2.65E-06	1.45E-04	9.51E-05	4.71E-05	0.07	0.04	0.28	0.29	0.19
3x1, 8mm, BUCK	0.00018	0.00010	0.00007	0.00005	0.00025	1.98E-05	9.91E-06	7.68E-06	4.18E-06	4.88E-05	0.11	0.10	0.11	0.08	0.19
3x1, 12.5mm, BUCK	0.00019	0.00011	0.00008	0.00006	0.00006	1.52E-05	1.06E-05	7.82E-06	5.94E-06	9.21E-07	0.08	0.09	0.10	0.10	0.02
5x1, 8mm, Unbuckled	0.00056	0.00035	0.00024	0.00017	0.00014	1.05E-04	7.72E-05	5.19E-05	3.80E-05	3.62E-05	0.19	0.22	0.22	0.22	0.25
5x1, 12.5mm, Unbuckled	0.00051	0.00035	0.00023	0.00017	0.00014	8.16E-05	6.47E-05	5.30E-05	3.68E-05	3.17E-05	0.16	0.18	0.23	0.22	0.23
5x1, 8mm, BUCK	0.00009	0.00004	0.00003	0.00002	0.00002	9.53E-06	2.88E-06	3.42E-06	2.69E-06	2.47E-06	0.11	0.07	0.12	0.11	0.12
5x1, 12.5mm, BUCK	0.00005	0.00003	0.00002	0.00003	0.00002	5.87E-06	1.72E-06	1.51E-06	2.98E-06	7.60E-07	0.11	0.07	0.07	0.12	0.04

Table 28. Performance index evaluation for the reverse swept experiments.

Reverse Sweep <--	I					SD					CV				
	0.2	0.3	0.4	0.5	0.6	0.2	0.3	0.4	0.5	0.6	0.2	0.3	0.4	0.5	0.6
Reverse															
Glue, 8mm, Unbuckled	0.00033	0.00019	0.00013	0.00009	0.00008	3.68E-05	2.75E-05	1.83E-05	1.16E-05	9.54E-06	0.11	0.14	0.14	0.12	0.13
Glue, 12.5mm, Unbuckled	0.00051	0.00031	0.00021	0.00015	0.00012	6.65E-05	3.07E-05	3.17E-05	2.10E-05	1.47E-05	0.13	0.10	0.15	0.14	0.12
Glue, 8mm, BUCK	0.00027	0.00018	0.00013	0.00011	0.00009	5.01E-05	2.95E-05	1.99E-05	1.63E-05	1.30E-05	0.19	0.16	0.15	0.15	0.14
Glue, 12.5mm, BUCK	0.00063	0.00040	0.00026	0.00018	0.00014	1.33E-04	7.32E-05	3.96E-05	3.32E-05	2.67E-05	0.21	0.19	0.15	0.18	0.19
Pin, 8mm, Unbuckled	0.00036	0.00023	0.00015	0.00011	0.00009	2.86E-05	1.63E-05	2.48E-05	1.84E-05	1.55E-05	0.08	0.07	0.17	0.17	0.17
Pin, 12.5mm, Unbuckled	0.00031	0.00018	0.00014	0.00010	0.00008	4.25E-05	3.74E-05	2.34E-05	1.97E-05	1.52E-05	0.14	0.20	0.17	0.19	0.19
Pin, 8mm, BUCK	0.00016	0.00009	0.00005	0.00009	0.00008	1.07E-05	1.09E-05	7.14E-06	2.07E-05	1.92E-05	0.07	0.12	0.14	0.23	0.23
Pin, 12.5mm, BUCK	0.00014	0.00008	0.00006	0.00004	0.00003	2.73E-05	1.26E-05	5.91E-06	1.26E-05	7.28E-06	0.20	0.15	0.11	0.33	0.27
3x1, 3mm, Unbuckled	0.00054	0.00032	0.00021	0.00016	0.00012	9.16E-05	5.21E-05	3.93E-05	3.03E-05	2.34E-05	0.17	0.16	0.19	0.19	0.20
3x1, 8mm, Unbuckled	0.00069	0.00043	0.00029	0.00022	0.00016	9.63E-05	4.25E-05	4.14E-05	3.16E-05	2.89E-05	0.14	0.10	0.14	0.15	0.18
3x1, 12.5mm, Unbuckled	0.00057	0.00036	0.00023	0.00018	0.00013	7.98E-05	6.64E-05	4.37E-05	2.85E-05	2.73E-05	0.14	0.18	0.19	0.16	0.20
3x1, 3mm, BUCK	0.00026	0.00013	0.00007	0.00005	0.00013	2.72E-05	1.43E-05	9.43E-06	1.48E-05	3.46E-05	0.11	0.11	0.13	0.28	0.26
3x1, 8mm, BUCK	0.00028	0.00021	0.00020	0.00015	0.00015	3.39E-05	4.97E-05	4.35E-05	3.35E-05	3.41E-05	0.12	0.24	0.22	0.22	0.23
3x1, 12.5mm, BUCK	0.00033	0.00015	0.00009	0.00006	0.00014	3.60E-05	1.98E-05	1.26E-05	5.96E-06	3.43E-05	0.11	0.13	0.14	0.10	0.24
5x1, 8mm, Unbuckled	0.00035	0.00025	0.00017	0.00010	0.00009	4.26E-05	2.61E-05	3.06E-05	1.56E-05	1.48E-05	0.12	0.11	0.18	0.16	0.17
5x1, 12.5mm, Unbuckled	0.00030	0.00017	0.00013	0.00010	0.00008	1.62E-05	2.25E-05	1.94E-05	1.53E-05	1.21E-05	0.05	0.13	0.14	0.16	0.16
5x1, 8mm, BUCK	0.00025	0.00017	0.00012	0.00008	0.00006	4.01E-05	3.31E-05	2.11E-05	1.61E-05	1.42E-05	0.16	0.20	0.18	0.20	0.22
5x1, 12.5mm, BUCK	0.00016	0.00011	0.00007	0.00007	0.00006	2.25E-05	8.89E-06	1.37E-05	1.67E-05	1.46E-05	0.14	0.08	0.18	0.23	0.23

Table 29. NPD metric for the forward swept experiments.

Forward Sweep ---->	NPD					NPD Avg
Forward	0.2	0.3	0.4	0.5	0.6	
Glue, 8mm, Unbuckled	0.030	0.020	0.015	0.013	0.011	0.018
Glue, 12.5mm, Unbuckled	0.054	0.038	0.028	0.022	0.018	0.032
Glue, 8mm, BUCK	0.037	0.025	0.020	0.014	0.012	0.022
Glue, 12.5mm, BUCK	0.057	0.058	0.039	0.029	0.023	0.041
Pin, 8mm, Unbuckled	0.095	0.056	0.040	0.023	0.014	0.046
Pin, 12.5mm, Unbuckled	0.084	0.049	0.035	0.020	0.015	0.041
Pin, 8mm, BUCK	0.028	0.014	0.008	0.021	0.016	0.018
Pin, 12.5mm, BUCK	0.024	0.014	0.010	0.019	0.014	0.016
3x1, 3mm, Unbuckled	0.149	0.087	0.061	0.043	0.034	0.075
3x1, 8mm, Unbuckled	0.168	0.097	0.068	0.046	0.037	0.083
3x1, 12.5mm, Unbuckled	0.163	0.091	0.062	0.044	0.035	0.079
3x1, 3mm, BUCK	0.021	0.014	0.049	0.030	0.021	0.027
3x1, 8mm, BUCK	0.024	0.015	0.010	0.010	0.020	0.016
3x1, 12.5mm, BUCK	0.024	0.015	0.011	0.008	0.008	0.013
5x1, 8mm, Unbuckled	0.064	0.040	0.027	0.020	0.017	0.034
5x1, 12.5mm, Unbuckled	0.062	0.043	0.027	0.021	0.016	0.034
5x1, 8mm, BUCK	0.012	0.006	0.004	0.003	0.003	0.006
5x1, 12.5mm, BUCK	0.008	0.003	0.002	0.003	0.003	0.004

Table 30. NPD metric for the reverse swept experiments.

Reverse Sweep <---	NPD					NPD Avg
Reverse	0.2	0.3	0.4	0.5	0.6	
Glue, 8mm, Unbuckled	0.050	0.031	0.020	0.015	0.012	0.025
Glue, 12.5mm, Unbuckled	0.086	0.050	0.034	0.024	0.018	0.042
Glue, 8mm, BUCK	0.051	0.034	0.024	0.019	0.015	0.029
Glue, 12.5mm, BUCK	0.126	0.078	0.041	0.029	0.023	0.059
Pin, 8mm, Unbuckled	0.046	0.029	0.019	0.014	0.011	0.024
Pin, 12.5mm, Unbuckled	0.043	0.025	0.019	0.013	0.011	0.022
Pin, 8mm, BUCK	0.023	0.013	0.008	0.010	0.009	0.013
Pin, 12.5mm, BUCK	0.032	0.014	0.011	0.009	0.008	0.015
3x1, 3mm, Unbuckled	0.077	0.045	0.032	0.022	0.018	0.039
3x1, 8mm, Unbuckled	0.086	0.055	0.036	0.027	0.021	0.045
3x1, 12.5mm, Unbuckled	0.079	0.051	0.031	0.024	0.018	0.040
3x1, 3mm, BUCK	0.041	0.019	0.011	0.010	0.016	0.019
3x1, 8mm, BUCK	0.068	0.030	0.026	0.019	0.017	0.032
3x1, 12.5mm, BUCK	0.049	0.022	0.012	0.008	0.017	0.022
5x1, 8mm, Unbuckled	0.040	0.027	0.020	0.012	0.010	0.022
5x1, 12.5mm, Unbuckled	0.038	0.021	0.016	0.012	0.009	0.019
5x1, 8mm, BUCK	0.046	0.021	0.014	0.010	0.008	0.020
5x1, 12.5mm, BUCK	0.022	0.016	0.012	0.010	0.009	0.014

Table 31. FoM_{BW} metric for the forward sweep experiments.

Forward Sweep --->	FoMv					FoMv Avg	FoMbw					FoMbw Avg
	0.2	0.3	0.4	0.5	0.6		0.2	0.3	0.4	0.5	0.6	
Forward												
Glue, 8mm, Unbuckled	1.29E-05	1.29E-05	1.29E-05	1.42E-05	1.47E-05	1.35E-05	6.68E-07	6.76E-07	6.78E-07	7.51E-07	7.78E-07	7.10E-07
Glue, 12.5mm, Unbuckled	2.37E-05	2.50E-05	2.44E-05	2.40E-05	2.35E-05	2.41E-05	8.48E-07	8.96E-07	8.73E-07	1.02E-06	9.96E-07	9.26E-07
Glue, 8mm, BUCK	1.64E-05	1.67E-05	1.78E-05	1.56E-05	1.58E-05	1.65E-05	3.57E-07	3.57E-07	5.16E-07	6.18E-07	9.30E-07	5.56E-07
Glue, 12.5mm, BUCK	3.24E-05	4.79E-05	3.82E-05	3.48E-05	3.13E-05	3.69E-05	1.21E-06	2.17E-07	1.49E-06	3.36E-06	3.67E-06	1.99E-06
Pin, 8mm, Unbuckled	4.24E-05	3.66E-05	3.41E-05	2.36E-05	1.80E-05	3.09E-05	1.66E-06	2.33E-06	3.66E-06	2.78E-06	2.36E-06	2.56E-06
Pin, 12.5mm, Unbuckled	3.88E-05	3.28E-05	3.04E-05	2.17E-05	1.95E-05	2.86E-05	1.76E-06	2.15E-06	2.95E-06	2.42E-06	2.34E-06	2.32E-06
Pin, 8mm, BUCK	1.67E-05	1.28E-05	1.06E-05	2.20E-05	1.94E-05	1.63E-05	9.79E-07	1.23E-06	1.42E-06	3.12E-06	2.89E-06	1.93E-06
Pin, 12.5mm, BUCK	1.49E-05	1.28E-05	1.25E-05	2.02E-05	1.74E-05	1.56E-05	9.74E-07	1.33E-06	2.24E-06	2.70E-06	2.67E-06	1.98E-06
3x1, 3mm, Unbuckled	6.73E-05	5.75E-05	5.16E-05	4.47E-05	4.20E-05	5.26E-05	2.01E-06	2.61E-06	3.11E-06	2.65E-06	2.62E-06	2.60E-06
3x1, 8mm, Unbuckled	6.78E-05	5.84E-05	5.37E-05	4.61E-05	4.35E-05	5.39E-05	2.33E-06	2.43E-06	2.83E-06	2.60E-06	2.77E-06	2.59E-06
3x1, 12.5mm, Unbuckled	7.33E-05	5.96E-05	5.28E-05	4.63E-05	4.30E-05	5.50E-05	3.13E-06	3.23E-06	3.63E-06	3.50E-06	3.37E-06	3.37E-06
3x1, 3mm, BUCK	1.34E-05	1.45E-05	4.14E-05	3.31E-05	2.76E-05	2.60E-05	1.38E-06	1.24E-06	6.67E-06	5.46E-06	5.08E-06	3.97E-06
3x1, 8mm, BUCK	1.21E-05	1.20E-05	1.09E-05	1.35E-05	2.60E-05	1.49E-05	8.74E-07	1.15E-06	1.33E-06	1.89E-06	5.58E-06	2.16E-06
3x1, 12.5mm, BUCK	1.13E-05	1.12E-05	1.09E-05	1.04E-05	1.36E-05	1.15E-05	4.10E-07	7.96E-07	1.12E-06	1.20E-06	1.08E-06	9.21E-07
5x1, 8mm, Unbuckled	2.40E-05	2.21E-05	2.02E-05	1.88E-05	1.83E-05	2.07E-05	3.32E-07	5.32E-07	6.94E-07	6.45E-07	8.16E-07	6.04E-07
5x1, 12.5mm, Unbuckled	2.55E-05	2.57E-05	2.17E-05	2.03E-05	1.91E-05	2.24E-05	5.85E-07	1.25E-06	1.04E-06	9.01E-07	9.77E-07	5.90E-07
5x1, 8mm, BUCK	5.38E-06	3.87E-06	3.55E-06	4.13E-06	4.53E-06	4.29E-06	1.52E-07	1.95E-07	1.83E-07	2.78E-07	3.83E-07	2.38E-07
5x1, 12.5mm, BUCK	3.51E-06	2.01E-06	2.13E-06	3.83E-06	3.68E-06	3.03E-06	2.80E-08	2.44E-08	3.49E-08	2.44E-07	2.87E-07	1.24E-07

Table 32. FoM_{BW} metric for the reverse sweep experiments.

Reverse Sweep <---	FoMv					FoMv Avg	FoMbw					FoMbw Avg
	0.2	0.3	0.4	0.5	0.6		0.2	0.3	0.4	0.5	0.6	
Reverse												
Glue, 8mm, Unbuckled	2.16E-05	1.98E-05	1.74E-05	1.59E-05	1.52E-05	1.80E-05	6.79E-07	6.25E-07	5.58E-07	5.06E-07	4.84E-07	5.70E-07
Glue, 12.5mm, Unbuckled	3.77E-05	3.30E-05	2.93E-05	2.62E-05	2.37E-05	3.00E-05	1.36E-06	1.19E-06	1.05E-06	1.03E-06	1.00E-06	1.13E-06
Glue, 8mm, BUCK	2.57E-05	2.59E-05	2.37E-05	2.36E-05	2.34E-05	2.44E-05	4.23E-07	4.24E-07	9.54E-08	9.54E-07	2.69E-06	9.17E-07
Glue, 12.5mm, BUCK	6.86E-05	6.16E-05	3.93E-05	3.53E-05	3.19E-05	4.74E-05	3.37E-06	4.25E-06	3.36E-06	2.41E-06	2.65E-06	3.21E-06
Pin, 8mm, Unbuckled	2.32E-05	2.13E-05	1.86E-05	1.65E-05	1.58E-05	1.91E-05	7.98E-07	1.22E-06	1.32E-06	1.23E-06	8.60E-07	1.09E-06
Pin, 12.5mm, Unbuckled	2.24E-05	1.91E-05	1.85E-05	1.60E-05	1.63E-05	1.85E-05	8.10E-07	1.05E-06	1.52E-06	1.22E-06	1.06E-06	1.13E-06
Pin, 8mm, BUCK	1.38E-05	1.27E-05	9.19E-06	1.41E-05	1.35E-05	1.27E-05	9.78E-07	1.92E-06	8.11E-07	1.37E-06	1.65E-06	1.35E-06
Pin, 12.5mm, BUCK	2.29E-05	1.49E-05	1.43E-05	1.37E-05	1.35E-05	1.59E-05	3.39E-06	2.90E-06	2.35E-06	1.99E-06	1.24E-06	2.38E-06
3x1, 3mm, Unbuckled	3.50E-05	2.95E-05	2.69E-05	2.35E-05	2.22E-05	2.74E-05	1.19E-06	1.10E-06	1.08E-06	1.11E-06	1.22E-06	1.14E-06
3x1, 8mm, Unbuckled	3.97E-05	3.72E-05	3.23E-05	3.02E-05	2.74E-05	3.34E-05	1.04E-06	1.75E-06	1.39E-06	1.79E-06	1.72E-06	1.54E-06
3x1, 12.5mm, Unbuckled	3.87E-05	3.65E-05	2.95E-05	2.77E-05	2.53E-05	3.15E-05	1.45E-06	2.16E-06	1.61E-06	1.86E-06	1.90E-06	1.80E-06
3x1, 3mm, BUCK	2.83E-05	1.76E-05	1.23E-05	1.58E-05	2.46E-05	1.97E-05	5.88E-06	1.52E-06	1.98E-07	1.38E-06	3.27E-06	2.45E-06
3x1, 8mm, BUCK	6.05E-05	2.93E-05	2.89E-05	2.59E-05	2.51E-05	3.39E-05	6.67E-06	3.35E-06	2.18E-06	2.98E-06	2.79E-06	3.59E-06
3x1, 12.5mm, BUCK	3.25E-05	1.91E-05	1.35E-05	1.13E-05	2.60E-05	2.05E-05	5.92E-06	2.45E-06	1.49E-06	1.49E-06	3.80E-06	3.03E-06
5x1, 8mm, Unbuckled	1.62E-05	1.59E-05	1.55E-05	1.18E-05	1.14E-05	1.42E-05	1.22E-07	2.94E-07	3.98E-07	5.09E-07	4.15E-07	3.48E-07
5x1, 12.5mm, Unbuckled	1.66E-05	1.40E-05	1.40E-05	1.30E-05	1.19E-05	1.39E-05	4.11E-07	4.56E-07	7.27E-07	6.19E-07	6.53E-07	5.73E-07
5x1, 8mm, BUCK	2.99E-05	1.71E-05	1.48E-05	1.28E-05	1.14E-05	1.72E-05	1.63E-06	2.17E-06	2.48E-06	1.54E-06	1.10E-06	1.79E-06
5x1, 12.5mm, BUCK	1.14E-05	1.67E-05	1.56E-05	1.50E-05	1.45E-05	1.46E-05	8.31E-07	4.24E-06	4.14E-06	4.28E-06	4.15E-06	3.53E-06

Table 33. Swept volume, input displacement at max, and mass for the forward swept experiments.

Forward Sweep --->	Vol (mm ³)					Y0 (m)					Mass (Kg)
Forward	0.2	0.3	0.4	0.5	0.6	0.2	0.3	0.4	0.5	0.6	
Glue, 8mm, Unbuckled	3295	3295	3295	3295	3295	1.67E-04	2.56E-04	3.44E-04	4.39E-04	5.27E-04	0.0117
Glue, 12.5mm, Unbuckled	3385	3385	3385	3385	3385	1.81E-04	2.71E-04	3.59E-04	4.39E-04	5.27E-04	0.0117
Glue, 8mm, BUCK	3295	3295	3295	3295	3295	1.85E-04	2.69E-04	3.69E-04	4.58E-04	5.70E-04	0.0117
Glue, 12.5mm, BUCK	3385	3385	4210	4210	4210	3.07E-04	4.32E-04	5.27E-04	6.20E-04	6.91E-04	0.0117
Pin, 8mm, Unbuckled	5770	5770	5770	5770	5770	2.68E-04	3.82E-04	4.80E-04	5.81E-04	7.57E-04	0.0117
Pin, 12.5mm, Unbuckled	5860	5860	5860	5860	5860	2.90E-04	4.02E-04	5.01E-04	6.47E-04	7.70E-04	0.0117
Pin, 8mm, BUCK	5770	5770	5770	10170	10170	4.81E-04	7.56E-04	1.06E-03	8.45E-04	9.75E-04	0.0117
Pin, 12.5mm, BUCK	5770	5770	5770	10170	10170	4.98E-04	7.84E-04	1.16E-03	8.61E-04	9.66E-04	0.0117
3x1, 3mm, Unbuckled	5120	5120	5120	5120	5120	2.55E-04	3.60E-04	4.54E-04	5.49E-04	6.44E-04	0.0117
3x1, 8mm, Unbuckled	5220	5220	5220	5220	5220	2.05E-04	3.03E-04	3.97E-04	4.97E-04	5.92E-04	0.0117
3x1, 12.5mm, Unbuckled	5310	5310	5310	5310	5310	2.57E-04	3.66E-04	4.61E-04	5.58E-04	6.49E-04	0.0117
3x1, 3mm, BUCK	5120	5120	8420	8420	8420	5.16E-04	9.13E-04	6.32E-04	8.28E-04	1.04E-03	0.0117
3x1, 8mm, BUCK	5220	5220	5220	5220	8520	3.28E-04	5.33E-04	7.79E-04	1.02E-03	1.00E-03	0.0117
3x1, 12.5mm, BUCK	5310	5310	5310	5310	5310	2.90E-04	4.78E-04	6.76E-04	8.88E-04	1.17E-03	0.0117
5x1, 8mm, Unbuckled	4945	4945	4945	4945	4945	1.68E-04	2.49E-04	3.32E-04	4.15E-04	4.95E-04	0.0117
5x1, 12.5mm, Unbuckled	5035	5035	5035	5035	5035	2.06E-04	2.94E-04	3.86E-04	4.79E-04	5.62E-04	0.0117
5x1, 8mm, BUCK	4945	4945	4945	4945	4945	2.30E-04	3.72E-04	5.18E-04	7.07E-04	9.30E-04	0.0117
5x1, 12.5mm, BUCK	5035	5035	5035	5035	5035	2.25E-04	3.46E-04	4.72E-04	6.36E-04	7.90E-04	0.0117

Table 34. Swept volume, input displacement at max, and mass for the reverse swept experiments.

Reverse Sweep <---	Vol (mm ³)					Y0 (m)					Mass (Kg)
Reverse	0.2	0.3	0.4	0.5	0.6	0.2	0.3	0.4	0.5	0.6	
Glue, 8mm, Unbuckled	3295	3295	3295	3295	3295	1.71E-04	2.60E-04	3.56E-04	4.39E-04	5.27E-04	0.0117
Glue, 12.5mm, Unbuckled	3385	3385	3385	3385	3385	1.83E-04	2.73E-04	3.59E-04	4.48E-04	5.27E-04	0.0117
Glue, 8mm, BUCK	3295	3295	3295	3295	4210	2.38E-04	3.54E-04	4.57E-04	5.76E-04	7.08E-04	0.0117
Glue, 12.5mm, BUCK	3385	3385	4210	4210	4210	2.80E-04	3.92E-04	5.14E-04	6.42E-04	7.26E-04	0.0117
Pin, 8mm, Unbuckled	5770	5770	5770	5770	5770	3.38E-04	4.78E-04	6.26E-04	7.67E-04	8.64E-04	0.0117
Pin, 12.5mm, Unbuckled	5860	5860	5860	5860	5860	3.74E-04	5.22E-04	6.56E-04	7.97E-04	9.21E-04	0.0117
Pin, 8mm, BUCK	5770	5770	5770	10170	10170	4.92E-04	8.34E-04	9.73E-04	1.48E-03	1.57E-03	0.0117
Pin, 12.5mm, BUCK	5770	10170	10170	10170	10170	6.97E-04	1.51E-03	1.57E-03	1.67E-03	1.83E-03	0.0117
3x1, 3mm, Unbuckled	5120	5120	5120	5120	5120	2.55E-04	3.60E-04	4.54E-04	5.49E-04	6.44E-04	0.0117
3x1, 8mm, Unbuckled	5220	5220	5220	5220	5220	2.68E-04	3.85E-04	5.18E-04	6.26E-04	7.38E-04	0.0117
3x1, 12.5mm, Unbuckled	5310	5310	5310	5310	5310	3.10E-04	4.40E-04	5.86E-04	7.00E-04	8.26E-04	0.0117
3x1, 3mm, BUCK	5120	5120	5120	5120	8420	5.93E-04	6.97E-04	8.13E-04	1.20E-03	1.41E-03	0.0117
3x1, 8mm, BUCK	5220	8520	8520	8520	8520	1.01E-03	1.08E-03	1.11E-03	1.29E-03	1.30E-03	0.0117
3x1, 12.5mm, BUCK	5310	5310	5310	5310	8610	5.56E-04	6.58E-04	7.79E-04	9.74E-04	1.44E-03	0.0117
5x1, 8mm, Unbuckled	4945	4945	4945	4945	4945	1.99E-04	2.87E-04	3.77E-04	4.58E-04	5.58E-04	0.0117
5x1, 12.5mm, Unbuckled	5035	5035	5035	5035	5035	2.40E-04	3.51E-04	4.50E-04	5.58E-04	6.54E-04	0.0117
5x1, 8mm, BUCK	4945	7420	7420	7420	7420	5.16E-04	7.05E-04	8.78E-04	1.06E-03	1.21E-03	0.0117
5x1, 12.5mm, BUCK	5035	7510	7510	7510	7510	3.31E-04	1.11E-03	1.30E-03	1.36E-03	1.49E-03	0.0117

CURRICULUM VITA

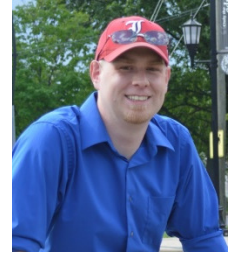
Daniel Allen Porter

Mechanical Engineering

Nationality: U.S.A

Email: xquicksilverx@gmail.com or daport02@louisville.edu

Phone: 502-558-4551



Education

- 9/10–5/15 **Ph.D. in Mechanical Engineering**
University of Louisville Speed School of Engineering, Louisville, KY
Dissertation: ‘*Bi-stable Buckled Energy Harvesters Actuated via Torque Arms*’
- 12/07–8/10 **M.S. in Mechanical Engineering**
University of Louisville Speed School of Engineering, Louisville, KY
Thesis: ‘*Die Separation Strength for Deep Reactive Ion Etched Wafers*’
- 1/04–12/07 **B.S., Mechanical Engineering**
University of Louisville Speed School of Engineering, Louisville, KY

Professional Experience

- 8/10–5/15 **University of Louisville, Louisville, KY.**
Position: *Research Assistant and PhD Candidate*
- Macro and MEMS level fabrication of a novel energy harvester device.
 - Parameter performance evaluation using experimental and FEA data.
 - Silicon wafer fracture mechanics.
 - Buckled diaphragm sensor modeling and testing.
 - 3D printer construction, operation, and modification.
 - Experimental vibration table design and construction.
 - Data acquisition circuit construction and testing.
 - PZT and PVDF sol gel deposition methods.
 - Piezoelectric electroding and poling methods.
 - Corona polling station design and construction.
 - High voltage (10k) supply design and construction.
 - Additive manufacturing methods for in-situ poling of PVDF.

- 1/13 – 4/13 **MicroWerks**, Louisville, KY.
 Position: *Independent Contractor*
- Precision micro patterning in glass substrates.
 - Parameter characterization for etching solutions.
- 1/10 – 8/10 **Sandia National Laboratories**, Albuquerque, NM.
 Position: *Student Engineering Intern*
-Acquisition of Government Security Clearance (L).
- Defense Advance Research Project Agency (DARPA) project participant (Phase 4).
 - Construction of automated MEMS valve testing apparatus.
 - Created (new) dynamic LabVIEW program for micro valve testing system.
 - Gas chromatograph column coating and evaluation.
 - LabVIEW valve programming for LOC (Lab On a Chip) testing.
 - Design and testing of macro valve for MEMS assembly incorporation.
- 1/08 – 8/08
- Defense Advance Research Project Agency (DARPA) project participant (Phase 3).
 - Macro valve design, research, and testing.
 - Created dynamic VB 6 program for micro valve testing system.
 - Data acquisition and evaluation for thin film nano-particle chemical sensors (Chemistor).
 - Circuit board design for low chatter valve operations.
- 8/06 – 5/07
- Testing and evaluation of pivot plate resonators (PPR) chemical sensors.
 - Produce Sol Gel for nano-porous chemical sensing coatings.
 - Coating of PPRs using ultra sonic nebulizer.
 - Program data acquisition and graphing routines in VB 6 for PPR devices.
 - PIC programming for custom PPR circuit board control.
 - Gas-chromatograph modification and oven operations for chemical sensing.
- 5/05 – 8/05
- Circuit board layout for pivot plate resonators (PPR).
 - Model and order custom parts for chemical pre-concentrators, signal acoustic wave (SAW) sensors, and gas-chromatograph columns.
 - Population of circuit boards.
 - Design, fabrication, and assembly of custom parts.

Publications

Journal Articles

Porter, Daniel A. and Berfield Thomas A. (2014). Constraint Effects on Torque Actuated Bi-Stable Energy Harvesters.

Pending...

Porter, Daniel A. and Berfield Thomas A. (July 2014). 'A bi-stable buckled energy harvesting device actuated via torque arms'. *Smart Materials and Structures* **23**(7), 075003 (12 pp.).

[ISSN 09641726](#)

Porter, Daniel A. and Berfield Thomas A. (Aug. 2013). 'Die separation and rupture strength for deep reactive ion etched silicon wafers'. *Journal of Micromechanics and Microengineering* **23**(8), 085020 (8 pp.).

[ISSN 0960-1317](#)

Manginell, R., Adkins, D., Moorman, M., Rameen, H., Copic, D., Porter, D., Anderson, J., Wheeler, D., Pfeifer, K., and Rumpf, A. (2008). 'Mass sensitive, Lorentz-Force actuated, MEMS preconcentrator and chemical sensor'. *Chemical Sensors 8: Chemical (Gas, Ion, Bio) Sensors and Analytical Systems* **16**(11), p 155-163.

[ISSN 19385862](#)

Conferences

Porter, D., Gowrishetty, U., Phelps, I., Walsh, K., and Berfield, T. (2012). Mechanics of buckled structure MEMS for actuation and energy harvesting applications. ASME International Mechanical Engineering Congress and Exposition, Proceedings (IMECE), v 9, p 49-54.

[ISBN 9780791845257](#)

Porter, D., Gowrishetty, U., Phelps, I., Walsh, K., and Berfield, T. (2012). Mechanics of buckled structure energy harvesting MEMS. ASME International Mechanical Engineering Congress and Exposition, Presentation (IMECE).

Presentation Only

Porter, Daniel A. and Berfield Thomas A. (2010). Die separation strength for deep reactive ion etched wafers. Society for Experimental Mechanics – SEM Annual Conference and Exposition on Experimental and Applied Mechanics 2010 **2**, pp 1549-1557.

[ISSN 21915644](#)

Honors and Activities

- Wilhelm Solar Flight Competition 2014.
 - Co-captain. 1st place.
 - Design solar powered RC airship with thrust vectoring.
- Engineering Expo Graduate Competition Winner 5th place.
- Wilhelm Solar Flight Competition 2013.
 - Co-captain. 1st place.
 - Designed solar powered RC airplane.
- UofL Rocket Team 2013.
 - *Recovery Electrical/Mechanical.*
 - *NASA Student Launch Initiative Competition 2nd place.*
 - *ASME Diversity Grant Winner.*

-
- Graduate Student Counsel ME Representative 2012-2014.
 - International Workshop on Piezoelectric Materials and Applications 2011
 - UofL ME Graduate Fellowship Recipient 2010
 - Society of Experimental Mechanics Conference 2010
 - Mechanical Engineering Department Alumni Award 2009
 - Robert Craig Ernst Scholarship Award 2008
 - Senior Year Academic Achievement Award 2007
 - Dean's List, UofL 2004-2008
 - ASME Student Member
 - Nintendo Entertainment System Emulator Development (QS NES, VB6)

Skills

Clean-room Fabrication

- Dry photo-resist lamination
- Wet photo-resist spinning
- Dry photo-resist techniques
- Wet bench (acid, base, RCA, and solvent hoods)
- PVD
- Oxidation
- Hot plate
- Mask aligner
- UV exposure
- RIE and DRIE
- Tube furnace
- PECVD
- Profilometer
- Ion milling
- Wire bonding
- Ellipsometer

FEA:

- Static and transient solid
- Large displacement buckling analysis
- Snap through
- Static and transient thermal
- Harmonic
- Modal

Programming:

- C/C++
- Visual Basic 6
- LabVIEW
- MATLAB

Design:

- Circuit
- Circuit board
- Component and assembly
 - *Solid Works*
- MEMS devices
- FDM hotend design
- Extruder for FDM
- Cartesian bot design and fabrication
- Laser cutter design
- Material testing stand design
- Three and four point testing rigs
- Corona polling station
- Gear boxes
- Robot kinematics
 - Skytower
 - Open-chain links
 - Inverse-kinematics solutions

Misc:

- Grant writing
 - *NSF*
- X-ray diffraction
- Scanning electron microscope
- White light interferometry
- FTIR
- High pressure tank operations
- DAQ and graph programming
- Gas Chromatography
 - *GC column coating & performance*
- Remote control applications
- Small scale construction
- Quad copter design

Machining:

- Drill press
- Milling machine
- Lathe
- Band saw
- Electric sander
- Router
- 3D CNC bots
- MIG welding

Electronics:

- Soldering
- Oscilloscope
- Waveform generators
- Data acquisition
- Microcontrollers
 - *Arduino*
 - *PIC*
 - *Basic Stamp*
- LCD displays
- Super capacitor energy storage
- DC-DC converters
- Pressure sensors
- Relay implementation
- Data acquisition